Contribution to the investigation of the compressive strength and delamination of continuous fibers laminated composites in the context of competitive sailing

Monia Grabow

Monia Grabow. Contribution to the investigation of the compressive strength and delamination of continuous fibers laminated composites in the context of competitive sailing. Materials. Université de Bretagne Sud, 2021. English. NNT : 2021LORIS599 . tel-03563613

HAL Id: tel-03563613
https://theses.hal.science/tel-03563613v1
Submitted on 9 Feb 2022

THÈSE DE DOCTORAT DE

L'UNIVERSITÉ DE BRETAGNE SUD

ÉCOLE DOCTORALE N° 602
Sciences pour l'Ingénieur
Spécialité : *Mécanique des Solides, des Matériaux, des Structures et des Surfaces*

Par
Monia GRABOW

Contribution to the investigation of the compressive strength and delamination of continuous fibre laminated composites in the context of competitive sailing

Thèse présentée et soutenue à Lorient, le 2 juillet 2021
Unité de recherche : Institut de Recherche Dupuy de Lôme UMR CNRS 6027
Thèse N° : 599

Rapporteurs avant soutenance :

Laurent GUILLAUMAT	Professeur des Universités, ENSAM Angers
Nadia BAHLOULI	Professeure des Universités, UNISTRA Strasbourg

Composition du Jury :

Examinateurs :	Loïc DARIDON	Professeur des Universités, Université de Montpellier
Examinateurs :	Denis CARTIÉ	Coriolis Composites
Dir. de thèse :	Vincent KERYVIN	Professeur des Universités, Université Bretagne Sud
Co-dir. de thèse :	Christophe BALEY	Professeur des Universités, Université Bretagne Sud
Co-dir. de thèse :	Jean-Claude GRANDIDIER	Professeur des Universités, ENSMA Poitiers

"Humility is the first milestone to true greatness."
—R.G.

Acknowledgements

Completed after defence.

Résumé français

Les travaux de recherche du présent mémoire de thèse portent sur deux thèmes liés aux hydrofoils de navires en matériaux composites. Les hydrofoils sont dimensionnés en termes de résistance en compression et en résistance hors plan.

Le premier porte sur la confrontation des résistances en compression de sept matériaux différents (fibres de carbon/matrice époxy), déterminées par deux méthodes expérimentales différentes. L'une contient des essais de traction bibiais, la détermination de l'angle de désalignement de fibres et l'application des solutions analytiques de Budiansky & Fleck et Grandidier et al.. Et l'autre est basée sur des essais de flexion 4 points (4PB). Ce sujet se concentre sur la détermination des angles de désalignement dans le plan et hors plan en utilisant la méthode de Yurgartis. L'objectif est de relier l'angle de désalignement déterminé à la confrontation des résistances en compression. Par conséquent, des cartographies de la distribution spatiale des fibres sont établies afin d'évaluer les résultats.

Le second sujet traite de l'influence du processus de fabrication des cornières en carbone/époxy sur la réponse du matériau, particulièrement sur la résistance hors plan (ILTS). Les hydrofoils sont aujourd'hui traditionnellement fabriqués à la main, par drapage de plis pré-imprégnés, et plus récemment, par la technologie de placement automatisé de fibres (AFP). Des cornières unidirectionnelles sont donc fabriquées par les deux technologies, elles sont testées en flexion 4 points et les résultats sont confrontés. Le lien au processus de fabrication est analysé.

Partie II : La résistance en compression X_c

La première partie commence par une brève introduction aux modèles de micro flambage de fibres. Le *kink-band* modèle de Budiansky & Fleck [1993], ainsi que le modèle de Grandidier et al. [2012], qui prend en compte l'effet de structure, sont présentés.

Grandidier et al. [2012] mentionne que la plasticité de la matrice a un impact déterminant sur le développement des mécanismes d'instabilité du matériau dans des régions locales, et que l'angle de désalignement de fibres contribue à ces développements d'instabilité.

Dans la littérature, l'angle de désalignement est considéré comme paramètre clé dans la détermination de la résistance en compression. C'est pour cette raison que les termes *"fibre misalignment"* et *"fibre waviness"* sont définis dans la suite en se référant à la littérature. Ensuite, une étude sur l'origine du désalignement de fibres liée au processus de fabrication est effectuée. L'étude de Potter [2009] est mentionnée, car son diagramme taxonomique visualise bien les origines des différents types de défauts, entre autres les origines du désalignements de fibres. L'impact du désalignement de fibre sur les propriétés mécaniques des structures composites est ensuite discuté. Enfin, différentes méthodes existantes pour déterminer l'angle de désalignement sont présentées. Les avantages et les limites, ainsi que des références de la littérature y sont données.

La méthode de Yurgartis est introduite en expliquant les différentes directions de découpe, le long de l'épaisseur et le long de la largeur de l'éprouvette, ainsi que les fonctions trigonométriques permettant de calculer les angles de désalignement dans le plan et hors plan. Deux paramètres, le diamètre des fibres et l'axe majeur de l'ellipse, sont nécessaires pour le calcul. En pratique, plusieurs étapes sont réalisées pour passer de l'échantillon brut à l'angle de désalignement plan et hors plan : découpe de l'éprouvette le long de l'épaisseur et le long de la largeur, enrobage et polissage des plots, prise d'image avec un microscope optique, post-traitement des images avec *ImageJ* [Rueden et al., 2017], calcul des angles de désalignement en prenant un écart type de la loi normale.

Pour la détermination des angles de désalignement, une étude de sensibilité sur le diamètre de fibres est réalisée. Les angles de désalignement de fibres déterminés à partir de quatre sources de diamètres différents sont comparés. La moyenne du premier diamètre est déterminée en sectionnant les spécimens perpendiculairement à la direction des fibres (diamètre constant). Cette approche est celle appliquée dans la méthode de Yurgartis. La deuxième source de diamètre correspond à la valeur donnée sur la fiche technique des fibres de carbone (diamètre constant). Enfin, l'axe mineur des ellipses est considéré comme troisième source de diamètre (diamètre variable). La valeur moyenne des axes mineurs constitue la quatrième source (diamètre constant).
Il est constaté que le diamètre déterminé selon la méthode de Yurgartis, ainsi que la valeur moyenne des axes mineurs sont les sources de diamètre cohérentes dans la détermination des angles de désalignement. La valeur moyenne des axes mineurs est finalement choisie dans la suite de l'étude car elle ne nécessite pas une section perpendiculaire à la direction de fibres.
Grâce à cette étude de sensibilité, il est également constaté que la section de fibres des séries 1 et 2 n'est pas circulaire, mais déformées, ressemblant à des *"haricots"*. Des observations similaires sont données dans Paluch [1994]. Les diamètres moyens de fibres des séries 1 et 2 ne sont donc pas déterminés correctement. Les séries 1 et 2 sont donc exclues dans la suite de l'étude.

La première méthode expérimentale nécessite la réalisation d'essais de traction bibiais pour déterminer les paramètres de la loi de Ramberg-Osgood (RO). Ces essais sont réalisés selon la norme NF EN ISO 14129 (NF EN ISO, 1998). Tous les paramètres nécessaires (ceux de la loi de RO et l'angle de désalignement de fibres) sont donc déterminés pour appliquer les solutions analytiques de Budiansky & Fleck et Grandidier et al..
La deuxième méthode expérimentale pour déterminer la résistance en compression nécessite la réalisation des essais de flexion quatre points (4PB). Cela est fait conformément à la norme ASTM D6272 (ASTM, 2008).
Pour obtenir des informations détaillées sur la mise en œuvre des tests, le lecteur est invité à se reporter vers Mechin et al. [2019].

La confrontation des résistances en compression déterminées par les deux méthodes est réalisée en les traçant en fonction des angles de désalignement de fibres dans le plan et hors plan. Les résultats ont été évalués par rapport aux distributions spatiales de fibres le long des axes x et y. Ainsi, des cartographies des distributions d'alignement de fibres ont été créées et l'arrangement de fibres a été classé en différentes catégories : regroupements de fibres inférieurs ou supérieurs à un écart type ($\leq$-1σ ou $\geq$1σ), fibres individuelles fortement désalignées ou distributions de fibres inhomogènes.

Il est constaté que, lorsque la résistance en compression analytiquement estimée en utilisant l'angle de désalignement hors plan, la coïncidence entre les deux résistances est lié à la distribution spatiale de l'angle de désalignement observée.
Cela veut dire que lorsque les deux résistances en compression sont proches ou égales, peu de fibres groupés ou de fibre fortement désaligné sont observées. Lorsqu'elles ne sont pas proches, peu de regroupement de fibres ou fibres fortement désalignées sont présentes. Cela correspond à 70-80 % des cas observés.
Les mêmes observations ne sont pas faites pour les résistances en compression déterminées analytiquement en utilisant l'angle de désalignement plan. Seulement dans 10-50 % des cas, la coïncidence entre les résistances en compression peut être liée à la distribution spatiale de fibres.

Pour les études futures, il est proposé de coder un algorithme détectant les dimensions (axes majeur et mineur) et les positions de toutes les ellipses à partir des images prises le long de la largeur et le long de l'épaisseur des spécimens, afin de définir plus précisément l'angle de désalignement de fibres, et d'introduire un autre paramètre dans la discussion : la fraction volumique locale des fibres.

Partie III : La résistance hors plan (ILTS)

La deuxième partie commence par une bibliographie sur la détermination de la résistance hors plan en lien avec la fabrication d'éprouvettes, ainsi que sur la confrontation des résultats mécaniques d'éprouvettes de différentes formes fabriquées à la main et par la technologie de placement de fibres automatisé.
Des études d'essais de traction [Kitching et al., 1984; Lagace & Weems, 1989; Hodgkinson et al., 1992], et des essais sur des éprouvettes en forme courbée (semi-circulaires Hiel et al. [1991]; Ko & Jackson [1989], semi-elliptiques Hiel et al. [1991]; Ko & Jackson [1990], type cornière Charrier et al. [2016]; Jackson & Ifju [1996]; Ranz et al. [2017]; Shivakumar et al. [1994], *horseshoe* Ko & Jackson [1990], and *humpback* Wisnom & Jones [1996]), chargées dans différentes configurations, sont abordée.
La configuration développée par Jackson & Ifju [1996], ainsi que les solutions analytiques de Lekhnitskii [1968] et de Kedward et al. [1989] ont été mises en œuvre dans la norme ASTM D6415 / D6415M-06a [2013], et constituent, aujourd'hui, la base pour la détermination de la résistance hors plan des composites unidirectionnels.

Trois outils développés dans le cadre de cette étude pour confronter les résultats des cornières fabriquées à la main et par la technologie de placement de fibres automatisé,

testées en flexion quatre points, sont présentés.
L'outil analytique comprend la maîtrise des solutions analytiques de Lekhnitskii [1968] et de Kedward et al. [1989]. Les deux solutions sont codées en langage python. L'outil analytique est validé avec des résultats se trouvant dans la littérature [Charrier et al., 2016]. L'outil expérimental comprend la conception du banc d'essai. Des aspects géométriques, mécaniques et technologiques sont abordés. En outre, l'instrumentation appliquée (stéréo-corrélation d'image, émission acoustique, LVDT, jauges), lors de l'essai, ainsi que la mise en œuvre de l'essai sont présentés. L'outil numérique, la création du modèle éléments finis, est finalement introduit. Le code commercial Abaqus 6, version 6.14, est utilisé. Afin d'automatiser la création du modèle, des scripts codés en python et en Abaqus python sont développés. Des études de sensibilité sur l'influence du maillage de la cornière et du matériau choisi pour les rouleaux sur les résultats numériques sont menées. Le maillage a été affiné jusqu'à l'obtention de différences inférieures à 1 % sur les diagrammes force-déplacement. Les rouleaux sont considérés comme rigides, car la déformation des rouleaux est négligeable. Enfin, l'outil numérique est validé avec les résultats se trouvant dans la littérature [Charrier et al., 2016].

Ensuite, les propriétés matériaux, ainsi que les procédés de fabrication des cornières à partir de pré-imprégnés carbone-époxy, le drapage manuel et le drapage par la technologie de placement de fibres automatisé, sont présentés. Un protocole sur la réalisation des essais de flexion quatre points sur cornières est donné.

Tout d'abord, une explication de la non-linéarité des diagrammes force-déplacement au début de l'essai est donné. Des calculs d'éléments finis sont effectués pour apercevoir que la non-linéarité est le résultat d'un changement du point de contact entre la cornière et la pointe du LVDT à cause d'une légère différence dans l'alignement vertical des rouleaux inférieures.

Ensuite, il est constaté que la solution analytique de Kedward et al. [1989] donne des résultats de résistance hors-plan plus proches du calcul numérique que la solution de Lekhnitskii [1968]. Le pourcentage d'erreur de la solution de Kedward et al. est inférieur à 5 %. Celle de Lekhnitskii [1968] diffère entre 10 et 15 % des valeurs numériques. En reproduisant Fig. 5.2 de Kedward et al. [1989] avec les propriétés élastiques du matériau utilisé dans cette étude, et en ajoutant les calculs d'éléments finis, il est constaté que la solution de Kedward et al. [1989] est plus proche du calcul numérique.

Les résultats des essais de flexion quatre points des cornières drapé à la main et par la technologie de placement de fibres automatisé sont ensuite confrontés.

Une grande reproductibilité de tests est constatée pour les deux types de cornière.

Les différences de largeur et de rayon intérieur des deux types de cornières se situent dans les limites de la précision des instruments de mesure et sont donc considérées comme

négligeables. Les angles initiaux entre la ligne horizontale et les bras des spécimens des deux types de cornières sont également les mêmes.
Les épaisseurs des cornières drapées à la main et par la technologie de placement de fibres automatisé se distinguent au niveau du rayon et des bras. Au niveau du rayon, les cornières drapées à la main sont plus minces que celle drapées par la technologie de placement de fibres automatisé. Les bras des cornières drapées manuellement sont plus épais que ceux des cornières drapées par le robot. Il est observé que les variations dans l'épaisseur des cornières drapées à la main sont deux fois plus grandes que celles drapées par la technologie de placement de fibres automatisé. Il est constaté que cela est lié au mode de compactage pendant le processus de fabrication.

Les deux types de cornières sont ensuite comparés en termes de rigidité. Aucune différence de comportement n'est constatée entre le drapage manuel et la fabrication par le robot en termes d'élasticité.

Les localisations des premières fissures de rupture sont comparés analytiquement, numériquement et expérimentalement. La solution analytique de Lekhnitskii [1968] et le calcul numérique donnent une localisation de première rupture à environ 0,3 (valeur normalisée sur l'épaisseur) du rayon intérieur. Cela correspond à une localisation de rupture théorique située entre les plies 12 et 13 (empilement de 42 plies). Expérimentalement, cinq sur sept cornières fabriquées par la technologie de placement de fibres automatisé fissurent à un endroit très proche de la localisation analytique/numérique. Aucune des cornières drapées à la main ne se fissure près de la localisation radiale théorique. Il est donc conclu que les cornières drapées manuellement ne cassent pas à la position radiale de la contrainte hors plan maximale à cause des défauts de matériaux et des hétérogénéités qui provoquent une rupture prématurée du matériau. Au contraire, les cornières drapées par le robot atteignent leur limite mécanique. Dans ce cas, les défauts de matériaux sont supposés être suffisamment petits pour exclure une rupture prématurée du composite.

Les deux types cornières sont étudiés en termes de défauts macroscopiques. Les spécimens sont polis et examinés en utilisant un stéréo microscope. Aucun défaut macroscopique, l'apparition de gerçures (défaut d'ondulation de pli $> 4°$), susceptible de provoquer une rupture prématurée des cornières n'a pu être observé.

Les cornières drapées par le robot atteignent des résultats en résistance hors plan bien plus élevés que celles drapées à la main. Les forces à ruptures moyennes des deux types de cornières se distinguent de 40.2 %. La même différence est trouvée pour la résistance hors plan analytiquement estimées. Les valeurs de résistance hors plan des cornières drapées par le robot sont 40.2 % plus élevées que celles des cornières drapées à la main. La différence du résultats numérique s'élève à 43.0 %. En calculant la valeur de la résistance hors plan numérique à la localisation de la première fissure de rupture observée expérimentalement, la différence s'augmente à 46.8 %.
Une explication de cette différence est trouvée dans les modes de compactage au cours

des processus de fabrication. Le compactage intermédiaire sous vide tous les trois plis lors du drapage manuel est normal à la surface du pré-imprégné et non au moule, comme cela est le cas pour les plis posés par la technologie de placement de fibres automatisé [Marchandise, 2020].
Lors de la pose manuelle, des variations dans l'épaisseur de plis sont créées. Puisque le compactage intermédiaire est appliqué tous les trois plis, la longueur développée du troisième pli est toujours plus longue que celle du premier pli (le premier pli est posé sur un pli compacté). Il en résulte des tensions de fibres différentes dans une séquence de trois plis. Des irrégularités sur les surfaces compactées sont une conséquence. Ces petites irrégularités géométriques sont exacerbées pendant la cuisson en autoclave (à 7 bar), car la viscosité du pré-imprégné (10 Pa s) est 1000 fois inférieure à celle du compactage intermédiaire (10 000 Pa s, à 1 bar). Les différences dans l'épaisseur, mentionnées ci-dessus, entre le rayon et les bras des cornières drapées à la main sont une conséquence macroscopique. Pour les cornières drapées par le robot, la surface avant cuisson en autoclave est suffisamment régulière et la rigidité de la caul plate suffit pour corriger les petites irrégularités surfaciques.

Les cornières fabriquées par la technologie de placement automatisé de fibres n'ont pas montré de grandes zones de porosité localisée. Elles étaient plutôt diffuses et situées entre les bandes. Le chemin de la fissure était translaminaire et traversait plusieurs plis. Il présentait de nombreuses branches.
Pour les cornières drapées à la main, des grandes zones de porosité localisée ont été observées. La fissure en provenait principalement. Le chemin de la fissure était le long de la largeur et principalement intralaminaire, cependant il était interlaminaire lorsque des poches de porosité étaient observées.

Pour les études futures, il est proposé d'étudier les facteurs liés au mode de compactage et leurs conséquences (compactage normal à la surface du pré-imprégné, variation dans l'épaisseur du pli, génération de petits défauts à la surface du pré-imprégné, différences en fraction volumique de fibres dans le rayon et des bras des cornières, les variations macroscopiques de la géométrie, et les porosités) qui conduisent à la faible réponse mécanique des cornières drapées à la main.
De plus, l'attention est attirée sur le fait que les cornières représentent une géométrie simplifiée du coude de l'hydrofoil. Les défauts créés lors du processus de fabrication des semi-structures ou des hydrofoils ont un impact plus important sur le comportement du matériau (effet de taille). À ce jour, cela n'est pas un sujet maîtrisé.
Les solutions analytiques et le modèle numérique supposent de plus des cornières parfaites. Leur application aux cornières drapées avec le robot est donc plus cohérents que pour les cornières drapées à la main. En raison de l'effet de taille, le développement de tels outils pour les semi-structures et les hydrofoils est une tâche complexe.

Contents

Part I Introduction

Part II The Compressive Strength X_C

Part III The InterLaminar Tensile Strength (ILTS)

Part IV Summary and Perspectives

Communications and Publications

Annexes

Latin Symbol List - Lowercase Letters

Sign	**Description**	**SI Unit**
a_i	Major axes of ellipses (out-of-plane case).	m
$a_{i,mean}$	Mean value of the overall major axes of ellipses (out-of-plane case).	m
a'_i	Major axes of ellipses (in-plane case).	m
b_i	Minor axes of ellipses (out-of-plane case).	m
$b_{i,mean}$	Mean value of the overall minor axes of ellipses (out-of-plane case).	m
b'_i	Minor axes of ellipses (in-plane case).	m
$b'_{i,mean}$	Mean value of the overall minor axes of ellipses (in-plane case).	m
d	Diameter of an ellipse or diameter of a fibre.	m
d_f	Displacement at failure for L-beam specimens tested in 4PB.	m
d_F	Fibre diameter: $d_{90°,mean}$, b_i (b'_i), $b_{i,mean}$ ($b'_{i,mean}$) or d_{DS}.	m
$d_{90°,mean}$	Mean fibre diameter in Yurgartis' method.	m
d_{DS}	Fibre diameter from data sheets.	m
d_x	Horizontal distance between the vertical centrelines of one upper and one lower loading bar.	m
e_b	Horizontal distance between the contact points of the L-beam specimen and the upper loading bars.	m
e_b	Characteristic thickness related to the mode of microbuckling according to the ply location and the loading in Drapier et al. [1997] [Grandidier et al., 2012].	m
e'_b	Horizontal distance between the contact points of the L-beam specimen and the upper loading bars defined in the scope of this research study.	m
e_{ply}	Thickness of the ply that is involved in the instability mode in Grandidier et al.'s Equ. 2.5.	m
e_t	Horizontal distance between the contact points of the L-beam specimen and the lower loading bars.	m

Sign	Description	SI Unit
e'_t	Horizontal distance between the contact points of the L-beam specimen and the lower loading bars defined in the scope of this research study.	m
f	Fibre volume ratio in Grandidier et al.'s Equ. 2.5.	-
f	Fibre volume fraction.	-
h_{MFIA}	Domain side length used in MFIA method.	m
l_0	Lever arm; perpendicular distance from the rotation axis to the line of action of the force.	m
l_b	Horizontal distance between the vertical centrelines of the lower loading bars.	m
l'_b	Horizontal distance between the vertical centrelines of the lower loading bars defined in the scope of this research study.	m
l_t	Horizontal distance between the vertical centrelines of the upper loading bars.	m
l'_t	Horizontal distance between the vertical centrelines of the upper loading bars defined in the scope of this research study.	m
n_{UD}	Strain hardening coefficient in RO's law.	-
$nxArc$	Number of nodes along the curved segment of a L-beam specimen.	-
$nxArm$	Number of nodes along the legs length of a L-beam specimen.	-
ny	Number of nodes along the width of a L-beam specimen.	-
r_i	Inner radius of a L-beam specimen.	m
$r_{i,mean}$	Mean inner radius of L-beam specimens.	m
$r_{failure}$	Location of the first failure crack observed experimentally.	m
r_{FE}	Location of the first failure crack calculated numerically.	m
r_{gf}	Fibre gyration radius in Grandidier et al.'s Equ. 2.5.	m
r_{max}	Radial position of the maximum interlaminar tensile stress.	m
r_o	Outer radius of L-beam specimen.	m

Sign	**Description**	**SI Unit**
t	Time a wave takes to travel the distance between two AE sensors.	t
t	Thickness of L-beam specimen.	m
t_{max}	Maximum measured L-beam thickness.	m
$t_{max,mean}$	Thickness mean value of all measured maximum thicknesses (L-beam specimens).	m
t_{mean}	Calculated L-beam mean thickness.	m
$t_{mean,mean}$	Thickness mean value of all intermediate (mean) thicknesses (L-beam specimens).	m
t_{min}	Minimum measured L-beam thickness.	m
$t_{min,mean}$	Thickness mean value of all measured minimum thicknesses (L-beam specimens).	m
v	Velocity of wave with that the wave pass through the material.	$\frac{\mathrm{m}}{\mathrm{s}}$
w	Width of L-beam specimen.	m
w_{mean}	Mean width of L-beam specimens.	m
x	Distance between two Acoustic emission (AE) sensors.	m
x'	Projected distance between two AE sensors.	m

Latin Symbol List - Uppercase Letters

Sign	**Description**	**SI Unit**
A_f	Cross section surface of a fibre.	m^2
A_j	Set of square domains used in Multiple field image analysis (MFIA) method.	-
C_S	Material constant of a ply in Grandidier et al.'s Equ. 2.5.	m
D	Diameter of upper/lower loading bars.	m
D_{inf}	Diameter of the lower loading bars.	m
D_{sup}	Diameter of the upper loading bars.	m
E_θ	Elastic modulus in circumferential direction (0°-direction).	$\frac{\mathrm{kg}}{\mathrm{ms}^2}$
E_C	Young modulus in fibre direction of an unidirectional ply in Grandidier et al.'s Equ. 2.5.	$\frac{\mathrm{kg}}{\mathrm{ms}^2}$
E_F	Longitudinal elastic modulus of fibres in Grandidier et al.'s Equ. 2.5.	$\frac{\mathrm{kg}}{\mathrm{ms}^2}$
E_M	Young's modulus of the matrix in Grandidier et al.'s Equ. 2.5.	$\frac{\mathrm{kg}}{\mathrm{ms}^2}$
E_r	Elastic modulus in radial direction (out-of-plane direction).	$\frac{\mathrm{kg}}{\mathrm{ms}^2}$
E_{steel}	Elastic modulus of steel used in FE simulations.	$\frac{\mathrm{kg}}{\mathrm{ms}^2}$
F	Load at failure applied by the testing machine.	$\frac{\mathrm{kgm}}{\mathrm{s}^2}$
F_0	Preload applied in 4PB tests (L-beam specimens).	$\frac{\mathrm{kgm}}{\mathrm{s}^2}$
F_f	Load at failure of L-beam specimens tested in 4PB.	$\frac{\mathrm{kgm}}{\mathrm{s}^2}$
F_{lbar}	(Concentrated) load on one lower loading bar (4PB test setup for L-beam specimens).	$\frac{\mathrm{kgm}}{\mathrm{s}^2}$
G_{12}	Shear modulus of an unidirectional laminate.	$\frac{\mathrm{kg}}{\mathrm{ms}^2}$
G_{UD}^{RO}	Shear modulus in RO constitutive law.	$\frac{\mathrm{kg}}{\mathrm{ms}^2}$
I	Geometrical moment of inertia of one lower loading bar.	kgm^2
I	Light intensity used in MFIA method.	cd
I_f	Moment of inertia of a cylinder.	kgm^2

Sign	**Description**	**SI Unit**
L	Leg length of L-beam specimen.	m
L_{lbar}	Length of one lower loading bar.	m
N	Number of points within a domain used in MFIA method.	-
P_b	Reaction force acting on one lower loading bar.	$\frac{\text{kgm}}{\text{s}^2}$
P	Reaction force acting on the lower loading bars.	$\frac{\text{kgm}}{\text{s}^2}$
R_m	Mean radius of curved L-beam segment.	m
S	Cross section of a ± 45° laminated specimen tested in tension.	m^2
S_{ij}	Numeric stresses calculated along the width and the thickness of a L-beam specimen.	$\frac{\text{kg}}{\text{ms}^2}$
S_{11}	Numerical stress in circumferential direction of a L-beam specimen.	$\frac{\text{kg}}{\text{ms}^2}$
S_{12}	Numerical shear stress in 1-2-direction of a L-beam specimen (1 = circumferential, 2 = transverse).	$\frac{\text{kg}}{\text{ms}^2}$
S_{13}	Numerical shear stress in 1-3-direction of a L-beam specimen (1 = circumferential, 3 = radial).	$\frac{\text{kg}}{\text{ms}^2}$
S_{22}	Numerical stress in transverse direction of a L-beam specimen (along the width).	$\frac{\text{kg}}{\text{ms}^2}$
S_{23}	Numerical shear stress in 2-3-direction of a L-beam specimen (2 = transverse, 3 = radial).	$\frac{\text{kg}}{\text{ms}^2}$
S_{33}	Numerical stress in radial direction of a L-beam specimen (along the thickness).	$\frac{\text{kg}}{\text{ms}^2}$
$S_{33,max}$	Maximum radial (out-of-plane) stress calculated numerically.	$\frac{\text{kg}}{\text{ms}^2}$
X_c	Compressive strength.	$\frac{\text{kg}}{\text{ms}^2}$
X_c^{ANA}	Compressive strength analytically determined.	$\frac{\text{kg}}{\text{ms}^2}$
X_c^{EXP}	Compressive strength experimentally obtained.	$\frac{\text{kg}}{\text{ms}^2}$
$X_{c,EXP}^{mould}$	Compressive strength on the mould side experimentally obtained through 4PB tests.	$\frac{\text{kg}}{\text{ms}^2}$
$X_{c,EXP}^{sealant}$	Compressive strength on the sealant side experimentally obtained through 4PB tests.	$\frac{\text{kg}}{\text{ms}^2}$

Greek Symbol List - Lowercase Letters

Sign	**Description**	**SI Unit**
γ_y^{UD}	Critical shear yield strain in RO constitutive law.	-
γ_{12}	In-plane shear strain.	-
δ	Intensity variation parameter used in the MFIA method.	rad
ε_{11}	Deformation in circumferential direction (0° fibre direction) of a L-beam specimen.	-
ε_{33}	Deformation in radial direction (out-of-plane direction) of a L-beam specimen.	-
ε_c	Local critical strain in Grandidier et al. [2012]'s analytical solution.	-
ε_C	Deformation on the compression side of a specimen tested in 4PB.	-
ε_L	Longitudinal deformation of a ± 45° laminated specimen tested in tension.	-
ε_T	Transverse deformation of a ± 45° tensile specimen tested in tension.	-
ε_T	Deformation on the tensile side of a specimen tested in 4PB.	-
κ	Coefficient of anisotropy.	-
σ	One standard deviation (for fibre misalignment angle).	°
σ_c	Compressive failure stress in Budiansky & Fleck's and Grandidier et al.'s analytical solutions.	$\frac{\mathrm{kg}}{\mathrm{ms}^2}$
σ_{lbar}	Maximum stress acting within one lower loading bar.	$\frac{\mathrm{kg}}{\mathrm{ms}^2}$
$\sigma_{33,Lekhn.}$	Radial (out-of-plane) stress in Lekhnitskii's solution.	$\frac{\mathrm{kg}}{\mathrm{ms}^2}$
$\sigma_{33,Kedw.}$	Radial (out-of-plane) stress determined using Kedward et al.'s solution.	$\frac{\mathrm{kg}}{\mathrm{ms}^2}$
$\sigma_{\theta\theta}, \sigma_{11,Lekhn.}$	Circumferential stress (stress in 0°-direction) in Lekhnitskii's solution.	$\frac{\mathrm{kg}}{\mathrm{ms}^2}$
σ_{33}	Out-of-plane (radial) stress.	$\frac{\mathrm{kg}}{\mathrm{ms}^2}$
ϕ	Angle between the horizontal line and the specimen's legs.	rad

Sign	Description	SI Unit
ϕ_i	Initial angle (undeformed state) between the horizontal line and the specimen's arms.	rad
θ	Misalignment angle (angle of wavy fibres inclined to the nominal fibre direction).	rad
λ	Maximum span of wavy fibres referenced to the nominal fibre direction (length of the wavy region).	m
$\tau_{r\theta}$	Shear stress in the $\tau_{r\theta}$ plane in Lekhnitskii's solution.	$\frac{\mathrm{kg}}{\mathrm{ms}^2}$
τ_{12}	In-plane shear stress (1 = circumferential direction, 2 = transverse direction).	$\frac{\mathrm{kg}}{\mathrm{ms}^2}$
ν_{12}	Poisson's ratio in 1-2-direction (1 = circumferential direction, 2 = transverse direction).	-
ν_{32}	Poisson's ratio in 3-2-direction (2 = transverse direction, 3 = radial direction).	-
ν_M	Poisson's ratio of the matrix in Grandidier et al.'s Equ. 2.5.	-
ν_{steel}	Poisson's ratio of steel in FE simulations.	-
ω_i	Angle between the sectioning plane and the axis of the misaligned fibres (out-of-plane case).	-
$\omega_{i,mean}$	Mean value of the overall angles between the sectioning plane and the axis of the misaligned fibres in out-of-plane direction.	-
ω_i'	Angle between the sectioning plane and the axis of the misaligned fibres (in-plane case).	-
$\omega_{i,mean}'$	Mean value of the overall angles between the sectioning plane and the axis of the misaligned fibres in the plane.	-

Greek Symbol List - Uppercase Letters

Sign	**Description**	**SI Unit**
Δ	Vertical stroke displacement of tensile machine.	m
Φ	Angle from horizontal of the specimen legs in [°].	rad
Φ_i	In-plane fibre misalignment angle in Yurgartis's method.	rad
Φ_{PC}	Plane cut angle for specimen sectioning along the thickness used in Yurgartis's method.	rad
Φ_0	Initial inclination angle of a kink-band.	rad
Θ	Inclination angle used in the MFIA method.	rad
Θ_i	Out-of-plane fibre misalignment angle in Yurgartis's method.	rad
Θ_{PC}	Plane cut angle for specimen sectioning along the width used in Yurgartis's method.	rad

Acronyms

4PB Four point bending. 3, 4, 10–13, 15, 19–21, 31, 34–37, 53, 58, 71, 72, 75, 87–89, 91–93, 96, 108, 110, 114, 119, 121, 123–129, 135, 137, 140–146, 148, 150–152, 154, 156–174, 176–188, 190–192, 194, 196, 198, 200, 202, 204, 207–210, 220, 221, 225, 226, 231, 241–246, 249, 250

AE Acoustic emission. 11, 12, 17, 37, 127, 140, 143, 144, 146, 151, 155, 156, 160, 171, 173, 177–179, 186, 193, 209

AFP Automated fibre placement. 3, 11–13, 37, 52, 119, 129–133, 144, 150–175, 177–179, 181–183, 186–204, 209–212, 221–225, 243–247, 250

CBS Curved beam strength. 38, 138, 187, 191–193, 246

CFRP Carbon fibre reinforced polymer. 47, 56, 58–61, 63–67, 114, 120, 126, 207, 209, 241

CV Coefficient of variation. 155–157, 170, 178, 179, 185, 225, 231, 250

DIC Digital image correlation. 11, 12, 37, 52, 60, 127–129, 140, 142, 144, 146, 151, 155, 156, 158–160, 173, 178–181, 193, 209, 221, 226, 243–247

DT Direct tracking method. 9, 41, 62

FEM Finite element method. 11, 12, 19, 22, 37, 38, 46, 52, 89, 123, 125–129, 136, 144, 147–151, 156, 161, 163, 166, 167, 170, 171, 173, 177, 180, 182, 183, 185, 194, 203, 210, 225, 231, 243–245, 250

FT Fourier transform method. 9, 41, 62, 63, 249

HBM Hottinger Baldwin Messtechnik. 89

HDT Hit definition time. 146

HLT Hit lockout time. 146

HM High modulus. 31, 58, 64

HRMA High resolution misalignment analysis. 67, 249

HT Hough transformation method. 9, 41, 63, 249

ILTS Interlaminar tensile strength. 3, 9, 11, 12, 29–33, 36–38, 119–124, 126, 128, 130, 132, 134, 135, 137–143, 150–152, 156, 165–168, 170, 171, 173, 174, 177, 181–183, 185–189, 191, 194–196, 199, 201–203, 207, 209–211, 225, 231, 241, 243, 244, 250, 251

IM Intermediate modulus. 31, 68, 71, 85, 88

LVDT Linear variable differential transformer. 6, 37, 127–129, 140, 142, 144, 146, 155, 156, 158, 161, 163, 171, 178, 181, 188, 192, 209, 210, 243–246

MAN Manually laid-up. 12, 13, 37, 38, 144, 173–175, 177–204, 209–212, 226–231, 245–247, 250, 251

MFIA Multiple field image analysis. 9, 16, 19–21, 23, 41, 64–66, 241, 249

N/A Not available. 64, 164

PC Polycarbonate. 154, 176, 245

PDT Peak definition time. 146

PE Polyethylene. 92

PEEK Polyether ether ketone. 53, 64

PLA Fibre reinforced polylactide. 61

RO Ramberg-Osgood. 4, 16, 19, 21, 35, 36, 44, 58, 89–91, 94, 208, 249

RTM Resin transfer moulding. 50, 241

SD Standard deviation. 21, 63, 64, 73, 79, 82, 95, 155, 157, 170, 178, 179, 185, 208, 225, 231, 242, 250

SEM Scanning electron microscope. 57, 58, 63, 77

ST Structure tensor method. 9, 41, 61

UD Unidirectional. 63, 66

X-ray CT (Micro) X-ray computed technology. 9, 41, 60, 61, 249

PART I

INTRODUCTION

"There is nothing either good or bad, but thinking makes it so."

—WILLIAM SHAKESPEARE

1

Thesis context and problem description

Contents

Ch. 1 is assigned to the thesis context and the problem description of the present research work.

Starting in Sec. 1.1 with an introduction to the Vendee Globe, and the advantage of the application of hydrofoils in open sea racing, the emphasis will be then on two important dimensioning parameters of those appendices, the compressive strength and the interlaminar tensile strength (ILTS).

From these two parameters, the problem description and the motivation of the present study will then be introduced in Sec. 1.2 and Sec. 1.3.

The first part will describe the importance of the fibre misalignment parameter in the determination of the compressive strength. Two experimental methods to estimate the compressive strength will be presented, and their results confronted. The focus will be on the determination of the in- and out-of-plane fibre misalignment angles using Yurgartis's method [Yurgartis, 1987].

In the second part, the emphasis will be on the fabrication processes of hydrofoils. They are, to date, fabricated by traditional hand lay-up, and since recently, more and more by automated fibre placement. The second part deals hence with the topic of the influence of the fabrication process of L-beam specimens tested in four-point bending on the material behaviour, in particular on the ILTS.

1.1 The compressive strength X_c and the interlaminar tensile strength (ILTS) in hydrofoil design

Hydrofoils have revolutionized open sea racings such as the Vendee Globe, one of the toughest non-stop regatta race for single-handed skippers in the world. It takes place every four years, starting and finishing in the French department of Vendée in the seaside town Les Sables-d'Olonne on the Atlantic Ocean. The route of the Vendée Globe races leads, as the name suggests, once around the globe and lasts about two (and a half) months.

During the 9th edition of Vendée globe in 2020, 19 of the 30 participating racing boats, which belonged all to the Imoca monohull class, were equipped by hydrofoils. The present part will focus on these Imocas monohulls racing yachts. A schematic is given in Fig. 1.1.

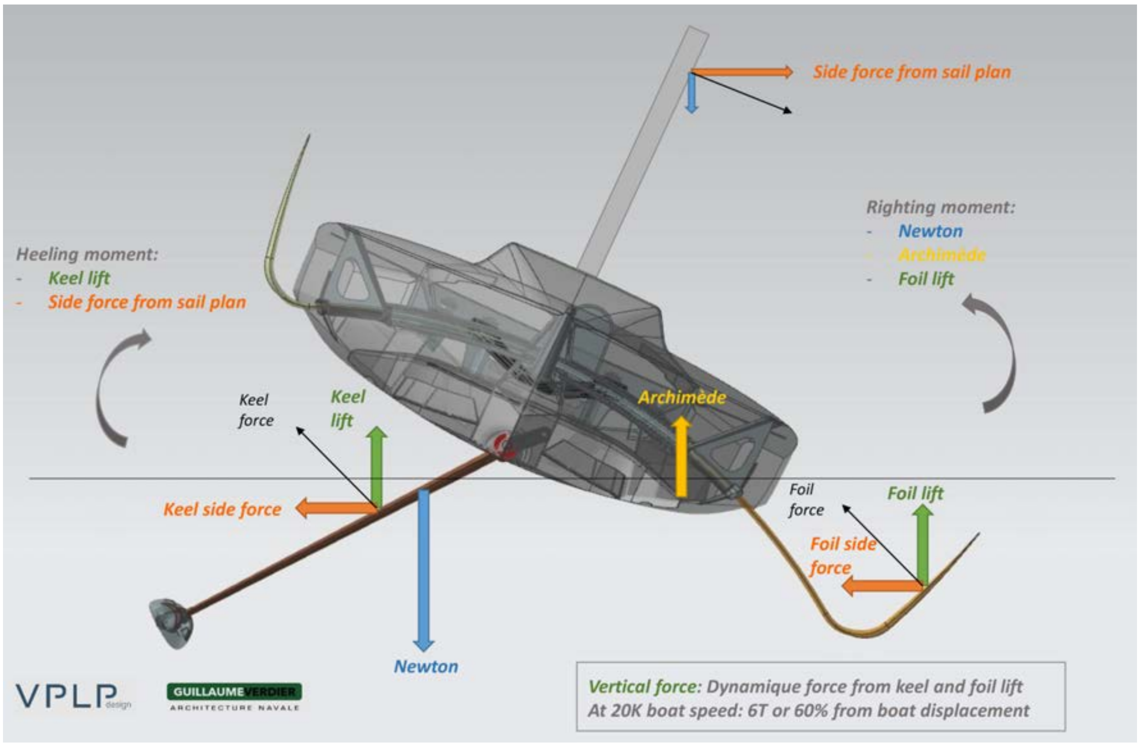

Fig. 1.1. *Schematic of Imoca racing boat and acting forces.* [Imoca, 2021]

In the sailing sports scene, hydrofoils are seen to be indispensable in future sailing races. Hydrofoils are appendices that lift up the racing boats out of the water to minimize the sliding contact between the boat and the water, to avoid the lateral drag and thus to permit to sail faster over the sea. Speeds up to 20 % higher can therefore be achieved [Ouestfrance, 2020]. The participants of the 9th edition of Vendée globe agree that future races will be won by an Imoca equipped by hydrofoils.

There are different types and forms of hydrofoils whose functions are all based on the same basic physical principle, the dynamic lift, schematically shown in Fig. 1.2. The hydrofoil moves through the water, driven by wind force that hits the sail. The dynamic lift occurs when the current velocity on the upper side of the hydrofoil (blue dotted line) is greater than on the lower side (red dotted line). This leads to a lower pressure on the top side compared to the bottom side and thus to an upward lifting force (orange arrow).

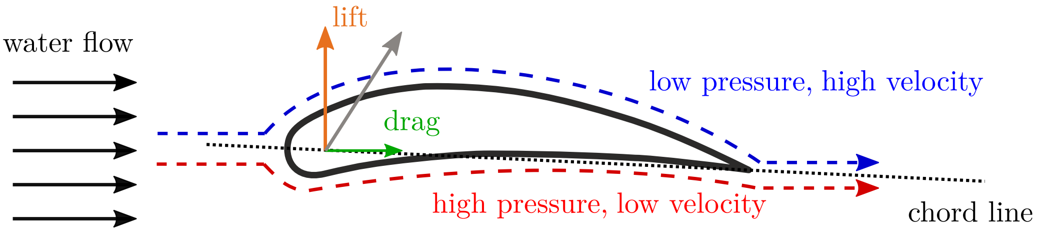

Fig. 1.2. *Schematic explanation of the dynamic lift.*

The production of one hydrofoil for an application at the Vendée Globe requires a few months, and is characterised by a repetitive exchange between the architects and the design office before passing to the production step and to the first experimental tests.
Hydrofoils are laminated composite materials made from an epoxy matrix which is reinforced by Intermediate modulus (IM) or High modulus (HM) carbon fibres. In the scope of this study, the elastic modulus of IM carbon fibres in longitudinal direction are ranged between 260 and 320 GPa, that of HM carbon fibres between 320 and 460 GPa.
The different scale levels for layered composite materials are exhibited in Fig. 1.3. The constituents level (fibres and matrix) is called micro-scale. A layer, consisting of fibres and matrix, is called *ply* and is represented by the meso-scale. Successively stacking of several layers on top of each other to form a composite laminate is assigned to the macro-scale. Last, the zone between two layers is called fibre/matrix interface.

Nowadays, hydrofoils are dimensioned in terms of compressive or out-of-plane strengths occurring in the lower bearing zone or in the elbow of the hydrofoil, respectively. This is schematically depicted in Fig. 1.4 for a L-shape hydrofoil.

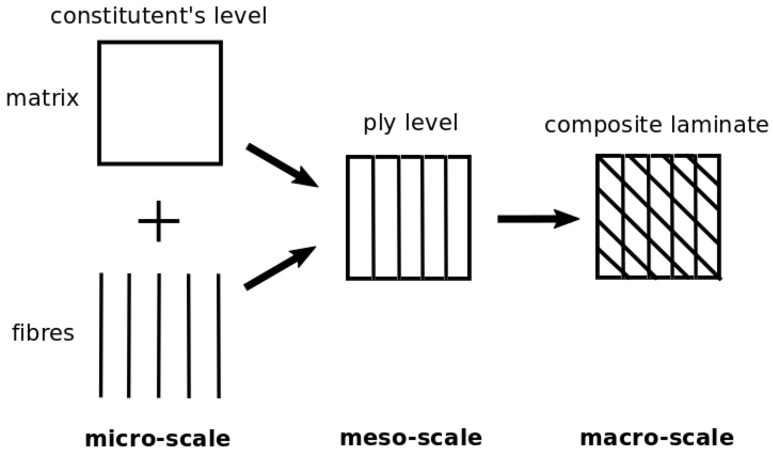

Fig. 1.3. *Scaling levels of layered composite materials.*

The compressive loading, indicated by lightblue arrows in Fig. 1.4, is the highest when the moment is at its maximum, i.e. when the boat is gliding over the water.
The compressive strength of the composite material is nowadays characterised reliably by four point bending (4PB) tests.
This is not the case for the determination of the out-of-plane strength.

When the racing yacht is moving at high speed across the water, the hydrofoil lifts the yacht out of the water thanks to the dynamic lift, marked by orange arrows in Fig. 1.4. The moment created in the hydrofoil elbow leads to a negative (compressive) stress in the out-of-plane direction. Now it may happen that the yacht tips over due to manoeuvring errors, excessive swell or other reasons. This causes the hydrofoil to open as demonstrated by green arrows in Fig. 1.4, also called inversion of the dynamic lift. When this case occurs, a moment in the opposite direction is generated in the hydrofoil's elbow, which creates a positive (tensile) stress in the out-of-plane direction. There is always a moment generated in the hydrofoil's elbow. However, in radial direction, a distinction must be made between the compressive and the tensile stress, as the maximum strength in compression is much higher (about −200 MPa) than that in tension (40 MPa). In the case of the inversion of the dynamic lift, the hydrofoil structure can hence, if it is too high, cause the hydrofoil elbow to fail by delamination. Delamination is a failure mode in which the individual layers of the composite material become detached. Delamination failure is most likely triggered at one of the interfaces between the layers.

Unlike the experimental determination of the compressive strength of layered composite materials, that of the out-of-plane strength is still a challenge, nowadays. Both are, however, determining parameters in the design of the hydrofoil application.

Therefore, in the following, a brief outline of the evolution of the determination of the out-of-plane strength at the University of South Brittany in Lorient will be given.

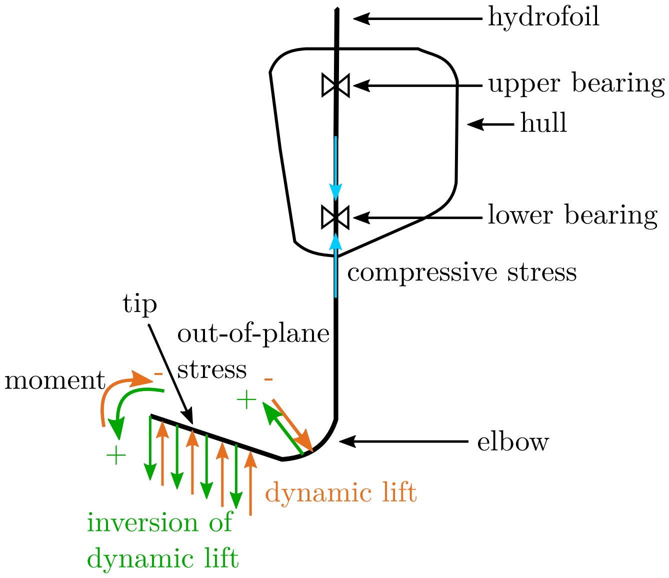

Fig. 1.4. *Schematic explanation of compressive and out-of-plane stresses, occurring in a L-shape hydrofoil.*

ILTS determination at the University of South Brittany in Lorient

The out-of-plane strength which is linked to the delamination and thus for the material failure in the hydrofoil elbow was to be determined for the first time in 2016 within a research study at the University of South Brittany in Lorient as part of the dimensioning of the hydrofoils of a racing yacht.

Since the aim of skippers was to go faster over the sea, anything in the water that slowed down the racing yacht needed to be reduced, thus, the hydrodynamic drag should be zero. In order to be correctly placed in the context, it must be noted that the evolution of the application of hydrofoils has gone from yachts and boats, on which hydrofoils *just* reduced the drag and the drift force and where out-of-plane stresses were not so high, to semi-flying and flying racing yachts. This means that the size of hydrofoils is more important nowadays, and thus, the out-of-plane strength gets more important, as well, in particular when the inversion of the dynamic lift occurs.

Hence, in 2016, a racing team decided to test a semi-structure in hinge loading, as shown in Fig. 1.5, to determine the out-of-plane strength. The objective was to validate the out-of-plane strength that was previously used in the dimensioning of the hydrofoil. However, the sample failed at half of the expected out-of-plane strength. Since the timing of the hydrofoil part of the project was at stake, knowing that there were few weeks between the tests and the lay-up of the first ply to fabricate the hydrofoil, a fast test method to determine the out-of-plane strength had to be developed.

Thus, interlaminar tensile tests by axial specimen loading were carried out, as depicted in Fig. 1.6. Cylindrical samples were cut out of a layered plate by water jet and tested in out-of-plane direction. The results of the tests were satisfactory for the skipper team.

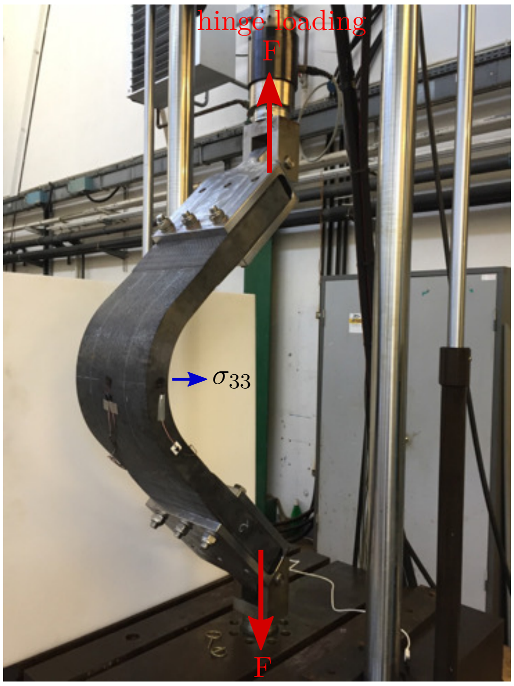

Fig. 1.5. *Interlaminar tensile test by hinge loading on semi-structure.*

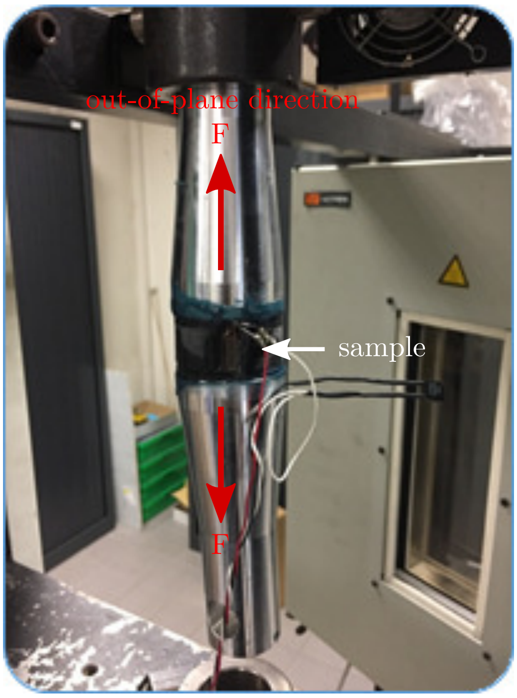

Fig. 1.6. *Layered cylindrical composite sample tested in axial loading to determine the ILTS.*

The measured out-of-plane strength was low but achieved the minimum strength that was taken for the design and thus confirmed the calculation hypotheses.

Even though, these tests were in perfect agreement with the skipper team's specifications, and fitted well into the industrial context, from a scientific point of view, these tests also resulted in high dispersion, non-negligible edge effects, bonding issues and mixed stresses. Aware of the industrial problem and with certainty that less dispersive, more homogeneous and therefore more reliable tests were possible, a research team of the University of South Brittany in Lorient took up the subject and looked for an alternative test method to determine the out-of-plane strength, which is also called interlaminar tensile strength. They referred to Charrier [2013] describing the determination of out-of-plane strengths of carbon reinforced composite L-shape specimens using a four-point-bending (4PB) test setup for aeronautical applications. By assuming that L-beams represent a simplified geometry of the hydrofoil elbow and by knowing that this test configuration permits to have the purest possible out-of-plane stress field in the curved region of the L-beam specimen, this testing method had thus to be appropriated.

From the context given above, two research studies, which will be presented in Sec. 1.2 and Sec. 1.3, have hence resulted from.

1.2 Motivation and objective of Part II

The compressive strength X_c is one of two principal dimensioning parameters in the design of L-shape hydrofoils in sailing sport. The maximum compression load, which the laminated composite may experience, predominantly occurs in the zone of the lower bearing. If the occurring compressive stress reaches the maximum determined compressive strength, the hydrofoil may fail.

Even if the compressive strength can *easily* be determined by 4PB tests, nowadays, from a scientific point of view, the compressive strength is an issue that never rests, as it is not completely mastered today.

Research works in the recent decades have extensively studied the compression failure of fibre reinforced composite materials. Micromechanical failure theories had been developed in order to describe the fibre-matrix behaviour of laminated structures under compression. It was stated that the material instability may be triggered by local initial fibre misalignment in the lamina. Fibre misalignment is therefore a predominant factor to be taken into account in the design of fibre reinforced composite structures when those are loaded in compression.

The compressive strength X_c of fibre reinforced composite lamina and the determination of fibre misalignment in those structures will be hence in the focus of the present Part II. Therefore, Ch. 2 will first give a brief comprehension on different micromechanic models to determine the compressive strength X_c of fibre reinforced composites, as well as the significance of fibre misalignment on the material instability (Sec. 2.1). Then, in Sec. 2.2, a definition of fibre misalignment and its origin related to the manufacturing process will be given. Further, the impact of fibre misalignment on the mechanical properties of composite lamina, and the appearance of fibre misalignment in the marine sector will discussed, briefly. Last, different methods of fibre misalignment determination will be presented in Sec. 2.3.

The theoretical part shall give a solid basis for passing to the core of Part II: the experimental confrontation of a (i) complete experimental method to determine analytically the compressive strength X_c^{ANA}, with the (ii) experimental determined compressive strength X_c^{EXP} calculated by means of 4PB tests. The objective is to confront those experimental methods by applying both approaches on seven different carbon/epoxy prepreg materials and to compare the resulting compressive strengths X_c^{ANA} and X_c^{EXP} with each other. Tab. 1.1 shows the two methods and illustrates the content of each approach.

To calculate the (i) compressive strength X_c^{ANA}, the kink band model from Budiansky & Fleck [1993] and that from Grandidier et al. [2012], which takes into account the structural effect, will be used. The focus will be on the determination of the in- and out-of-plane fibre misalignment angles using Yurgartis' method. The initial fibre misalignment angle is one of four parameters to be determined in order to be able to estimate X_c^{ANA} using Budiansky & Fleck's solution. Yurgartis' method will be explained in detail in Ch. 3 in order to adopt a solid understanding on this topic.

The first (i) method requires further the implementation of tensile tests on ±45° specimens to identify the parameters of the RO's constitutive law, the shear modulus G_{UD}^{RO}, the critical shear yield strain γ_y^{UD} and the strain hardening coefficient n_{UD}, for an unidirectional laminate, representing hence the three missing parameters. This part will be introduced in Ch. 4.

In order to determine the (ii) compressive strength X_c^{EXP}, 4PB tests on the same prepreg materials needed to be carried out. The implementation of these tests, as well as the analysis will also be given in Ch. 4.

Afterwards, the compressive strength X_c^{ANA}, determined by the (i) analytical solutions from Budiansky & Fleck [1993] and Grandidier et al. [2012], will finally be compared to the compressive strength X_c^{EXP}, determined by 4PB tests. Cartographies of the spatial fibre alignment distribution will be established and used as tool to evaluate the (mis-)matching of the compressive strengths. A hypothesis will be made that the studied zones in which the in- and out-of-plane fibre misalignment angles were determined corresponded to the failures zone of the 4PB specimens. A questioning procedure will be presented in order to interpret clusters of misaligned fibres, or single fibres strongly misaligned with regard to the fibre misalignment angle determination, and to the (mis-)matching of X_c^{EXP} and X_c^{ANA}. Statements on which angle is more suitable in the application of the analytical solutions will be given.

Tab. 1.1. *Confrontation of the two experimental approaches for determining the compressive strengths of 7 different material series.*

7 different carbon/epoxy material series	
(i) X_c^{ANA}	(ii) X_c^{EXP}
Model used: Budiansky & Fleck [1993], Grandidier et al. [2012] (Kink band model, + structural effect)	4PB tests according to the standard ASTM D6272 (ASTM, 2008)
Determination of X_c^{ANA} requires:	Determination of X_c^{EXP} requires:

Yurgartis' **method:**	**Determination of the initial in- (Φ_i) and out-of-plane (Θ_i) fibre misalignment angles.**	Input data:	Specimen metrology, dimension of the 4PB test setup, lay-up plan, elastic parameters of plies, data recorded during testing.
±45° tensile tests:	Standard NF EN ISO 14129 (NF EN ISO, 1998) to identify the RO law parameters G_{UD}^{RO}, γ_y^{UD}, n_{UD}.	Calculation steps:	(i.) second moment of area, (ii.) stress in the outermost ply.
Structural effect:	Elastic properties of micro-scale components and geometrical data of 4PB specimens.		

1.3 Motivation and objective of Part III

The out-of-plane tensile strength, also called inter-laminar tensile strength (ILTS), through-the-thickness strength or across-thickness strength in literature, is, apart from the compressive strength X_c, one important parameter in the design of hydrofoils. The ILTS occurs normal to the plane (ply), in the out-of plane direction as indicated in Fig. 1.7. In the present research work, the terms out-of-plane (tensile) strength and ILTS will be predominantly used.

The ILTS is generated in the curved part of the hydrofoil, in the hydrofoil elbow, in radial direction. As schematically depicted in Fig. 1.4, the stress is either negative if the hydrofoil undergoes the dynamic lift or positive if the inverse case occurs. If the latter is the case, i.e. the hydrofoil gets open, and the ILTS gets predominant, the hydrofoil elbow may fail by delamination. Delamination refers to the detachment of the layers in laminated material compounds or in this case, in the hydrofoil elbow. Low ILTS properties may thus lead to interlaminar failure of the composite structure.

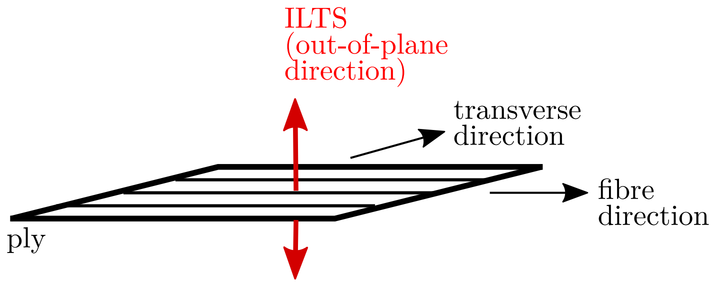

Fig. 1.7. *Schematic illustration of the ILTS acting normal to the plane.*

Until recently, hydrofoils were traditionally laid-up by hand. So far, this is still the most common production method, today. In the mean time, AFP technology was progressively introduced to manufacture these composite structures.

In sailing sport, however, the influence of the manufacturing process of hydrofoils on the ILTS has not been sufficiently investigated yet. This fact justifies the necessity of the present research study. The objective of Part III is the investigation of the influence of the fabrication process on the material behaviour, especially on the ILTS.

For this, a bibliographic overview on the determination of the ILTS for different sample geometries and different test configurations will be given first, in Ch. 5. Emphasis will be placed on the specimen manufacturing processes. Further, literature reviews will be given which compare test results of hand laid-up samples with those of samples manufactured by AFP technology. Advantages and inconveniences of both fabrications methods will be presented.

For the experimental study, curved unidirectional carbon fibre reinforced composites L-beam specimens, representing a simplified geometry of the hydrofoil elbow, were manufactured by traditional hand lay-up and by AFP technology. The L-beam specimens were made from the same material.

Inspired by the research works of Charrier [2013], those specimens were then tested in 4PB, according to the standard ASTM D6415 / D6415M-06a [2013]. This test configuration permitted to have the purest possible out-of-plane stress field in the curved region of the L-beam specimen.

In order to implement this study, three tools needed to be developed to determine the ILTS experimentally, analytically and numerically. The development of these tools will be presented in Ch. 6.

The analytical tool consisted of the application of the analytical solutions of Lekhnitskii [1968] and Kedward et al. [1989]. This part will be presented and validated in Sec. 6.1. The experimental tool contains the design of the 4PB test setup and the application of different measuring instruments (DIC, AE, LVDT and strain gauge) during test execution. These works will be presented in Sec. 6.2. Last, the numerical tool, given and validated in Sec. 6.3, consisted of the design of a FE model permitting the simulation of a L-beam specimen loaded in 4PB.

The material used to manufacture the L-beam specimens, as well as the fabrication processes of both specimen types will be presented in Sec. 7.1 for L-beams manufactured by AFP technology (in the following denoted as AFP L-beams/specimens), and in Sec. 8.1 and Sec. 8.2 for those fabricated by traditional hand lay-up (referred to as MAN L-beams/specimens).

The results of the 4PB tests, the analytic estimations of the ILTS and the numeric FE calculations will be presented for AFP and MAN L-beams in Sec. 7.3 and Sec. 8.4, respectively.

The test campaigns will be analysed in terms of test reproducibility and crack distributions over specimen thickness, and compared to Lekhnitskii's solution with which the analytical radial position r_{max} of the maximum ILTS is determined. An evaluation of the results of the AE prior to failure, as well as of the ILTS will be done. Further, the issue concerning the non-linearity of the load-displacement curves at test beginning will be discussed. An explanation of why the analytical solution of Kedward et al. fits better the FE model will also be given. The normalized stress distributions over the normalized specimen thicknesses and the widths, numerically calculated, will be compared to the analytical estimations.

The results of both test campaigns will be finally compared in Ch. 9 in terms of test reproducibility, specimen metrology, Curved beam strength (CBS) and stiffness, first failure crack location, loads at failure and ILTS, macroscopic defects, and porosity. Lastly, the influence of the manufacturing process on the ILTS will be discussed. The differences between the compaction modes applied during manual hand lay-up and automated tape lay-up will be given. Resulting material defects leading to the observed lower ILTS values for MAN L-beam specimens will be discussed.

PART II

THE COMPRESSIVE STRENGTH X_C

> *"Anger is fear, I knew. Every angry person is a frightened one, dreading some loss."*
>
> —RICHARD BACH

2

Role of fibre misalignment and fibre waviness in the design of laminate composites with regard to the compressive strength X_c

Contents

Fibre misalignment and fibre waviness have a high influence on the mechanical behaviour of fibre-reinforced composite structures. Especially the compressive strength, but also other material properties are influenced by these material defects which are mainly introduced during the manufacturing process. Sec. 2.1 hence discusses first the development of different fibre buckling models. It will be clarified that fibre misalignment has a high influence on the compressive strength. Sec. 2.2 depicts sources of fibre misalignment with regard to the manufacturing processes. Within this section, a definition of fibre misalignment and fibre waviness will be given as well as consequences of misalignment defects on the mechanical properties. Last, different methods for fibre misalignment and fibre waviness determination and their advantages and drawback will be listed in Sec. 2.3.

2.1 Significance of the misalignment angle Φ_0 in the determination of the compressive strength X_c

In sailing sport, compressive failure is a limiting factor in the design of hydrofoils. In the past, micromechanical failure theories have been developed that attempted to predict the compressive strength of unidirectional fibre reinforced composites. The failure modes that are considered within these theories are (i) microbuckling, (ii) kinking, (iii) fibre failure and (iv) longitudinal cracking.

Microbuckling describes the deformation in which fibres are considered to act individually as columns inside the matrix, is expected to be controlled by the matrix shear stiffness and depends on initial material defects (fibre misalignment and waviness, residual stresses coming from matrix shrinkage, porosity). Kinking describes a localized shear deformation of the matrix with failure of a fibre band that is defined by the kink band width, the angle of the rotated fibres and the angle of the kink band. Direct fibre failure is expected to have a major role for materials that are weak in compression, e.g. Kevlar, and can be neglected as failure mode for fibres with strong compression properties as this is the case for carbon and glass. Last, longitudinal cracking, related to delamination failure in laminates, may appear in composites with strong fibres and brittle matrices or weak interfaces, is generally controlled by the fracture toughness of the matrix and the interface and may be affected by the difference between the Poisson's parameters of the fibre and the matrix. [Schultheisz & Waas, 1996]

Rosen [1965] first studied the microbuckling failure mode when investigating glass/epoxy laminates under compressive loading. His model was assumed to be two dimensional where linearly elastic fibres were considered as perfectly straight and evenly spaced plies were embedded in an linearly elastic matrix. In the case of material failure, two possible failure modes, as shown in Fig. 2.1, may occur according to Rosen [1965]: (i) In the extension failure mode, vicinal layers deform out-of-phase. (ii) In the shear mode failure, vicinal layers deform in-phase and the matrix is primarily subjected to shear stress. Further,

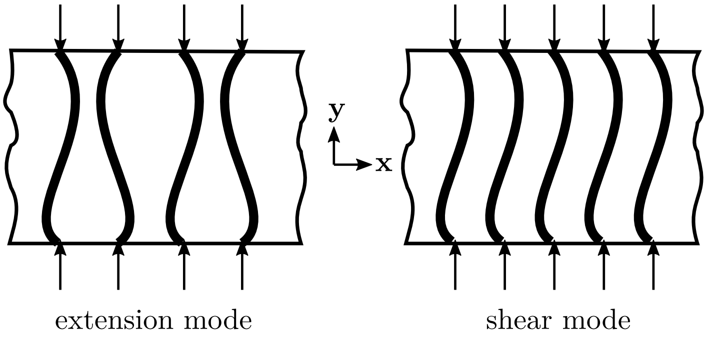

Fig. 2.1. *Possible failure modes according to [Rosen, 1965].*

Rosen [1965] dealt the problem of the periodic deformation of single fibres caused by matrix shrinkage after curing. The author suggested that the buckle period varies linearly with the fibre diameter. Similar results were found by Sadowsky et al. [1967] who stated, in addition, that the thermal expansions coefficients of the fibre and the matrix, and the elastic fibre buckling load form the basis of fibre waviness during matrix shrinkage.

Compared to other authors who developed similar models, assuming linear elasticity and straight fibres, that of Rosen [1965] is useful for comparison because of its simplicity and its prediction of the lowest critical buckling loads [Schultheisz & Waas, 1996]. A review of similar methods are extensively discussed in [Schultheisz & Waas, 1996].

Nevertheless, it was found that the microbuckling approach was not suitable for advanced fibre composites. Rosen's failure model overestimated the compressive failure stress. It was found by several authors [Lager & June, 1969; Weaver & Williams, 1975; Chaplin, 1977; Parry & Wronski, 1981] that Rosen's model depends on the material used. For this reason, different investigations such as (i) microbuckling near a free surface [Waas et al., 1990], (ii) debonding of interfaces [Steif, 1988], (iii) interphase effects in the scope of a single fibre [Waas, 1992], (iv) material non-linearity [Hahn & Williams, 1986] and (v) fibre misalignment and waviness [Davis, 1975; Yurgartis, 1987; Wisnom, 1990] were conducted to improve the microbuckling failure model [Schultheisz & Waas, 1996].

The non-linearity of the matrix and the fibre waviness or misalignment were generally used simultaneously to estimate microbuckling stresses that are lower than the results of Rosen's failure model for straight fibres [Schultheisz & Waas, 1996].

Rosen's elastic shear buckling model was reconsidered by Argon [1972] when he examined the kinking phenomenon. He assumed that the origin of the material instability came from a local initial fibre misalignment, from a plastic shearing of the matrix in the zone containing the misaligned fibres and from a fibre bending component at the edges of this zone.

Budiansky [1983] extended the approach of Argon [1972] considering the effects of plastic deformation using a matrix model with elastic perfectly plastic shear behaviour. According to Budiansky [1983], localised deviations from the optimal fibre orientation, due to inclusions, voids or inhomogeneities in the fibre spacing, induce sections of angular displacement due to elastic deformations and those sections position themselves in inclined zones. *These rotations then induce plastic kinking into similarly inclined kink bands* [Budiansky, 1983]. Based on these statements Budiansky & Fleck [1993] developed a kink-band model describing the compressive failure stress σ_c resulting from compressive tests

$$\sigma_c = \frac{G_{UD}^{RO}}{1 + n_{UD} \cdot \left(\frac{3}{7}\right)^{\frac{1}{n_{UD}}} \left(\frac{\frac{\Phi_0}{\gamma_y^{UD}}}{n_{UD}-1}\right)^{\frac{n_{UD}-1}{n_{UD}}}} , \tag{2.1}$$

where G_{UD}^{RO} represents the in-plane elastic shear modulus of the unidirectional ply, and Φ_0 the initial inclination angle of the kink-band. n_{UD} and γ_y^{UD} are respectively the strain hardening coefficient and the critical shear yield strain originate from the Ramberg-Osgood [Ramberg & Osgood, 1943] constitutive law,

$$\gamma_{12}(\tau_{12}) = \frac{\tau_{12}}{G_{UD}^{RO}} \cdot \left(1 + \frac{3}{7} \cdot \left(\frac{\tau_{12}}{G_{UD}^{RO} \cdot \gamma_y^{UD}}\right)^{n_{UD}-1}\right) , \tag{2.2}$$

describing the non-linear shear response of the ply (τ_{12} represents the in-plane shear stress). Grandidier et al. [2012] mentioned, that Equ. 2.1 is not sufficient for compressive failure determinations resulting from pure bending tests. Grandidier et al. [2012] thus searched for an expression describing the contribution of the structural effect of the composite on the fibre buckling instability at the early beginning stage of matrix plasticity, as this was considered to be a key element in the approach of Budiansky & Fleck's work. Inspired by the experimental work of Drapier et al. [1997], Grandidier et al. [2012] described the contribution of the structural effect as the ratio between a constant C_S of the ply, which is involved in the instability mode, and a characteristic thickness e_b, depending on the ply thickness e_{ply}.

Grandidier et al. [2012] described hence the local critical strain ε_c in fibre direction for a ply within a lay-up as

$$\varepsilon_c = \frac{G_{UD}^{RO}}{E_C\left(1 + n_{UD} \cdot \left(\frac{3}{7}\right)^{\frac{1}{n_{UD}}} \left(\frac{\frac{\Phi_0}{\gamma_y^{UD}}}{n_{UD}-1}\right)^{\frac{n_{UD}-1}{n_{UD}}}\right)} + \frac{C_s}{e_b}\ , \tag{2.3}$$

and C_s as

$$C_s = \frac{1}{E_C}\,(2\pi r_{gf})\sqrt{\frac{E_M E_F}{1-\nu_M^2} f(1-f)}, \tag{2.4}$$

where E_C denotes the Young modulus in fibre direction of the unidirectional ply, E_M and ν_M the Young's modulus and the Poisson's ratio of the matrix, respectively, E_F and f the longitudinal elastic modulus of the fibre and the fibre volume fraction, r_{gf} the fibre gyration radius and f the fibre volume ratio.

The compressive failure stress taking into account the structural effect was then calculated through

$$\sigma_c = \frac{G_{UD}^{RO}}{1 + n_{UD} \cdot \left(\frac{3}{7}\right)^{\frac{1}{n_{UD}}} \left(\frac{\frac{\Phi_0}{\gamma_y^{UD}}}{n_{UD}-1}\right)^{\frac{n_{UD}-1}{n_{UD}}}} + \frac{C_s}{e_b}\ . \tag{2.5}$$

In his work, Grandidier et al. [2012] stated that the matrix plasticity seemed to be an impacting and strong governing parameter for the development of fibre instability mechanisms in local regions, and that geometric defects such as fibre misalignment are the main impacting parameters.

Wisnom [1990] developed an analytical model to calculate the change in compressive strength with fibre misalignment for an unidirectional XAS/914 carbon/epoxy composite. The author found that small fibre misalignments between the fibres and the loading axis have a strong impact on the compressive strength. Further, Wisnom [1990] stated that the shear instability of the matrix drastically reduces the compressive strength even for very small fibre misalignments. For a fibre misalignment angle of 0.25 °, the compressive strength dropped by 32 % in comparison to the compressive strength without fibre misalignment, and decreased further up to 74 % for a misalignment angle of 3.0 ° [Wisnom, 1990].

The same author developed in Wisnom [1993] a FE model, with non-linear geometry and orthotropic material properties with non-linear shear response, to simulate the compressive failure due to shear instability. The author validated the model by a single element test case since the same compressive strength for a misalignment angle of 2.0 ° was found as previously estimated using the analytical model presented in [Wisnom, 1990]. Nevertheless, applied to the analysis of a short gauge compression sample with uniformly misaligned fibres, the author stated that the FE model predicted a smaller strength decrease compared to the analytical model. [Wisnom, 1993] attributed these observations to the lateral constraint imposed by the clamping device which prevented overall shearing of the sample.

Yurgartis [1987] presented a technique permitting the measuring of the in- and out-of-plane misalignment distribution of continuous fibre composites to address the problem of how the compressive strength is influenced by fibre misalignment. The fibre misalignment angles are determined from the major and minor axes of ellipses which are obtained by samples sectioning parallel or perpendicular to their fibre direction at predefined angles. This method will be presented in more detail in Ch. 3. Yurgartis [1987] studied the misalignment distributions of a [0/90] and an unidirectional APC-2 laminate, a carbon fibre/polyether ether-ketone composite. The author criticized carefully his method. He stated that the largest uncertainty of this method results from the distribution of the fibre diameters. Indeed, an hypothesis of Yurgartis's approach is that all fibres have the same diameter. Further, the authors mentioned that polishing of the section surface can damage the fibre edges. Moreover, the manual collection of the ellipses' data is a long process. Yurgartis also criticized that the shape of the fibre curvature is unknown, even if the fibre angle distribution can be determined.

The literature review above has illustrated how the authors have addressed the phenomenon of fibre buckling or kinking using a two dimensional model with linear elastic matrix and fibres [Rosen, 1965], matrix models with elastic perfectly plastic shear behaviour [Budiansky, 1983] or the addition of a structural effect as this was done in Grandidier et al. [2012]. Further, it was stated that fibre misalignment has a determined effect on the matrix plasticity, which is responsible for instability mechanisms in the composite material, and thus influences strongly the compressive strength of continuous fibre composites.

In the scope of this study, the definition of fibre misalignment, its origin, different determination methods and an experimental study on the fibre angle determination according to Yurgartis' method are in the focus. In the following Sec. 2.2, the origin of fibre misalignments in composite materials will be discussed in more detail.

2.2 Source of fibre misalignment in composite materials

In Sec. 2.1 the influence of the fibre misalignment angle in the estimation of the compressive strength was discussed. The fibre misalignment angle has a strong impact on the matrix plasticity which is responsible for the local instability mechanisms in composite laminates [Grandidier et al., 2012]. In literature not only the term *fibre misalignment* but also the term *fibre waviness* are used. In the following, their definitions will be clarified first in Sec. 2.2.1, by referring to the literature, before sources of fibre misalignment and waviness will be discussed in more detail in Sec. 2.2.2.

2.2.1 Definition of fibre misalignment and fibre waviness

There are few publications in the literature that specify the definition of fibre misalignment and fibre waviness.

Paluch [1994] discussed the origin of low compressive strengths of unidirectionally reinforced composites, and that this is principally due to geometric fibre imperfections in the material. The author focused on the determination of the center coordinates of the fibre section surfaces and on the determination of the fibre path of individual fibres. Therein, the author used the terms *fibre ondulation* and *fibre misalignment* in order to define fibre imperfections on the micro scale level within a ply.

Joyce et al. [1997] defined fibre misalignment as *partial or localized misorientation of the reinforcing fibres with respect to the nominal fibre axis*. Further, fibre misalignment describes, according to Joyce et al. [1997], *spatial orientation-imperfections in the fibrous reinforcement* whereas *fibre waviness describes sinusoidal-like deformations induced during processing*. The same author also stated, that fibre misalignment is *attributed to the prepregging process or ply layup error*, whereas fibre waviness is *commonly induces during processing*. Moreover, Joyce & Moon [1997] categorised fibre waviness as in- and out-of-plane fibre waviness. The latter, known as layer or ply waviness, involves the cooperative movement of several layers through the laminate thickness, whereas the former involves the cooperative deformation of many fibres within the plane of the laminate [Joyce & Moon, 1997].

Wang et al. [2012] used the term fibre waviness within a study based on artificially generated out-of-plane fibre waviness during fabrication of Carbon fibre reinforced polymer (CFRP) composites. Out-of-plane fibre waviness was defined by the waviness length λ, the amplitude δ and the misalignment angle θ as shown in Fig. 2.2. The misalignment angle θ describes in this case the deviation of a ply from the nominal fibre direction (ply level).

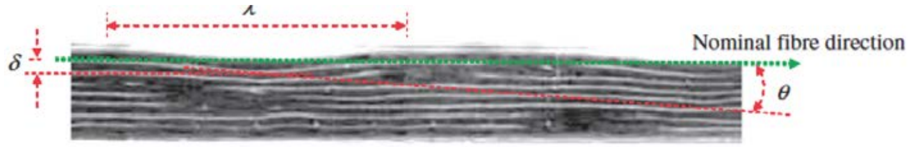

Fig. 2.2. *Out-of-plane waviness within a ply described by the waviness length λ, the amplitude δ and the misalignment angle θ. Wang et al. [2012]*

Wu et al. [2018] described fibre waviness using the three parameters λ, δ and θ, as already done by Wang et al. [2012], and referred to a similar graph as that given in Fig. 2.2. In addition, Wu et al. [2018] mentioned two types of fibre waviness occurring in composite structures: (i) *wavy bending, generated by restrained fibers in fibrous layer, is called in-plane waviness or in- plane buckling*, (ii) *Bending of a single layer or multilayer, resulted from that fibres departed from fibrous layer, is named as out-of-plane waviness or* *out-of-plane wrinkling.*

Kulkarni et al. [2020] characterised in-plane fibre waviness as *deviation of fibre from the normal fibre direction in a plane of the lamina* and out-of-plane fibre waviness as *bending of a single or multiple fibre separated from the laminate fibrous layer*. The author stated further that fibre waviness results from the axial compression of the fibres due to a non-uniform pressure distribution between the plies. Also, thermal properties of the tool material may produce fibre waviness in the composite material [Kulkarni et al., 2020].

From the individual definitions found in the literature, fibre misalignment and fibre waviness will be defined in the scope of this study as follows.

Fibre waviness is attributed to the ply level and describes a sinusoidal arrangement of the fibres in in- or out-of-plane direction. In out-of-plane direction, fibre waviness is defined by the three parameters λ, δ and θ. The term fibre waviness is not used to describe a single fibre waviness locally, but a bundle of fibres that is affected globally.

Fibre misalignment, on the other hand, is given when single fibres are locally affected by misortientations, i.e. at the fibre/matrix level. The fibre misalignment angle in out-of-plane direction of one single fibre should therefore not be confused with the misalignment angle θ of a bundle of fibre given in Fig. 2.2.

In the following, the term fibre misalignment will be employed to describe the misalignment of fibres in in- and out-of plane direction locally. This choice was made since Yurgartis' method with which in- and out-of-plane misalignment angles can be determined, is in the focus of this research work. Yurgartis [1987] used the term fibre misalignment in particular to describe fibre misorientations of his material.

2.2.2 Review of the origin of fibre misalignment, fibre waviness and other material defects related to the manufacturing process

Talreja [2015] reviewed a few common manufacturing defect types in aerospace applications and their effects on the performance of polymer matrix composites. The author categorized those defects in (i) matrix (incomplete curing and voids), (ii) fibre (misalignments, waviness, broken fibres, and irregularities of the fibre distribution in the matrix) and (iii) interface (unbonded regions on fibre surfaces and between layers, i.e. delamination) defects.

Void formation can thus be controlled by the parameters of the manufacturing process such as vacuum pressure, resin viscosity, cure temperature and consolidation pressure [Talreja, 2015]. According to Talreja [2015], voids are a consequence of trapped air in ply interfaces formed during the composite layup or by evaporation of water and volatile substances inside the prepregs during curing. This can be favoured by vacuum and applied pressure during the autoclave curing process [Talreja, 2015].

As expected, Talreja [2015] assigned the decrease of material properties such as compression strength and material stiffness to fibre misalignment and fibre waviness in the composite material. However, statements about the relation of fibre misalignment, fibre waviness and broken fibres to the manufacturing process were not given in Talreja [2015]. According to Talreja [2015], interface defects were assigned to unbonded regions of the fibre surface due to non-optimal bonding conditions between the fibres and the matrix. Resin infusion may not wet the whole fibre surface, prepreg sheet stacking can cause air to be trapped between the layers [Talreja, 2015]. Talreja [2015] describes further delamination as separation of bonded layers and interfaces due to air rich zones in interlaminar regions that flatter during consolidation and build planes preventing the layers from bonding correctly.

Swift [1975] indicates possible causes of fibre buckling in continuous fibre reinforced composites produced during the manufacturing process which may decrease the elastic properties of the material. The author mentioned the following influencing factors. For (ii), (v) and (vi) axial compression is expected to be the source of fibre buckling [Swift, 1975]:

i. *Machine vibration during filament winding, especially when performed under low tension.*

ii. *Placing material sheets or strips in a closed mould whose length is smaller than the sheet length.*

iii. *Electrostatic repulsion of fibres [...].*

iv. *Disturbance caused by the application of the resin, especially when the resin contains inhomogeneities.*

v. *Non-uniform curing and cooling shrinkages.*

vi. *Fibre kinking caused by cutting and straightening out sheet or tape produced from a continuously wound cylinder.*

Paluch [1994] showed that the fibres have a shape very close to a sinusoid. For example for a T300/914, the average wavelength is around 900 µm and the amplitudes are in a range of 0.05 µm to 6.2 µm. This sinusoid has also been observed by I. Grandsire-Vinçon at ONERA with a simple light microscopic on monofilament specimens. This particular configuration taken by the fibre suggested to some authors [Jochum & Grandidier, 2000; Jochum et al., 2008] that the waviness defects in the laminates may also be the consequence of microbuckling appearing during the manufacturing process.

Potter [2009] reviewed material defect sources in composite parts that are manufactured for the aircraft sector. According to the author, there is a large interaction between decisions on part and process design and the variability in materials and processes. The interaction of all factors is very complex. Therefore, Potter [2009] created a toxometric diagram in order to better understand the interaction of the different factors, and to identify common characteristics underlying the different defect types. Fig. 2.3 exhibits the overall taxonomic approach showing the diagram with the respective classifications. Below, fibre misalignment as defect type will be considered in more detail.

Potter [2009] took a closer look at prepregs as they are received from the manufacturer. He suggested that the most likely cause of fibre misalignment comes from wrapping the prepreg onto the drum for storage reasons [Potter, 2009]. Assuming a 300 mm diameter drum with a prepreg thickness of 0.25 mm, Potter [2009] set an example, that the prepreg's outer surface length is 0.167 % longer than the inner surface length and thus, fibres curl

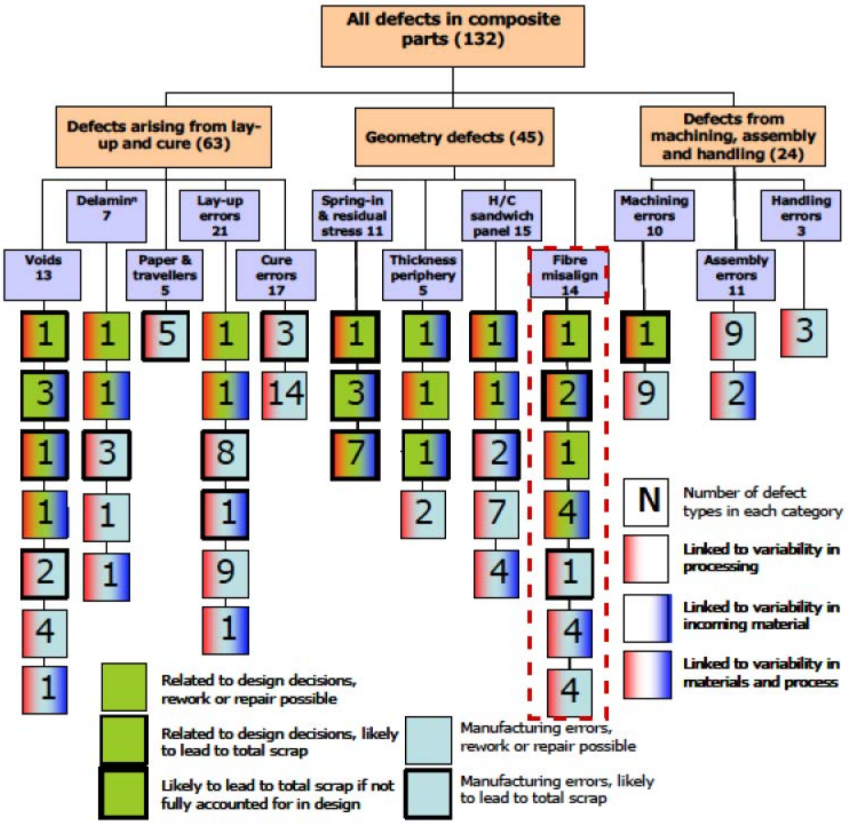

Fig. 2.3. *Taxonomy of defect types in RTM and autoclave mouldings according to Potter [2009].*

and form folds on the inside surface in order to compensate the difference. Numerically determined, Potter [2009] found a maximum angle of 4.7 ° (sinusoidal wrinkle) for an excess length of 0.167 %. The author added that as the prepreg is unrolled, the wrinkle will not be zero, due to the visco-elastic behaviour of the material. Potter [2009] hence assumed, that fibre waviness, which can be observed in flat prepregs, comes from wrapping the prepreg onto the drum for storage and transport reasons.

Potter [2009] discussed further the origin of defects due to the lay-up process. As known, the design of composite components is based on the properties of flat laminates. However, considering more complex geometries such as curved compounds, straight continuous fibres are formed to a radius [Potter, 2009]. Consequently, a similar case happens as described above. Fibres on the radius inside of a ply are loaded in compression, and compact to form a zone of wavy fibres [Potter, 2009]. This is depicted in Fig. 2.4. Uniform green color indicates undistorted, red or blue areas distorted fibre regions. Potter [2009] distinguished between fibre waviness and misalignment. The author stated, that fibre waviness is not significantly changed by laying-up around a corner, but fibre misalignment is. The author added further, that this is thus not due to poor manufacturing, but to the design process in which the geometry of the part was defined.

Potter [2009] discussed further the effect of compound consolidation and resin flow on fibre misalignment formation. Considering once again a more complex geometry such as curved components as given in Fig. 2.5, fibre misalignment can be induced on the outer side of the curved region due to a low friction coefficient which leads to a movement between tool and material during consolidation [Potter, 2009]. Contact stresses and strains are

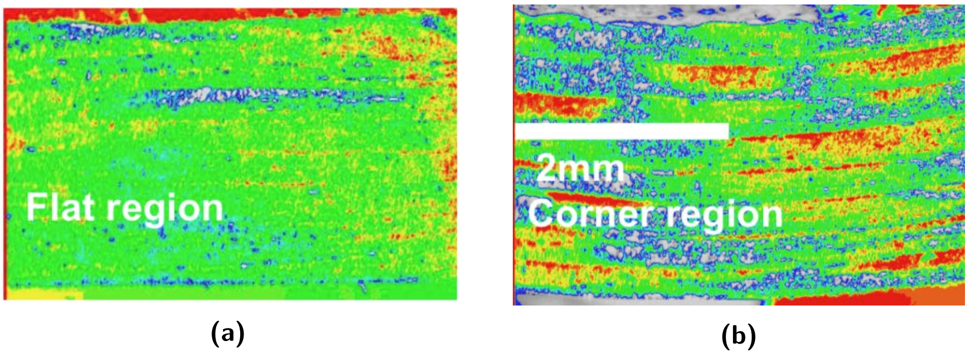

Fig. 2.4. *Fibre misalignment in a (a) flat and (b) curved composite. The region close to the radius inside of the ply is loaded in compression. [Potter, 2009]*

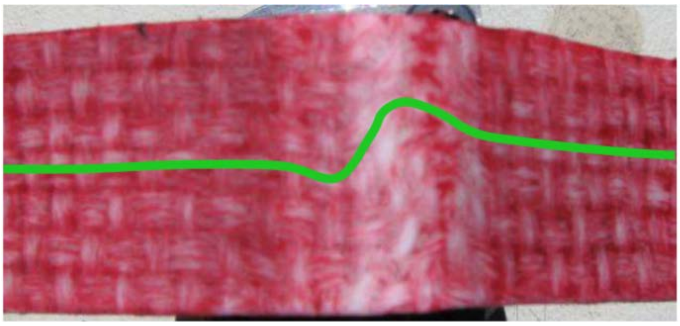

Fig. 2.5. *Region of very significant fibre misalignment in the outer side of the curved part of the laminate. [Potter, 2009]*

generated due to different thermal expansion coefficients [Kulkarni et al., 2020]. Fig. 2.5 shows an example of fibre misalignment that had appeared during consolidation of a laminate made from fabrics (blended glass/polyester yarns) [Potter, 2009].

Kulkarni et al. [2020] provided a large overview of fibre misalignment or fibre waviness formation in fibre reinforced polymer composites and its effect on the mechanical properties. The author employed primarily the term fibre waviness. He stated that fibre waviness depends on the manufacturing process and the processing parameters. The author mentioned further four sources of fibre waviness generation resulting from the manufacturing process: (i) different thermal expansion coefficients of fibre and matrix lead to a temperature gradient, (ii) consolidation, (iii) interaction between material components and moulding tool (iv) fibre mismatch when prepregs are laid-up over a curved mould.

In the following, the influence of fibre misalignment on the mechanical properties of composite materials will be discussed.

2.2.3 Consequences of fibre misalignment and fibre waviness on the mechanical properties of the composites

Different authors treated the question of the impact of fibre misalignment and fibre waviness on the material properties of laminated composites. Reviews by Piggott [1995], Schultheisz & Waas [1996], Joyce & Moon [1997] and Kulkarni et al. [2020] provide a detailed outline of the work carried out in the recent decades. Details of the mechanical response of composite materials on fibre misalignment and fibre waviness are discussed in more detail below.

Tensile strength and stiffness

Bloom et al. [2013] studied the effect of localised fibre wrinkling defects on the tensile strength of glass reinforced epoxy laminates. The tensile strengths were calculated as load per area. The authors found that with the highest measured misalignment and kink angle, a reduction in strength of 40 % compared to the sample without defects was found. The author further used DIC and Video Gauge techniques during tensile testing to show localised strains at the wrinkles. Strain concentrations were highly localised around the wrinkle. They found that the strain values in wrinkled zones reached the double of that of zones without defects. This seemed to be an indicator of reduced stiffness due to fibre misalignment [Bloom et al., 2013]. Further, the author observed a crack that propagated through the material, by following a misalignment path, and which fractured wrinkled plies, but not the straight ones [Bloom et al., 2013]. Last, the author stated that misaligned fibres experience high stresses, especially the kinked fibres during tensile testing.

Mukhopadhyay et al. [2015] investigated experimentally and numerically the effects of out-of-plane fibre waviness on the tensile damage of quasi-isotropic fibre-reinforced composite laminates made from IM7/8552 prepreg tapes, laid up by hand. The author used a high resolution camera in order to take images monitoring the initiation and interaction of different damage mechanisms during tensile loading. Fig. 2.6 exhibits the induced out-of-plane wrinkle of such a specimen. The authors created then a 3D FE model of the tested specimens and used the experimental data to develop user material subroutines. They implemented them in *Abaqus/explicit as continuum damage and cohesive zone models for intra- and inter-ply failure respectively* [Mukhopadhyay et al., 2015]. The authors found a good correlation between the experimental observations and the numeric results. Further, the author observed that wrinkles act as local shear stress (through-the-thickness) concentrators. Mukhopadhyay et al. [2015] also stated that for laminates with different stacking sequences, the appearance of in-plane shear stress localisations near the laminate edge increases the effect. The combination of both shear stresses leads to fibre tensile damage occurring earlier than expected [Mukhopadhyay et al., 2015].

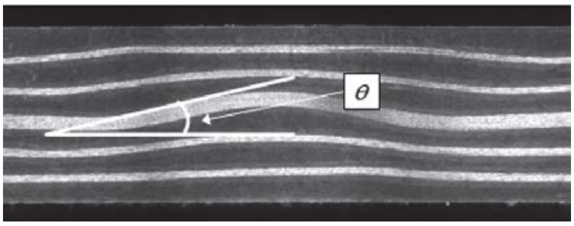

Fig. 2.6. *Specimen with induced out-of-plane fibre wrinkle tested in tensile loading to determine the effect on the tensile damage. [Mukhopadhyay et al., 2015]*

Zhao et al. [2017] studied the influenced of induced in-plane fibre waviness on the tensile properties of unidirectional EH104/D12 slit prepreg tows manufactured by AFP. The in-plane fibre waviness was described as sinusoid model. In order to predict the tensile strength of the unidirectional lamina, with induced in-plane fibre waviness, the authors proposed a maximum tensile stress criterion basing on the hypothesis that the failure of the whole lamina happens as fibre failure occurs in the region where the misalignment angle is maximum. The author found that the tensile properties decrease dramatically with increasing fibre waviness degree. The authors manufactured further specimens with different degrees of in-plane fibre waviness. They found that the failure mode of the unidirectional laminates is influenced by the degree of in-plane fibre waviness. According to Zhao et al. [2017], fibre waviness should be avoided during the manufacturing process in order to obtain correct material performances.

Compressive strength and modulus

The impact of fibre misalignment and fibre waviness on the material behaviour in compression was introduced in Sec. 2.1. The failure model of Rosen, the advanced models of Budiansky & Fleck and Grandidier et al. have shown approaches to estimate the compressive strength when fibre microbuckling and kinking trigger the local instability of the matrix. Budiansky & Fleck [1993], Wisnom [1990] and Grandidier et al. [2012] argued that fibre misalignment has a strong influence on the stability mechanisms of the matrix and hence on the compressive strength.

Due to the large amount of research work carried out in recent years concerning the influence of fibre misalignment and fibre waviness on the compressive strength, only some of them will be discussed below. For further studies the interested reader is referred to the reviews of Schultheisz & Waas [1996], Joyce & Moon [1997] and Kulkarni et al. [2020].

Two studies were performed by Mrse & Piggott [1993] to examine the influence of fibre misalignment on the compressive strength and the Young's modulus. First, fibre misalignment of unidirectional plies, made of carbon reinforced PEEK and four different types of prepreg, were measured using Yurgartis's method. These specimens were then tested in 4PB in order to determine their compressive strengths. Second, laminates with prepregs that were crimped in order to obtain different degrees of waved plies were made. The in-plane fibre misalignment was estimated by measuring the wavelength and the amplitude of the waviness with a microscope, and the samples were tested by compact sandwich 4PB method [Mrse & Piggott, 1993].

The results of the first study have shown that the compressive strength and modulus decreased with increasing fibre misalignment and that the compressive modulus decreased with increasing strain while the tensile modulus increased [Mrse & Piggott, 1993].

The results of the second study have shown that the compressive modulus and strength decreased by increasing misalignment [Mrse & Piggott, 1993]. This was examined in more detail: Mrse & Piggott [1993] used then Bolotin's approach in order to explain the correlation between fibre waviness and Young's modulus. Bolotin's analysis considered alternating elastic layers consisting of a reinforcement and a matrix, wherein the reinforcement layers are curved randomly. Bolotin established a relation between the compliance of the layer and the mean square angular deviation in order to estimate the Young's modulus. This approach was then applied by Mrse & Piggott on the crimped and non-crimped prepregs. The authors found that Bolotin's approach worked well for non-crimped laminates as the deviations are small, as seen in Fig. 2.7. Then, Mrse & Piggott [1993] used a sine wave assumption to describe fibre waviness in crimped prepregs in order to compare them to those without crimping. As seen in Fig. 2.8, for crimped prepregs, deviations are more significant [Mrse & Piggott, 1993].

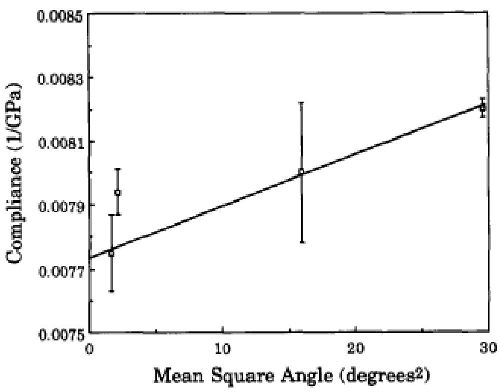

Fig. 2.7. *Compliance of laminates (estimated from zero strain) as a function of the mean square fibre misalignment angle for unwrinkled prepregs. The deviation is small. [Mrse & Piggott, 1993]*

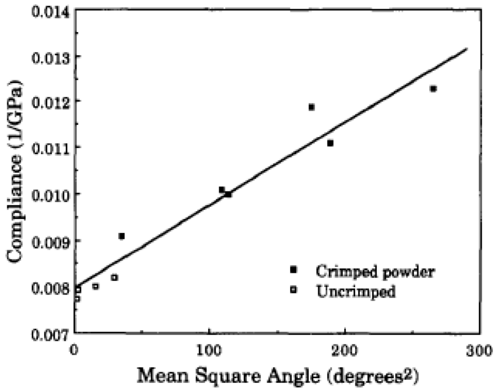

Fig. 2.8. *Compliance of laminates (estimated at zero strain) as a function of the mean square fibre misalignment angle for crimped and non-crimped prepregs. The deviation of crimped prepregs is higher than for non-crimped ones. [Mrse & Piggott, 1993]*

Mrse & Piggott [1993] stated last, that *fibre waviness does not appear to be a major factor affecting the decreasing compressive modulus with increasing fibre strain. [...] Instead, at relatively low strains, the compressive moduli are reduced by fibre waviness, and the strain dependence of modulus appears to be mainly caused by the fibres themselves, [...].*
Adams & Bell [1995] investigated the compressive strengths of specimens with different 0 ° and 90 ° stacking sequences, with and without induced ply waviness. The specimens were made from IM7/8551-7A carbon/epoxy prepreg tapes. Specimens without ply waviness differed from the total number of 0 ° plies. Specimens with ply waviness differed further from the number of wavy 0 ° plies and the wave fraction induced.
In order to estimate the compressive strengths of specimens without ply waviness, the mean compressive strength from a specimen with five 0 ° plies was determined, first, experimentally. Then, using the rule of mixture approach from Agarwal et al. [1990], and the assumption that the stresses in the 0 ° and 90 ° plies remained in the same ratio as their respective elasticity [Adams & Bell, 1995], the compressive strengths of the specimens without induced ply waviness and with different number of 0 ° plies were calculated. Those results served as references, as specimens with the same varying number of 0 ° plies, but with induced ply waviness were then tested experientially. The results were finally compared to those without induced fibre waviness. The authors observed a compressive strength reduction of 35 % when more then 33 % of the 0 ° plies contained waviness.
Hsiao & Daniel [1996] investigated the effect of fibre waviness on the decrease of material stiffness and strength of unidirectional carbon/epoxy composites under axial compression. The classical lamination theory and an incremental analysis were used to estimate stresses and strains in the laminates. Local ply failures were predicted by the Tsai-Wu failure criterion. A progressive damage methodology was applied for graded and localized waviness to visualize stress redistribution after failure initiation. The author stated that

interlaminar shear stresses were found to be the dominant stress components and caused thus the material to fail. According to Hsiao & Daniel [1996], failure was hence initiated by local interlaminar shear stresses and followed by delaminations and layer buckling. Fig. 2.9 depicts the sequence of events occurring during test execution of an unidirectional carbon/epoxy composite loaded in axial compression.

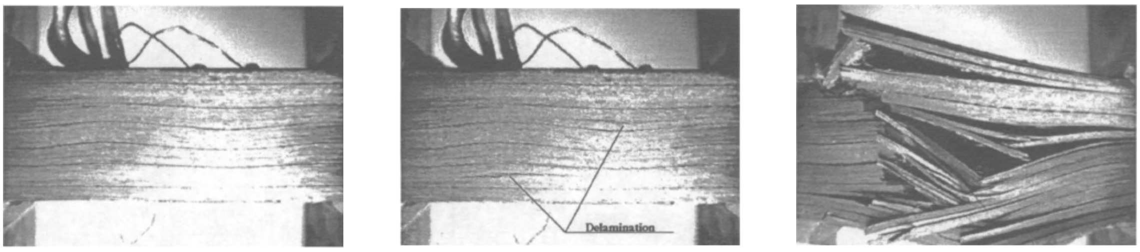

(a) *Specimen with graded fibre waviness before test execution.* **(b)** *Failure initiation through delamination.* **(c)** *Final failure.*

Fig. 2.9. *Unidirectional carbon/epoxy composite loaded in axial compression with graded fibre waviness. [Hsiao & Daniel, 1996]*

Drapier et al. [2001] compared a numeric structural plastic microbuckling model, that was presented in Drapier et al. [1999], with results given in the literature. The model enabled to calculate at ply scale stresses and strains at failure, taking into account the parameters that were governing the microbuckling effect: *size and shape of the initial imperfection, stiffness drop associated with the matrix plastic behaviour, and structural data across the plate thickness (thickness, bending or compression loading, stacking sequence)* [Drapier et al., 2001]. Some of their investigations and conclusions are briefly given below.

The authors exhibited that initial fibre imperfections and the matrix non-linearity influenced the microbuckling mechanism and compared their observations to the those made by Budiansky & Fleck [1993] (kink-band model).

The authors investigated the impact of the wavelength λ on the mechanical response of the material. They stated that the failure strain depends on the wavelength and that there is a critical wavelength range for which failure strains are the lowest. They concluded that in this zone, the failure strain depends principally on the fibre misalignment.

The authors investigated further the effect of the spatial distribution of misaligned fibres on the compressive strength. They modelled an unidirectional ply with boundary conditions, representing the position of the unidirectional ply within the laminate, and with fibres which were distributed in three different manners across the thickness: constantly, modal or anti-modal. The initial fibre misalignment angle and the wave length were set to 1 ° or 2.5 ° and 0.63 mm, respectively. Drapier et al. [2001] stated that the lowest strength was obtained from the constant fibre distribution as large zones are affected by high plastic matrix flow. The authors hence emphasised that the fibre angle distribution is an important parameter to be taken into account in the detection of the spatial distribution wherein plasticity develops. For modal and anti-modal fibre distributions, the authors found that the development of the plastic microbuckling is the result of a combined effect of the geometrical instability distribution and the material non-linearity.

The authors further studied numerically four more fibre distributions. Those are schematically depicted in Fig. 2.10. The four different patterns were periodically distributed in transverse and axial directions in a ply with similar boundary conditions as given above. The authors stated that independently of the fibre distribution the ply response remained the same, but the strains at failure differed significantly (fibre distributions a), b), c) and d) resulted in failure strains of 1.69 %, 2.14 %, 1.63 % and 1.93 %, respectively). The authors stated that the evolution of the material instability is highly influenced by matrix shearing through bending. The authors explained in more detail, that the configurations a) and c), which resulted in lowest strengths, induced a high matrix shearing that favours plastic matrix flow. The other distributions induced a more complex strain state in the matrix that delayed the development of plasticity [Drapier et al., 2001]. According to the authors, the difference between the in-phase and anti-phase distributions is mainly due to the contribution of the elastic mode, i.e. the geometrical non-linearity [Drapier et al., 2001].

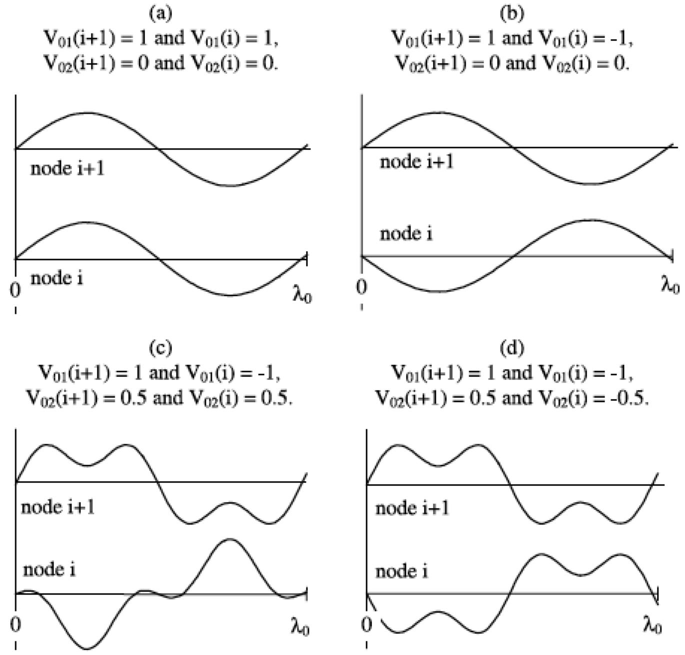

Fig. 2.10. *Shape imperfections of fibres described by different amplitudes in Drapier et al. [2001].*

Jumahat [2011] studied the influence of nanosilica that was incorporated into a epoxy resin on the compressive strength, and on the in-plane shear properties of CFRP composites. In order to describe the quality of the investigated laminates, fibre misalignment was measured using Yurgartis's method. Additionally, static uniaxial compression and tensile tests on $[0]_8$ and $[\pm 45]_{2s}$ laminates were performed [Jumahat, 2011]. Since the authors observed microbuckling and plastic kinking during test conduction, they developed a combined model based on the fibre microbuckling model from Berbinau et al. [1999] and the kink band model from Budiansky & Fleck [1993] to predict the compressive strength.

The results have shown that the presence of nanosilica particles results in a smaller standard deviation of the fibre distribution compared to the unmodified system. In addition to this, the author has shown that nanosilica particles reduced the fibre misalignment up

to ± 1.5 °. The author stated that this might due to the fact that the lower coefficient of thermal expansion of the nanomodified resin reduces the thermal mismatch between fibre and the matrix during curing [Jumahat et al., 2010].
How the fibre waviness influenced the compressive strength was, however, not explained further. Instead, the author cited the following reference Jumahat et al. [2010]: *For instance, the compressive failure strength [...], which has an initial fibre misalignment of* 5 ° *is* 61 % *lower than that of laminate with* 1 ° *initial fibre misalignment.* Therefore, Jumahat [2011] deduced that the strength of the composite reduces with increasing fibre misalignment angle.
Wang et al. [2018] studied the effect of micro in-plane fibre waviness on the compressive strength and modulus of unidirectional fabric composites. The fabrics were made of MR50S carbon and glass fibres which were embedded in an epoxy resin. To evaluate the experimental results, Wang et al. [2018] used a back-out method, basing on the classical lamination theory, to estimate the compressive moduli and compressive strengths. The author found that the decrease of the compressive strength due to the in-plane fibre waviness is significant when the fibre volume fraction amounts to 60 %. Wang et al. [2018] stated further that the in-plane fibre waviness has a stronger impact on the compressive strength than on the compressive modulus. A numerical analysis confirmed these observations.

Fatigue endurance

Lam & Piggott [1989] investigated the durability of carbon fibre epoxy composites which underwent a controlled matrix shrinkage. They used a two-parameter Weibull distribution for pooling the data and to estimate the fatigue life of the material. The authors found that reducing the cure shrinkage stresses of the resin increases the fatigue endurance assuming that the interfacial adhesion between fibre and matrix was not reduced. The authors suggested further that fibre misalignment impacts strongly the interface and matrix fatigue.
Piggott & Lam [1991] examined tensile-tensile fatigue tests on carbon/epoxy specimens with drilled circular holes. The authors investigated how fibre misalignment and fibre waviness impact bending and tensile stresses which led to specimen failure during the fatigue test. After test completion, Piggott & Lam [1991] examined the fracture surfaces by means of a SEM. The authors observed residues of polymer powder which they assigned to fibre wavinesses in the specimen. The authors stated that at the antinodes (point along the fibre misalign wave where the amplitude is maximum) of the waves, transverse stresses may lead to fibre debonding and splitting of the matrix [Piggott & Lam, 1991].
A chain reaction then take place: Once debonded, fibres slide into the debonded regions which leads to abrasion. Cyclic stressing leads then to oscillation of the matrix powder which slides into the curves of the fibre profiles and increases the fibre curvature. The Poisson's ratio, and the width of the hole increase, whereas the Young's modulus decreases. Finally, fibre curvature may increase to a maximum where resulting bending and tensile stresses are high enough to cause fibre failure. [Piggott & Lam, 1991]

2.2.4 Composite materials in the marine sector

There are very few sources in the literature that bring together fibre misalignment or fibre waviness, CFRP and the marine sector. In literature, fibre misalignment or fibre waviness are often referred to inherent material defects which are introduced during the manufacturing process.

Vassilopoulos [2013] provided an overview of fatigue life modelling and prediction methods for wind turbine blade composite materials. The author stated that material defects such as wrinkles, fibre misalignments and voids can lead to failure mechanisms like matrix cracking, transverse-ply cracking, interface cracking and debonding [Vassilopoulos, 2013].

The research work of Mechin et al. [2019] belongs to the sailing sport domain. The author established a complete experimental protocol to measure all necessary parameters (ply thickness e_{ply}, initial fibre misalignment angle Φ_0, fibre volume fraction f, fibre diameter d, elastic modulus in longitudinal direction of the fibres E_F, Young's modulus of the matrix E_M, Poisson's ratio of the matrix ν_M and the parameters of the RO constitutive law γ^c_{UD}, G_{UD}, n_{UD}) to estimate the compressive strength of high modulus CFRP composites using the advanced Equ. 2.5 from Grandidier et al. [2012] which takes into account the structural part of the specimen. The objective of this study was to compare the compressive strength analytically determined by the failure criterion (with the beforehand determined necessary parameters) with the compressive strength experimentally determined by 4PB tests on the same composite material. The presented protocol was divided into two parts. The first one contained a microstructure analysis to measure the parameters related to the structural effect. The microstructural observations to measure e_{ply} were carried out using an optical microscope. Φ_0 was determined using Yurgartis' method (presented in more detail in Sec. 3.3). A Scanning electron microscope (SEM) was used to identify f and d. The latter was further used to determine the fibre gyration radius r_{gf}.

The second part dealt with mechanical tests to obtain E_F, E_M and ν_M and the parameters of the RO constitutive law (γ^c_{UD}, G_{UD}, n_{UD}) to determine the elasto-plastic shear behaviour of the unidirectional ply.

E_M and ν_M were determined by performing tensile tests on the matrix to measure its elastic properties. In order to determine E_F, tensile tests were performed on fibres that were isolated beforehand from uncooked pre-impregnated carbon plies. Last, tensile tests on ±45° laminates were carried out to characterise the shear behaviour of the unidirectional ply and to determine γ^c_{UD}, G_{UD}, n_{UD}.

Mechin et al. [2019] stated that the structural part of Grandidier et al. [2012]'s Equ. 2.5 contributes to approximately 15 % of the compressive strength, thus r_{gf}, E_F, E_M and ν_M f have a minor role in the compressive strength determination, and e_{ply} has in turn an influence on the structural part. Further, Mechin et al. [2019] found that the initial inclination angle of the fibres Φ_0 is highly important and decreases the compressive strength by 20 %. Further, Mechin et al. [2019] stated that the analytical estimation and the experimentally determined value result in similar compression strengths when two standard deviations of the fibre misalignment distribution are taken.

2.3 Review on methods for fibre misalignment and fibre waviness determination

In the last decades, several methods had been developed in order to determine fibre misalignment and fibre waviness of fibre reinforced composite structures. Different methods that can be found in literature will be presented from Sec. 2.3.1 to Sec. 2.3.9. Within these sections, research works of authors who had applied these methods will be briefly presented and their conclusions will be mentioned. Further, advantages and limitations of the methods basing on the statements of the authors will be given.

2.3.1 Ultrasound scanning method

Ultrasonic scanning is a non-destructive testing technique for the 3D characterisation and analysis of fibre waviness in composite materials [Kulkarni et al., 2020].
Zardan et al. [2013] examined the ultrasonic deviation in order to detect layer waviness in CFRP laminates, as shown in Fig. 2.11. The authors stated that ultrasound velocity measurements permit the detection of ply waviness, but not their identification. Further the authors have shown that, in order to identify ply waviness, the deviation of the ultrasonic beam needs to be taken into account [Zardan et al., 2013].
Chakrapani et al. [2012] investigated out-of-plane wavinesses in thick composite panels with applications for wind turbine blades. Therefore, the authors used air coupled ultrasonics. The applied method resulted in a high sensitivity to the detection and characterization of fibre waviness [Chakrapani et al., 2012] in the investigated material.
Hoerrmann et al. [2015] studied the fatigue damage initiation and progression due to the presence of the manufacturing defects in CFRP composites. The authors used ultrasonic and microscopy analysis in order to examine the configuration of the composite material.
Tab. 2.1 shows characteristics of the Ultrasound scanning method.

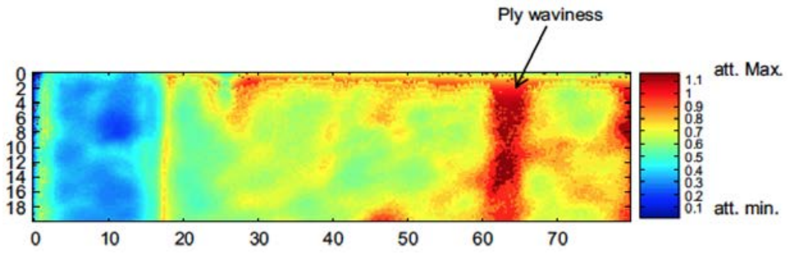

Fig. 2.11. *Typical attenuation C-Scan of a CFRP specimen showing ply waviness [Zardan et al., 2013].*

Tab. 2.1. *Characteristics of the Ultrasound scanning method.*

Advantages:	Scanning of large areas possible [Smith et al., 2015], method used in the industries due to scanning speed and rapid flaw detecting capacities [Kulkarni et al., 2020], high sensitivity to detection and characterization of fibre waviness [Chakrapani et al., 2012].
Limitations:	Only fibre waviness detection possible, not their identification [Kulkarni et al., 2020].

Applied in:	Zardan et al. [2013] (CFRP), Chakrapani et al. [2012] (glass fibre reinforced composites, application: wind turbine blades), Hoerrmann et al. [2015] (CFRP).

2.3.2 (Micro) X-ray computed technology

In micro X-ray computed technology, the object is rotated around its axis in order to obtain X-ray projections from different angles. The projections are then the measured values of the total attenuation that X-rays experience on their way through the object. [Pyrz, 1999]

The (Micro) X-ray computed technology (X-ray CT) is one of the most accurate, advanced and precise method for the observation and investigation of fibre waviness, since it provides a detailed description of the defect in three dimensions [Kulkarni et al., 2020]. In fibre waviness determination, X-ray CT permits thus to characterize the 3D fibre orientation and localisation.

Pyrz [1999] investigated the applicability of X-ray CT to characterize advanced composite materials. Using commercial X-ray scanners, the smallest detail that could be detected was close to 2 µm [Pyrz, 1999]. The author mentioned in particular the advantages of X-ray CT: non-destructive method, in-situ material characterisation and observations of the evolution of the microstructure under mechanical loading or aggressive environments are possible.

Wang et al. [2014] studied the 3D failure pattern of kink bands developed due to compressive loading using the X-ray CT. The aim of the the study was to demonstrate the 3D geometry of kink bands and the interactions between observed damage mechanisms [Wang et al., 2014]. The authors found that two narrow bands which were formed at the points of the highest deflection caused the development of the kink band which led to the final material failure.

Yoshimura et al. [2016] presented a method to analyse fibre orientations in CFRP laminates by applying DIC to images recorded by X-ray CT. The principle concept of this method lies in tracking the brightness patterns resulting from radiodensity differences between fibres and the matrix [Yoshimura et al., 2016]. This method was validated by comparing the results obtained with those determined experimentally using a microscope. The authors stated that the results of this method agreed well with those experimentally measured.

Garcea et al. [2018] reviewed technical aspects of the X-ray CT such as *obtaining sufficient contrast, examination of thin panels, sample size/resolution issues, quantification of damage and defects, and image-based modelling.* Further, the authors provided information *across applications ranging from manufacturing processes, through tensile and compression loading to fatigue and impact damage.* Moreover, Garcea et al. [2018] discussed the advantages of laboratory and synchrotron X-ray CT. Garcea et al. [2018] stated that in the last decades, the spatial resolution of X-ray CT has improved significantly, so that fibre-matrix debonding can be detected, and constituents of CFRP materials can be distinguish using phase contrast approaches. Not only *ex-situ* X-ray CT on composite materials in unloaded condition can be made, but also X-ray scans *in-situ* during experiments or time-lapse studies due to stable and high rotation speeds [Garcea et al., 2018].

Tab. 2.2. *Characteristics of the X-ray CT.*

Advantages:	Accurate and precise method [Kulkarni et al., 2020], non-destructive method, in-situ characterisation, observation of the microstructure under mechanical loading/aggressive environments possible [Pyrz, 1999], complete 3D analysis [Kulkarni et al., 2020].
Limitations:	Time consuming, expensive, not applicable for larger specimens [Kulkarni et al., 2020], small samples are necessary to achieve a high resolution [Garcea et al., 2018].
Applied in:	Pyrz [1999] (polymer composites), Krause et al. [2010] (ceramic matrix composites, glass fibre reinforced plastics), Wang et al. [2014] (CFRP), Graupner et al. [2014] (flax/PLA, Cordenka/PLA), Yoshimura et al. [2016] (CFRP), Garcea et al. [2018] (polymer composites).

2.3.3 Structure tensor method

The concept of the structure tensor is known from the image processing field, where it is used for the detection of edges in images, image segmentation, visualization and quantification of the microstructure of tissues, quantification of the structural anisotropy in tissues and for analysing textures in images [Straumit et al., 2015].

The Structure tensor method (ST) method is a mathematical derivative-based or gradients method, permitting the derivation of the local orientation and anisotropic properties of the microstructure shown in a grey scale image. It is assumed that the fibre direction is orthogonal to the fibre surface normal, i.e. to the grey value gradient direction. [Syerko et al., 2019]

In Krause et al. [2010] the authors presented an algorithm for computing the quantitative fibre orientation distribution basing on the structure tensor. The authors also provide a local X-ray transform for denoising and fibre segmentation. Basic assumptions, characteristics of the fibre orientation and the properties of the structure tensor are given in Krause et al. [2010]. The author stated that for homogeneous material (e.g. fabrics) the structure tensor is ideal for determining the fibre orientation distribution.

Straumit et al. [2015] applied structure tensors for determining the orientation of fibres in 3D micro-CT images of textile composites and for segmenting the image into its material components. The aim of Straumit et al. [2015] was to provide an automatically generated voxel-based description of the representative volume element. The material component segmentation was applied on CFRP samples by thresholding or clustering in a 2D parameter space [Straumit et al., 2015].

The authors found that the uncertainty of the method, with respect to the standard deviation, is low (up to 0.9 °). They also stated that the uncertainty depends on the voxel size in the image and the size of the integration window. Further, they concluded that clustering allows not only the separation of the matrix from the fibres but also the differentiation of different primary orientations. [Straumit et al., 2015]

Tab. 2.3. *Characteristics of the Structure tensor method.*

Advantages:	Easy to implement, fast algorithm relying on local properties of the given reconstruction, ideal method for determining fibre orientation distributions in homogeneous materials (fabrics) [Krause et al., 2010].
Limitations:	The voxel size sets the limit on the maximum volume of the material [Straumit et al., 2015].
Applied in	Krause et al. [2010] (fabric-reinforced C/SiC, short-fibre-reinforced C/SiC, glass fibre-reinforced plastics), Straumit et al. [2015] (carbon/epoxy, steel/epoxy).

2.3.4 Direct tracking method

In direct tracking, binary images are required as data input to track the actual pixels of lines directly [Pourdeyhimi et al., 1996]. Compared to the Fourier transform method (FT) method, which is significantly affected by the line thickness (number of pixel), the tracking method is relatively insensitive to it [Pourdeyhimi et al., 1997]. Nevertheless, it was criticized that the algorithm of the Direct tracking method (DT) is time consuming, so that the application of this method is often found in research and development [Ghassemieh et al., 2002]. Ghassemieh et al. [2002] also stated, that *in denser structures, as the number of crossover points increases, this method becomes less efficient.*

Tab. 2.4. *Characteristics of the Direct tracking method.*

Advantages:	Suitable in determining fibre orientation distribution in nonwoven fabrics regardless of their structural characteristics, optimal choice in terms of accuracy [Pourdeyhimi et al., 1997].
Limitations:	Time consuming algorithm, not suitable in denser structures [Ghassemieh et al., 2002].
Applied in:	Pourdeyhimi et al. [1996] (non-woven fabrics), Pourdeyhimi et al. [1997] (non-woven fabrics).

2.3.5 Fourier transformation method

Fourier methods are based on the principle of transforming a spatial gray scale intensity image into a frequency spectrum with appropriate magnitude and phase values [Pourdeyhimi et al., 1996].

The frequency domain is a space in which each image value at image position F represents the amount by which the intensity values in image I vary over a specific distance related to F. In the frequency domain, changes in image position correspond to changes in the spatial frequency or the rate at which image intensity values are changing in the spatial

domain image I. [Ghassemieh et al., 2002]
The FT permits to determine the rate at which intensity transitions occur in a certain direction in the image corresponding to the spatial frequency [Pourdeyhimi et al., 1996]. The spatial frequency image is that of interest, since image compression, levelling the image brightness and contrast and enhancement can be done more easily on the frequency spectrum [Ghassemieh et al., 2002]. As mentioned above, one of the main applications of the FT method is the measure of the given orientation [Ghassemieh et al., 2002].
Common methods are the discrete and the fast FT method. The latter is a faster version of the discrete one. The mathematical principles of the Fourier transformation is given in the literature (Bracewell [1986], Pourdeyhimi et al. [1996]) and will not be discussed further here. Advantages and limitations of this method are given in Tab. 2.5.

Tab. 2.5. *Characteristics of the FT method.*

Advantages:	Fairly accurate and reliable method [Pourdeyhimi et al., 1997], low calculation time (fast algorithm) [Ghassemieh et al., 2002], detect randomly distributed fibre misalignment [Kratmann et al., 2009], reliable in measurement accuracy, fast in execution time and flexible in its application [Sander & Barocas, 2009].
Limitations:	Method tends to overestimate the SD of the distribution [Pourdeyhimi et al., 1997], not suitable for on-line applications since its speed is slow and its motion blur problems [Pourdeyhimi & Kim, 2002].
Applied in:	Pourdeyhimi et al. [1997] (non-woven fabrics), Pourdeyhimi & Kim [2002] (non-woven fabrics), Ghassemieh et al. [2002] (non-woven fabrics), Kratmann et al. [2009] (UD CFRP laminates manufactured by pultrusion or prepregs), Sander & Barocas [2009] (engineered tissues and biomaterials).

2.3.6 Hough transformation method

The Hough transformation method (HT) is an image transform technique permitting the estimation of the fibre distribution directly. The HT method bases on the detection of various forms as straight lines segments [Hough, 1962] which are revealed as peaks [Sklansky, 1978]. The point-line duality is therefore the fundamental concept for the line localisations [Davies, 1990], followed by the main process involving the transformation of a line in the cartesian space into a point in the parametric space [Xu & Yu, 1997]. The actual orientation of the lines is included directly in the computation of the transform [Ghassemieh et al., 2002]. High quality photos with high field depth at high magnifications are important when applying the HT method [Ghassemieh et al., 2002]. In Ghassemieh et al. [2002], the authors used the SEM to obtain such high quality images.

Tab. 2.6. *Characteristics of the HT method.*

Advantages:	Suppression of image noises and ability to deal with fibres containing gaps and breaks [Xu & Yu, 1997], suitable for the detection of regular lines such as curves, circles, ellipses [Ghassemieh et al., 2002].

Limitations:	Dependent on subsequent procedures to isolate the peaks [Pourdeyhimi & Kim, 2002], high computation time, especially for larger-scale images with higher accuracy [Ghassemieh et al., 2002].
Applied in:	Xu & Yu [1997] (non-woven fabrics), Ghassemieh et al. [2002] (non-woven fabrics), Pourdeyhimi & Kim [2002] (non-woven fabrics).

2.3.7 Stereological method (Yurgartis [1987]' method)

The Stereological methods are based on a sectioning technique permitting the determination of the spatial orientation of fibres in continuous fibre composites by measuring the major and minor axes of the ellipsoids on the sectioning surface. Several authors referred to the sterology in order to determine the angular misalignment in fibre reinforced composites.

In Blanc et al. [2006], the authors presented an image processing approach based on the stereological method in order to estimate the principal directions and fibre orientation distribution of a single section.

Yurgartis [1987] referred to the stereology as he presented a technique for measuring the volume fraction distribution of the fibre misalignment angles in CFRP (APC-2) composites. This method assumed that (i) the fibres are straight over short distances and (ii) that all fibres have the same circular diameter [Yurgartis, 1987]. Yurgartis's method will be presented in more detail in Ch. 3 using different schematics (Fig. 3.2 to Fig. 3.6) for easily assimilating the topic.

Mrse & Piggott [1993] used Yurgartis [1987]' method to quantify fibre misalignments, and related these to the compressive strength and modulus of carbon/PEEK laminates.

Creighton et al. [2001] compared the MFIA method (presented below) to Yurgartis [1987]' method when determining fibre misalignment in CFRP composites with high fibre alignment degrees and significant fibre wavinesses.

Tab. 2.7. *Characteristics of Yurgartis's method.*

Advantages:	Cost effective method that can be implemented by simple means.
Limitations:	Assumption of circular fibre sections and straight fibres [Paluch, 1994], serial sectioning to determine the alignment of individual fibres along their length is time consuming and is prone to errors [Clarke et al., 1995], cumbersome method, angle misalignment determination only of a small number of fibres at a few locations, inherently destructive method, unsuited to quality control requirements during monitoring of production operations [Creighton et al., 2001], sensitive to irregular fibre shapes, specimen preparation remains difficult and is time consuming, high quality polishing and micrographs with high resolution are necessary [Kratmann et al., 2009].
Applied in:	Creighton et al. [2001] (CFRP, SD = N/A), Mrse & Piggott [1993] (AS4-PEEK prepregs, SD = N/A), Jumahat et al. [2010] (CFRP, SD = 2σ), Mechin et al. [2019] (HM CFRP, SD = σ, 2σ).

Jumahat et al. [2010] applied Yurgartis [1987]' method in order to investigate the compressive response of commercial and nanosilicia-filled CFRP composites.
Mechin et al. [2019] used Yurgartis [1987]' method to establish an experimental protocol for measuring the fibre misalignment angle parameter which affects the compressive strength of CFRP composites.

2.3.8 The Multiple field image analysis (MFIA) method

In Creighton et al. [2001], the authors presented the MFIA method, to characterize fibre misalignment in CFRP composites. The authors compared the new approach with Yurgartis's method. Similarities and differences of both methods are mentioned below.

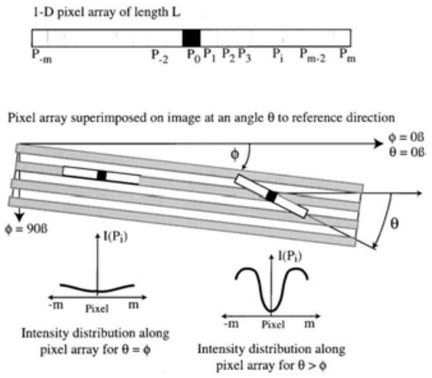

Fig. 2.12. *Schematic principle of MFIA method: Depending on the brightness of elongated features in the image, the width of light intensity of the pixel array is either equal ($\Theta = \Phi$) or narrower ($\Theta \geqq \Phi$) to the pixel array. [Creighton et al., 2001]*

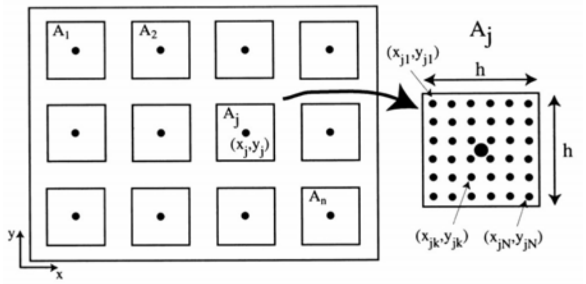

Fig. 2.13. *Schematic principle of a set of square domains that represent the field of interest. The fibre orientation is measured within each domain. [Creighton et al., 2001]*

The MFIA uses the confocal scanning laser microscope and an image analysis algorithm to characterise fibre misalignment. The microscope records larger regions of the specimens surface than the optical microscope used in Yurgartis' work. Samples are cut parallel to the pultrusion direction whereas samples in Yurgartis's method are cut at a given angle to the 0°-fibre-direction.
The principle of the MFIA method is based on the variation of light intensities I given by dark elongated features in the image. These features might represent fibres, or matrix between fibres, or bundles of fibres which can be oriented at a angle Φ to the reference direction. Considering a pixel array inclined at an angle Θ close to - or different from Φ, as shown in Fig. 2.12, the width of the light intensity I is equal - or narrower to the width of the array. [Creighton et al., 2001]
A set of square domains, A_j, as shown in Fig. 2.13, needs to be defined in order to calculate the fibre misalignment from the elongated features on the samples surface. A_j contains the coordinates of the centroid, (x_j, y_j), the domain side length h_{MFIA} and the number of points, N, within the domain at which the analysis will be carried out. [Creighton et al., 2001]

An intensity variation parameter δ is then defined by sampling the light intensities along the pixel array and by calculating the corresponding value. Interested readers are referred to [Creighton et al., 2001] for more detailed information on the applied equations.

Two studies on two different materials were hence carried out in Creighton et al. [2001]. First, on an epoxy-67 vol% CFRP composite with two grades of pultruded material: (i) free of any pores and (ii) containing porosity (approximately 3.5 %). Second, on an epoxy-61 vol% CFRP composite made from prepreg sheets. [Creighton et al., 2001]

The authors performed both methods on these materials to determine the fibre misalignment angles. At least, they concluded the following:

For the pultruded material, 180 fibres were examined by Yurgartis' and 60 domains by the MFIA method. Low fibre misalignment up to 1 ° was observed by both methods. However, the authors observed slightly higher misalignment angle values for Yurgartis' method which was, according to them, due to uneven stray fibres that are easier picked up by single fibre methods as the Yurgartis' one. The authors also argued *that such single fibre effects are of limited interest, since they are unlikely to affect the macroscopic failure behaviour.*

Tab. 2.8. *Characteristics of the MFIA method.*

Advantages:	Suitable for characterising large material volumes, not time consuming, also suitable for composite specimens exhibiting long-range spatial variations in fibre alignment (i.e. fibre waviness), the method is robust, sensitive and experimentally convenient [Creighton et al., 2001], low polishing quality is sufficient [Kratmann et al., 2009].
Limitations:	Cannot detect randomly distributed fibre misalignment, the method computes average orientations and a true measure of the random misalignment within the domains cannot be obtained, it is difficult to visually control whether a computed orientation is a good match for the local fibre orientation, the method is sensitive to surface scratches [Kratmann et al., 2009], the measured average misalignment angle tends to fluctuate as a result of significant variations in local fibre alignment within the domain [Creighton et al., 2001], limited to a specific spatial resolution, requires extensive computational effort [Wilhelmsson & Asp, 2018].
Applied in:	Creighton et al. [2001] (CFRP composites, pultruded and prepreg sheets), Kratmann et al. [2009] (UD CFRP laminates manufactured by pultrusion or prepreg), Sutcliffe et al. [2012] (CFRP).

2.3.9 Other methods

Finally, other methods found in literature are briefly listed in tabular form, below.

Tab. 2.9. *Characteristics of the Single-slit projection method.*

Single-slit projection method	
Method:	Based on a single-slit Fraunhofer diffractometry, the diffraction of waves through a slit onto a projection at a long distance from the diffracting object [Goris & Osswald, 2015] permits the determination of fibre orientation and fibre length distribution.
Advantages:	Accurate measurements in fibre orientation distributions with little effort, can be used in-line during a quality control process or can confirm fibre orientations of models during the design step [Hernandez et al., 2003].
Limitations:	Application to the fully three-dimensional random fibrous structures is not possible [Syerko et al., 2019].
Applied in:	Hernandez et al. [2003] (glass-mat reinforced thermoplastics, fibre reinforced polyamides), Goris & Osswald [2015] (composites with glass or natural fibres).

Tab. 2.10. *Characteristics of the High resolution misalignment analysis (HRMA).*

High resolution misalignment analysis	
Method:	Measures fibre misalignment angles from fibre waviness in two dimensions, basing on an image analysis in Matlab, where the angle of individual fibre segments is measured in detailed micrographs (direct method). [Wilhelmsson & Asp, 2018]
Advantages:	Accurate measurements on composites with high fibre waviness, does not use complex computations, resulting in high speed and spatial resolution, is computationally efficient, only one fitting-parameter (threshold), offers measurements on individual fibres, providing statistics of tens of thousands of fibres from one micrograph. [Wilhelmsson & Asp, 2018].
Limitations:	Micrographs are required where individual fibres can be identified, relatively small cells are needed for high accuracy, limited by the characteristic length of the measured objects, i.e. the fibre diameter [Wilhelmsson & Asp, 2018].
Applied in:	Wilhelmsson & Asp [2018] (CFRP).

Tab. 2.11. *Characteristics of the Mean intercept length method.*

Mean intercept length method	
Method:	Common stereological measurement method to quantify structural anisotropy [Sander & Barocas, 2009].

Advantages:	Representation of the results by a convex polygon makes the evaluation of the fibre orientation directions visually easier [Luo et al., 1991].
Limitations:	Elliptical distribution of the material assumed [Sander & Barocas, 2009].
Applied in:	Sander & Barocas [2009] (cellular and acellular fibrin tissue), Luo et al. [1991] (fibrous materials).

2.3.10 Assessment on the methods to determine the fibre misalignment angle

The above presented methods to determine the fibre misalignment angles are characterised by the fact that they involve complex techniques that are specified on low volume areas requiring a lot of experimental technical resources, as well as accessible image analysis software.

In the scope of this study, Yurgartis's method was chosen to determine the in- and out-of plane fibre misalignment angles, because it was immediately applicable, the required equipment (sectioning and polishing machines, optical microscope, analysing software) was available, and effort and benefit fitted in the time schedule of the present research work.

In the scope of this study, a protocol containing five steps to determine the fibre misalignment angles was established. These steps will be presented in Sec. 3.3.1 to Sec. 3.3.5.

The present study describes hence an original study on the fibre misalignment angle determination of seven material series consisting of different IM carbon fibres and epoxy resins, frequently used in the nautical sector, using Yurgartis's method. Specimens are sectioned along the thickness and width to determine the in- and out-of-plane fibre misalignment angles from at least 1000 ellipses. A further distinction is made on the investigated zones. In- and out-of-plane fibre misalignment angles are determined on the mould and sealant sides in order to investigate the impact of the fabrication process. Further, a discussion on the choice of the fibre diameter, which is necessary to determine the fibre misalignment angles, will be made in Sec. 3.2.3. Lastly, the creation of cartographies showing the spatial fibre angle distribution completes the study on the fibre misalignment determination of the seven series and provides information on how the in- and out-of-plane fibre misalignment angles are applicable in the analytical solutions of Budiansky & Fleck [1993] and Grandidier et al. [2012].

3

Determination of the in- and out-of-plane fibre misalignment angles using Yurgartis' method

Contents

In the present Ch. 3, Yurgartis' method will be applied to continuous carbon fibre specimens from seven different material series. The objective is to determine their fibre misalignment angles which correspond to one of four parameters to analytically calculate the compressive strength X_c^{ANA} using the analytical solutions of Budiansky & Fleck [1993] and Grandidier et al. [2012].

Therefore, in Sec. 3.1 the materials of the seven series will be presented, first. Then, in Sec. 3.2, Yurgartis' method will be introduced by defining the in- and out-of plane directions, the specimen sectioning directions and the necessary equations to calculate the fibre misalignment angles. Afterwards, in Sec. 3.3, Yurgartis' method will applied to the specimens of the seven series. The steps from the raw specimens to the fibre misalignment angles will be described in detail. Within this section, a method will be proposed which permits to determine the fibre mean diameters without perpendicularly specimen sectioning, beforehand, as this is done in Yurgartis' method. Last, in Sec. 3.4, the fibre misalignment angles as a function of the diameter will be presented. As stated in the literature, the sensitivity of Yurgartis' method to the fibre shape will be confirmed, exemplarily.

3.1 Presentation of the material for fibre misalignment angle determination

The present studies on the misalignment angle determination, as well as on the tensile and 4PB tests, which will be presented in Sec. 4.1, were carried out as part of a collaborative research project with the racing team MACIF, and the design office Gsea Design. Their objective was, on the one hand, to design a new version for their hydrofoils, and on the other hand, to evaluate their calculation methods. For this purpose, 7 different prepreg materials were selected which form the basis of the following investigations.

The misalignment angles of those seven prepregs were determined using Yurgartis' method. The prepregs, whose main characteristics are listed in Tab. 3.1, were all made of IM carbon fibres and epoxy resins whose glass transition temperatures were at 120 °C. They were manufactured to panels with a [+45°/ 0_9°/-45°/0_{11}°/-45°/0_9°/+45°] stacking sequence by CDK Technologies in Lorient and cut into several specimens by water jet for 4PB testing after autoclave curing. More information concerning the fabrication process of these specimens will be given in Sec. 4.1.

Fig. 3.1 shows the specimens which were recovered from the 4PB tests and which were used for the fibre misalignment angle determination.

The coordinate system in Fig. 3.1 will be used in the following to define the in- and out-of-plane directions of (mis-)aligned fibres.

In the following Sec. 3.2, the implementation of Yurgartis' method to determine the fibre misalignment angles of the presented specimens will be demonstrated.

Tab. 3.1. *Main characteristics of the seven prepregs whose in- and out-of-plane fibre misalignment angles were to be determined.*

N° of series	Series 1	Series 2	Series 3	Series 4	Series 5	Series 6	Series 7
Suppliers	STRUCTIL		GURIT		VITECH	SHD	HEXCEL
Fibres	T800H		IM2C		IMS65	T800S	IM2C
Filament No.	12K		12K		24K	24K	12K
Matrices	R374-1	R367-2	SE84 LV	SE84 Nano	XB3515	MTC9810	M79
Resin mass Impregnation rate ± 3 %	38.8	37.0	35.2	35.7	37.6	36.0	36.0

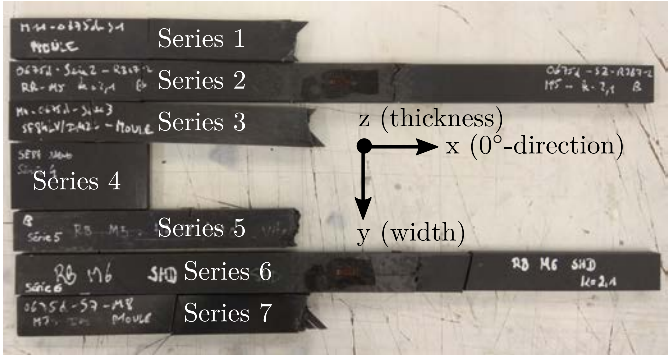

Fig. 3.1. *Specimens from 4PB tests taken to determine the fibre misalignment angles according to Yurgartis' method.*

3.2 Introduction to Yurgartis' method

Yurgartis [1987] describes a procedure to determine the in- and out-of-plane misalignment angles Φ_i and Θ_i of unidirectional continuous fibre composites. Samples are cut parallel or perpendicular to their fibre direction at predefined angles Φ_{PC} and Θ_{PC}. Using the geometric properties of the ellipses on the section surface, the in- and out-of-plane fibre misalignment angles Φ_i and Θ_i can then be determined using simple trigonometric calculations. This approach is based on the assumption that short fibres section are approximately straight and that all fibres have the same circular diameter [Yurgartis, 1987]. In the following, Yurgartis [1987]'s method will be presented in more detail.

3.2.1 Definition of the in- and out-of-plane fibre misalignment orientations

Using Yurgartis' method, it is advantageous to define a reference system which describes the specimen position in the system, the 0°-fibre-direction and the planes in which fibres can be misaligned.

Fig. 3.2 shows a coordinate system whose x-, y- and z-directions coincide with the length, width and thickness of the 4PB specimens presented in Fig. 3.1. The x-direction corresponds to the 0°- direction of well aligned fibres.

Fibre misalignment can occur either in the plane, out-of-plane or in both directions. Fig. 3.2 depicts perfectly aligned fibres in the x-direction, and one fibre that is misaligned in in- and out-of-plane directions. The projection of the misaligned fibre on the XZ plane will thus be defined in the following as out-of-plane fibre misalignment, that on the XY plane as in-plane fibre misalignment. The angle describing the out-of-plane fibre misalignment is defined as Θ_i, that describing in-plane fibre misalignment as Φ_i. These definitions will maintained in the following study.

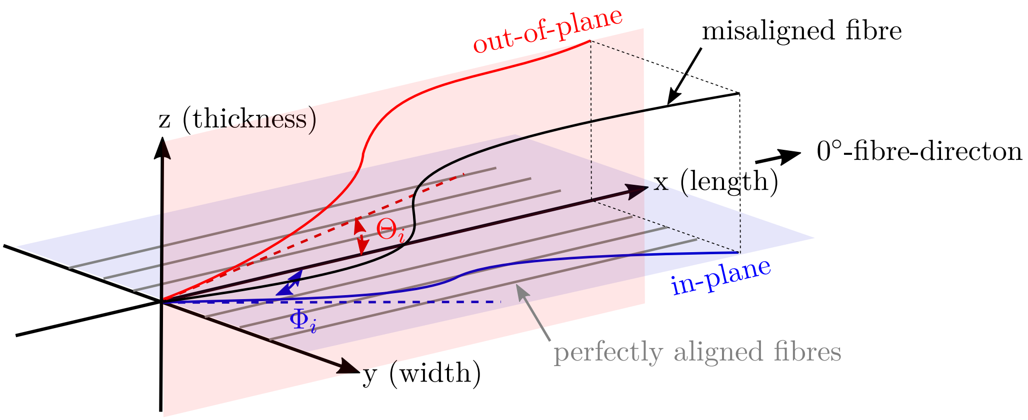

Fig. 3.2. *Schematic explanation of in- (Φ_i) and out-of-plane (Θ_i) fibre misalignment orientations.*

3.2.2 Definition of the sectioning directions

Yurgartis' method requires specimen sectioning at two angles to their fibre direction.

When fibres are aligned in x-direction as depicted in Fig. 3.3a, sectioning along the spec-

imen's width with a plane cut angle Θ_{PC} (Fig. 3.3b), corresponding to a rotation around the y-axis, leads to a section surface with ellipses (Fig. 3.3c) permitting the determination of the out-of-plane misalignment angles of the fibres.
Sectioning the specimen along the thickness with a plane cut angle Φ_{PC} (Fig. 3.4b), corresponding to a rotation around the z-axis, leads to a section surface with ellipses for the determination of the in-plane fibre misalignment angles (Fig. 3.4c).
These two sectioning types form the basis of the following analytical determination of the in- and out-of-plane fibre misalignment angles.

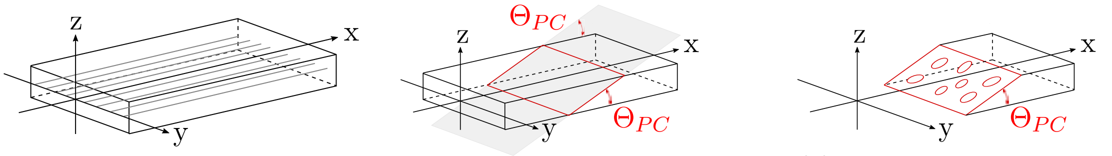

(a) *Unidirectional continuous fibres in x-direction.*

(b) *Out-of-plane sectioning along the specimen width.*

(c) *Ellipses on section surface after out-of-plane sectioning.*

Fig. 3.3. *Specimen sectioning along the width with a plane cut angle Θ_{PC} to determine the out-of-plane misalignment angles Θ_i.*

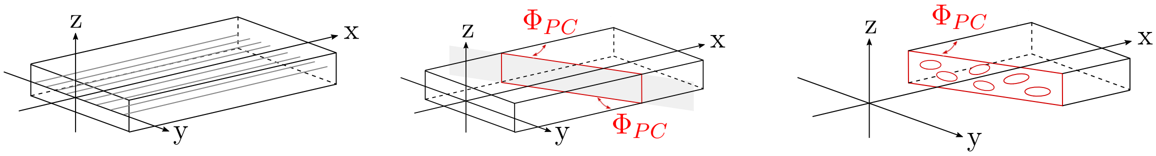

(a) *Unidirectional continuous fibres in x-direction.*

(b) *In-plane sectioning along the specimen thickness.*

(c) *Ellipses on section surface after in-plane sectioning.*

Fig. 3.4. *Specimen sectioning along the thickness with a plane cut angle Φ_{PC} to determine the in-plane misalignment angles Φ_i.*

In the following Sec. 3.2.3, the necessary equations, for the determination of the in- and out-of-plane misalignment angles Φ_i and Θ_i from the ellipses on the sectioning surfaces, will now be presented.

3.2.3 Determination of the misalignment angles in in- and out-of-plane direction

The estimation of the fibre misalignment angles in out-of-plane (in-plane) direction required the knowledge of three parameters: the length of the major axes of the ellipses a_i (a'_i), and the fibre diameter to calculate the angles between the sectioning plane and the axes of the (mis-)aligned fibres ω_i (ω'_i), as well as the plane cut angle Θ_{PC} (Φ_{PC}) to determine the out-of-plane (in-plane) fibre misalignment angles Θ_i (Φ_i).
In Yurgartis [1987], the fibre diameter was determined through specimen sectioning perpendicularly to the fibre direction and by calculating the mean value of the overall fibres diameters $d_{90°,mean}$ on the section surface. Hence, Yurgartis found a mean diameter of 6.93 µm with a SD of 0.31 µm measured from 742 XAS carbon fibres. The a_i (a'_i) data were measured by a microcomputer program, and the sectioning angle Θ_{PC} (Φ_{PC}) was defined as the mean value $\omega_{i,mean}$ ($\omega'_{i,mean}$) of the overall ω_i (ω'_i).
The same approach was applied in the scope of this study, with the following supplement.

On the one hand, the fibre diameter was determined as it was done in the research work of Yurgartis [1987] (perpendicularly specimen sectioning and fibre diameter mean value determination $d_{90°,mean}$). On the other hand, the fibre diameter was referred to the minor axes lengths b_i (b'_i) of the ellipses or to the mean value of all minor axes lengths $b_{i,mean}$ ($b'_{i,mean}$). As last option, the fibre diameter d_{DS} was taken directly from the data sheet. The choice of determining the fibre misalignment angles from four different diameter sources was done, since Yurgartis' method requires an additional step, specimen sectioning at 90°, whereas the fibre diameters are directly indicated on the data sheet or can, when the fibre diameter is set equal to the minor axes, be determined individually for each ellipse and from this the resulting mean value when using the image processing software *ImageJ.*Thus, within this study, four different fibre diameters $d_{90°,mean}$, b_i (b'_i), $b_{i,mean}$ ($b'_{i,mean}$) and d_{DS} were applied to estimate the fibre misalignment angles Θ_i (Φ_i). The major axes of the ellipses a_i (a'_i) were also determined using *ImageJ*. This part will be presented in more detail in Sec. 3.3.4.

The determination of the in- and out-of-plane fibre misalignment angles Φ_i and Θ_i was finally performed in two steps. After diagonal specimen sectioning, as presented in Fig. 3.3 and Fig. 3.4, ω_i (ω'_i) were determined, first, entering the values of the major axes a_i (a'_i) and the fibre diameter d_F ($d_{90°,mean}$, b_i (b'_i), $b_{i,mean}$ ($b'_{i,mean}$) or d_{DS}) in Equ. 3.1 (Equ. 3.3). Then, using Equ. 3.2 (Equ. 3.4) and with given sectioning angle Θ_{PC} (Φ_{PC}), corresponding to $\omega_{i,mean}$ ($\omega'_{i,mean}$), the out-of-plane (in-plane) fibre misalignment angles Θ_i (Φ_i) were determined.

To conclude this part, the relation between the different angles Θ_i, Θ_{PC}, ω_i (Φ_i, Φ_{PC}, ω'_i) and the major and minor axes a_i, b_i (a'_i, b'_i) are complementarily shown in Fig. 3.5 (Fig. 3.6).

The above described procedure was applied to the specimens of the present research study. The practical realisation will be presented in the following Sec. 3.3.

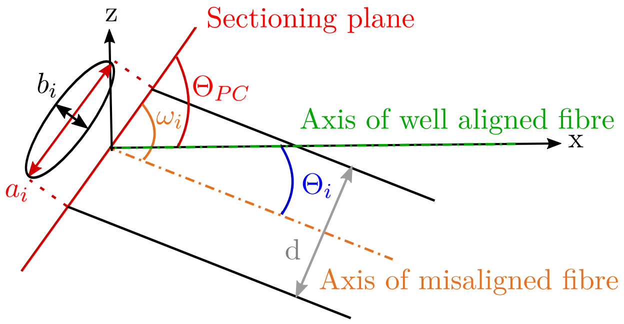

$$\omega_i = \arcsin\left(\frac{d_F}{a_i}\right) \qquad (3.1)$$

$$\Theta_i = \omega_i - \Theta_{PC} \qquad (3.2)$$

$$\Theta_i = \omega_i - \omega_{i,mean}$$

Fig. 3.5. *Schematic explication of the definition of* Θ_{PC}, Θ_i *and* ω_i.

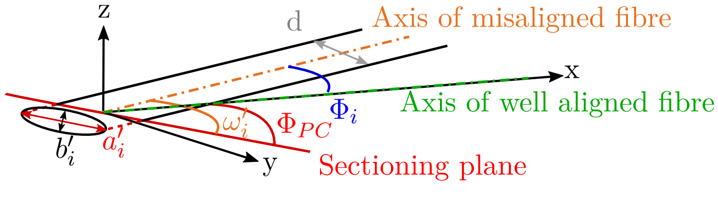

$$\omega'_i = \arcsin\left(\frac{d_F}{a'_i}\right) \qquad (3.3)$$

$$\Phi_i = \omega'_i - \Phi_{PC} \qquad (3.4)$$

$$\Phi_i = \omega'_i - \omega'_{i,mean}$$

Fig. 3.6. *Schematic explication of the definition of* Φ_{PC}, Φ_i *and* ω'_i.

3.3 Practical implementation of Yurgartis' method

The 4PB specimens that were presented in Sec. 3.1 were used to perform the fibre misalignment angle determination according to Yurgartis' method. The reference system presented in Fig. 3.2, the sectioning directions given in Fig. 3.3 and Fig. 3.4, and the Equ. 3.1 to Equ. 3.4 formed the basis for the fibre misalignment angle determination. Therefore, the practical implementation consisted of

1. Specimen sectioning along the width and the thickness.
2. Resin coating and polishing of specimens.
3. Image recording using an optical microscope.
4. Image post-processing with *ImageJ* software.
5. In- and out-of plane misalignment angle determination.

These steps will be presented in more detail in the following Sec. 3.3.1 to Sec. 3.3.5.

3.3.1 Sectioning of specimens along the width and the thickness

As schematically depicted in Fig. 3.3 and Fig. 3.4, the specimens needed to be sectioned along the width and the thickness in order to obtain surfaces permitting the determination of the in- and out-of-plane misalignment angles by means of the ellipses on the section surfaces and Equ. 3.1 to Equ. 3.4.

The present work aimed to differentiate between misalignment angles close to the mould and close to the sealant side, as failure is produced at these sides when specimens are tested in 4PB. Therefore, ellipses in those zones were investigated.

Sectioning along the width thus provided two samples, one *mould side* sample with a zone of interest close to the mould side and one *sealant side* sample with a zone of interest close to the sealant side, as depicted in Fig. 3.7. Sectioning along the thickness provided hence one sample containing a zone close to the mould and a zone close to the sealant side, as exhibited in Fig. 3.8.

Therefore, for each specimen of the seven series, ellipses of four zones were investigated. In order to obtain conclusive results, 1000 ellipses of each zone were analysed at least.

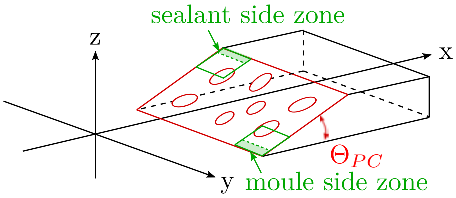

Fig. 3.7. *Sectioning along the width provides two samples, one with a zone to be analysed close to the mould side, the other sample with a zone close to the sealant side.*

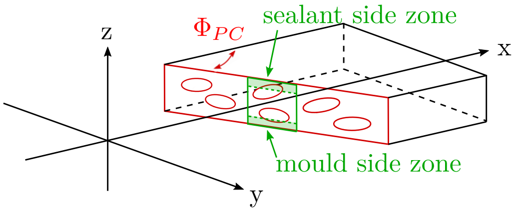

Fig. 3.8. *Sectioning along the thickness provides one sample with zones to be analysed close to the mould and sealant sides.*

In Yurgartis [1987], a very small sectioning angle of 5° was chosen, in particular for sensitivity reasons. He mentioned that (i) the sensitivity of a_i (a'_i) to ω_i (ω'_i) is greater for

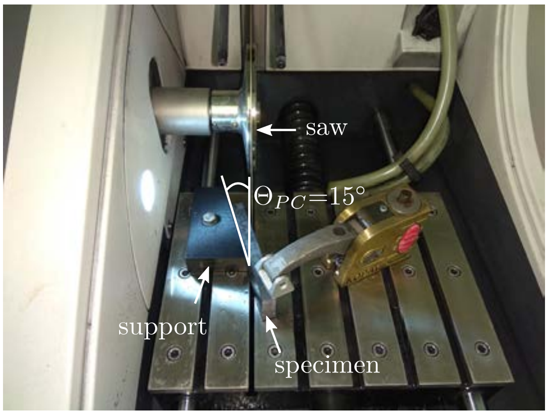

Fig. 3.9. *Specimen sectioning along the width with Θ_{PC} = 15°.*

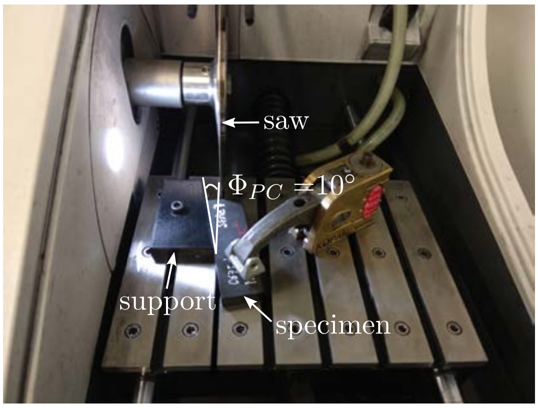

Fig. 3.10. *Specimen sectioning along the thickness with Φ_{PC} = 10°.*

small ω_i (ω_i'). This results in a higher angular resolution. However (ii) as ω_i (ω_i') is too small, the assumption that the measured fibre segments are straight is less given. Last, he mentioned that (iii) ω_i (ω_i') is less sensitive to fibre diameter variations when ω_i (ω_i') is small. [Yurgartis, 1987]

Taking into account the arguments of Yurgartis [1987], slightly higher sectioning angles were chosen in the scope of this study to reduce the cutting path along the specimen's width and thickness and thus to reduce possible deviations from the ideal section path. The sectioning angles were thus set to $\Theta_{PC} = 15\,°$ for sectioning along the width and to $\Phi_{PC} = 10\,°$ for specimens sectioned along the thickness.

A support, 3D printed beforehand, was used to align the specimens at the correct angle to the saw blade as depicted in Fig. 3.9 and Fig. 3.10. The rotation and cutting speed of the saw blade was 2000 $\frac{\text{tr}}{\text{m}}$ and 1000 $\frac{\text{mm}}{\text{s}}$, respectively. Water was used as lubricant. Fig. 3.11 exhibits a specimen after cutting along the width and the thickness. For specimens cut along the width, the investigated zones are framed and marked in green.

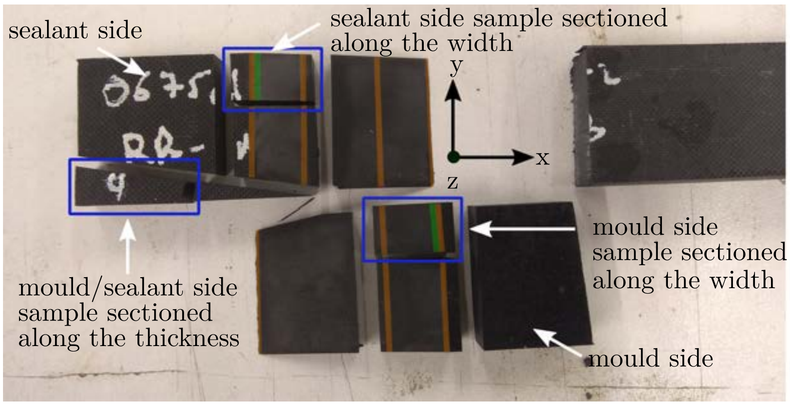

Fig. 3.11. *Example of a specimen that was sectioned along the width and along the thickness. The samples used in the present study for the fibre misalignment determinations are framed. Those samples contain the zones of interest (marked in green for specimen sectioning along the width) in which at least 1000 ellipses were analysed. Orange zones mark the ±45 plies.*

3.3.2 Resin coating and polishing of specimens

The samples were coated with a resin and a catalyst, ratio 10:1, from PRESI. For sample polishing, the automatic polishing machine Tegramin-25 from Struers with a specimen holder for clamping six specimens was used. The polishing programme consisted of six steps which are given in Tab. 3.2. Abrasive papers from Struers of SiC Papers from #500 to #4000 (Steps 1-4) were first used permitting to penetrate the material. Then, a fine polishing (diamond particles) of 3 µm (Step 5) and of 1 µm (Step 6) were applied allowing to obtain a sufficiently smooth surface with the expected ellipses which were then observed under the microscope.

Tab. 3.2. *Polishing program of samples sectioned along the thickness and width.*

Step	Abrasive paper	Suspension	Lubricant	Applied force [N]	Rotation speed $[\frac{t}{mn}]$	Time [mn]
1	SiC Paper #500		Water	20	300	0:30
2	SiC Paper #1000		Water	25	300	1:00
3	SiC Paper #2000		Water	25	150	1:00
4	SiC Paper #4000		Water	25	150	1:10
5	MD Dur	DP-Dur 3 µm		30	150	10:00
6	MD Nap	DP-Nap-B 1 µm		25	150	10:00

3.3.3 Image recording

Initially, an attempt was made to record the images using a SEM. However, it soon turned out that this was very time-consuming and did not lead to the desired image quality. The contrast between matrix and fibres, especially in the pointed part of the ellipses, was not sufficient. Using finally an optical microscope, as this was done by Yurgartis [1987], images with good fibre-matrix contrasts were obtained. In the scope of this study, an OLYMPUS BX51 optical microscope coupled with an OLYMPUS DP 25 camera were therefore used. A sufficient number of images were taken in the zones close to the mould and sealant sides in order to get a number of at least 1000 ellipses per zone during the subsequent image post-processing step with *ImageJ* (Sec. 3.3.4). Fig. 3.12 exhibits a schematic of how the images were taken with the optical microscope for a specimen sectioned along the width. The green and orange zones correspond to the zones of interest marked in Fig. 3.11. To complete, the same schematic is given in Fig. 3.13 for specimens sectioned along the thickness. Therefore, images were always taken from the first 0 ° ply next to the 45 ° ply corresponding to the outermost ply of the sealant or mould side of a specimen. The magnification of the microscope was set to x50 corresponding to an image size of 331 µm (height) x 421 µm (width) in *ImageJ*. Assuming a fibre diameter of 5 µm and sectioning angles of $\Theta_{PC} = 15\,°$ and $\Phi_{PC} = 10\,°$ for out-of-plane and in-plane sectioning, respectively, a maximum of $66.2 \cdot 21.8 = 1443$ ellipses for the former and $66.2 \cdot 14.6 = 966$ for the latter case could have been taken within one image, provided that the image was perfectly packed with ellipses. Obviously, there were no images perfectly packed, so that, depending on the fibre density and fibre arrangement of each series, a corresponding number of successive images close to the mould and sealant sides, marked by a red dotted flashes in Fig. 3.12 and Fig. 3.13, had to be taken to obtain at least 1000 ellipses for each zone of interest.

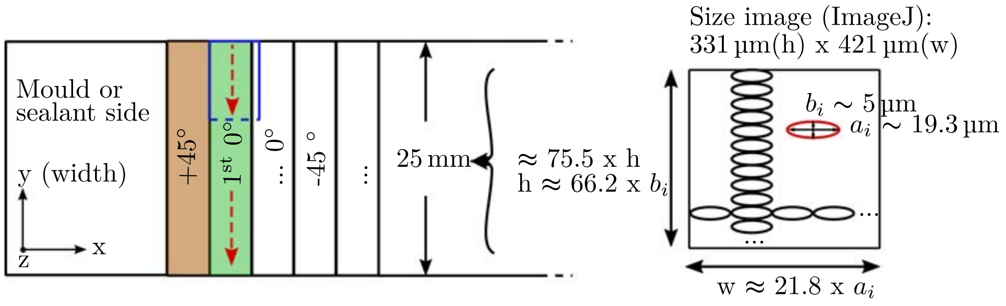

Fig. 3.12. *Image recording schema of specimens sectioned along the width.*

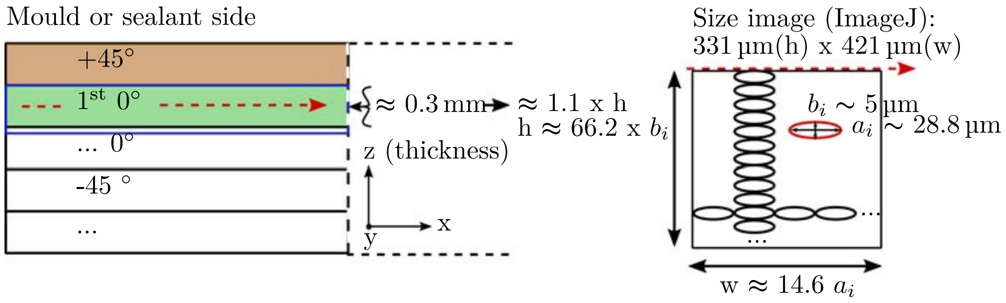

Fig. 3.13. *Image recording schema of specimens sectioned along the thickness.*

3.3.4 Image post-processing with *ImageJ*

The image post-processing part was done with the software *ImageJ*, version 2.0.0-rc-43/1.52n. The scale was set to 5.8 px/µm, corresponding to an accuracy of 1 px per 0.17 µm.

Fig. 3.14 shows the sequence of steps conducted to post-process the images. The raw image was first binarised. Then, using the plugin *Ellipse Split* and defining the order of magnitude of the major and (for $d_F = b_i$ (b_i')) the minor axes of the ellipses, the contours of each ellipse were detected automatically. The subsequent manual checking of the correct detecting of the contour of each ellipse was, however, very time-consuming and represents thus a drawback of this method. The ratio of detected ellipses to the totality of ellipses on one image was generally higher for images resulting from sectionings along the width (15 °) than for those from sectionings along the thickness (10 °).

Finally, a total of over 28.000 ellipses was analysed for the seven series presented in Tab. 3.1. Their major a_i (a_i') and minor b_i (b_i') axes lengths were exported to .csv files and used in the following Sec. 3.3.5 to determine the in- and out of plane fibre misalignment angles Φ_i and Θ_i.

3.3.5 Determination of the in- and out-of plane misalignment angles

The required data to determine the out-of plane (in-plane) fibre misalignment angles Θ_i (Φ_i), the major and minor axes a_i and b_i (a_i' and b_i') of the ellipses, were exported from *ImageJ*. The analysis of the data was performed using a script, written in python language,

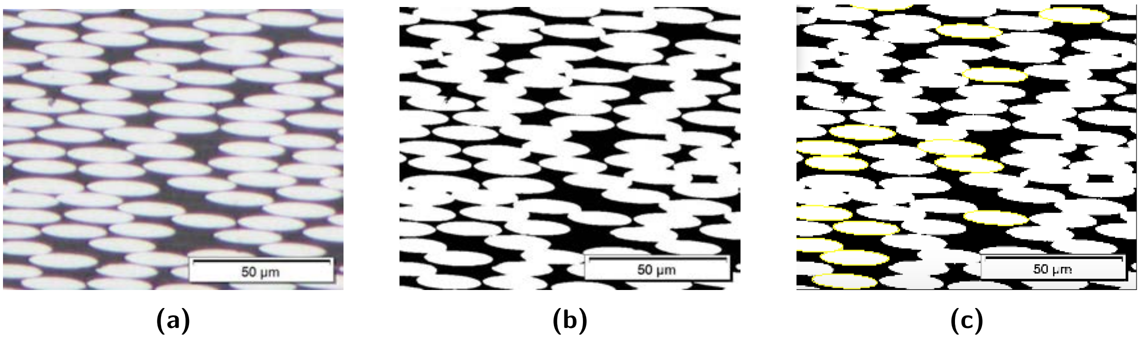

(a) (b) (c)

Fig. 3.14. *(a) Detail of a raw image taken with the optical microscope from the sample of series 4, mould side, sectioned along the width. (b) Making binary of the raw image. (c) Applying the plugin Ellipse Split for detecting the ellipses' contours automatically (yellow contours).*

coded within a Jupyter notebook (distribution Anaconda 3), beforehand.

First, ω_i (ω'_i) was calculated for all ellipses detected in the given zones for four different fibre diameters ($d_{90^\circ,mean}$, b_i (b'_i), $b_{i,mean}$ ($b'_{i,mean}$) and d_{DS}) using Equ. 3.1 (Equ. 3.3). Second, the mean value $\omega_{i,mean}$ ($\omega'_{i,mean}$) was calculated corresponding to true sectioning angle Θ_{PC} (Φ_{PC}). Third, using Equ. 3.2 (Equ. 3.4), Θ_i (Φ_i) was calculated. The distribution of the initial fibre misalignment angles Θ_i (Φ_i) was finally made according to a normal law, as depicted in Fig. 3.15. As given in Tab. 2.7, literature references that used Yurgartis [1987]'s method have chosen either one or two SD, or did not specify their choice. One SD finally seemed to be an appropriated choice in the scope of this study to describe the out-of-plane (in-plane) fibre misalignment angles. The results are discussed in the following Sec. 3.4.

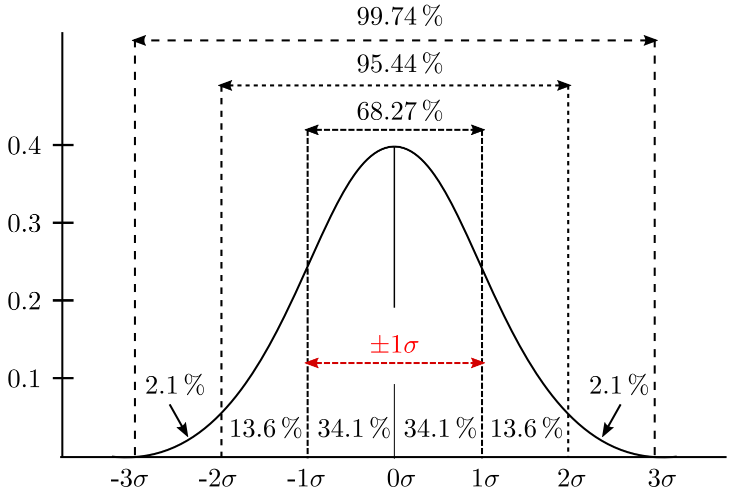

Fig. 3.15. *One SD of the normal distribution to define the out-of-plane (in-plane) fibre misalignment angle.*

3.4 Results of fibre misalignment determination

In Sec. 3.3, Yurgartis' method was applied to he seven series presented in Sec. 3.1 in order to determine their in- and out-of-plane misalignment angles.

Within the post-treatment of the images of series 1 and 2, using *ImageJ* to detect the major and minor axes of the ellipses, the following problem occurred.

The ellipses that could be seen on the surface after sectioning at 15 ° along the width and at 10 ° along the thickness were not elliptical and could thus not correctly be detected by *ImageJ*. Fig. 3.16a depicts a detail of a typical image of series 2 showing deformed ellipses. The same observations were made for the images of series 1.

Perpendicularly sectioning at 90 °, for the fibre mean diameter determination, had shown that the fibres of series 1 and 2 were not circular but had shapes as *kidney beans*. This is exemplarily seen in Fig. 3.16b for the specimen of series 2. Similar observations were made by Paluch [1994] for different fibres, i.a for T800 carbon fibres whose cross sections were non-circular.

For comparison, the shapes of the fibres from series 3 to 7 were circular (see Fig. 3.17). Their ellipses were therefore well formed.

The explication for the circularity or non-circularity of the fibres of the different series can be found in the materials' certificates of conformity. Fibres undergo during their fabrication different processes. They were either *twisted*, *twisted and then untwisted* or *never twisted*. In the case of the fibres of the series 1 and 2 (both T800H), the fibres underwent a twisting and untwisting process during fabrication. This may explain the observation of the non-circularity of the fibres when sectioned perpendicularly to their fibre directions.

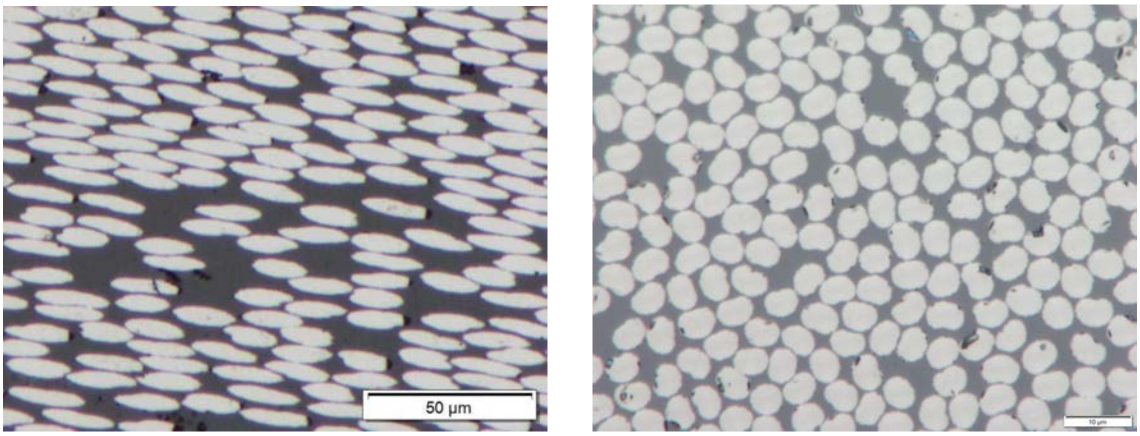

(a) **(b)**

Fig. 3.16. *(a) Detail of a raw image taken with the optical microscope from a sample of series 2, mould side, sectioned along the width. The shape of the ellipses is not elliptical. (b) sample of series 2 sectioned perpendicularly (at 90°) to its fibre direction. The fibres are not circular, but have a kidney beans shape.*

For the fibres of the series 3 (IM2C), 4 (IM2C), 6 (T800S) and 7 (IM2C) the fibre fabrication processes were indicated as never twisted. It can therefore be concluded that the fibres of these series are circular, as they have never been twisted. The material certificate of conformity of series 5 (fibres IMS65) did not provide any information on the twisting process. As the fibres are circular, it can be assumed that they had never been twisted as well.

Some limits of Yurgartis' method, presented in Sec. 2.3.7, can thus be confirmed: The method is sensitive to irregular fibre shapes. The twisting process of series 1 and 2 led to non-circular fibre shapes (*kidney bean* shape) and thus to deformed ellipses that could not be detected correctly by *ImageJ*. Hence, for series 1 and 2, the misalignment angles could not be determined and will thus be excluded in the following discussion.

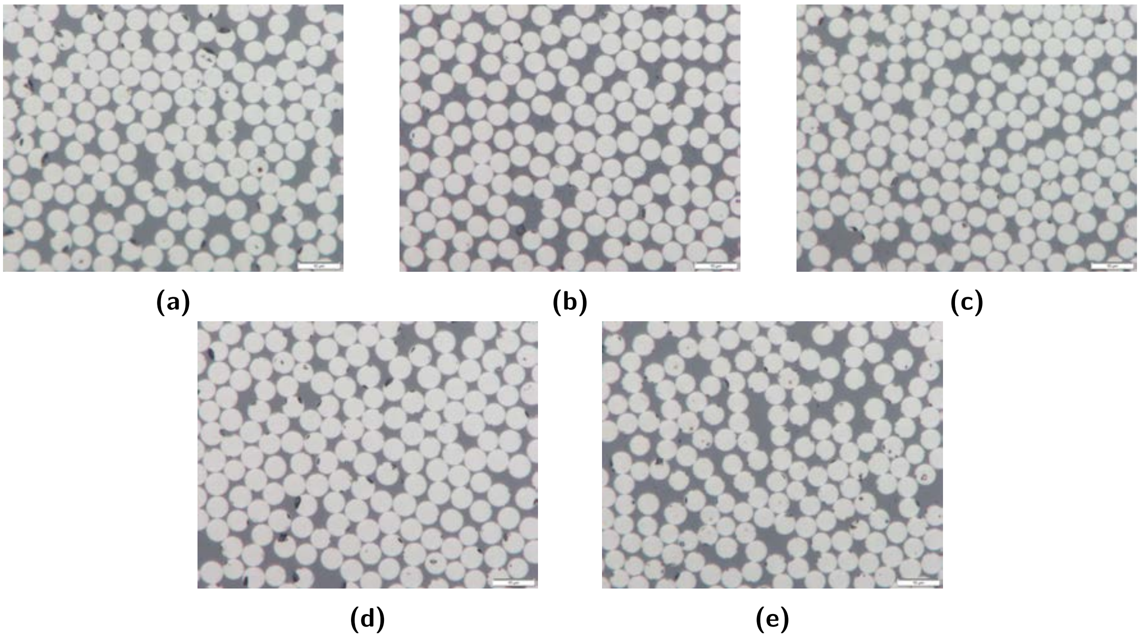

(a) (b) (c) (d) (e)

Fig. 3.17. *Specimens of series (a) 3, (b) 4, (c) 5, (d) 6 and (e) 7 sectioned perpendicularly (at 90°) to their fibre direction. The fibres are circular.*

3.4.1 In- and out-of- plane fibre misalignments of mould and sealant side for series 3 to 7 from four different fibre diameter sources

As introduced in Sec. 3.2.3, fibre diameters from four different sources were taken in order to determined the fibre misalignment angles in in- and out-of-plane directions. Tab. 3.3 lists the diameter data for the series 3 to 7.

d_{DS} represents the diameter values that are indicated on the materials' certificates of conformity. No difference was made between the mould and the sealant sides.

$d_{90^\circ,mean}$ denotes the mean diameter determined through specimen sectioning at 90 ° perpendicularly to the fibre direction as this is the approach in [Yurgartis, 1987]. In the present study, $d_{90^\circ,mean}$ was determined from at least 100 fibres for each series. No difference between the mould and the sealant sides was made, as well.

b_i and b'_i, representing the minor axes of the ellipses on the section plane of a specimen sectioned along the width and along the thickness, respectively, were individually determined. From the b_i and b'_i data, the mean values $b_{i,mean}$ and $b'_{i,mean}$ were calculated and represent thus the fourth option with which the in- and out-of- plane fibre misalignment angles Φ_i and Θ_i were determined in the scope of this study.

Fig. 3.18 and Fig. 3.19 depict the fibre misalignment angle distributions on the mould and sealant sides for series 3 and 5 determined from four different diameter sources. In Sec. A.1, the diagrams of series 4, 6 and 7 are given complementarily. Tab. 3.4 provides the corresponding data of the in- and out-of-plane fibre misalignment angles. These results are accompanied by a standard deviation obtained by the dispersion observed on the fibre diameter measurements.

For all investigated specimen zones it was found that as the fibre diameter increases, the out-of-plane (in-plane) fibre misalignment angles increase. This was to be expected on closer examination of Equ. 3.1 (Equ. 3.3), where d_F is in the numerator.

Consequently, it was observed that as fibres are rather constant in diameter (IM2C from series 3, 4 and 7), the fibre misalignment angles on the mould and sealant sides are close (Fig. 3.18), whereas fibres whose dispersion over the diameter is a little larger (IMS65 from series 5), differences in the fibre misalignment angles can be observed, for series 5 especially when the misalignment angles are determined using the fibre diameters b_i and b'_i (Fig. 3.19).

In Yurgartis [1987] the sensitivity of fibre misalignment to constant fibre diameters was also investigated. The author found that a SD of about 0.31 µm in fibre diameter resulted in an uncertainty in fibre misalignment of about ±0.04 ° [Yurgartis, 1987]. Comparing to results found in this study, those were almost in the same range, for example, the SD of the mean diameter $b_{i,mean}$ measured on the mould (5.03±0.31 µm) and sealant (4.95±0.31 µm) sides for series 5, resulted in a SD of 1.14±0.07 ° for the sealant and of 1.01±0.06 ° for the mould side in out-of-plane direction.

As given for series 6 (T800S) in Tab. 3.3, differences in fibre diameters measured by *ImageJ* and by specimen sectioning at 90 ° ($d_{90^\circ,mean} = 5.51 \pm 0.21$ µm) compared to the diameter given in the materials' certificates of conformity ($d_{DS} = 5.0$ µm) were found and could not be explained completely. However, similar observations on differences in the fibre diameters were also done by Wu et al. [2015] and Van de Werken et al. [2019]. Both authors found an average fibre diameter of 5.5 µm compared to the reported diameter of 5.0 µm as given in the materials certificates of conformity. Beyond these observations, little larger dispersions over the diameter for misalignment angles determined by d_{DS} and by b_i and b'_i were also observed for series 6. $d_{90^\circ,mean}$, $b_{i,mean}$ and $b'_{i,mean}$ resulted in closer fibre misalignment angle distributions on the mould and sealant sides as given in Fig. A.2.

Therefore, for all series, it seemed to be reasonable to chose in the further study either $d_{90^\circ,mean}$, or $b_{i,mean}$ and $b'_{i,mean}$ to determine the fibre misalignment angles on the mould and sealant sides, as both diameters led to close results (compare Θ_i and Φ_i from $d_{90^\circ,mean}$ with Θ_i and Φ_i from $b_{i,mean}$ and $b'_{i,mean}$ in Tab. 3.4). Lastly, the choice was made for $b_{i,mean}$ and $b'_{i,mean}$, as the vertical specimen sectioning step was not required.

Comparing Θ_i and Φ_i determined by $b_{i,mean}$ and $b'_{i,mean}$ on the mould and sealant sides, it can be stated that in 80 % of the cases, in-plane fibre misalignment is greater than out-of-plane fibre misalignment.

For instance, for series 3, the in-plane fibre misalignment Φ_i (1.24±0.05 °) on the sealant side is greater than the out-of-plane fibre misalignment Θ_i on the sealant side (0.91±0.03 °). Comparing the in-plane fibre misalignment Φ_i (0.78±0.03 °) of series 3 on the mould side to the out-of-plane fibre misalignment Θ_i (0.82±0.03 °) on the mould side, it can be stated that this example belongs to the 20 % where the out-of-plane fibre misalignment angle is greater (even if only slightly). These observations are marked in bold in Tab. 3.3 for all fibre misalignment angles of the series 3 to 7.

Last, in-plane fibre misalignment on the mould and sealant sides, or out-of-plane fibre misalignment on the mould and sealant sides are compared. It was found that in 70 % of the cases the misalignment angle on the sealant side is greater than that on the mould side.

For instance, for series 3, the in-plane fibre misalignment on the sealant side (1.24±0.05 °) is greater than on the mould side (0.78±0.03 °).
For series 5, the in-plane fibre misalignment on the mould side (1.52±0.11 °) is greater than on the sealant side (1.37±0.1 °). The latter example belongs to the 30 % where the misalignment angles on the mould side is greater. These observations are marked in italic in Tab. 3.3.

Tab. 3.3. *Measured fibre diameter data from four different sources.*

Diameter		Series 3 (SE84LV/IM2C)		Series 4 (SE84Nano/IM2C)		Series 5 (XB3515/IMS65)		Series 6 (MTC9810/T800)		Series 7 (M79/IM2C)	
		Sealant	Mould	Sealant	Mould	Sealant	Mould	Sealant	Mould	Sealant	Mould
d_{DS}	[µm]	5.2		5.2		5.0		5.0		5.2	
$d_{90^\circ,mean}$	[µm]	5.03±0.18		5.11±0.15		4.83±0.21		5.51±0.21		5.06±0.17	
b_i	[µm]	Individual for each ellipse (15 ° width sectioning, mould/sealant side).									
b'_i	[µm]	Individual for each ellipse (10 ° thickness sectioning, mould/sealant side).									
$b_{i,mean}$	[µm]	5.23±0.19	5.11±0.20	5.12±0.23	5.14±0.18	4.95±0.31	5.03±0.31	5.56±0.40	5.49±0.22	5.18±0.19	5.22±5.19
$b'_{i,mean}$	[µm]	5.14±0.21	5.15±0.20	4.76±0.28	5.00±0.24	4.94±0.34	5.00±0.36	5.55±0.39	5.46±0.23	5.20±0.20	5.16±0.20

Tab. 3.4. *In-and out-of-plane fibre misalignment data of series 3 to 7 from four different diameter sources.* Θ_i *corresponds to the out-of-plane fibre misalignment angles (sectioning at* 15 ° *along the width),* Φ_i *denotes the in-plane fibre misalignment angles (sectioning at* 10 ° *along the thickness).*

Misalignment angle (diameter source)		Series 3 (SE84LV/IM2C)		Series 4 (SE84Nano/IM2C)		Series 5 (XB3515/IMS65)		Series 6 (MTC9810/T800)		Series 7 (M79/IM2C)	
		Sealant	Mould	Sealant	Mould	Sealant	Mould	Sealant	Mould	Sealant	Mould
Θ_i (d_{DS})	[°]	0.90	0.83	1.17	0.67	1.15	1.00	1.18	0.71	1.25	0.95
Φ_i (d_{DS})	[°]	1.26	0.79	1.16	0.95	1.39	1.52	1.37	1.50	1.34	1.76
Θ_i ($d_{90^\circ,mean}$)	[°]	0.87±0.03	0.80±0.03	1.14±0.03	0.66±0.02	1.11±0.05	0.96±0.04	1.31±0.05	0.79±0.03	1.22±0.04	0.96±0.03
Φ_i ($d_{90^\circ,mean}$)	[°]	1.22±0.04	0.76±0.03	1.14±0.03	0.93±0.02	1.34±0.06	1.47±0.06	1.52±0.06	1.66±0.07	1.30±0.04	1.71±0.06
Θ_i (b_i)	[°]	0.85	0.76	1.19	0.64	0.84	0.83	0.97	0.71	1.24	0.93
Φ_i (b'_i)	[°]	1.19	0.73	1.13	0.85	1.24	1.31	1.42	1.62	1.31	1.57
Θ_i ($b_{i,mean}$)	[°]	*0.91±0.03*	**0.82±0.03**	***1.15±0.05***	0.66±0.02	*1.14±0.07*	1.01±0.06	*1.32±0.10*	0.79±0.03	*1.25±0.05*	0.96±0.03
Φ_i ($b'_{i,mean}$)	[°]	***1.24±0.05***	0.78±0.03	*1.06±0.06*	**0.91±0.04**	**1.37±0.1**	***1.52±0.11***	**1.53±0.11**	***1.65±0.07***	**1.34±0.05**	***1.74±0.07***

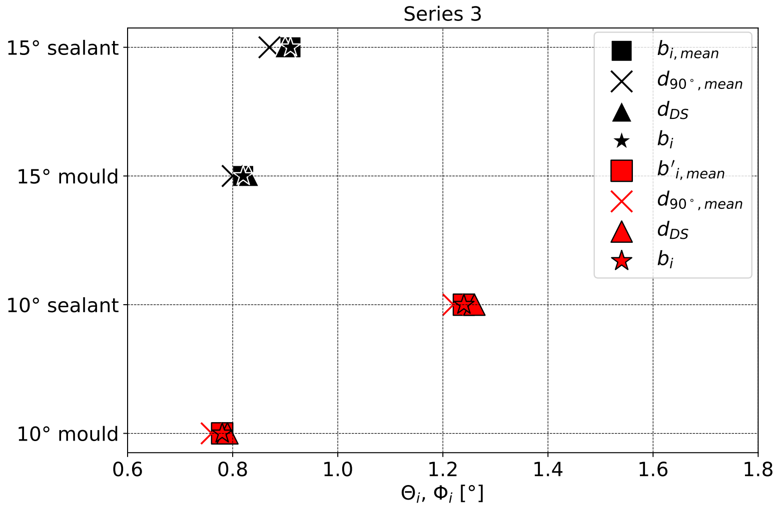

Fig. 3.18. *Confrontation of fibre misalignment angles as a function of different fibre diameters for series 3. Constant fibre diameter results in close fibre misalignment angles on the mould and sealant sides.*

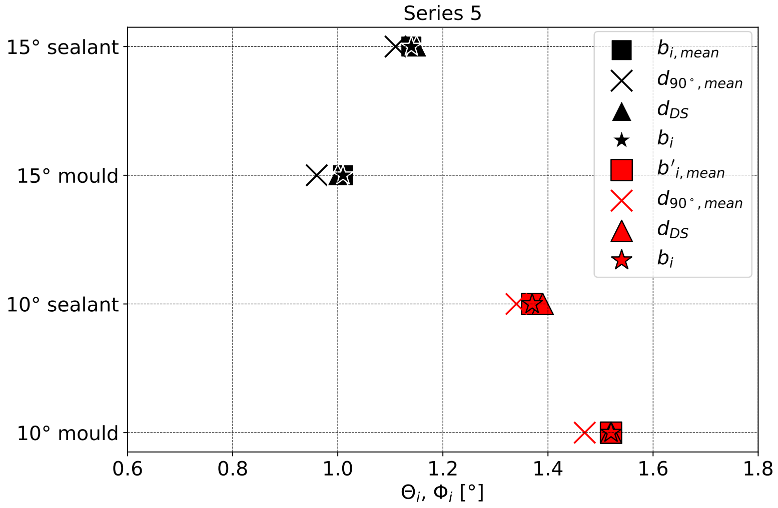

Fig. 3.19. *Confrontation of fibre misalignment angles as a function of different fibre diameters for series 5. Little dispersion over the diameter leads to differences in the fibre misalignment angles.*

3.5 Conclusion

The aim of the present Ch. 3 was to determine the fibre misalignment angles of seven different material series. The fibre misalignment angle is one of four parameter in Grandidier et al.' Equ. 2.5 to be determined in order to be able to estimate the compressive strengths of fibre reinforced composite materials.

The material of these series, presented in Sec. 3.1, consisted of different continuous IM carbon fibres embedded in different epoxy resins.

After an introduction to Yurgartis' method in Sec. 3.2, this method was applied to the specimens of the seven series in order to determine their in- and out-of plane fibre misalignment angles on the mould and sealant sides. The procedure was described in detail in Sec. 3.3.

As stated in Kratmann et al. [2009], it was also found that Yurgartis' method was sensitive to the fibre shape. Indeed, the fibres of series 1 and 2 (both T800H) had been *twisted* and *untwisted* during their production which led to the fact that the fibres, when sectioned perpendicularly to their fibre direction, were not circular but had a shape as *kidney beans*. For this reason, only the fibre misalignment angles for the series 3 to 7 could be determined in the scope of this study. The fibres of these series had *never* been *twisted* during production.

Within this study, the fibre diameters were further measured by four different methods and the fibre misalignment angles, as a function of these diameters, were compared.

It was found that as fibres are rather constant in diameter, the fibre misalignment angles on the mould and sealant sides are close (Fig. 3.18, Fig. A.1, Fig. A.3), whereas fibres whose dispersion over the diameter is a little larger, differences in the fibre misalignment angles can be observed (Fig. 3.19, Fig. A.2).

Further, the mean diameters $b_{i,mean}$ and $b'_{i,mean}$ resulted in fibre misalignment angles close to those determined using the mean diameter $d_{90^\circ,mean}$ obtained by perpendicularly specimen sectioning to the fibre axis, as this is the applied method in Yurgartis [1987]. Since the data to determine $b_{i,mean}$ and $b'_{i,mean}$ can directly be exported from *ImageJ* and does not require any additional specimen sectioning, the fibre misalignment angles determined through $b_{i,mean}$ and $b'_{i,mean}$ will hence be used in the following Ch. 4 to compare the experimentally and analytically determined compressive strength.

4

Confrontation of two experimental methods to measure or estimate the compressive strengths

Contents

As illustrated in Tab. 1.1, the objective of the present Part II is to confront two experimental methods permitting the estimation of the compressive strength of carbon fibre reinforced epoxy composite materials in two different ways.
The present Ch. 4 deals with the question, how the solutions of Budiansky & Fleck [1993] and Grandidier et al. assess the compressive strength X_c^{EXP} of the material series 3 to 7, experimentally determined through 4PB tests.

The solutions require four parameters, one of which, the misalignment angle, was determined in Ch. 3 for series 3 to 7.

The determination of the three other parameters will be the content of Sec. 4.1.1 and the results will be briefly presented in Sec. 4.1.2. The same applies to the 4PB tests, whose implementation and results will be summarized in Sec. 4.1.3 and Sec. 4.1.4.

These works originate from previous studies conducted by Mechin et al. [2019] and were taken up by a PhD student[1] of the University of South Brittany in Lorient, in collaboration with the racing team MACIF.

Then, in Sec. 4.2, the missing data for the determination of the analytical compressive strength X_c^{ANA} will be presented.

Afterwards, in Sec. 4.3, a tool, the cartographies of the spatial fibre alignment distribution to support the confrontation of the compressive strengths X_c^{EXP} and X_c^{ANA}, will be introduced. Passing by a clearly arranged presentation of the X_c^{EXP}/X_c^{ANA} versus Θ_i/Φ_i diagrams and the corresponding cartographies in Sec. 4.4, the analysis and discussion on the results will be done in Sec. 4.5. A conclusion on the results will be then given in Sec. 4.6, before finishing by a synthesis about the applied method and a perspective on future studies in Sec. 4.7.

4.1 4PB and tensile tests of ±45° laminates to determine X_c^{EXP} and X_c^{ANA}

Basing on the research works of Mechin et al. [2019][1], 4PB tests on straight and tensile tests on ±45° specimens were performed in collaboration with the racing team MACIF. Information on the sample preparation and on the experimental procedures, as well as on the results presented in this Ch. 4, were taken from these works and serve in the following as supplement to obtain a holistic understanding of the aim of the present research work: How misalignment angles determined by Yurgartis' method can be used for the analytical prediction of the compressive strength of continuous fibre reinforced composite materials using the analytical solutions of Budiansky & Fleck [1993] and Grandidier et al. [2012]?

As mentioned in Sec. 3.1, different prepreg materials, made from IM carbon fibres and epoxy resins, of which for five the misalignment angles were determined in Sec. 3.4, formed the basis in the experimental and analytical determination of the compressive strengths. The main characteristics of those prepregs were summarized in Tab. 3.1.

Different ±45° panels for tensile tests were thus manufactured (intermediate debulking every three plies at 0.8 bar during 20 min), cured in an autoclave at 6 bars, and cut by water jet into several specimens in order to determine the shear behaviour of an unidirectional laminate.

Straight panels for 4PB tests were manufactured (intermediate debulking as for ±45° panels), also cured in an autoclave at 6 bars, and cut by water jet into several specimens to determine the maximum compressive strength of the unidirectional laminates.

The prepregs that were used for both specimen types came from the same material batch. The different panels were manufactured using a process as equivalent as possible to that

---

[1] and A. Launay, PhD student at the University of South Brittany in Lorient (defence in 2021)

used in the manufacturing of hydrofoils.

The following sections will describe in more detail the design of the two different specimen types and the respective test implementations, and will further explain the determination of the three parameters that are still missing for the application of the analytical solutions of Budiansky & Fleck [1993] and Grandidier et al. [2012].

4.1.1 ±45° tensile specimens and test procedure

The objective of testing ±45° specimens in tension was to identify the parameters of RO's constitutive law, the shear modulus G_{UD}^{RO}, the critical shear yield strain γ_y^{UD} and the strain hardening coefficient n_{UD}, for an unidirectional laminate. These parameters are part of Budiansky & Fleck [1993]'s Equ. 2.1 with which the compressive strength of series 3 to 7 should be estimated analytically.

In the following, the implementation of the tensile tests will be given, first. Thereafter, the analysis of the tensile tests as well as the procedure to obtain G_{UD}^{RO}, γ_y^{UD} and n_{UD} will be presented in Sec. 4.1.2.

The standard NF EN ISO 14129 (NF EN ISO, 1998) explains the procedure how to determine the shear behaviour of a unidirectional laminate through tensile tests of ±45° stacked plies. In the scope of this study, the fabrication of the ±45° specimens and the experimental procedure were inspired by this standard with some exceptions. The standard recommends a balanced symmetrical stacking with plies oriented successively at +45° and −45°. However, for reasons of material savings, the specimens were only made up of six 300 $\frac{\text{g}}{\text{m}^2}$ plies. Hence, a balanced anti-symmetrical stacking sequence $[+45°; -45°]_3$ was chosen. FE calculations have shown that this had no quantitative incidence on the RO parameters [Mechin, 2017]. The geometrical dimension of one specimen was 250x25x2 mm. Further, 2 mm-thick grips were glued to the ends of the specimens following a common nautical procedure.

Tab. 4.1. *Characteristics of testing machine used for ±45° tests and applied instrumentation.*

Testing machine	Instron 5567 Load cell: 30 kN Test speed: 2 $\frac{\text{mm}}{\text{min}}$ Software: BlueHill
Recording system	HBM Spider 8 acquisition box
Software	HBM CATMAN
Strain gauge	KYOWA, biaxial Gauge resistance: 120 Ω ± 0.2 %

For the implementation of the tensile tests, an Instron 5567 traction machine and self-clamping jaws were used. A biaxial strain gauge was applied to measure the longitudinal ε_L and the transversal ε_T strain of the tensile specimens. The test speed was set to 2 $\frac{\text{mm}}{\text{min}}$. The applied force, the crosshead displacement as well as ε_L and ε_T were recorded during test execution. In total, a minimum of five test specimens per series were tested since reproducibility was not an issue. Tab. 4.1 lists the characteristics of the tensile test machine, the data recording system and the strain gauges applied. Fig. 4.1a depicts an image of a tensile test specimen during loading and Fig. 4.1b a schematic indicating the ±45° directions (1-, 2-directions) of the stacked laminates and the position of the strain gauges, measuring the longitudinal and transversal strains (L-, T-directions) of the specimen.

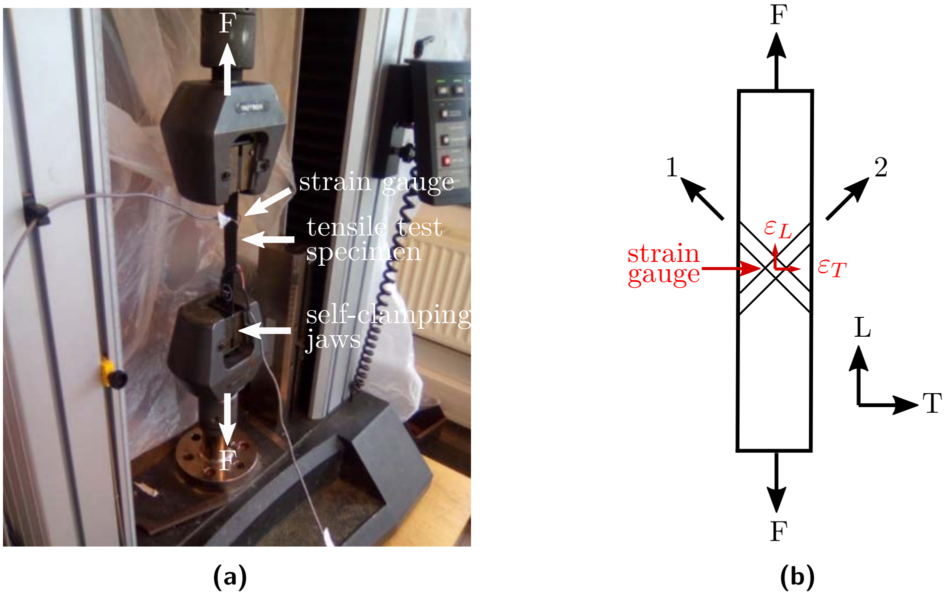

Fig. 4.1. *(a) Tensile tests on a ±45° specimen and (b) schematic representation of a tensile specimen with ±45° (1-, 2-directions) stacked plies and a gauge measuring the longitudinal and transversal strains (L-, T-directions) of the specimen during test execution.*

4.1.2 Analysis of tensile tests on ±45° specimens

In order to determine the parameters of RO's constitutive law, G_{UD}^{RO}, γ_y^{UD} and n_{UD} (Equ. 2.2), from tensile tests on ±45° specimens, the following procedure was applied:

i. Obtaining the in-plane shear stress τ_{12} and the in-plane shear strain γ_{12} through the applied force F, the specimen's geometry and the deformations in longitudinal ε_L and transversal ε_T directions.

ii. Calculation of the shear modulus G_{12} using the formula given in the standard NF EN ISO 14129 (NF EN ISO, 1998).

iii. Fitting the evolution of γ_{12} versus τ_{12} using the non-linear elastic constitutive law from RO.

iv. Identification of the parameters G_{UD}^{RO}, γ_y^{UD} and n_{UD}.

The analysis were carried out using a script coded in python language within a Jupyter notebook using the Anaconda 3 distribution.
The (i) in-plane shear stress τ_{12} was thus first calculated by

$$\tau_{12} = \frac{F}{2 \cdot S}, \tag{4.1}$$

where F and S denoted the force applied at failure and the cross section of the specimen measured using a calliper prior to specimen testing.
γ_{12} was defined as the sum of the longitudinal and the transverse deformations

$$\gamma_{12} = \varepsilon_L + (-\varepsilon_T)\,, \tag{4.2}$$

where ε_L and ε_T represented the longitudinal and transverse deformations (see Fig. 4.1b) recorded by the strain gauges, respectively.
The (ii) shear modulus G_{12} was then calculated using the formula described in the standard NF EN ISO 14129 (NF EN ISO, 1998)

$$G_{12} = \frac{\tau''_{\gamma_{12}} - \tau'_{\gamma_{12}}}{\gamma''_{12} - \gamma'_{12}}. \tag{4.3}$$

Using the (iii) non-linear elastic constitutive law of RO, which was already given in Equ. 2.2 and is replicated below,

$$\gamma_{12} = \frac{\tau_{12}}{G_{UD}^{RO}} \cdot \left(1 + \frac{3}{7} \cdot \left(\frac{\tau_{12}}{G_{UD}^{RO} \cdot \gamma_y^{UD}}\right)^{n_{UD}-1}\right),$$

the evolution of the shear strain γ_{12} was modelled as a function of the shear stress τ_{12}.
From the measured longitudinal deformation field and the calculated shear stress field the different parameters of the RO law, G_{UD}^{RO}, γ_y^{UD} and n_{UD}, were then determined (iv). The data are given in Tab. 4.2.
With these values and the fibre misalignment angles given in Tab. 3.4, determined using the diameter $b_{i,mean}$ and $b'_{i,mean}$, all parameters that were necessary to estimate analytically the compressive strengths X_c^{ANA} of the series 3 to 7 using the solutions of Budiansky & Fleck and Grandidier et al. were determined. The results will be presented in Sec. 4.2.

Tab. 4.2. *Synthesis of the non-linear regression parameters by the RO constitutive law.*

N° of series		Series 3	Series 4	Series 5	Series 6	Series 7
Fibres		IM2C		IMS65	T800S	IM2C
Matrices		SE84 LV	SE84 Nano	XB3515	MTC9810	M79
G_{UD}^{RO}	[GPa]	4.75±0.1	6.57±0.13	3.78±0.16	4.01±0.06	3.69±0.07
γ_y^{UD}	[%]	1.1±0.01	0.9±0.02	1.17±0.03	1.24±0.02	0.94±0.02
n_{UD}	[-]	6.61±0.25	7.27±0.39	5.40±0.07	6.27±0.1	6.58±0.19

4.1.3 4PB test specimens and test procedure

The objective of testing straight specimens in 4PB was to determine the compressive strengths of series 3 to 7 experimentally by applying an analysis method that will be presented in Sec. 4.1.4. Before this, the implementation of the 4PB tests will be briefly presented below.
The dimensions of the 4PB specimens were defined according to a collaborative research

and development work with GSea Design, a design company for high performance composites, located in Lorient [Mechin, 2017; Mechin et al., 2019]. The dimension of one 4PB specimen was 500x30x10 mm with a fibre weight content of 300 $\frac{\mathrm{g}}{\mathrm{m}^2}$. The applied stacking sequence, which is classical for racing yachts, is given in Tab. 4.3. The 4PB test were carried out with the same testing machine that was used for the ±45° tensile tests, and whose characteristics were listed in Tab. 4.1. The 4PB test implementation based on the standard ASTM D6272 (ASTM, 2008), and has been extended in Keryvin et al. [2020]. The 4PB test setup is given in Fig. 4.2a exhibiting a specimen under load, and schematically depicted in Fig. 4.2b, showing its dimensions. The 4PB test setup consisted of a lower and an upper spreader with loading bars which transferred the applied force over PE plates to the specimen. The PE plates served to reduce stress concentrations under the loading bars. 10-mm mono-strain-gauges whose characteristics are given in Tab. 4.1 were fixed in the center on the compression and tension side of the specimen. The vertical displacement speed during test execution was 5 $\frac{\mathrm{mm}}{\mathrm{min}}$. The applied force, the crosshead displacement and the deformation on the compression ε_C and the tension ε_T side were recorded during test execution. A minimum of five 4PB specimens per series and per side (sealant versus mould) were tested at least.

Tab. 4.3. *Stacking sequence of 4PB specimens.*

Ply orientation [°]	+45°	0°	−45°	0°	−45°	0°	+45°
No. of plies	1	9	1	11	1	9	1

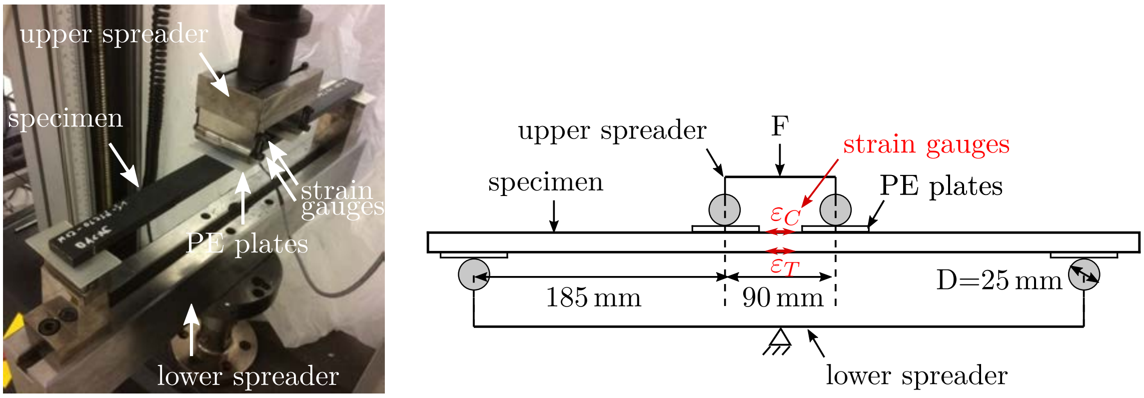

(a) **(b)**

Fig. 4.2. *(a) Specimen tested in 4PB and (b) schematic illustration of 4PB test setup.*

4.1.4 Analysis of 4PB tests

The analysis of the 4PB tests required the following information:

- The specimen metrology (height, width, and thickness of off-axis plies and thickness of unidirectional blocks),
- the dimension of the 4PB test setup (loading bar distances),
- the lay-up plan with fibre/matrix type, stacking sequence,

- the elastic modulus of the off-axis plies,
- the data recorded during the test: load [N], cross beam displacement [mm], deformations in the centre, on the compression and tensile side [µm/m].

The exact data of the 4PB specimens of the series 3 to 7 can be found in the research works of Mechin et al. [2019][1].

With these data, the following steps had to be carried out in order to determine the experimental compressive strengths of the series 3 to 7:

(i.) calculation of the second moment of area of the specimen,

(ii.) calculation of the stress in the outermost ply.

These steps will not further be explained in the scope of this study, as this would go beyond of the present research work. For complete information, the interested reader is referred to research works by Mechin et al. [2019][1].

Tab. 4.4 finally resumes the experimentally determined compressive strengths, calculated through the steps (i) and (ii), for specimens of series 3 to 7 tested on the mould and sealant sides in 4PB.

In the following section Sec. 4.2, the experimentally determined and analytically estimated compressive strengths $X_{c,EXP}^{sealant}$, $X_{c,EXP}^{mould}$, and X_c^{ANA} will now be confronted.

Tab. 4.4. *$X_{c,EXP}^{sealant}$ and $X_{c,EXP}^{mould}$ calculated for 5 different series using the method of GSea Design.*

N° of series		Series 3	Series 4	Series 5	Series 6	Series 7
Fibres		IM2C		IMS65	T800S	IM2C
Matrices		SE84 LV	SE84 Nano	XB3515	MTC9810	M79
$X_{c,EXP}^{sealant}$	[MPa]	1546±66	1673±41	1310±109	1436±84	1400±26
$X_{c,EXP}^{mould}$	[MPa]	1684±82	1692±42	1410±18	1491±56	1555±36

4.2 Data for the calculation of the compressive strength X_c^{ANA}

The compressive strength X_c^{ANA} was calculated using Budiansky & Fleck [1993]'s (Equ. 2.1) and Grandidier et al. [2012]'s (Equ. 2.5) solutions. The latter is replicated below

$$\sigma_c = X_c^{ANA} = \frac{G_{UD}^{RO}}{1 + n_{UD} \cdot \left(\frac{3}{7}\right)^{\frac{1}{n_{UD}}} \left(\frac{\frac{\Phi_0}{\gamma_y^{UD}}}{n_{UD}-1}\right)^{\frac{n_{UD}-1}{n_{UD}}}} + \frac{C_s}{e_b} \cdot$$

C_S expresses the structural coefficient, initially introduced for deformations in Equ. 2.4, and replicated below for the stress state

$$C_s = (2\pi r_{gf}) \sqrt{\frac{E_M E_F}{1-\nu_M^2} f(1-f)} \cdot$$

Tab. 4.5. *Data for the calculation the structural coefficient* C_S*.*

N° of series		Series 3	Series 4	Series 5	Series 6	Series 7
Fibres		IM2C		IMS65	T800S	IM2C
Matrices		SE84 LV	SE84 Nano	XB3515	MTC9810	M79
E_M	[MPa]	4100	5800	3500	3500	3900
ν_M	[-]	0.4				
E_F	[MPa]	296000	296000	290000	290000	296000
f	[-]	0.554	0.57	0.51	0.5	0.55
e_{ply}	[µm]	0.309	0.293	0.308	0.328	0.295

The parameters of the RO constitutive law, G_{UD}^{RO}, γ_y^{UD} and n_{UD}, were given in Tab. 4.2 for the series 3 to 7.

To complete, Tab. 4.5 lists the data of the elastic parameters of the different matrices (E_M, ν_M) and those of the fibres (E_F), as well as the fibre volume fractions (f), and the ply thicknesses (e_{ply}) of series 3 to 7, to be found in the research works by Mechin [2017][1]. e_{ply} is used to calculate the characteristic thicknesses e_b from Drapier et al.'s determination rules for an unidirectional composite loaded in bending [Grandidier et al., 2012]

$$e_b = 0.4 \, e_{ply} \, . \tag{4.4}$$

The fibre gyration radius r_{gf} was calculated from the relationship between the fibre cross section surface A_f and the second moment of area of the fibre I_f

$$r_{gf} = \sqrt{\frac{I_f}{A_f}} = \sqrt{\frac{\pi \frac{b_i^4}{64}}{\pi \left(\frac{b_i}{2}\right)^2}} \, . \tag{4.5}$$

4.3 Creation of cartographies of fibre alignment distribution

As part of the confrontation of the compressive strengths X_c^{EXP} and X_c^{ANA}, cartographies of the spatial fibre alignment distributions of the zones from which the fibre misalignment angles were determined were created.

The hypothesis that was made was that the studied zone, which was not the failure zone and did not correspond to each tested specimen either, but to a *representative* location of the plate, made it possible to discuss the results.

As explained in Fig. 3.12 and Fig. 3.13, the images for the in- and out-of-plane fibre misalignment determinations were recorded successively along the x- and y-axes, using an optical microscope. Two-dimensional cartographies in the side view (Θ_i versus y-axis for out-of-plane, and Φ_i versus x-axis for in-plane fibre misalignment) and in the top view (x-axis versus y-axis, and y-axis versus x-axis, respectively) were hence established for the present study.

The position ($\mathrm{x_i}$, $\mathrm{y_i}$) of each fibre on one image was transmitted during the post-treatment of the images with ImageJ in Sec. 3.3.4.

For the creation of the cartographies, the overlay of the images was verified, first. If no overlay was found, image spacings of $2{\cdot}a_{i,mean}$ and $8{\cdot}b_{i,mean}$, for image recordings along the x- and y-axes, respectively, were assumed. Knowing the size of the recorded images (see (h)x(w) in Fig. 3.12 and Fig. 3.13), and the overlay between two images, the positions ($\mathrm{x_i}$, $\mathrm{y_i}$) of all fibres were known.

The in- and out-of-plane fibre misalignment angles Φ_i and Θ_i were then categorized in fibre misalignment within $\pm\ 1\sigma$, $\leq$-1σ, and $\geq 1\sigma$ (σ corresponds to one standard deviation of the normal distribution, see Fig. 3.15). The colors green, red, and blue were then assigned to these categories, respectively.

The cartographies were finally established for the mould and sealant sides using scripts encoded with python language.

In the following Sec. 4.4, the confrontation of both compressive strengths accompanied by these cartographies will now be presented.

4.4 Confrontation of X_c^{ANA} and X_c^{EXP}, and cartographies of fibre alignment distribution

The analytically estimated compressive strengths X_c^{ANA} of the series 3 to 7 were confronted to those experimentally calculated (see Tab. 4.4) by plotting X_c^{ANA}, using the equations and data presented in Sec. 4.2, as a function of increasing fibre misalignment angles, and $X_{c,EXP}^{sealant}$ and $X_{c,EXP}^{mould}$ as constant values.

The in- and out-of-plane fibre misalignment angles, listed in Tab. 3.4, determined using Yurgartis' method for fibre diameters $b_{i,mean}$ and $b'_{i,mean}$, and replicated in Tab. 4.6 (without SD), were then added to these plots using red (for the mould side) and green (for the sealant side) circle (for in-plane fibre misalignment angles Φ_i) and square (for out-of-plane fibre misalignment angles Θ_i) symbols. The signification of the rows *Fit Grandidier et al.* and *Fit Budiansky & Fleck*, the different cell colors (green, orange, red), and the percentage values in parentheses will be explained in Sec. 4.5.

For each series, two pages, schematically represented in Fig. 4.3 on the right, containing the diagrams, as well as the cartographies were created. As a reminder, Fig. 4.3 shows on the upper left the specimen sectioning along the specimen width (for out-of-plane fibre misalignment angle determination Θ_i), and on the lower left, the specimen sectioning along the specimen thickness (for in-plane fibre misalignment angle determination Φ_i), replicated from Fig. 3.7 and Fig. 3.8.

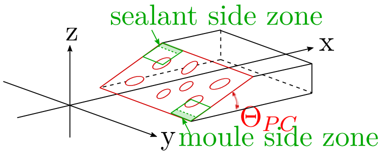

Page 1			
(a)	Diagram: X_c^{EXP}, X_c^{ANA} versus Θ_i Sealant side	(b)	Diagram: X_c^{EXP}, X_c^{ANA} versus Θ_i Mould side
(c)	Cartography: Sealant side - Side view		
(d)	Cartography: Sealant side - Top view		
(e)	Cartography: Mould side - Side view		
(f)	Cartography: Mould side - Top view		
Fig. Series N° - Matrix/Fibre composition - Θ_i			

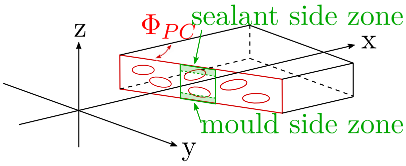

Page 2			
(a)	Diagram: X_c^{EXP}, X_c^{ANA} versus Φ_i Sealant side	(b)	Diagram: X_c^{EXP}, X_c^{ANA} versus Φ_i Mould side
(c)	Cartography: Sealant side - Side view		
(d)	Cartography: Sealant side - Top view		
(e)	Cartography: Mould side - Side view		
(f)	Cartography: Mould side - Top view		
Fig. Series N° - Matrix/Fibre composition - Φ_i			

Fig. 4.3. *Replication of the sectioning directions (upper left: along the width for Θ_i determination, lower left: along the thickness for Φ_i determination), and, on the upper and lower right, structure of pages picturing the X_c^{ANA}/X_c^{EXP}-Θ_i/Φ_i diagrams of each series, and the corresponding cartographies.*

The first page contains two diagrams. The first one shows X_c^{ANA} and X_c^{EXP} as a function of the out-of-plane fibre misalignment angle Θ_i for the sealant side, the second diagram shows X_c^{ANA} and X_c^{EXP} versus the out-of-plane fibre misalignment angle Θ_i for the mould side. Below these two diagrams, four cartographies are given. The first two cartographies belong to the first diagram, showing the side and the top views of the spatial out-of-plane fibre angle distribution of the investigated zone on the sealant side. The last two cartographies show the side and the top views of the spatial out-of-plane fibre angle distribution of the investigated zone on the mould side.

The second page was built up equally to the first page. The only difference was that the in-plane misalignment angle Φ_i was taken. Pages 1 and 2 were hence established for the series 3 to 7. These are given in Tab. 4.4 to Fig. 4.4.

In the following, the experimental comparison will be made on the fibre misalignment angles. The models will be inverted. From the experimental strength, which is given through 4PB tests, an estimate of the fibre misalignment angle (denoted *Fit Budiansky & Fleck* and *Fit Grandidier et al.* in the following) that would be required for specimen failure will be calculated from the two models of Budiansky & Fleck and Grandidier et al.. These misalignment angles will be then compared with those measured by Yurgartis' method. The analysis and discussion on the results with regard to the cartographies will be given in Sec. 4.5.

Tab. 4.6. *In- Φ_i and out-of-plane Θ_i fibre misalignment angles determined using Yurgartis's method and analytical fits to match the analytical solutions. Percentage values in parentheses represent the difference between experimentally measured and analytically fitted values.*

		Series 3 (SE84LV/IM2C)		Series 4 (SE84Nano/IM2C)		Series 5 (XB3515/IMS65)	
		Sealant	Mould	Sealant	Mould	Sealant	Mould
Fit Grandidier et al.	[°]	1.23	1.04	1.5	1.48	1.17	1.01
Θ_i ($b_{i,mean}$)	[°]	0.91 (-26.0 %)	0.82 (-21.2 %)	1.15 (-23.3 %)	0.66 (-55.4 %)	**1.14** (**-2.6** %)	**1.01** (0.0 %))
Φ_i ($b'_{i,mean}$)	[°]	**1.24** (0.8 %)	**0.78** (**-25.0** %)	1.06 (-29.3 %)	0.91 (-38.5 %)	1.37 (17.1 %)	1.52 (50.5 %)
Fit Budiansky & Fleck	[°]	1.05	0.9	1.3	1.27	0.99	0.86
Θ_i ($b_{i,mean}$)	[°]	0.91 (-13.3 %)	0.82 (-8.9 %)	1.15 (-11.5 %)	0.66 (-48.0 %)	**1.14** (15.2 %)	**1.01** (17.4 %)
Φ_i ($b'_{i,mean}$)	[°]	**1.24** (18.1 %)	**0.78** (**-13.3** %)	1.06 (-18.5 %)	0.91 (-28.3 %)	1.37 (38.4 %)	1.52 (76.7 %)

		Series 6 (SHD/T800)		Series 7 (M79/IM2C)	
		Sealant	Mould	Sealant	Mould
Fit Grandidier et al.	[°]	1.16	1.07	0.81	0.66
Θ_i ($b_{i,mean}$)	[°]	1.32 (13.8 %)	0.79 (-26.2 %)	1.25 (-54.3 %)	0.96 (45.5 %)
Φ_i ($b'_{i,mean}$)	[°]	1.53 (31.9 %)	1.65 (54.2 %)	1.34 (65.4 %)	1.74 (163.6 %)
Fit Budiansky & Fleck	[°]	0.99	0.93	0.68	0.6
Θ_i ($b_{i,mean}$)	[°]	1.32 (13.8 %)	0.79 (-26.2 %)	1.25 (-54.3 %)	0.96 (45.5 %)
Φ_i ($b'_{i,mean}$)	[°]	1.53 (31.9 %)	1.65 (54.2 %)	1.34 (65.4 %)	1.74 (163.6 %)

Page 1 of series 3

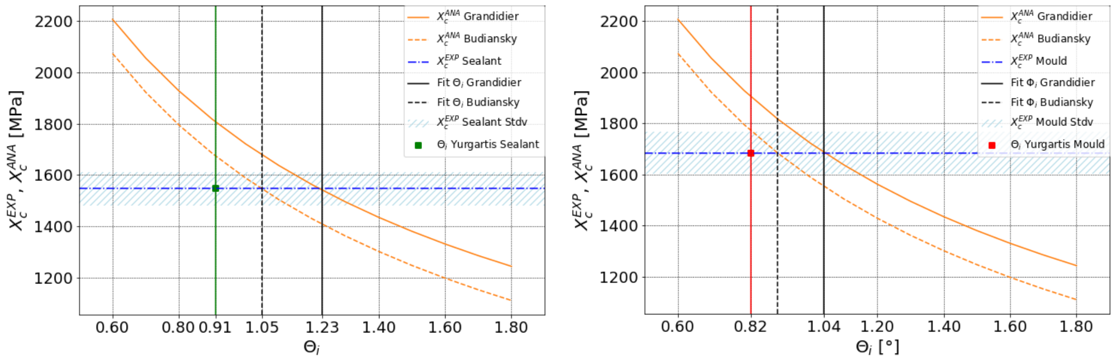

(a) X_c^{EXP} *versus* X_c^{ANA} *- Sealant side* **(b)** X_c^{EXP} *versus* X_c^{ANA} *- Mould side*

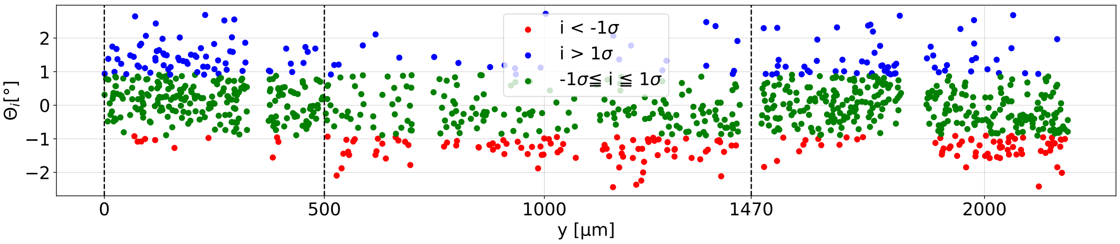

(c) *Sealant side - Side view*

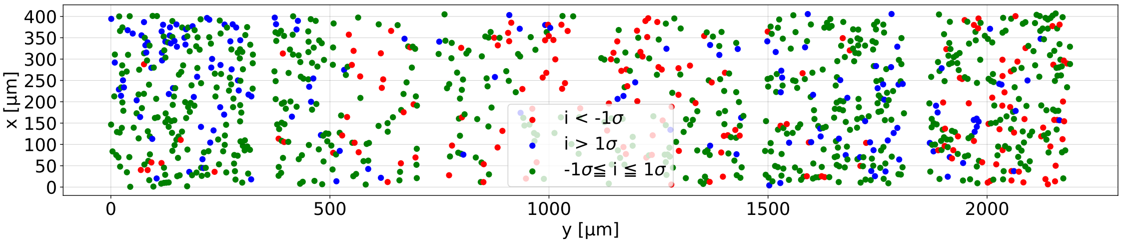

(d) *Sealant side - Top view*

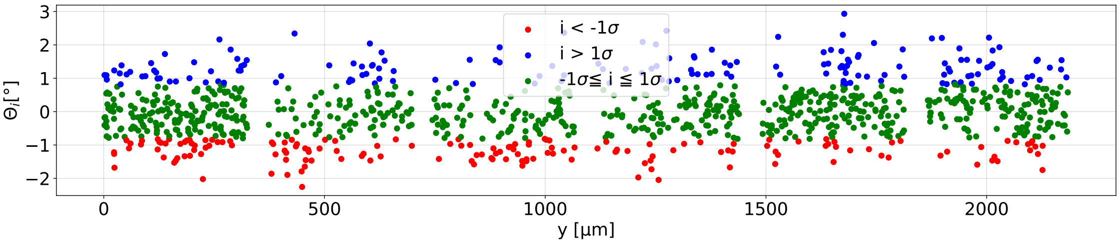

(e) *Mould side - Side view*

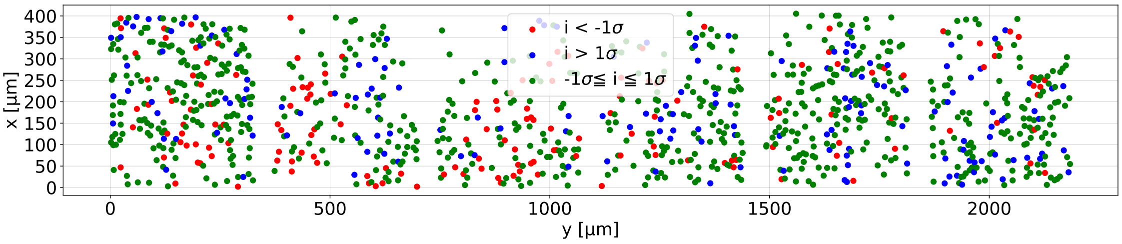

(f) *Mould side - Top view*

Fig. 4.4. *Series 3 - SE84 LV/IM2C - Out-of-plane fibre misalignment* Θ_i.

Page 2 of series 3

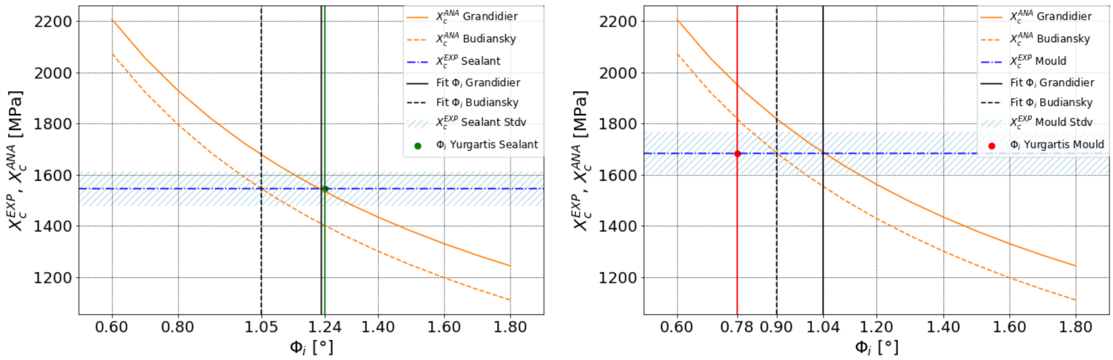

(a) X_c^{EXP} *versus* X_c^{ANA} *- Sealant side* **(b)** X_c^{EXP} *versus* X_c^{ANA} *- Mould side*

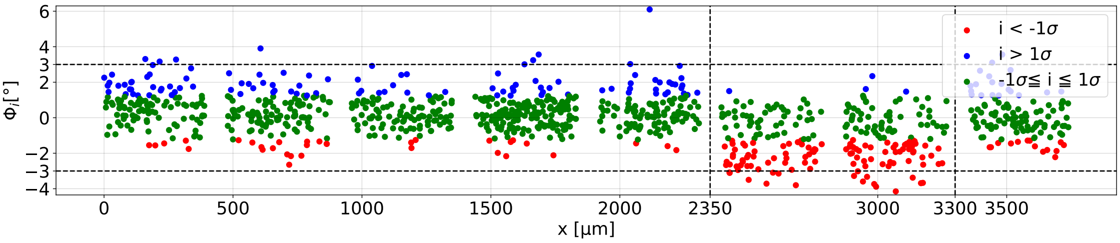

(c) *Sealant side - Side view*

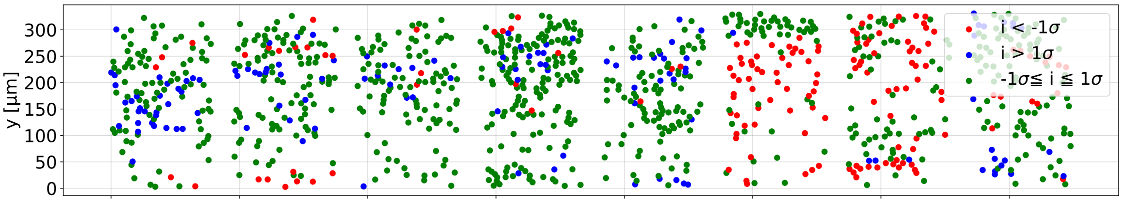

(d) *Sealant side - Top view*

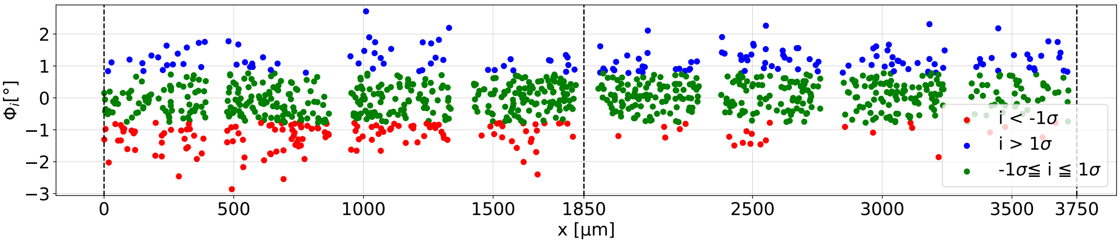

(e) *Mould side - Side view*

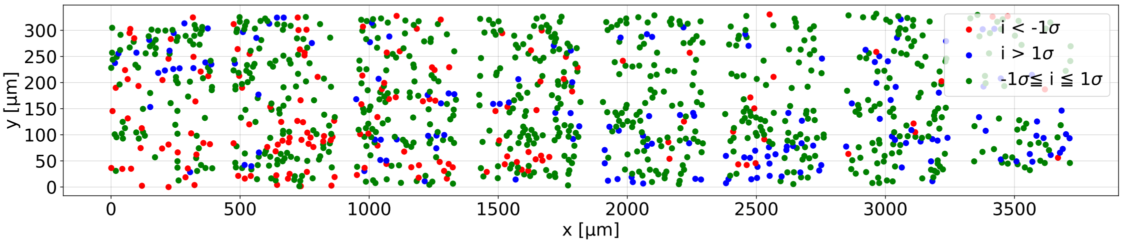

(f) *Mould side - Top view*

Fig. 4.5. *Series 3 - SE84 LV/IM2C - In-plane fibre misalignment* Φ_i.

Page 1 of series 4

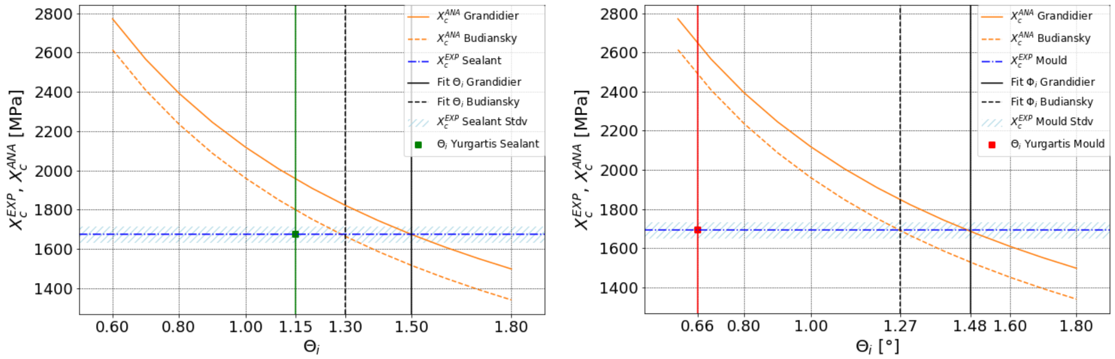

(a) X_c^{EXP} *versus* X_c^{ANA} *- Sealant side* **(b)** X_c^{EXP} *versus* X_c^{ANA} *- Mould side*

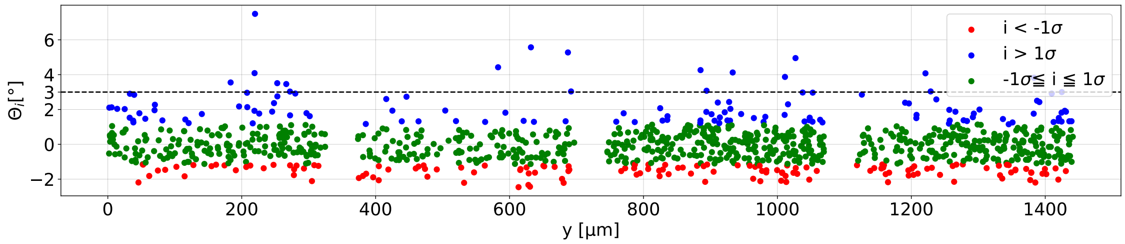

(c) *Sealant side - Side view*

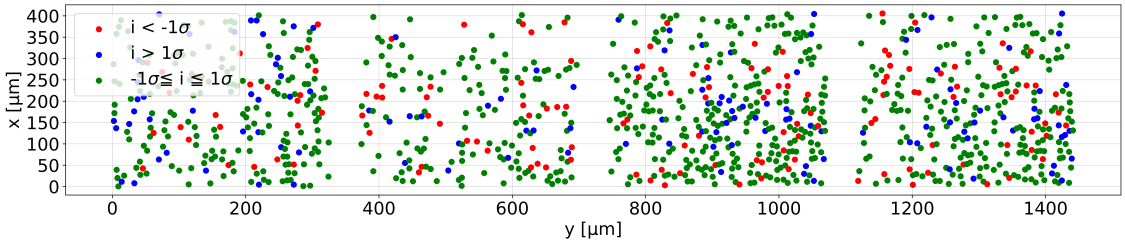

(d) *Sealant side - Top view*

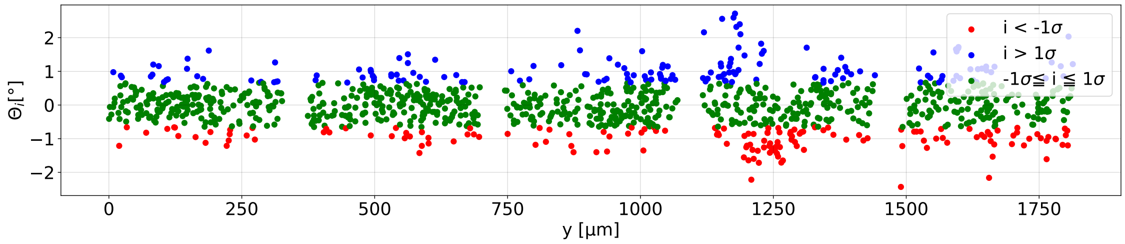

(e) *Mould side - Side view*

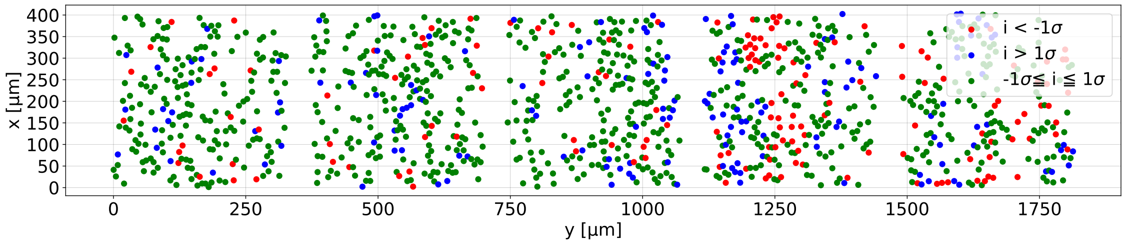

(f) *Mould side - Top view*

Fig. 4.6. *Series 4 - SE84 Nano/IM2C - Out-of-plane fibre misalignment* Θ_i.

Page 2 of series 4

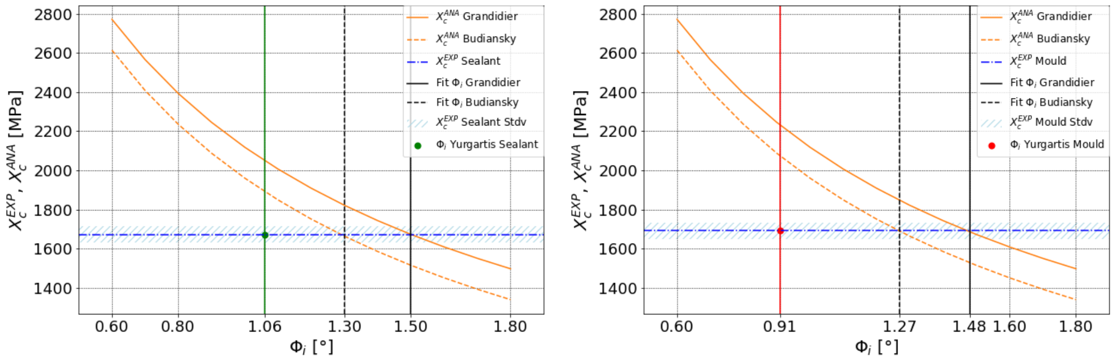

(a) *X_c^{EXP} versus X_c^{ANA} - Sealant side* **(b)** *X_c^{EXP} versus X_c^{ANA} - Mould side*

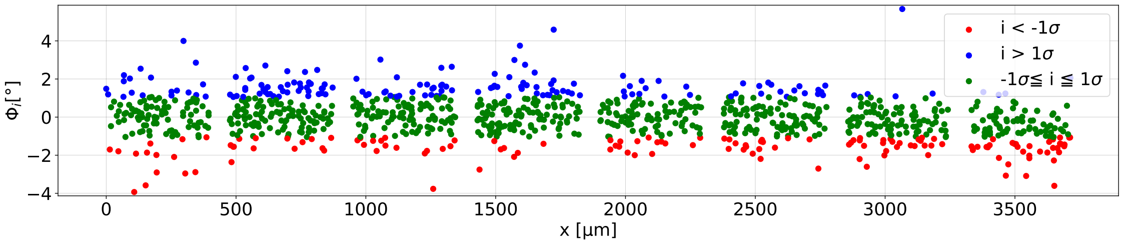

(c) *Sealant side - Side view*

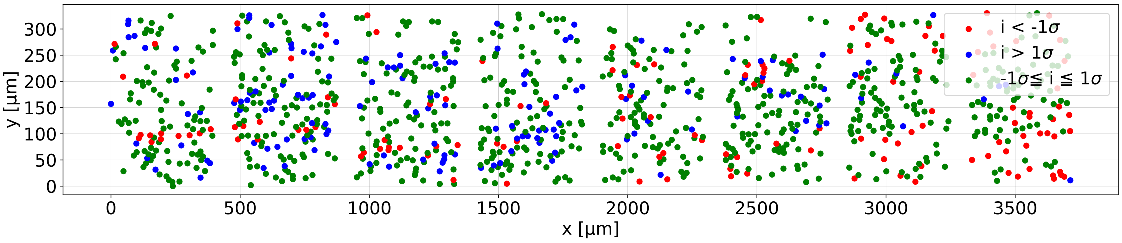

(d) *Sealant side - Top view*

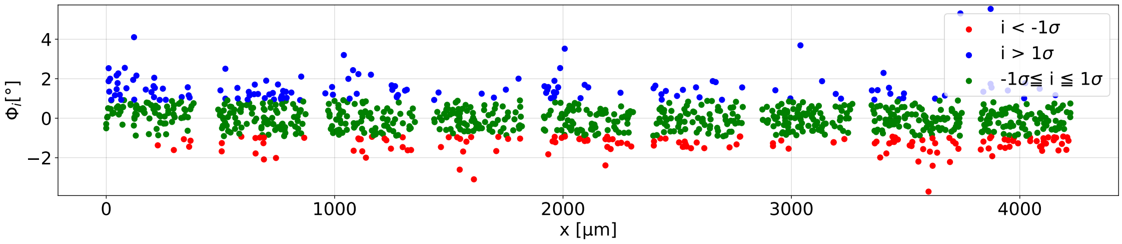

(e) *Mould side - Side view*

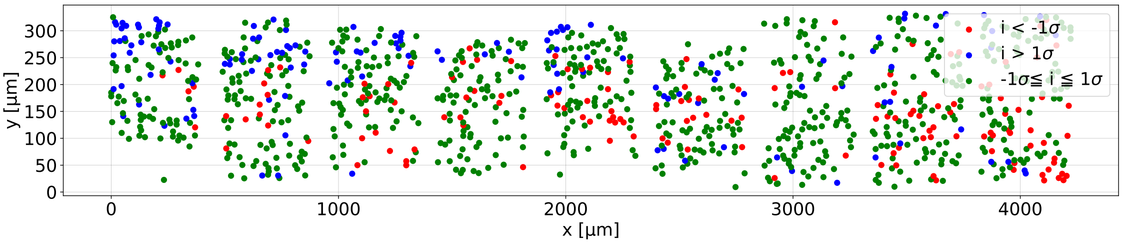

(f) *Mould side - Top view*

Fig. 4.7. *Series 4 - SE84 Nano/IM2C - In-plane fibre misalignment Φ_i.*

Page 1 of series 5

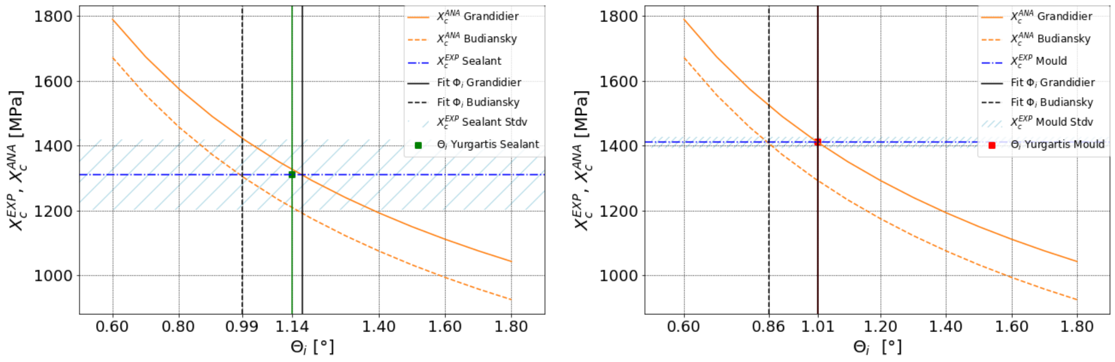

(a) X_c^{EXP} *versus* X_c^{ANA} *- Sealant side*

(b) X_c^{EXP} *versus* X_c^{ANA}

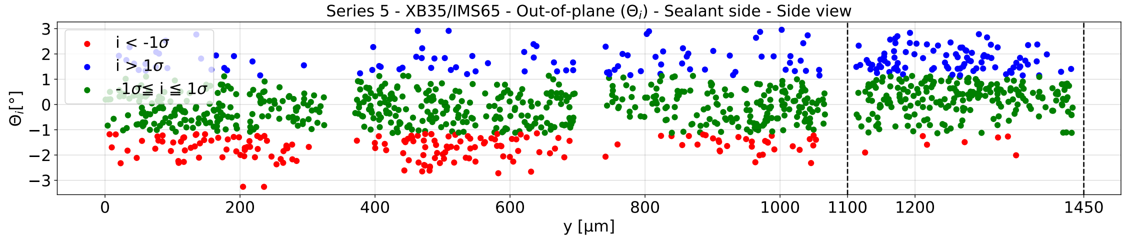

(c) *Sealant side - Side view*

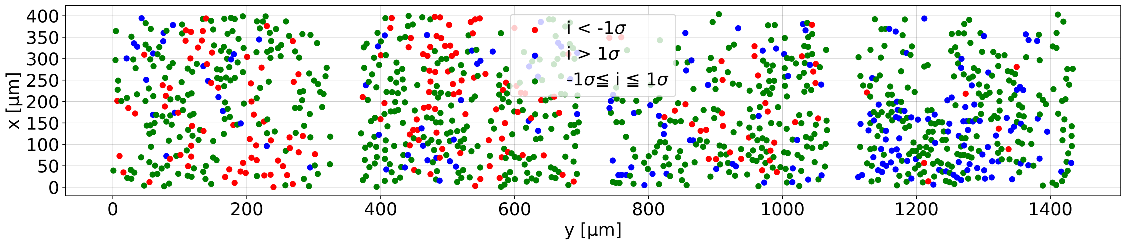

(d) *Sealant side - Top view*

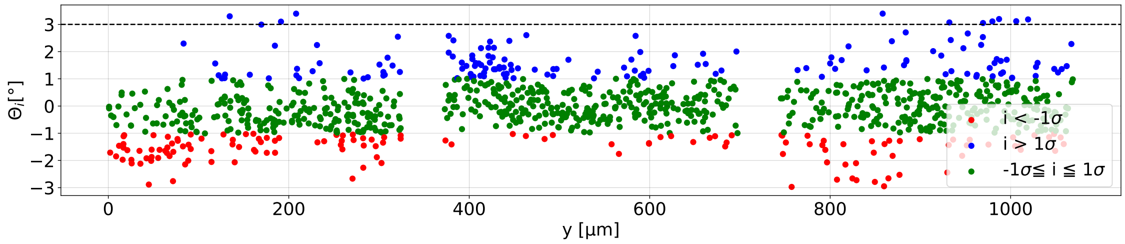

(e) *Mould side - Side view*

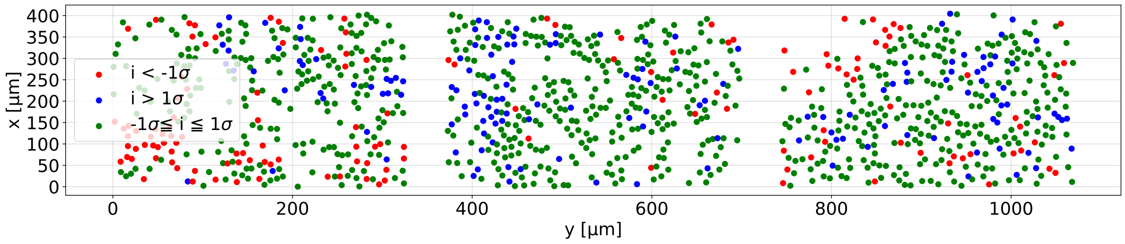

(f) *Mould side - Top view*

Fig. 4.8. *Series 5 - XB3515/IMS65 - Out-of-plane fibre misalignment* Θ_i.

Page 2 of series 5

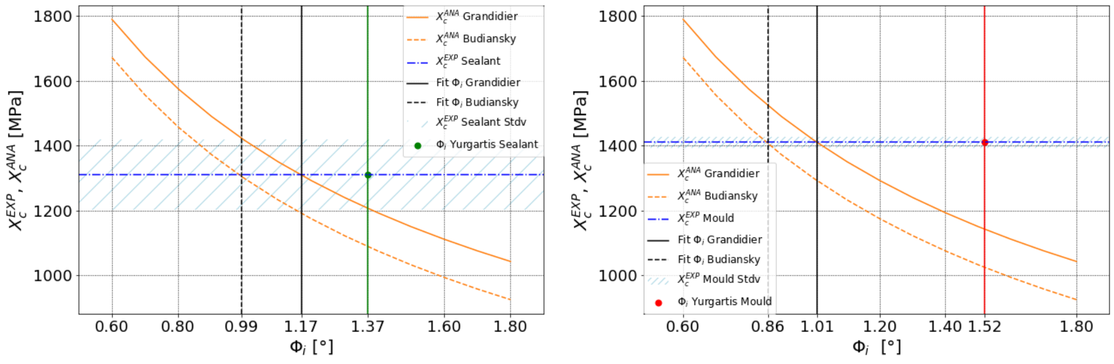

(a) X_c^{EXP} *versus* X_c^{ANA} *- Sealant side* **(b)** X_c^{EXP} *versus* X_c^{ANA} *- Mould side*

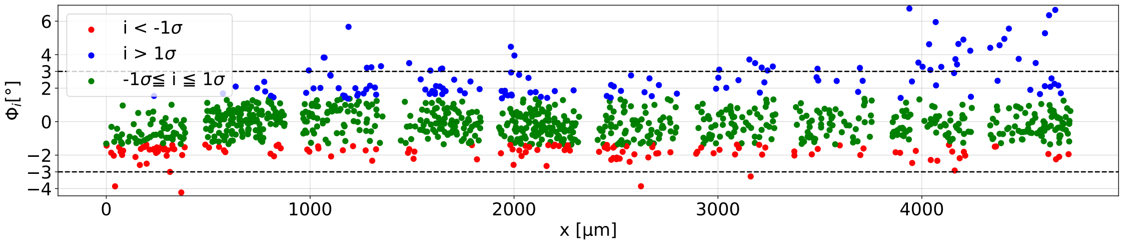

(c) *Sealant side - Side view*

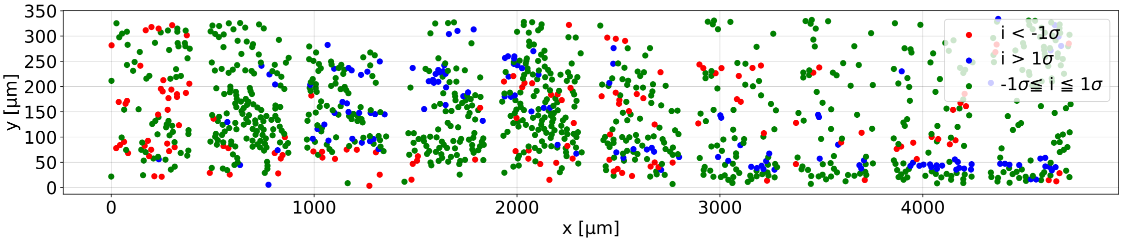

(d) *Sealant side - Top view*

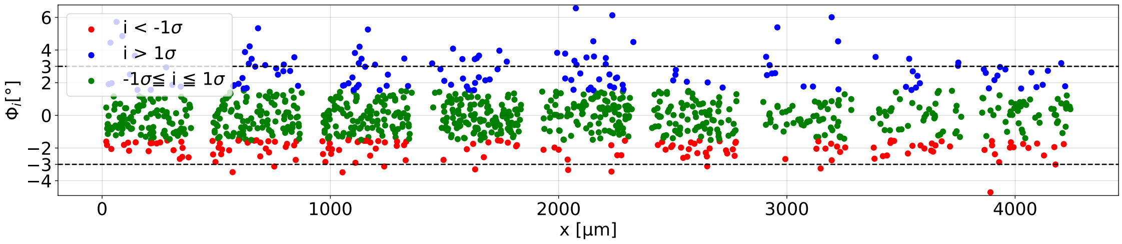

(e) *Mould side - Side view*

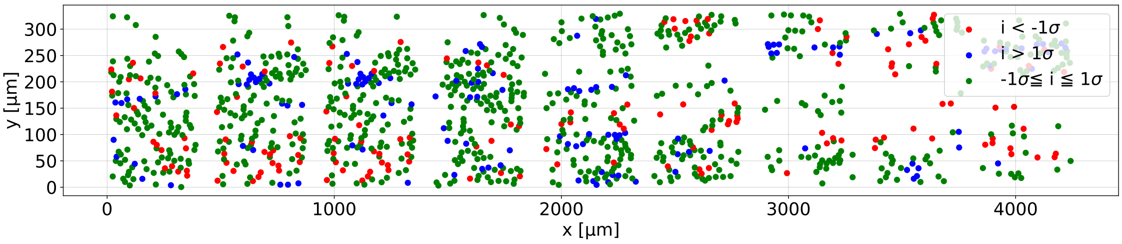

(f) *Mould side - Top view*

Fig. 4.9. *Series 5 - XB3515/IMS65 - In-plane fibre misalignment* Φ_i.

Page 1 of series 6

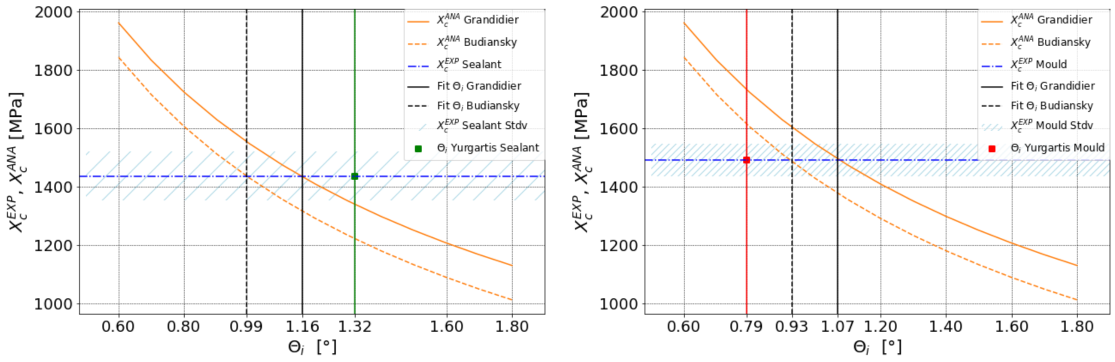

(a) X_c^{EXP} *versus* X_c^{ANA} *- Sealant side* **(b)** X_c^{EXP} *versus* X_c^{ANA} *- Mould side*

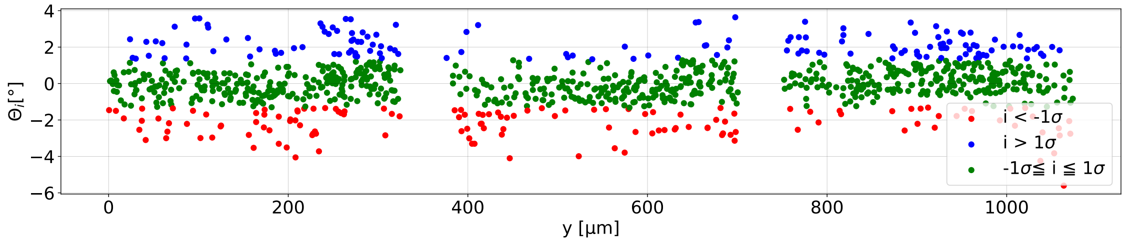

(c) *Sealant side - Side view*

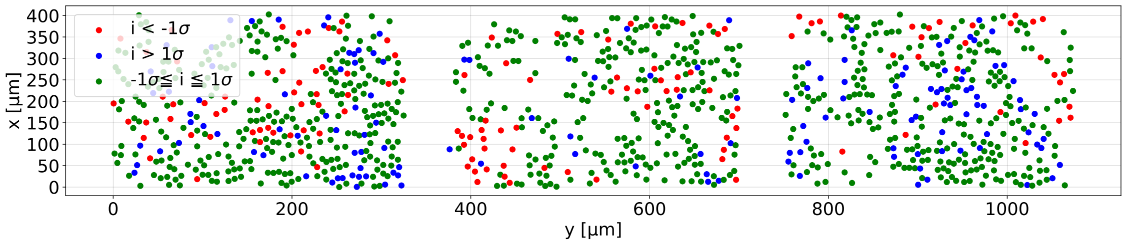

(d) *Sealant side - Top view*

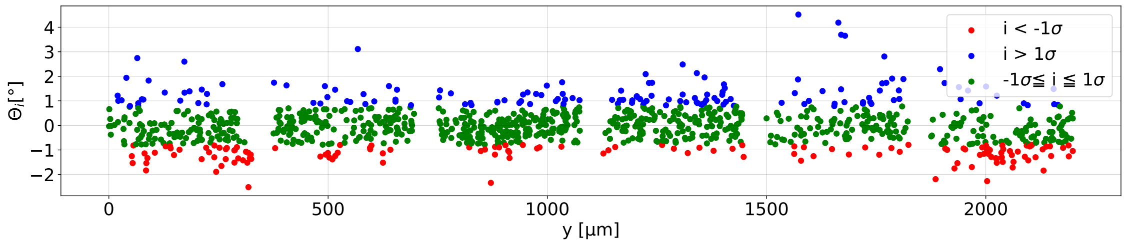

(e) *Mould side - Side view*

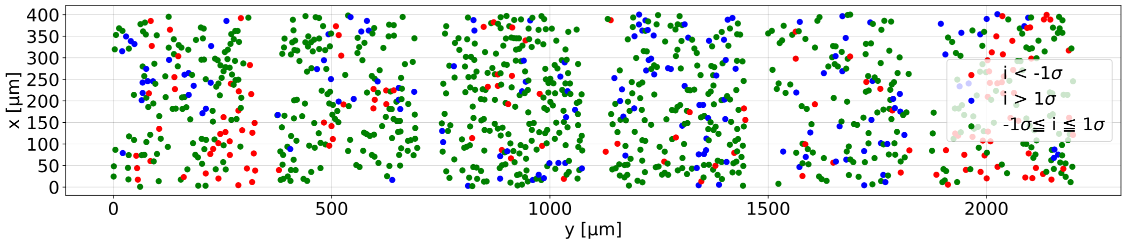

(f) *Mould side - Top view*

Fig. 4.10. *Series 6 - MTC9810/T800S - Out-of-plane fibre misalignment* Θ_i.

Page 2 of series 6

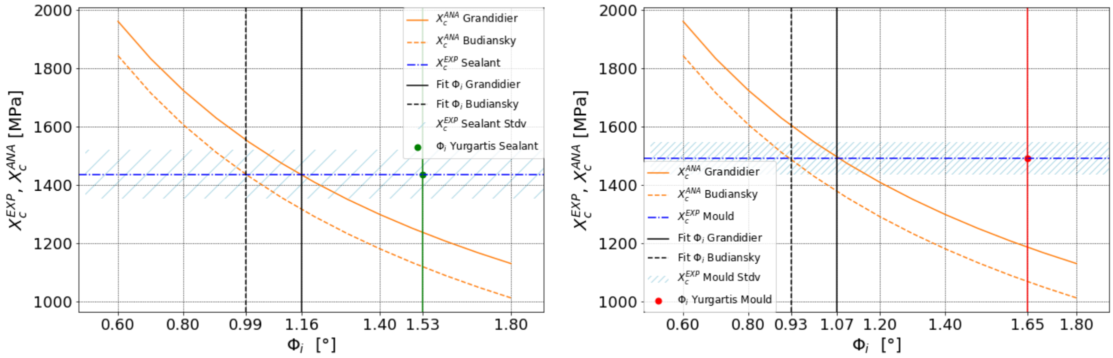

(a) X_c^{EXP} *versus* X_c^{ANA} *- Sealant side* **(b)** X_c^{EXP} *versus* X_c^{ANA} *- Mould side*

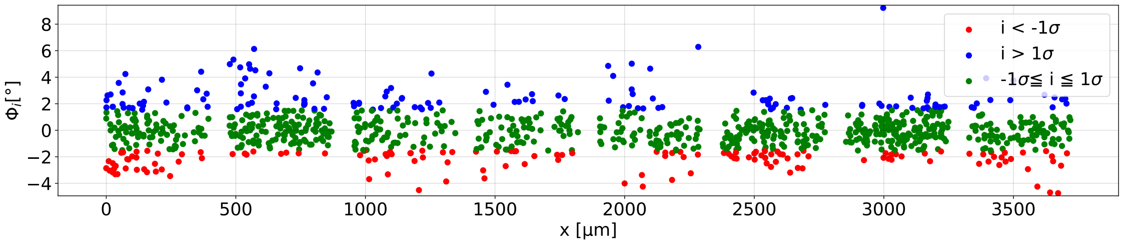

(c) *Sealant side - Side view*

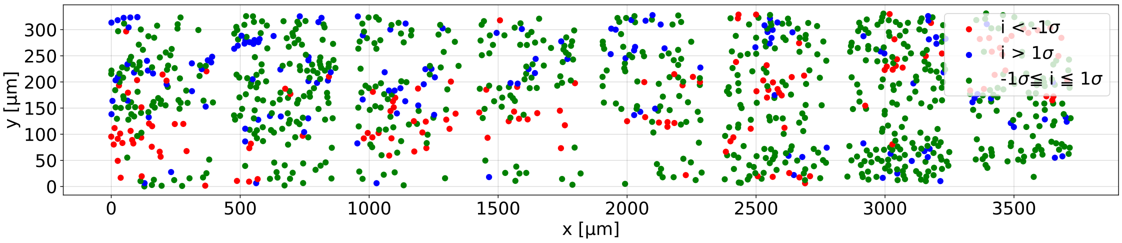

(d) *Sealant side - Top view*

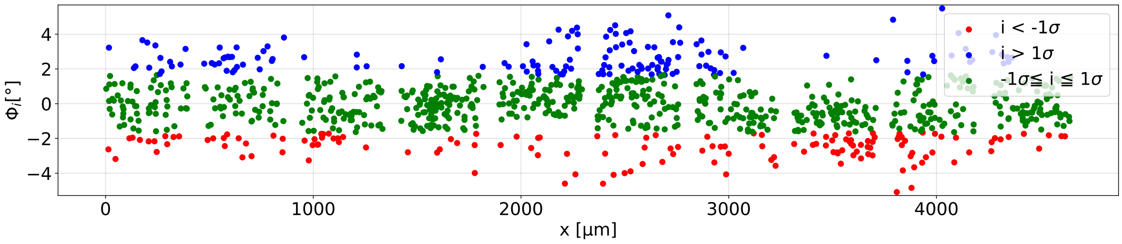

(e) *Mould side - Side view*

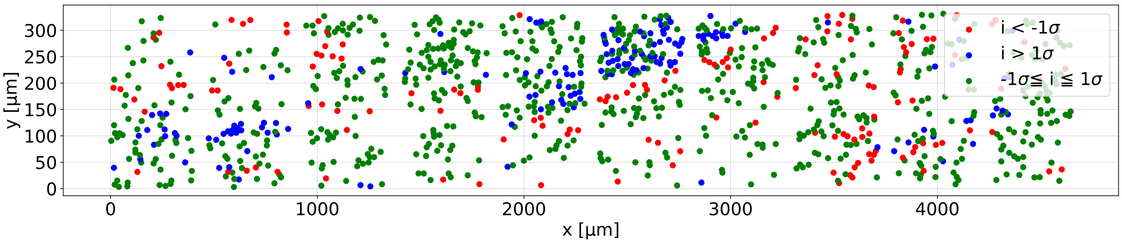

(f) *Mould side - Top view*

Fig. 4.11. *Series 6 - MTC9810/T800S - In-plane fibre misalignment* Φ_i.

Page 1 of series 7

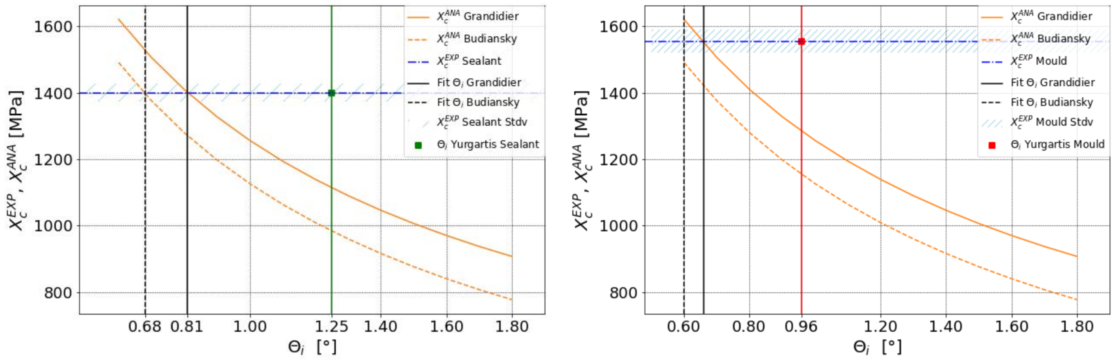

(a) X_c^{EXP} *versus* X_c^{ANA} *- Sealant side* **(b)** X_c^{EXP} *versus* X_c^{ANA} *- Mould side*

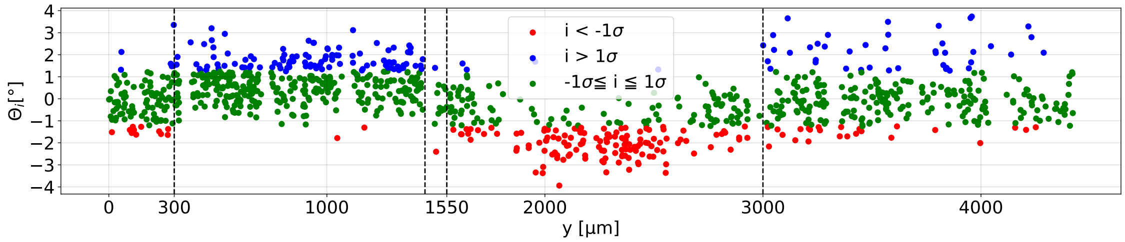

(c) *Sealant side - Side view*

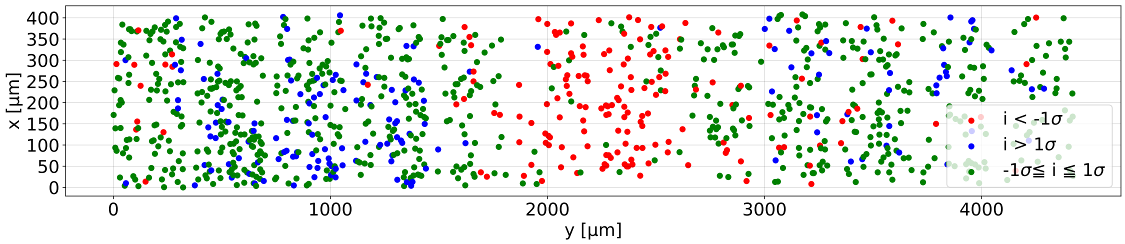

(d) *Sealant side - Top view*

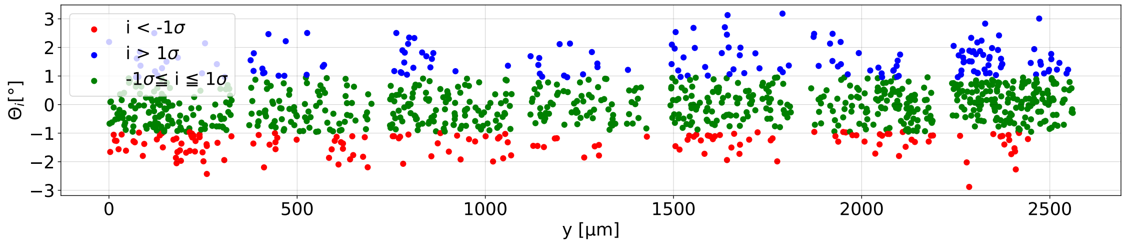

(e) *Mould side - Side view*

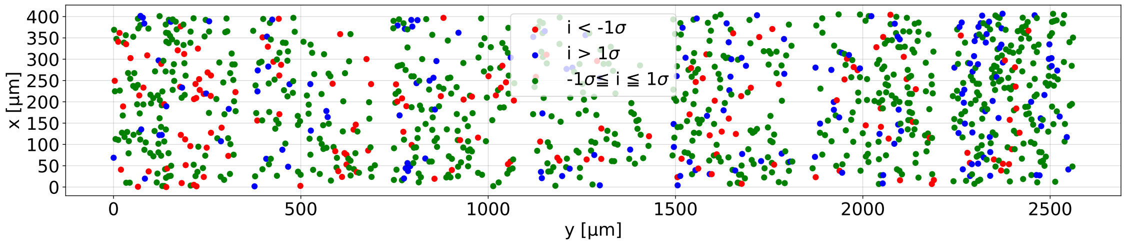

(f) *Mould side - Top view*

Fig. 4.12. *Series 7 - M79/IM2C - Out-of-plane fibre misalignment* Θ_i.

Page 2 of series 7

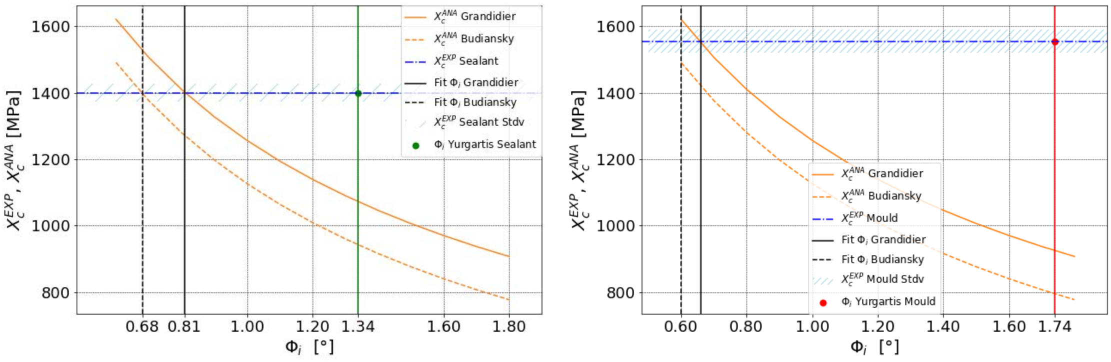

(a) X_c^{EXP} *versus* X_c^{ANA} *- Sealant side* **(b)** X_c^{EXP} *versus* X_c^{ANA} *- Mould side*

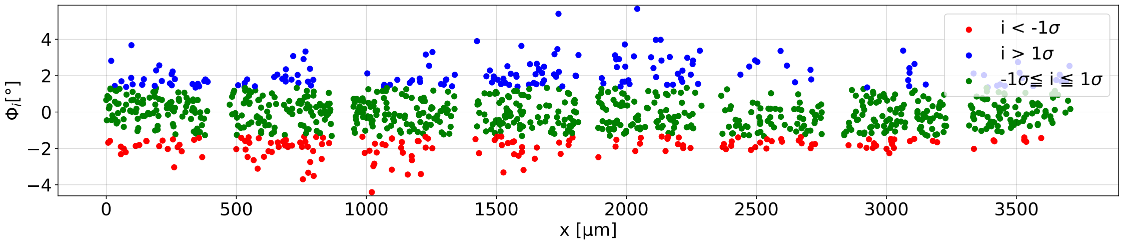

(c) *Sealant side - Side view*

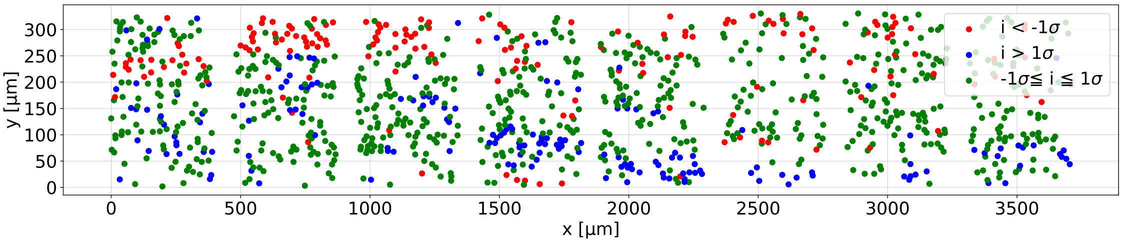

(d) *Sealant side - Top view*

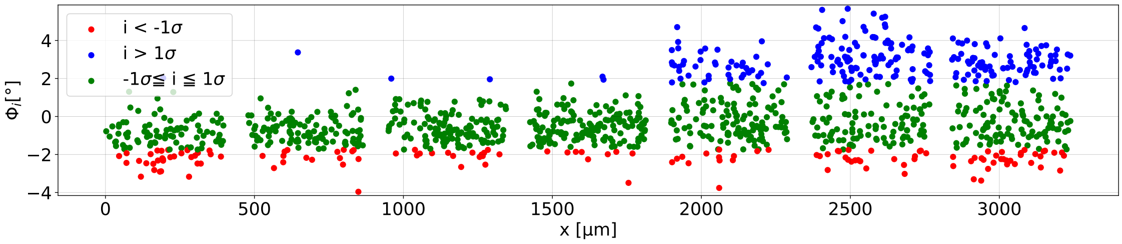

(e) *Mould side - Side view*

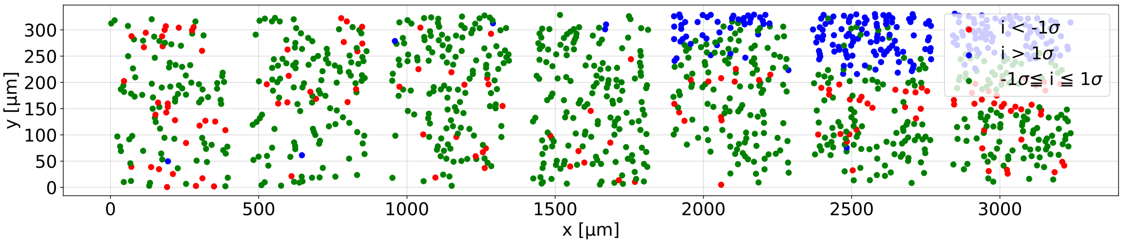

(f) *Mould side - Top view*

Fig. 4.13. *Series 7 - M79/IM2C - In-plane fibre misalignment* Φ_i.

4.5 Analysis and discussion on X_c^{EXP}/X_c^{ANA}-Θ_i, X_c^{EXP}/X_c^{ANA}-Φ_i diagrams with regard to fibre alignment distribution

The (non)-matchings of X_c^{EXP} with X_c^{ANA} were evaluated with regard to the determined fibre misalignment angles. Tab. 4.6 shows the in- and out-of-plane fibre misalignment angles Φ_i and Θ_i determined using Yurgartis [1987]'s method, and the analytical fits, permitting the prediction of X_c^{EXP} with the analytical models from Budiansky & Fleck's and Grandidier et al.'s as explained in Sec. 4.4.

Values in parentheses show the percentage differences between the fibre misalignment angles Φ_i and Θ_i, determined using Yurgartis [1987]'s method, and the analytically fitted value for Budiansky & Fleck's and Grandidier et al.'s solutions. This is the reason why Φ_i and Θ_i are replicated two times in Tab. 4.6.

For visual support, the cells are highlighted in green for differences in the range of 0 to $\leq$ 15 % (-15 % $\geq$ 0), in orange for differences between 15 % and $\leq$ 30 % (-30 % $\geq$ -15 %), and last, in red, for difference > 30 % (< -30 %). It was observed that all colors were more or less represented in Tab. 4.6.

As introduced in Sec. 4.3, the hypothesis that was made, was, that the studied zones from which the fibre misalignment angles were determined, represented the zones where specimens failure occurred during 4PB testing.

Therefore, the cartographies were used in order to provide a tool for explaining the observations of the (non)-matching of both compressive strengths.

The objective of the investigation of the cartographies was hence to identify for example clusters of misaligned fibres, single fibres strongly misaligned, or inhomogeneous fibre (mis-)alignment distributions that might have impacted the determination of the fibre misalignment angles, and hence the results of the compressive strengths. These three categories will first be presented in Sec. 4.5.1. A questioning procedure to structure the analysis of the diagrams and the cartographies will be given, after, in Sec. 4.5.2, before passing to a more detailed analysis of the diagrams and cartographies of the series 5 and 3 in Sec. 4.5.3 to Sec. 4.5.6.

4.5.1 Categories for classification of cartographies

Clusters of fibres $\leq$-1σ and $\geq$1σ

The first category contains clusters of misaligned fibres $\leq$-1σ and $\geq$1σ over a distance of several micrometers. Fig. 4.12c shows, for instance, the spatial distribution of the fibres in out-of-plane direction of series 7, sealant side, in the side view. A cluster of misaligned fibres $\geq$1σ can be found between 300 and 1550 µm, as well as between 1550 and 3000 µm ($\leq$-1σ).

Single fibres strongly misaligned

This category contains cartographies with single fibres which are strongly misaligned compared to the global fibre angle distribution. Fig. 4.6c exhibits, for instance, strongly misaligned fibres $\geq$ 3° of series 4, out-of-plane direction, sealant side.

Homogeneous distribution

The last category concentrates on a homogeneous fibre angle distributions. This includes well aligned, as well as homogeneously, in both directions misaligned fibres. This means that "$\leq$-1σ" and "$\geq$1σ" are approximately equally distributed along the x- and y-axes. Fig. 4.11d shows a homogeneous distribution of series 6, out-of-plane direction, sealant side.

Using these categories, the cartographies of all series in in- and out-of-plane direction for the mould and sealant sides were analysed, using the questioning procedure presented below, and the (non-)matchings of the compressive strengths were discussed. This will be exemplarily given for the series 5 and 3 in Sec. 4.5.3 to Sec. 4.5.6.

4.5.2 Questioning procedure

In order to structure the analysis of the categories, the question procedure in Tab. 4.7 was applied.

Tab. 4.7. *Questioning procedure for the evaluation of the fibre misalignment angles with regard to the spatial fibre distribution.*

→ $X_{c,EXP}$ matches $X_{c,ANA}$?		
↓ Yes	↓ No	↓ No
I. Hypotheses: i. Zone from which Θ_i/Φ_i were measured represents zone of failure ii. The analytical solution is assumed to be correct and can be applied to the present case.	III. Is the zone representative? Investigation of the cartography! → Are there clusters, single fibres strongly misaligned that could explain that the fibre misalignment angle measured in the representative zone does not represent correctly that in the failure zone?	IV. Is the analytical solution correct? → Investigations on the analytical solution need to be carried out.
II. Nevertheless, are there: Clusters, single fibres strongly misaligned, lots of fibres between $\pm 1\sigma$?		

The first question asked was whether X_c^{ANA} matched X_c^{EXP}. For this, the diagrams plotting the compressive strengths X_c^{EXP} and X_c^{ANA} as a function of the fibre misalignment angles Φ_i/Θ_i were investigated.
If the two results matched, it was assumed that (i) the zone from which the fibre misalignment angle was determined represented the zone where the specimen failure occurred. Nevertheless, those zones were (II.) investigated in terms of clusters, fibres that were

strongly misaligned, and (in-)homogeneous fibre angle distributions. Further, it was assumed that (ii.) the analytical solution was correct for the present case.
If the two results did not match, the (III.) representation of the examined zone was questioned, and the cartographies were examined in terms of clusters, and strongly misaligned fibres that might explain an erroneously determination of the fibre misalignment angle. Further, the (IV.) validity of the analytical solution was questioned.

4.5.3 Series 5, out-of-plane fibre misalignment (Θ_i), mould/sealant sides

Fig. 4.8a and Fig. 4.8b exhibited the diagrams of the compressive strengths X_c^{EXP} and X_c^{ANA} versus the out-of-plane fibre misalignment angle Θ_i for the sealant and mould sides of series 5. Both compressive strengths matched almost perfectly for both sides for the analytical solution of Grandidier et al. [2012]. The percentage differences of the measured and fitted fibre misalignment angles, given in Tab. 4.6, for the sealant and mould sides were -2.6 % and 0 %, respectively. It can therefore be assumed that the studied zone, from which Θ_i was determined, was representative for the zones in which specimen failure occurred. Further it can be assumed, that the solution of Grandidier et al. [2012] was applicable for the present case.
Taking a closer look at the cartography in Fig. 4.8c, only a little cluster of misaligned fibres between 1100 and 1450 µm was observed for the sealant side, and in Fig. 4.8e, a few strongly misaligned fibres ≥3° on the mould side. According to the hypothesis above, it can be concluded that the fibre angle distribution was similar to that in the failure zone of the 4PB specimens.

4.5.4 Series 5, in-plane fibre misalignment (Φ_i), mould/sealant sides

Fig. 4.9a and Fig. 4.9b exhibited the diagrams of the compressive strengths X_c^{EXP} and X_c^{ANA} versus the in-plane fibre misalignment angle Φ_i for the sealant and mould sides of series 5.
Both compressive strengths did neither match with the analytical solution of Grandidier et al. [2012], nor with that of Budiansky & Fleck [1993]. The fibre misalignment angle Φ_i differed by 17.1 % (sealant side) and 50.5 % (mould side) from Grandidier et al.'s, and by 38.4 % (sealant side) and 76.7 % (mould side) from Budiansky & Fleck's solution. These values are marked in orange and red in Tab. 4.6.
When examining the cartographies in Fig. 4.9c and in Fig. 4.9e, strongly misaligned fibres ≥3° and ≤-3° on the sealant and mould side could be observed. As smaller in-plane fibre misalignment angles were expected to match the analytical solutions, the question arises if the studied zone was representative of that of the failure zones of the 4PB specimens. Further, the question arises, if the analytical solutions were suitable for the present cases. A response will be proposed in Sec. 4.6.

4.5.5 Series 3, out-of-plane fibre misalignment (Θ_i), mould/sealant sides

Fig. 4.4a and Fig. 4.4b have shown the diagrams of the compressive strengths X_c^{EXP} and X_c^{ANA} versus the out-of-plane fibre misalignment angle Θ_i for the sealant and mould sides of series 3.
For the sealant side, X_c^{EXP} matched well X_c^{ANA} for Budiansky & Fleck's solution (-13.3 %). This is marked in green in Tab. 4.6. The cartography in Fig. 4.4c shows little clusters of misaligned fibres between 0 and 500 µm ($\geq 1\sigma$), as well as between 500 and 1470 µm ($\leq$-1σ)

For the mould side, X_c^{EXP} matched well X_c^{ANA} for Budiansky & Fleck's solution (-8.9 %), as well. This is marked in green in Tab. 4.6. The cartography in Fig. 4.4e in the side view does not show any remarkable fibre alignment distributions. The distribution is homogeneous.

4.5.6 Series 3, in-plane fibre misalignment (Φ_i), mould/sealant sides

Fig. 4.5a and Fig. 4.5b exhibited the diagrams of the compressive strengths X_c^{EXP} and X_c^{ANA} versus the in-plane fibre misalignment angle Φ_i for the sealant and mould sides of series 3.
For the sealant side, X_c^{EXP} matches almost perfectly X_c^{ANA}, estimated using Grandidier et al.'s solution (difference of 0.8 %, marked in green in Tab. 4.6). A closer look at the cartography (see Fig. 4.5c) shows a cluster of misaligned fibres $\leq$-1σ in the range of 2350 to 3300 µm, as well as single fibres strongly misaligned at $\leq$-3° and $\geq$3°.
The question arises, if the whole specimen structure was covered by those clusters and strongly misaligned fibres, and therefore if the studied zone was representative of that of the failure zone, or if the good matching was a coincidence. A conclusion on this will be proposed in Sec. 4.6.

The mould side of series 3 has show an intermediate matching of X_c^{EXP} and X_c^{ANA}. The in-plane fibre misalignment angle Φ_i determined using Yurgartis's method (0.78 °) compared to the fitted ones by Budiansky & Fleck [1993] (0.9 °) and Grandidier et al. [2012] (1.04 °), resulted in differences of -13.3 % and -25.0 %, respectively. These values are marked in orange in Tab. 4.6.
The corresponding cartography, given in Fig. 4.5e, contains from 0 to 1850 µm more misaligned fibres $\leq$-1σ than in the zone from 1850 to 3750 µm. The questions arise whether the studied zone contained more misaligned fibres that resulted in a higher in-plane fibre misalignment angle value, to fit better die analytical solutions, or whether the analytical solutions could not be applied to the present case. Further investigations on this would have to be carried out.

4.6 Conclusion on the observations

The cartographies of all series were classified in the categories given in Sec. 4.5.1 and related to the (non-) matching of the compressive strengths X_c^{EXP} and X_c^{ANA}.

Tab. 4.8 shows the results of the classification. The application of "X"-symbols in the cells has the following meaning. "XXX" denotes that the cartography completely matches the category, while no "X" represents no matching at all. "XX" or "X" represent a lot or little matching.

For the last category, it was easier to look for inhomogeneous fibre distribution zones, the reason why the column entitles *Inhomogeneous*.

Taking a closer look at the "X"-distribution in Tab. 4.8, it can thus be noted that three series show clusters of misaligned fibres over an important distance ("XXX"-symbols in the *Cluster* column), and five series clusters of intermediate, and less important fibre clusters ("XX"- and "X"-symbols in the *Cluster* column).

Single fibres which were strongly misaligned were almost observed on each cartography (see *Single fibres* column).

Last, it can be noted, that an inhomogeneous fibre distribution was often related to the presence of clusters of misaligned fibres, or single fibres strongly misaligned (see *Inhomogeneous* column).

Remembering the practical procedure for the in- Φ_i and out-of-plane Θ_i fibre misalignment angle determination, on can state that the proceeding for both angles was equal and implemented at the same time: specimen sectioning by Φ_{PC} and Θ_{PC} (Sec. 3.3.1), resin coating and polishing (Sec. 3.3.2), image recording (Sec. 3.3.3), image post-processing (Sec. 3.3.4), and the determination of the in- and out-of plane misalignment angles (Sec. 3.3.5). A difference in Φ_{PC} and Θ_{PC} had no impact on the results, as these two angles corresponded to the constant values $\omega'_{i,mean}$ and $\omega_{i,mean}$ (see Sec. 3.3.5), and the fibre misalignment angles Φ_i and Θ_i of each series were calculated via the normal law (Fig. 3.15), after using Equ. 3.2 and Equ. 3.4 .

Returning to the (non-)matching of X_c^{EXP} and X_c^{ANA} and taking into account the spatial fibre angle distribution, the following observations could be made:

It was found that for out-of-plane fibre misalignment angles Θ_i a higher presence of cluster and strongly misaligned fibres had tendency to result in a poor match of X_c^{EXP} and X_c^{ANA}. A lower presence of cluster and strongly misaligned fibres led to a better or perfect matching of X_c^{EXP} and X_c^{ANA}.

This train of thought was then applied to the in-plane fibre misalignment angle Φ_i. The same observations could not be made, as the *Match* column in Tab. 4.8 shows:

The first column *Grandidier et al. or Budiansky & Fleck [%]* replicates, from Tab. 4.6, the smallest percentage error between the experimentally measured misalignment angles (from Yurgartis's method) and the analytically fitted values, as well as the corresponding cell colors.

The column *Cartography* replicates the quantity of "X"-symbols from the *Cluster*, *Single fibres* and *Inhomogeneous* columns. The following cells colors were then applied to these cells. If the cell contained maximally two "X", which means that no or less clusters, strongly misaligned fibres, or inhomogeneous fibre (mis-)alignment distributions were observed, green was assigned to the cells of the *Cartography* column. Three or four "X"

in a cell were marked in orange, as this was assigned to an intermediate occurrence of clusters, strongly misaligned fibres, or inhomogeneous fibre (mis-)alignment distributions. And last, cells with more than four "X" were marked in red, as this signified lots of clusters, strongly misaligned fibres, or inhomogeneous fibre (mis-) alignment distributions.
The *Coincidence* column shows finally the results of the above mentioned observation. For out-of-plane fibre misalignment angles Θ_i, the observed spatial fibre alignment distribution coincided well with the observed (non-)matching of X_c^{EXP} and X_c^{ANA} (70-80 %). For in-plane fibre misalignment angles Φ_i, this was not the case (20-50 %).

For instance, for series 5, out-of-plane fibre misalignment (sectioned at 15°), mould side, X_c^{EXP} and X_c^{ANA} did match perfectly (difference of 0 % in the fibre misalignment angle, a green color cell was assigned). Only little fibres strongly misaligned, and a light inhomogeneity were observed (two "X"-symbols led to a green color cell). The coincidence was considered to be given ("yes" and a green color cell in the *Coincidence* column for two green color cells).
For series 6, out-of-plane fibre misalignment (sectioned at 15°), mould side, the match between X_c^{EXP} and X_c^{ANA} was intermediately (difference of -15.1 % in the fibre misalignment angle was marked in orange). Few single misaligned fibres, and little inhomogeneous fibre distributions were observed (two "X" symbols led to a green cell). As the cell colors did not match, "intermediate" and a orange color cell were hence assigned in the *Coincidence* column.
For series 5, in-plane fibre misalignment (sectioned at 10°), sealant side, the match between X_c^{EXP} and X_c^{ANA} was poor (difference of 50.5 % in the fibre misalignment angle led to a red color cell). Few single misaligned fibres were observed (two "X" symbols led to a green cell). As the cell colors did not match at all, "no" and a red color cell were hence assigned in the *Coincidence* column.
Last example, series 7, in-plane fibre misalignment (sectioned at 10°), mould side, X_c^{EXP} and X_c^{ANA} did not match (difference of 163.6 % in the fibre misalignment angle, red color was assigned to the cell). Lots of clusters of misaligned fibres over an important distance, and inhomogeneities were observed (more than four "X"-symbols led to a red cell). The coincidence was hence correct ("yes" and a green color cell for two red color cells).
It was found that the series 7 was a particular case since the models did never predict the compressive strengths without explanation.

According to these observations, it can first be concluded that some studied zones the out-of-plane fibre misalignment angle Θ_i determinations represented well the zones were specimen failure occurred.
The analytical solutions of Budiansky & Fleck [1993] and Grandidier et al. [2012] do not specify which angle should be used to estimate analytically the compressive strength X_c^{ANA}. From the upper observations, it can be second concluded, that the out-of-plane fibre misalignment angle Θ_i is more suitable in the estimation of the analytical compressive strength, than the in-plane fibre misalignment angle Φ_i.

4.7 Synthesis about the applied method and perspectives

In this research work, compressive strengths of different CFRP lamina obtained by the analytical solutions from Budiansky & Fleck [1993] and Grandidier et al. [2012] have been compared to those experimentally obtained through 4PB tests. The approach was not classical: more precisely, the experimental strengths were used to estimate fibre misalignment angles which permitted to obtain a good match between analytical predictions and experimental strength measurements (intersection of X_c^{EXP} and X_c^{ANA}). Then these fibre misalignment angles were compared to those obtained by Yurgartis's method.

The studied zone from which the fibre misalignment angles were determined was assumed to be representative for the zones where specimen failure occurred during 4PB test.

It was found that X_c^{EXP} and X_c^{ANA} matched well when the out-of-plane fibre misalignment angle Θ_i was used for the analytical estimation. Observed fibre alignment distributions (clusters, strongly misaligned fibres and (in-)homogeneous fibre alignment distributions) coincided with the (mis-)matching of X_c^{EXP} and X_c^{ANA}.

Nevertheless, the applied method in the scope of this study can be improved.

It would be advisable to code a programme that detects all ellipses along the specimen width and thickness, close to the mould and sealant sides, and to detect the positions ($\mathrm{x_i}$,$\mathrm{y_i}$) of all ellipses. Thus, not only the fibre misalignment angle could more precisely be determined, but also the fibre volume fraction could be included into the discussion. The latter is one important parameter in the analytical solution of Grandidier et al. [2012]. Statements about the compressive strength as a function of the spatial fibre distribution, and statements about the influence of fibre-rich or matrix-rich zones could be done.

To resume, the aim would be to enable the detection of each individual fibre on the micro scale, first. To determine the misalignment angle on the meso scale, second. Third, to use the cartographies to make hypotheses on the representation of the fibre misalignment angle on the overall material structure (macro scale), and to finally state if within this method, a more correct matching of X_c^{EXP} and X_c^{ANA} would be possible.

Tab. 4.8. *Classification of cartographies into different categories. The "X"-symbols indicate whether the series match the category totally ("XXX"), or not at all (no "X"). The Match column indicates if the (mis-)matching of X_c^{EXP} and X_c^{ANA} is conform to the observed spatial fibre distribution.*

Series		Side	Misalignment direction	Side view		Top view	Match			
				Clusters	Single fibres	Inhomogeneous	Grandidier et al. or Budiansky & Fleck [%]	Cartographie	Coincidence	
3	SE84 LV	sealant	10° – Φ (in-plane)	XXX	X	XXX	0.8	XXX X XXX	no	20-50 %
4	NANO			X	X	X	-18.5	X X X	yes	
5	XB3515			XX	XX	XX	17.1	XX XX XX	intermediate	
6	MTC9810				XX		31.9	XX	no	
7	M79				X	XX	65.4	X XX	intermediate	
3	SE84 LV	mould		XX		X	-13.3	XX X	no	
4	NANO				X	X	-28.3	X	intermediate	
5	XB3515				XX		50.5	XX	no	
6	MTC9810			X	X	XX	77.4	X X XX	intermediate	
7	M79			XXX	XX	XXX	163.6	XXX XX XXX	yes	
3	SE84 LV	sealant	15° – Θ (out-of-plane)	X		X	-13.3	X X	yes	70-80 %
4	NANO				X		-11.5	X	yes	
5	XB3515			X		X	-2.6	XX	yes	
6	MTC9810				X		13.8	X	yes	
7	M79			XXX	X	XXX	54.3	XXX X XXX	yes	
3	SE84 LV	mould			X		-8.9	X	yes	
4	NANO				X	X	-48.0	X X	non	
5	XB3515				X	X	0.0	X X	yes	
6	MTC9810				X	X	-15.1	X X	intermediate	
7	M79				X	X	60.0	X X	no	

PART III

THE INTERLAMINAR TENSILE STRENGTH (ILTS)

"Perfection is achieved, not when there is nothing more to add, but when there is nothing left to take away."
—ANTOINE DE SAINT-EXUPÉRY

5

Bibliographic review on the ILTS

Contents

The out-of-plane tensile strength is a determining parameter in the design of hydrofoils, as it can, if it is too high, cause the hydrofoil elbow to fail by delamination. In the past, L-beam specimens were tested in 4PB according to the standard ASTM D6415 / D6415M-06a [2013] to determine the ILTS. The 4PB test configuration permits to have the purest out-of-plane stress field possible in the curved region of the L-beam specimen. L-beams represent a simplified geometry of the hydrofoil elbow.

To date, hydrofoils are primarily produced by hand-lay up which is a long and a cost-intensive manufacturing technology. Moreover, the quality of the hydrofoil depends on the experience of the operator. The AFP technology is an alternative to the traditional manufacturing procedure which has progressively been used to manufacture hydrofoils in recent years.

In the scope of this study, a carbon/epoxy prepreg material has been used to manufacture L-beam specimens by two different lay-up methods: by traditional hand lay-up and by AFP technology. Both L-beam types experienced further the same curing cycle (autoclave).

In this section, the state of the art of the determination of the ILTS will be discussed first in Sec. 5.1, whereby the emphasis will be placed, if possible, on the manufacturing or machining process of the samples.

Then, in Sec. 5.2, literature will be presented dealing with sample manufacturing by hand lay-up and by AFP technology. Specimens manufactured within these research works are laminated samples tested in tension or compression in out-of-plane direction.

5.1 Out-of-plane strength σ_{33} determination with regard to the specimen production

Different approaches had been made to characterize the out of-the-plane strength which may be responsible for failure by delamination in curved composite materials. Indeed, several determination methods have been studied and discussed by authors in the literature. These test methods can be classified into (i) axial tensile loading of blocks and waisted (square cross section) samples and (ii) bending of curved samples. Selected studies on these methods found in the literature will be presented below. Special attention will be paid to the manufacturing and machining of the samples.
Martin & Sage [1986] investigated the across-thickness strength (out-of-plane strength) of waisted laminates loaded in tension. For this, 25 unidirectional CFRP laminates, made from the prepreg 914C-XAS, each one consisting of sixteen 0.125 mm thick plies, were stacked and bonded with an adhesive. The central section of the specimen was waisted in two dimensions. It was then bonded to aluminium shanks for loading in axial direction. A schema of the specimen is given in Fig. 5.1. An out-of-plane strength mean value of 75 MPa was measured. The result was lower than expected. Martin & Sage [1986] found that waisting the sample might have an influence on the specimen surface, i.e. this could cause cracks and leads to failure initiation sites. They also mentioned the difference of the Poisson value in fibre direction and that of the adhesive joining between the laminates, which may pose problems. The latter was 50 times that in the composite which thus could lead to stress concentrations. These observations and statements from Martin & Sage [1986] show thus the drawbacks of this method for determining the out-of-plane strength of laminated specimens.

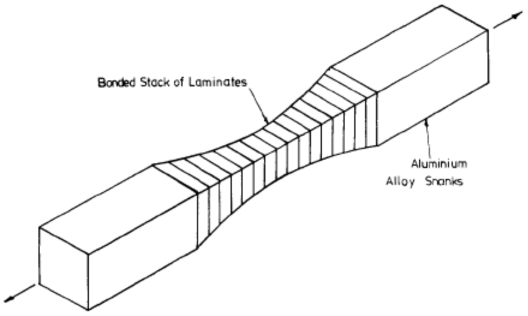

Fig. 5.1. *Bonded waisted specimen tested in out-of-plane direction in Martin & Sage [1986].*

Lagace & Weems [1989] tested specimens made of 3 mm thick laminates consisting of AS4 fibres and the epoxy 3501-6 with different lay-ups and waisted square cross-section. The measured out-of-plane tensile strength (interlaminar tensile strength) was lower than the transverse strength. It was found that the out-of-plane tensile strength appeared to be independent of the layup. Carefully machining of the specimens was necessary to prevent asymmetries of the waisted specimens and thus to avoid bending during loading. Nevertheless, failure occurred often close to the bond lines. Since misalignment between the specimen axis and the applied load could also be due to bad bonding of the specimen to the aluminium shanks, Lagace & Weems [1989] proposed to use a jig during bonding to improve the test performance. Despite these improvement suggestions, this method for out-of-plane strength determination stays complex: the samples must be properly bonded, samples are often long machined and the alignment between the specimen and the loading axe of the tension machine takes time and can not be ensured perfectly.

As a result, other methods, i.e. bending tests, were developed in order to determine the out-of-plane strength of laminated specimens.

Bending tests allowing the determination of the out-of-plane strength are referred to as indirect tensile curved tests since the tensile load applied on the test specimens does not act directly in the out-of-plane direction of the plies but creates a moment in the curved segment which generates an out-of-plane stress in radial direction. If the out-of-plane stress is too high, failure occurs by delamination. A number of specimens such as semi-circular [Ko & Jackson, 1989; Hiel et al., 1991], semi-elliptical [Ko & Jackson, 1990; Hiel et al., 1991], L-shape [Shivakumar et al., 1994; Jackson & Ifju, 1996; Charrier et al., 2016; Ranz et al., 2017], horseshoe [Ko & Jackson, 1990], and humpback [Wisnom & Jones, 1996], have been used to determine the out-of-plane strength through bending using analytical solutions. The origin of these solutions as well as several studies that can be found in literature are presented below.

Lekhnitskii [1968] derived first two elastic equations sets of a curved segment (girder) with cylindrical anisotropy loaded through (i) an end load and through (ii) a moment on each end, i.e. for each loading case the radial $\sigma_{33,Lekhn.}$ and circumferential $\sigma_{\theta\theta}, \sigma_{11,Lekhn.}$ stresses and the shear stress $\tau_{r\theta}$ in the $r-\theta$ plane. These stresses depend all on the angle Φ and the coefficient of anisotropy κ. The elastic equation of $\sigma_{33,Lekhn.}$ for an L-beam loaded in 4PB will be presented in more detail in Sec. 6.1. For all other equations interested readers are referred to Lekhnitskii [1968].

Kedward et al. [1989] developed a simplified solution for determining the ILTS in a curved beam subjected to pure bending. This solution will be introduced in Sec. 6.1. The solution is based on an approximation of the classical beam theory assuming that the maximum out-of-plane (radial) strength occurs on the radial distance $r_i \cdot r_o$, where r_i and r_o represents the inner and outer radii of the curved segment. Kedward et al. [1989] noted that the maximum radial stress in Lekhnitskii's solution depends on the degree of anisotropy while the approximated solution is independent of it. This can be seen in Fig. 5.2 where the approximated solution is identified by dashed and Lekhnitskii's solution by solid lines. For extreme geometrical configurations, i.e. for small $\frac{R_m}{t}$ ratio, the higher the anisotropy, the greater the overestimation of the out-of-plane strength in the approximated solution. R_m represents the mean radius and t the thickness of the curved segment. For $\frac{R_m}{t} \geq 2.5$ and $\frac{E_\theta}{E_r} \leq 6.0$, the maximum error resulting from Kedward et al.'s solution is $\leq 2.0\,\%$ [Kedward et al., 1989] and thus an acceptable approximation to the problem.

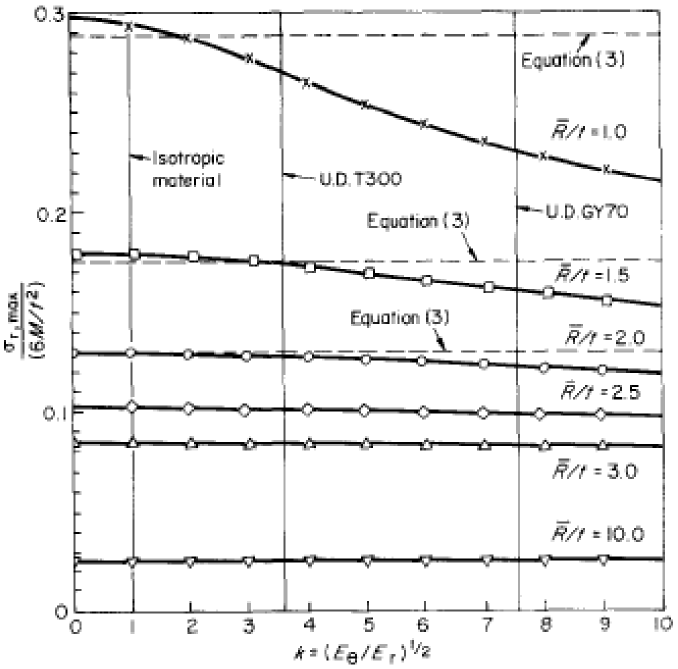

Fig. 5.2. *Normalized radial stress as a function of the anisotropy. Kedward et al.'s approximated and Lekhnitskii's solutions are represented by dashed and solid lines, respectively. For $\frac{R_m}{t} \geq 2.5$ and $\frac{E_\theta}{E_r} \leq 6.0$, the maximum error resulting from the approximated solution is $\leq 2.0\,\%$. [Kedward et al., 1989]*

Jackson & Martin [1993] studied the influence of the geometrical parameters, i.e. the width w, the loading arms length L, the thickness t and the inner radius r_i of curved L-beams on the through-the-thickness tensile (out-of-plane) strength using a hinge loading mechanism (end loading). The material was an AS4/3501-6 carbon/epoxy. The plies were hand laid-up in 0°-direction on an aluminium block. L-beams of 16, 24, 48 plies were manufactured and cured in an autoclave. It was not indicated if intermediate debulking during manufacturing or vacuum bagging during autoclave curing were done. For the 48-thick ply specimen a thermal blanket was additionally used to ensure uniform heating [Jackson & Martin, 1993] in the curing process. Prior to testing, the specimens were dried. Lekhnitskii's solution was adapted to the loading case in order to determine the ILTS. Jackson & Martin [1993] found, that the L-beam specimens developed all interlaminar and translaminar cracks. Jackson & Martin [1993] found, that the arm length L had a little and the width w a slight effect on the ILTS. The effects of the thickness t and inner radius r_i on the ILTS could not be determined due to variation in the laminate quality. The authors observed macroscopic flaws (voids and resin pockets), which may explain the low strength of some specimens. Analytical calculations have also shown that the location of the maximum radial stress moved away from the center and closer to the inner radius as thickness was increased (Fig. 5.3) [....] and as the inner radius increased, the maximum radial stress decreased, and the location of maximum radial stress moved towards the center of the thickness [Jackson & Martin, 1993].

Shivakumar et al. [1994] noted that the problem of load introduction was not addressed satisfactorily in previous studies. Hence, the authors proposed a tension loading fixture which introduced the load at the mid-thickness of the specimen. A schema of the loading fixture is given in Fig. 5.4a. L-shape specimens of different thicknesses (16, 24 and 32

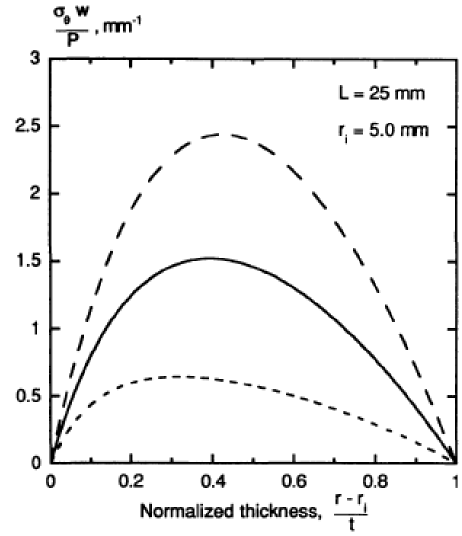

Fig. 5.3. *Normalized radial (through-the-thickness) stress for a 16-(long dashed line), 24-(solid line) and a 32-ply thick specimen (short dashed line). Jackson & Martin [1993]*

plies) were fabricated by laying up unidirectional plies over the corner ($r_i = 6.4\,\mathrm{mm}$) of an aluminium mould. The material used was an AS4/3501-6 graphite/epoxy laminate composite. Autoclave curing with vacuum bagging was applied. After machining of the samples to defined widths, the edges of the L-shape specimens were polished. Modified Lekhnitskii and Kedward et al.'s simplified solution were used to determine the ILTS. The analytical results were verified by a 2D finite element analysis. The resulting load-displacement diagrams are plotted in Fig. 5.4b, Fig. 5.4c and Fig. 5.4d. As expected, the thicker specimens were stiffer than the thinner ones. The non-linear response prior to failure of thick specimens was according to Shivakumar et al. [1994] due to the initiation of premature failures at rich-resin zones. The authors criticized that the quality of 32-ply thick specimens was poorer compared to the 16- and 24-ply thick ones since ply crimps and waviness after laying up about 25 plies were observed which led to resin-rich zones. This observation was also reflected in the determination of the ILTS. Decreasing strength with increasing specimen thickness might, according to Shivakumar et al. [1994], due to the probability of having more and larger defects in thick specimens. The distribution of the normalized radial stress through the thickness determined by Lekhnitskii's and Kedward et al.'s solutions compared to the FE analysis is given in Fig. 5.4e. As it was already observed in Jackson & Martin [1993], the failure location moves away from the center of the thickness towards the inner radius when the specimen thickness increases.

Jackson & Ifju [1996] pointed out that the hinge loading configuration in Jackson & Martin [1993] had drawbacks such as complex positioning, correct aligning of the specimen and difficulties of calculating the occurring stresses. Hence, Jackson & Ifju [1996] proposed the four-point-bending (4PB) configuration as an alternative to the hinge loading mechanism. The authors indicated the advantages of this loading configuration: pure bending moment generated in the curved segment of the L-shape specimen, self-aligning test configuration, constant moment in the test section, stresses are independent of the angular position and simplified analysis. [Jackson & Ifju, 1996]

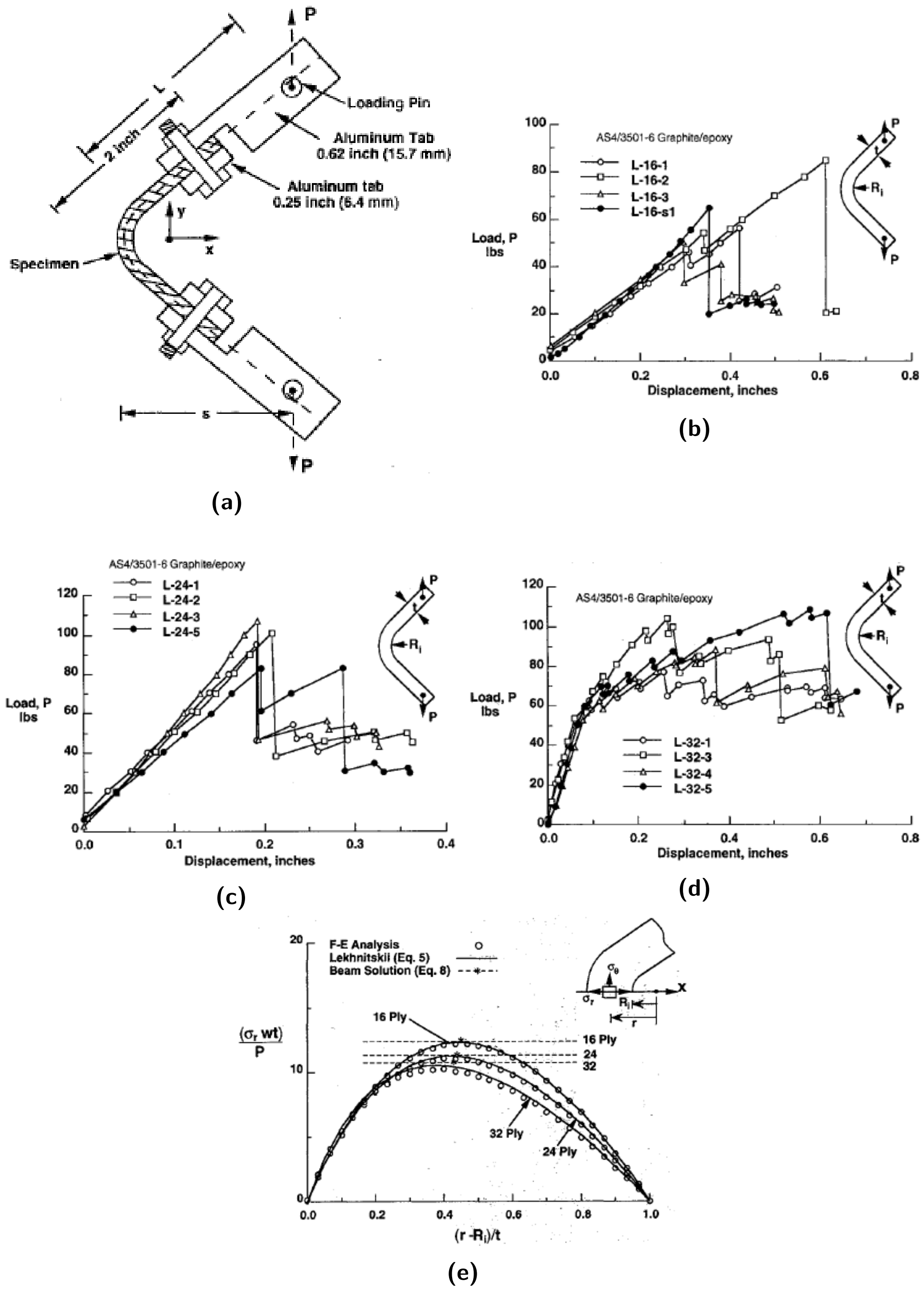

(a)

(b)

(c)

(d)

(e)

Fig. 5.4. *(a) Loading fixture used in Shivakumar et al. [1994] and resulting load-displacement plots of (b) 16-, (c) 24- and (d) 32-ply thick specimen and (d) distribution of the normalized radial stress through the thickness.*

The authors compared the two loading mechanisms in order to determine the through-the-thickness (out-of-plane) strength for composites made from textile preforms. Both test configurations had shown identical failure and almost identical stresses [Jackson & Ifju, 1996]. The 4PB configuration was however the preferred method due to the above mentioned advantages. The 4PB fixture was later implemented in the ASTM D6415 / D6415M-06a [2013].

Ranz et al. [2017] studied the influence of the specimen thickness on the out-of-plane strength. 4-, 8- and 12-ply tick specimens were fabricated by hand lay-up from an unidirectional carbon fabric (866 $\frac{g}{m^2}$) and an epoxy resin. The authors mentioned that during specimen manufacturing high attention was paid to correctly fibre alignment. Fig. 5.5 shows pictures of the manufacturing process of Ranz et al. [2017]. Information about the curing process or specimen's cutting was not specified by the authors. The L-shape specimens were tested in 4PB using the test fixture dimensions given ASTM D6415 / D6415M-06a [2013]. The authors indicated that the loading bars were mounted on roller bearings. Fig. 5.6 depicts the load-displacement plots for different thicknesses and lists the initial delamination locations for the corresponding failure loads. As expected, the 12-ply thick specimens were stiffer than the 8-ply thick and 4-ply thick specimens. As observed in Jackson & Martin [1993] and Shivakumar et al. [1994] a movement of the failure location towards the inner radius for increasing specimen thickness was also given for Ranz et al. [2017]. The table in Fig. 5.6 exhibits that for a specimen of 4 plies, the initial delamination location was at a specimen thickness of 50 % measured from the inner radius, for a 8-ply thick specimen at 38 % and for a 12-ply thick specimen at a specimen thickness of 33 % measured from the inner radius.

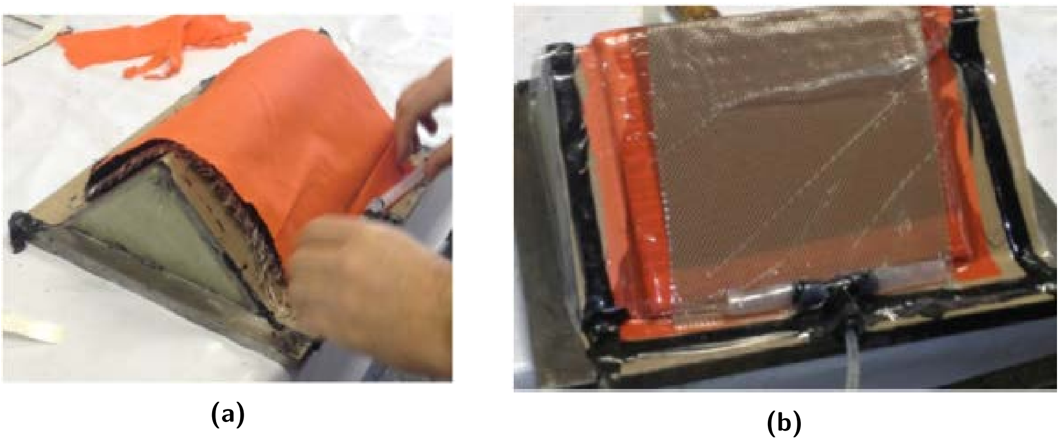
(a) **(b)**

Fig. 5.5. *Hand lay-up manufacturing of L-beam plate in Ranz et al. [2017].*

Ranz et al. [2017] also noted that for an increase of specimen thickness, a decrease in out-of-plane strength was observed. This may due to a higher number of defects (gaps and resin rich zones and higher residual stresses) in the thick specimens Ranz et al. [2017]. These statements agree with those of the studies presented by other authors above.

Zumaquero et al. [2018] studied the thickness dependence of L-beam specimens made from an AS4/8552 carbon/epoxy prepreg, tested in 4PB. Results were compared to finite element simulations using a geometrical non-linear solution (nlgeom = ON). Unidirectional 6-, 8-, 16-, 24-, 32-, 48- ply thick specimens with an inner radius r_i of 5 mm were manufactured by hand lay-up following the AITM1-0069 standard from Airbus. The weight of the resin content was 34 % and that of the fibres amounted to 194 $\frac{g}{m^2}$ per unit area. The plies were stacked over the corner of a steel mould. Before stacking of the first ply, Zumaquero et al. [2018] applied an unmolding liquid to the mould. Each ply was heated by an technical hair dryer and smoothed with pressure using a spatula as shown in Fig. 5.7.

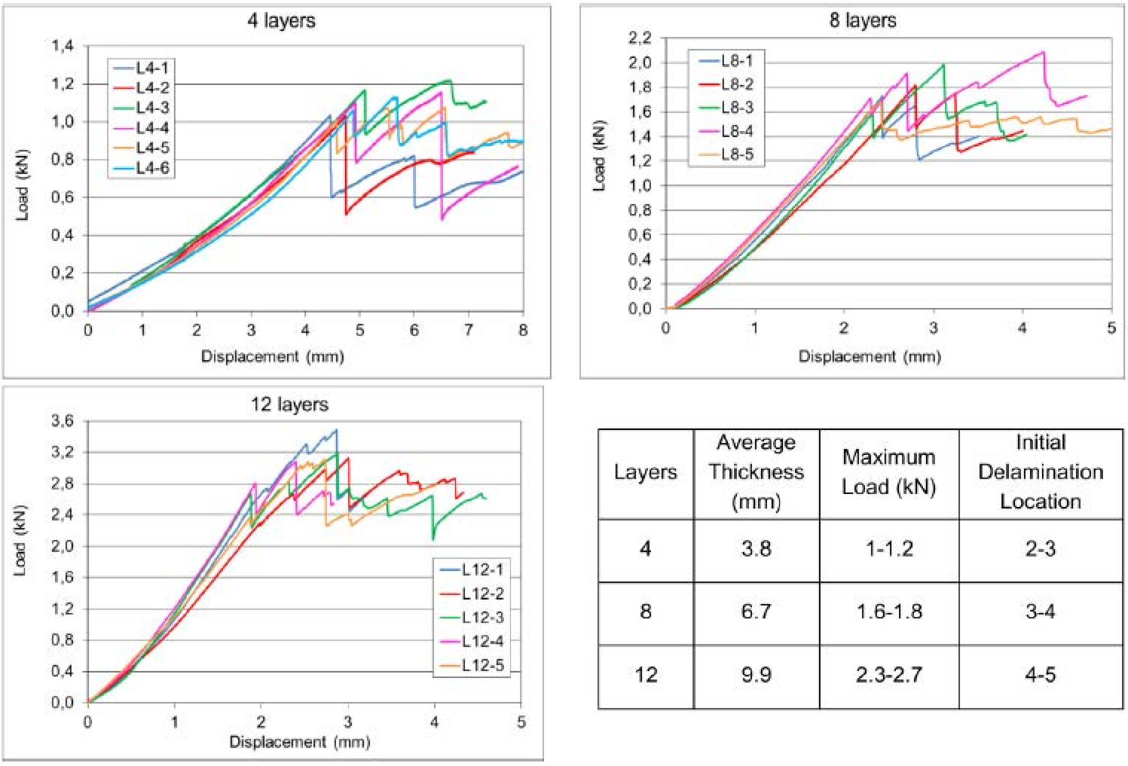

Layers	Average Thickness (mm)	Maximum Load (kN)	Initial Delamination Location
4	3.8	1-1.2	2-3
8	6.7	1.6-1.8	3-4
12	9.9	2.3-2.7	4-5

Fig. 5.6. *Load-displacement plots and first delamination location at failure load for different specimen thicknesses from Ranz et al. [2017].*

A vacuum compaction of the first ply and intermediate vacuum compaction every fifth ply during 10 min were applied. The L-beam parts were then cured under vacuum in an autoclave. 4PB tests were carried out according to ASTM D6415 / D6415M-06a [2013]. Zumaquero et al. [2018] noted the highest out-of-plane strength for 24-ply thick specimens, an increasing of the out-of-plane strength for 6-, 8-, 16-ply thick specimens and an decreasing for 32-, 48- ply thick specimens. The decrease in strength was explained by the thickness dependence of the ILTS. Finite element models for 8-, 16- and 32-ply thick specimens were created using Abaqus. Loading bars were made of rigid surfaces. The lower loading bars were fixed, the upper loading bars were subjected to a vertical displacement. Zumaquero et al. [2018] chose a geometrical non-linear solution due to high vertical displacements obtained in the experimental study. In Fig. 5.8a, Zumaquero et al. [2018] confronts the load-displacement (stroke displacement of the test machine) plots of the experimental results with the numerical simulations. The increased rigidity in the numerical models was explained by the fact that high fibre misalignment was observed in the curved area of the L-beam specimens at microscopic scale. Numerical studies have shown that fibre misalignment reduces the tangential elastic modulus (0°-direction) of a ply up to 50 % Zumaquero et al. [2018]. Fig. 5.8b shows the same plot, as seen in Fig. 5.8a, for reduced strengths. Zumaquero et al. [2018] concluded that the thickness dependence of the ILTS may due to fibre misalignment occurring during hand lay-up.

Charrier [2013] investigated the out-of-plane strength of CFRP L-beams with different stacking sequences and thicknesses (48-, 32- and 16-ply thick) made from T700GC/M21 (268 $\frac{\mathrm{g}}{\mathrm{m}^2}$) unidirectional prepreg plies, tested in 4PB. L-beams were manufactured by the

(a) (b)

Fig. 5.7. *Hand lay-up in Zumaquero et al. [2018]. (a) application of the heating of each ply using a technical hair dryer. (b) pressure smoothing of each ply using a spatula.*

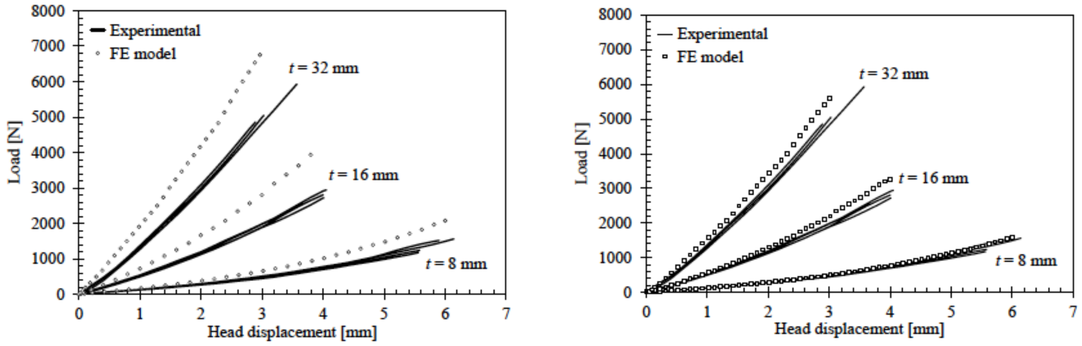

(a) (b)

Fig. 5.8. *Experimental-numerical correlation of load-stroke displacement (a) without and (b) with change of E_θ. E_θ was adjusted to simulate the effect of fibre misalignement in the curved segment of the L-beam on the decrease of rigidity. Zumaquero et al. [2018].*

company Duqueine Composites and by the institution CRITT from Toulouse. L-beams from the former were named STAF, those manufactured by the latter STRENGTH. Charrier [2013] noted that debulking were performed every forth to sixth ply for STAF and every second ply for STRENGTH L-beams. After 4PB tests, analysis were carried out using Lekhnitskii's solution. The author stated that L-beams with intermediate compaction every 2 plies resulted in a 10 % higher out-of-plane strength as L-beams with lower intermediate compaction (STAF). Thus, the author concluded that the out-of-plane strength depends highly on the fabrication process [Charrier, 2013].

The same author published in Charrier et al. [2016] some of those results obtained in Charrier [2013]. On STAF L-beams, 4PB tests with changing horizontal distances between the upper and lower loading bar centres, to ensure equal loading conditions, were carried out and compared to FE simulations. The distances of the loading bar centres depended on the specimens' thicknesses and were thus smaller for thinner than for thicker specimens. 4PB tests were equipped with Acoustic emissions (AE), Digital image correlation (DIC) and a Linear variable differential transformer (LVDT). Geometric dimensions of the L-beam

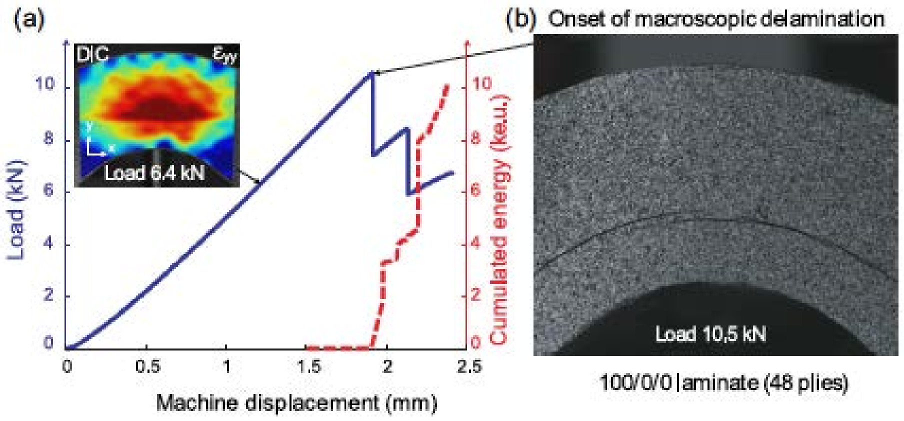

Fig. 5.9. *(a) Load-displacement plot and evolution of the cumulative acoustic energy during 4PB test and (b) delamination at failure for a unidirectional* 12.48 mm*-thick specimen. Charrier et al. [2016]*

specimens were as follows. Three different thicknesses 12.58 mm, 8.38 mm and 4.19 mm with a nominal ply thickness of 0.262 mm were manufactured by hand lay-up. For thick specimens the width w and inner radius r_i were 60 mm and 12 mm, for 8.38 mm-thick specimens 40 mm and 8 mm and for thin specimens 20 mm and 4 mm, respectively. In Charrier et al. [2016], the authors described more preciously the manufacturing process of the STAF L-beams. Attention has been paid during laying-up of the plies in order ensure geometrical tolerances and to avoid initial wavinesses in the curved segment of the L-beams [Charrier et al., 2016]. After debulking every fourth or sixth laid-up ply, the panels were cured in an autoclave during 120 min at 180 °C and a pressure of 7 bar. It was not indicated by the author whether a caul plate was used or not. For FE simulations, the Z-set finite element code package was used. The mesh of the L-beam specimen was built up of one solid linear element per ply thickness. The unidirectional ply was assumed to have a linear elastic behaviour. The loading bars were meshed with volume linear elements and were assumed to be isotropic linear elastic with the material properties of steel. The contact between loading bars and L-beam specimen was assumed to be frictionless. Charrier et al. [2016] explained this choice on the basis of roller bearings used in the experimental study. Vertical displacement were imposed on the upper loading bars, the lower loading bars were fixed in the same direction. The L-beam specimen was further limited in its movement in the other two directions. During 4PB test, Charrier et al. [2016] observed a sudden loss of rigidity (load drop) when the first delamination in the curved part of the specimen occurred. This is depicted in Fig. 5.9. The load-displacement curve (vertical stroke displacement) shows a quasi-linear material behaviour. Prior to the first load drop, corresponding to the first failure through delamination, no acoustic event happened. According to Charrier et al. [2016] this means that no transverse crack happened prior to failure. The location of the first delamination occurred independently from the stacking sequence between $\frac{1}{4}$ and $\frac{1}{2}$ from the inner radius and was in accordance with the DIC. No precision has been done whether for thin or thick L-beam specimens failure moved towards the thickness center or the inner radius (as stated by Jackson & Martin [1993]). Fig. 5.10 depicts the load-displacement plots recorded by the DIC and the LVDT as well as that of the FE simulation for a 8.38 mm-thick specimen with defined stacking sequence

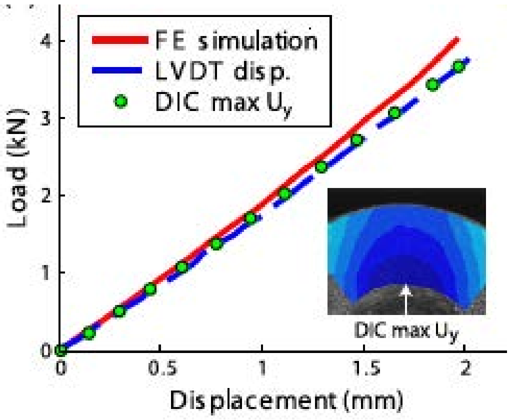

Fig. 5.10. *Comparison of load-displacement plots measured through DIC, Linear variable differential transformer (LVDT) and finite element simulation for a* 8.38 mm*-thick specimen with defined stacking sequence.* *Charrier et al. [2016].*

(non-unidirectional). While DIC and LVDT superpose perfectly, the load-displacement curve of the FE simulation shows a rigidification. Since a linear elastic material behaviour and no friction between the loading bars and the L-beam specimen were assumed, the rigidification would have to be from a geometrically non-linear solution. However, the author does not provide any information on this. Charrier et al. [2016] noted further that the out-of-plane strength is independent of the stacking sequences and of the specimen thickness even though a lower strength for thick specimens was determined. According to Charrier et al. [2016] this was due to a non-optimal choice of the curing cycle for the thick specimens.

Furthermore, the research work of Mespoulet [1998] shall be mentioned. The author gives a vast overview of different methods developed in the past with the aim to determine the out-of-plane tensile stress. Mespoulet [1998] outlines the studies conducted by Kitching et al. [1984], Lagace & Weems [1989] and Hodgkinson et al. [1992] for specimen tested in axial loading and the studies of Hiel et al. [1991], Jackson & Martin [1993] and Wisnom & Jones [1994] for curved specimens loaded through bending and compares them in terms of sample dimension, specimen preparation requirements, applied lay-up, tabs, jigs and tensile machines used, fixation of the specimen to the jigs, the samples' uniformity and purity in the gauge section and the material properties that can be measured.

Mespoulet [1998] underlined that bonded block and waisted specimens in axial loading are promising tensile test methods since the analysis is simple and the required laminate thickness to manufacture the specimens is acceptable. However, the main drawback is the important machining requirements, especially for waisted specimens.

A more recent overview of conducted research studies with the aim to determine the out-of-plane tensile stress of laminated specimens is given by Olsson [2011]. The authors shared the opinion of Mespoulet [1998] that waisted specimens require a complicated manufacturing. The author underlined the main advantages of the 4PB test setup: self-aligning specimens and simplified specimen preparation.

In the literature no research works were found that compare specimens manufactured by hand laid-up to specimens manufactured by AFP technology, both tested in 4PB. For this reason, the following section presents literature that shows the experience that were made with tensile or compression tests on flat laminate specimens produced by hand lay-up and by AFP technology. A short overview of the advantages and drawbacks of hand lay-up and AFP technology will be presented as well.

5.2 Classical hand lay-up and AFP technology

Kozaczuk [2016] compares the traditional hand lay-up with the AFP technology and shows advantages and disadvantages of both methods. Advantages of the hand lay-up are the possibility of producing complex shapes and the fact that expensive equipment is not required (with exception of the mould which can be costly). However, this method depends highly on the skills of the operator and requires high production times. Especially ply cut operations (ply shape cutting from a material roller) prior to hand lay-up and the debulking process contribute to a long production time. An other drawback is the quality of hand laid-up parts depending on the experience of the operator. Advantages of the AFP technology are the producibility, a part to part repeatability, and a low amount of material waste. Indeed, the upper mentioned disadvantage for traditional prepreg hand lay-up (time expenditure and quality) do not apply here. The roller on the head of an AFP robot applies a constant pressure on the composite tapes assuring a proper nesting, and eliminating the debulking operation before curing. The production time is thus be faster. From an economic point of view these are important aspects. Material waste is lower, since ply cut operations prior to lay-up are not necessary. Disadvantages of the AFP technology are the limitations to the mould shape. The roller diameter that compacts the plies during lay-up and the head geometry of the robot limits female mould radii. An other disadvantages are ply edges that are created by cutting layered tapes at the end of a tape path. Kozaczuk [2016]

McManus & Mak [1993] studied the tensile failure and damage tolerance of (un)notched panel specimens made of graphite/epoxy (IM7/977-2, AS4/938) laminates, manufactured by hand lay-up and by AFP technology, tested under axial tensile loading. Hand lay-up specimens were made of continuous unidirectional prepreg tapes. AFP specimens were fabricated on a 6-axis fibre placement machine. Autoclave curing was applied according to the manufactures' cure cycle. Samples were machined by band saw and were sanded afterwards. More detailed information on the manufacturing process of both specimen types were not given. McManus & Mak [1993] found that the damage tolerance and the progression from initial to final failure are dependent on the strain rate and the manufacturing technique. Elastic behaviour and failure loads are not dependent on these factors [McManus & Mak, 1993]. For notched AS4/938 specimens, failure initiation of AFP and hand laid-up specimens were at similar loads, but final failure loads were higher and the strain rate sensitivity was lower for AFP specimens [McManus & Mak, 1993]. Thus, strain rate and manufacturing technique have a strong effect on the progressive failure mechanisms in notched specimens [McManus & Mak, 1993].

Lan et al. [2015] investigated the influence of gaps and overlaps on the microstructure and on the tensile properties of carbon reinforced epoxy laminates made from a Hexcel prepreg (designation 8552/AS4/RC34/AW194). Specimens with and without defects were manufactured by hand lay-up and by AFP technology. Results of specimens without defects served as reference values and are considered in more detail in the following. Standard industrial practice was used for hand lay-up [Lan et al., 2015]. More details about the manufacturing process of hand laid-up samples were not given. For AFP manufactured specimens, an aeronautical procedure was applied using a robot from Coriolis Composite [Lan et al., 2015]. A compaction force of 100 N was exerted. Prepreg fibre tows were from the same material batch as used for hand laid-up specimens [Lan et al., 2015]. Both plates were cured in an autoclave using 2 mm thick aluminium caul plates. The authors noted fibre volume fractions of 58.8 % for hand laid-up and 59.7 % for AFP specimens. Fig. 5.11 exhibits the microstructure of hand laid-up and AFP specimens. Low porosity levels and only micro porosities in interply regions were noted by Lan et al.. However, it can be seen that the layers of AFP produced samples are better compacted that hand laid-up ones. This could be due to the constant compression of the roller head on the tows which ensure better tack between the plies. Nevertheless, the tensile tests of both specimen types resulted in similar material properties [Lan et al., 2015].

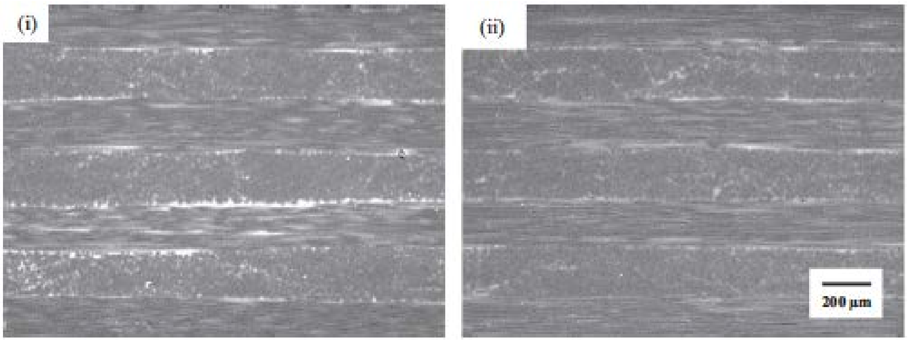

Fig. 5.11. *Microstructure of (left) hand laid-up specimens and (right) specimens manufactured by AFP. Low porosity levels were noted for both specimens types.* Lan et al. [2015]

Nguyen et al. [2019] studied the influence of gaps and overlap imperfections implemented in flat non-unidirectional laminated specimens manufactured by hand lay-up and by AFP technology. The material used was a Toray T800S/3900 prepreg. 8-ply thick specimens were manufactured for tension, 16-ply thick specimens for compression tests. The authors prepared specimens (*base-line panels*) without defects which served as reference. The hand lay-up and the AFP process were conducted as follows. For hand lay-up manufacturing, the prepreg was thawed to room temperature and cut into sheets. An aluminium mould, treated with layers of a release agent, was used for ply stacking. Intermediate compaction under vacuum (debulking) was applied every fourth ply. For panels manufactured by AFP technology, a robot with a head carrying eight spool slit tapes was used. The authors did not specify the robot type in more detail. Only the fabrication location (Electroimpact Inc.) was given. Nguyen et al. [2019] mentioned incidents that can occur during ply laying-up by AFP: Defects such as sub-optimal tack of tows and splice within the slit tapes. Vacuum sealing and autoclave curing were applied to each panel, following the manufacturer recommended cure cycle. Panels were de-moulded after cooling down to room-temperature. In the following, only specimens without indented defects will be considered in more detail. Fig. 5.12 depicts images of a hand-layup baseline specimens taken with a microscope. No voids or porosity could be detected. The toughening microparticles in the interlayers are material-related (Toray T800S/3900) [Nguyen et al., 2019]. Fig. 5.13 shows the microscopy results of specimen manufactured by AFP. Nguyen et al. [2019] found that even though no gaps or overlaps were expected, small gaps between the courses were detected. The authors also mentioned layup tolerances that cause larger gaps, which had, however, no impact on neighbouring plies. Results of tensile tests have shown that elastic modulus and tensile strength of both specimen types were almost equal with a standard deviation less than 3 % [Nguyen et al., 2019]. Moreover, no differences in the material properties between both lay-up technologies, as depicted in Fig. 5.14, were found. To conclude the analysis of tensile tests of hand laid-up and AFP specimens, Nguyen et al. [2019] stated that the main separation mechanism for both specimen types was intralaminar splitting instead of classical delamination. Compression tests, on both specimen types, resulted in a lower stiffness (7%), but higher strength (5%) for AFP- compared to hand laid-up specimens. The corresponding stress-strain plots are given in Fig. 5.15. The authors stated that fibre kinking and delamination can be observed in all cases.

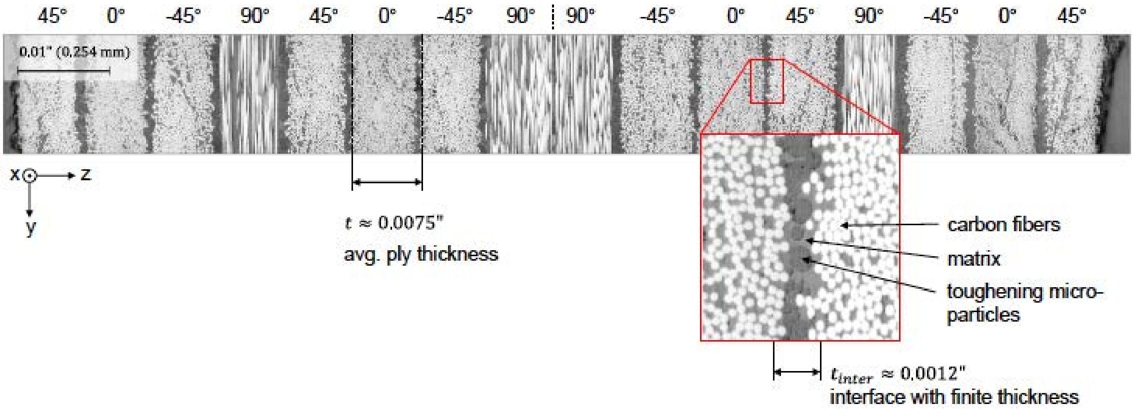

Fig. 5.12. *Microscopic through-the-thickness view of a quasi-isotropic hand laid-up specimen without indented defects. No voids or porosity can be detected.* Nguyen et al. [2019]

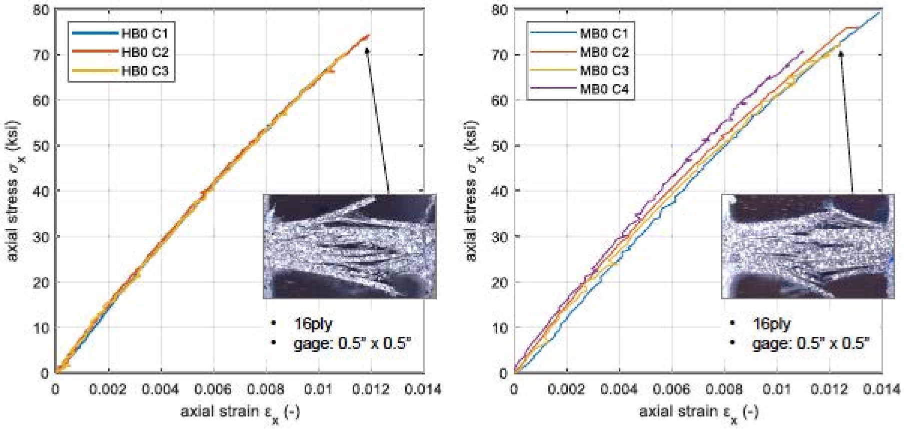

Fig. 5.15. *Stress-strain plots and failure modes of compressive tests for (left) hand lay-up specimens and (right) specimens manufactured by AFP.* Nguyen et al. [2019]

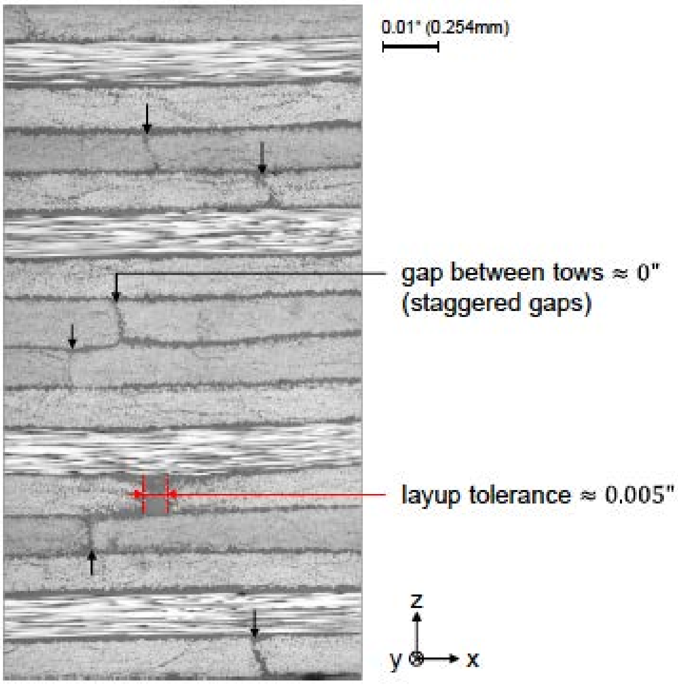

Fig. 5.13. *Microscopic through-the-thickness view of a quasi-isotropic specimen manufactured by AFP technology without indented defects. Nevertheless, small gaps could be detected between the courses.* Nguyen et al. [2019]

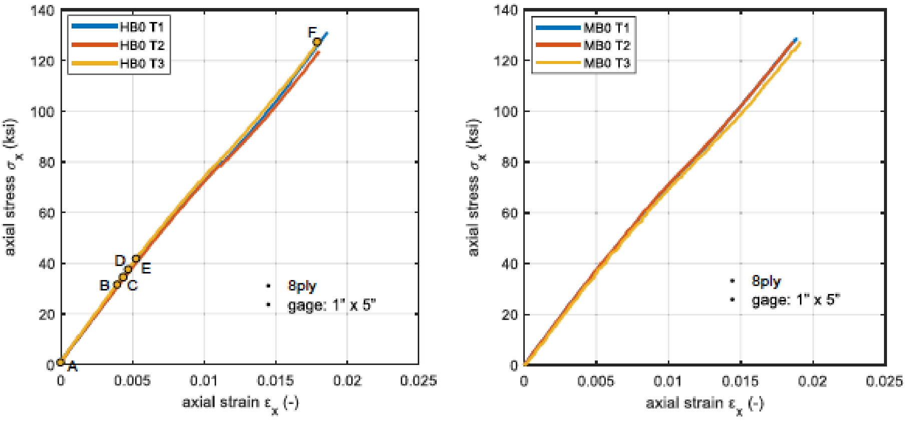

Fig. 5.14. *Stress-strain plots for tensile loaded (left) hand lay-up specimens and (right) specimens manufactured by AFP technology without any indented gaps or overlaps. No differences in the material properties between both lay-up technologies were found.* Nguyen et al. [2019]

6

Setting up of the analytical, the experimental and the numerical tool

Contents

In the present chapter, three tools which were developed in the scope of this research study in order to determine the ILTS of unidirectional carbon fibre reinforced L-beams will be presented. First, in Sec. 6.1, an introduction to the 4PB test setup will be given by defining the necessary parameters for the analytical estimation of the ILTS using the analytical solutions of Lekhnitskii [1968] and Kedward et al. [1989]. The analytical tool, a python script coded within this study containing both solutions, will be validated by comparing results found in the literature with those calculated by the analytical tool. Then, in Sec. 6.2 the experimental test setup will be presented. An overview of the test setup design will be given, taking into account the geometrical, mechanical and technological requirements. Afterwards, the applied instrumentation and their specific measuring characteristics will be listed. Last, in Sec. 6.3, the FE model of the L-beams will be presented and validated with results found in the literature. Sensibility studies on the mesh and on the choice of the material of the loading bars will be done.

6.1 Presentation of the analytical tool ANA

The most frequently test setup used for the ILTS determination of unidirectional laminated L-beam specimens is the 4PB test, shown in Fig. 6.1. This test configuration developed by Jackson & Ifju [1996] was implemented in the standard ASTM D6415 / D6415M-06a [2013] in 2013 [Olsson, 2011]. The L-beam sample is loaded in four-point bending in order to generate a uniform moment in the curved segment inducing an out-of-plane stress in radial direction which causes the material to fail by delamination when reaching the ILTS. Jackson & Ifju [1996] compared this test configuration to other methods (hinge load mechanism) that enabled the determination of the ILTS. The authors concluded that the analysis of the 4PB test is simplified, because only pure bending is produced in the test section and no end forces are applied on the specimens' legs. Further, the stresses are independent of the angular position and the moment that is generated is constant. In addition, the 4PB test configuration is self-aligning. [Jackson & Ifju, 1996]
The out-of-plane stress is hence induced by a moment generated by the force $P_b = \frac{P}{2}$ acting on the lower loading bars, and the distance l_0 along the specimens' legs. The exerted force P_b is exemplarily marked in Fig. 6.1 for the left part of the L-beam. The lever arm l_0 is thus given by:

$$l_0 = 2\,\frac{l_A}{2} + l_B = 2\left(\frac{D}{2} + \frac{t}{2}\right)\,\tan(\phi) + \frac{d_x}{\cos(\phi)} = (D+t)\,\tan(\phi) + \frac{d_x}{\cos(\phi)}\ , \tag{6.1}$$

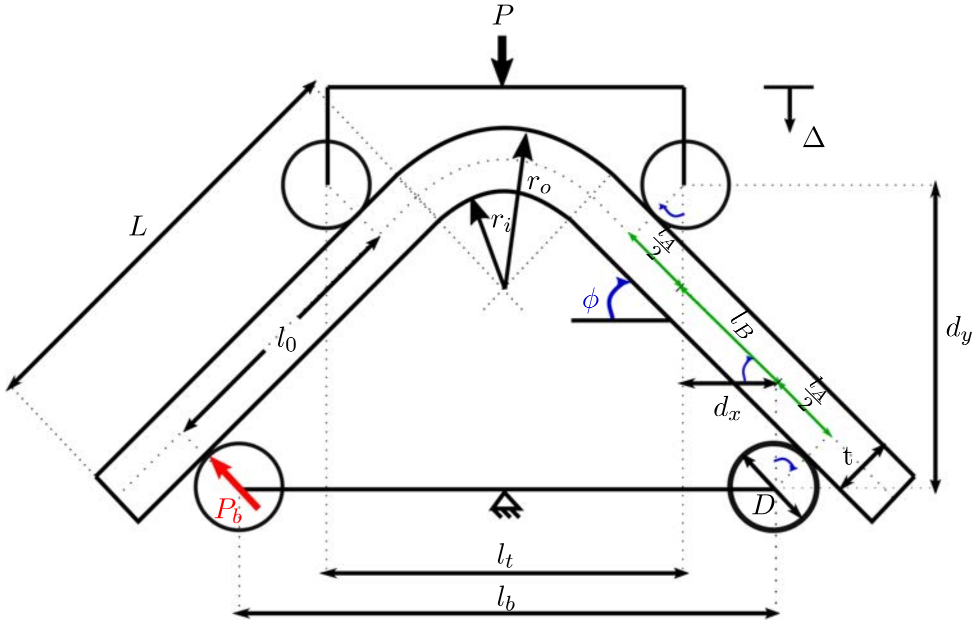

Fig. 6.1. *4PB test setup for ILTS determination.*

where t denotes the mean specimen thickness, ϕ the angle between the horizontal line and the specimen's legs, D the diameter of the cylindrical loading bars, and d_x the horizontal distance between the vertical centreline of one upper and one lower loading bar.

The acting bending moment per unit width, also referred to as CBS, is thus:

$$CBS = \frac{M}{w} = \frac{P_b l_0}{w} = \left(\frac{P}{2w\ \cos(\phi)}\right)\left(\frac{d_x}{\cos(\phi)} + (D+t)\tan(\phi)\right) \tag{6.2}$$

with w denoting the specimen mean width.
For a more accurate estimation of the applied moment, the standard ASTM D6415 / D6415M-06a [2013] recommends to used ϕ at failure as its value changes during loading:

$$\phi = \sin^{-1}\left(\frac{-d_x(D+t) + d_y\sqrt{d_x^2 + d_y^2 - D^2 - 2Dt - t^2}}{d_x^2 + d_y^2}\right)\ , \tag{6.3}$$

with

$$d_y = d_x \tan(\phi_i) + \frac{D+t}{\cos(\phi_i)} - \Delta\ , \tag{6.4}$$

corresponding to the vertical distance between the horizontal centreline of one upper and one lower loading bar, and ϕ_i and Δ represent the angle between the horizontal line and the specimen's legs at the undeformed state, and the vertical stroke displacement during testing, respectively.
Then, the ILTS, defined as the maximum out-of-plane stress at failure [ASTM D6415 / D6415M-06a, 2013], is determined according to Lekhnitskii through:

$$\sigma_{33} = -\frac{CBS}{r_o^2 g}\left[1 - \frac{1-\rho^{\kappa+1}}{1-\rho^{2\kappa}}\left(\frac{r_{max}}{r_o}\right)^{\kappa-1} - \frac{1-\rho^{\kappa-1}}{1-\rho^{2\kappa}}\rho^{\kappa+1}\left(\frac{r_o}{r_{max}}\right)^{\kappa+1}\right] \tag{6.5}$$

where

$$g = \frac{1-\rho^2}{2} - \frac{\kappa}{\kappa+1}\frac{(1-\rho^{\kappa+1})^2}{1-\rho^{2\kappa}} + \frac{\kappa\rho^2}{\kappa-1}\frac{(1-\rho^{\kappa-1})^2}{1-\rho^{2\kappa}}\ , \tag{6.6}$$

$$\kappa = \sqrt{\frac{E_\theta}{E_r}}\ , \tag{6.7}$$

$$\rho = \frac{r_i}{r_o}\ , \tag{6.8}$$

and

$$r_{max} = \left[\frac{(1-\rho^{\kappa-1})(\kappa+1)(\rho r_o)^{\kappa+1}}{(1-\rho^{\kappa+1})(\kappa-1)r_o^{-(\kappa-1)}}\right]^{\frac{1}{2\kappa}}. \tag{6.9}$$

For the application in the present study, the diameter of the cylindrical loading bars D was set to

$$D = \frac{D_{inf} + D_{sup}}{2}. \tag{6.10}$$

In the above equations, κ represents an anisotropic parameter, r_i and r_o the inner and outer radii of the curved element, r_{max} the radial location of the ILTS, and E_r and E_θ the elastic moduli in radial and circumferential directions. D_{inf} and D_{sup} denote the diameters of the lower and upper loading bars.
The solution of Lekhnitskii was developed for curved mono-layered anisotropic cylinders subjected by an end load. This solution assumes plane strain conditions.

The standard ASTM D6415 / D6415M-06a [2013] proposes a second solution, that developed by Kedward et al. [1989], basing on the bending theory, and assuming a linear distribution of the circumferential stresses

$$\sigma_{33} = \frac{3\,CBS}{2t\sqrt{r_i r_o}}. \tag{6.11}$$

Here, $\sqrt{r_i r_o}$ corresponds to the radial location of the ILTS which is independent of the degree of anisotropy. As depicted in Fig. 5.2, Equ. 6.11 overestimates the maximum radial stress with higher degrees of anisotropy for extreme geometrical configurations [Kedward et al., 1989]. It can be thus assumed, that the accuracy of Equ. 6.11 decreases as the $\frac{E_\theta}{E_r}$ ratio increases or the $\frac{r_i}{r_o}$ ratio decreases [ASTM D6415 / D6415M-06a, 2013].

6.1.1 Validation of the analytical tool

Lekhnitskii's and Kedward et al.'s solutions for the ILTS determination were encoded with python language to automate and accelerate the calculations. To ensure the correct calculation of the ILTS, the python script had to be validated. This was done by investigating the research work of Charrier et al. [2016], from which the geometrical dimensions of the investigated unidirectional L-beam specimens, the dimensions of the test setup and the material properties were taken and entered into the python script. The ILTS results were then compared with those given in Charrier et al. [2016]. In Tab. 6.1, an overview of the entered data from Charrier et al. [2016] and the ILTS results are given. The results show that the analytical tool, the developed python script, came to the same results as given in Charrier et al. [2016] (36.9 to 37.2 ± 2 MPa for thick, 43.7 to 43.5 ± 3.3 MPa for thin specimens). The analytical tool was thus validated and could be used in the following of the research study.

Tab. 6.1. *Data of L-beams with unidirectional stacking sequence from Charrier et al. [2016] used for the verification of the analytical tool.*

	Data	[unit]	L-beams		
			thick (48 plies)	intermediate (32 plies)	thin (16 plies)
Test setup	l_t	[mm]	53	42	30
	l_b	[mm]	79	74	66
	D	[mm]	15		
Geometric dimensions	t	[mm]	12.58	8.38	4.19
	w	[mm]	60	40	20
	r_i	[mm]	12	8	4
	ϕ	[°]	45		
Material properties	E_θ	[GPa]	115		
	E_r	[GPa]	8.4		
Experimental results	F_f	[N]	10972	3349	488
	d_f	[mm]	2.1	2.3	2.0
Charrier et al. [2016]	ILTS	[MPa]	37.2 ± 2	Not reported	43.7 ± 3.3
Analytical tool	ILTS	[MPa]	36.9	37.9	43.5

6.2 Presentation of the experimental tool EXP

The experimental tool consisted in the design of the 4PB test setup and the applied instrumentation on the L-beam specimen during the experimental test procedure. Below, the design of the test setup for testing L-beam specimens in 4PB as well as the presentation of the applied instrumentation are given.

6.2.1 Design of the test setup

A test setup for testing L-beams in 4PB, basing on the thesis of Charrier [2013] and the standard ASTM D6415 / D6415M-06a [2013], was developed[1].
Objectives that had to be fulfilled by the test setup were noted in the scope statement:

1. Meet the standard ASTM D6415 / D6415M-06a [2013] as best as possible.
2. Fixed centre-to-centre distance, no possible change in the distance between the upper and lower loading bars.
3. Possibility to apply the instrumentation listed below to compare the results obtained:
    - Strain gauge in the thickness,
    - Positioning of a LVDT,
    - 3D DIC (Aramis, GOM),
    - AE system.
4. The test setup should be designed for an ILTS of at least 100 MPa.
5. The contact between the loading bars and the L-beam specimen should be at the same position as given in the standard ASTM D6415 / D6415M-06a [2013].
6. The testing of L-beam specimens of different sizes should be possible:
    - Maximum width $w = 60\,\text{mm}$, minimum width $w = 25\,\text{mm}$,
    - Maximum thickness $t = 12.5\,\text{mm}$, minimum thickness $t = 2\,\text{mm}$,
    - Length $L = 90\,\text{mm}$.

In order to reach these objectives, the test setup was designed in terms of geometrical, mechanical and technological aspects. In the following, these aspects will be explained in more detail.

6.2.1.1 Geometrical and mechanical design of 4PB test setup

The standard ASTM D6415 / D6415M-06a [2013] gives a few specifications on how the 4PB test setup should be designed. The distances between the loading bar centres, $l_b = 100 \pm 2\,\text{mm}$ and $l_t = 75 \pm 2\,\text{mm}$, are given, as well as the diameter D of the loading bars which should be between 6 and 10 mm. The cylindrical loading bars should be

---

[1] Thanks to the Master 2 students for their help in designing the test setup.

mounted on roller bearings.

Since in the scope of this study the 4PB test setup should allow an ILTS up to 100 MPa for the given maximum sample size (w = 60 mm, t = 12.5 mm), the design of the test setup had to be adapted to that given in the standard [ASTM D6415 / D6415M-06a, 2013]. Indeed, although the diameter and distances between the loading bar centres were changed, the horizontal distances between the lower and upper contact points of the L-beam specimen and the loading bars, e_b and e_t, see Fig. 6.2, remained the same. According to ASTM D6415 / D6415M-06a [2013], e_b and e_t are, for a given l_b, l_t and D:

$$e_t = l_t - 2\cos(\Phi) \cdot D = 75 \pm 2\,\text{mm} - 2\cos(45) \cdot 3 = 70.8\,\text{mm for D} = 6\,\text{mm}, \tag{6.12}$$

$$e_t = l_t - 2\cos(\Phi) \cdot D = 75 \pm 2\,\text{mm} - 2\cos(45) \cdot 5 = 67.9\,\text{mm for D} = 10\,\text{mm}, \tag{6.13}$$

and

$$e_b = l_b + 2\cos(\Phi) \cdot D = 100 \pm 2\,\text{mm} + 2\cos(45) \cdot 3 = 104\,\text{mm for D} = 6\,\text{mm}, \tag{6.14}$$

$$e_b = l_b + 2\cos(\Phi) \cdot D = 100 \pm 2\,\text{mm} + 2\cos(45) \cdot 5 = 107\,\text{mm for D} = 10\,\text{mm}. \tag{6.15}$$

According to ASTM D6415 / D6415M-06a [2013], e_t should thus be in the range of 67.9 and 70.8 mm, and e_b in the range of 104 to 107.0 mm. For an ILTS of 100 MPa, the test setup was thus designed, taking into account e_b and e_t.

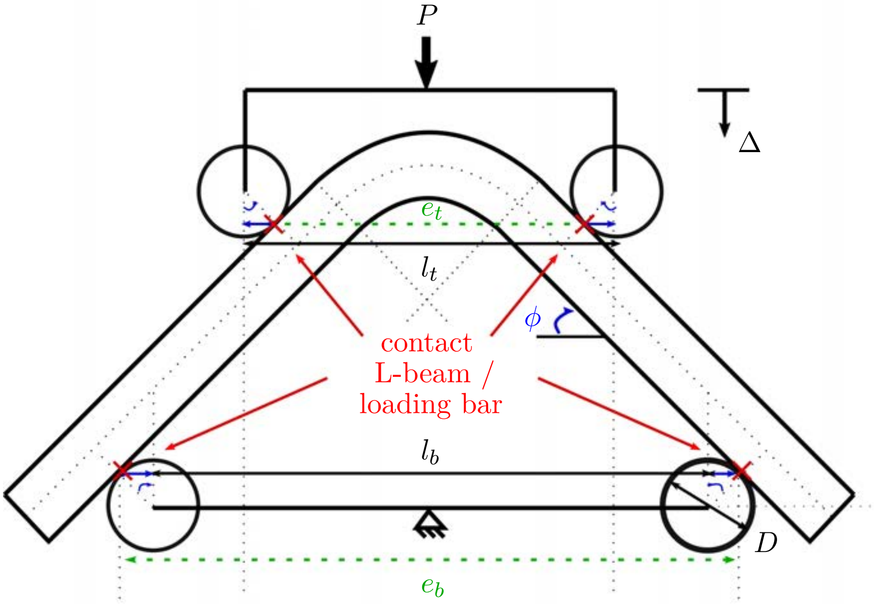

Fig. 6.2. *e_t and e_b represent the upper and lower horizontal distances of the contact points of the L-beam specimen and the loading bars, calculated from l_t, l_b and D, given in ASTM D6415 / D6415M-06a [2013]. Δ represents the vertical stroke displacement of the tensile machine, ϕ the angle between the horizontal line and the specimen's legs, and P the force acting on the lower loading bars. In the scope of this study, the 4PB test setup was dimensioned on the basis of e_t and e_b in order to permit an ILTS up to* 100 MPa.

Further, the dimension of the diameter of the loading bars D had to be defined. For this purpose, the maximum force acting on one lower loading bar had to be determined

analytically, first. The value $F_{lbar} = 21\,390\,\mathrm{N}$ was calculated for an ILTS of 100 MPa. This value was verified numerically.
Second, the bending moment had to be determined for a lower loading bar length L_{lbar} of 125 mm, previously defined, and for a force F_{lbar} as concentrated load:

$$M = \frac{F_{lbar} L_{lbar}}{4} \cdot \tag{6.16}$$

Third, the maximum stress acting on one lower loading bar σ_{lbar} was calculated through

$$\sigma_{lbar} = \frac{M_{lbar} D_{inf}}{2} \frac{1}{I}, \tag{6.17}$$

where D_{inf} is the diameter, and I the geometrical moment of inertia of one lower loading bar

$$I = \frac{\pi D^4}{64} \cdot \tag{6.18}$$

The material of the loading bars was a APX4 high-alloy stainless steel which is used in the aeronautical sector. This choice was taken since a high elastic material strength for the loading bars was required. In the case of APX4, the yield point was about 1000 MPa. By applying a safety factor of S = 1.5, σ_{lbar} had thus not to exceed

$$\frac{1000\,\mathrm{MPa}}{1.5} = 667\,\mathrm{MPa} \cdot \tag{6.19}$$

For $D_{inf} = 22\,\mathrm{mm}$, the maximum stress σ_{lbar} resulted in 639 MPa, hence $\leq 667\,\mathrm{MPa}$. $D_{inf} = 22\,\mathrm{mm}$ was thus the smallest possible diameter of the lower loading bars supporting the required load.
In contrast to the recommended distance between the centrelines of the lower loading bars $l_b = 100 \pm 2\,\mathrm{mm}$, given in the standard [ASTM D6415 / D6415M-06a, 2013], the distance was adapted by taking into account the previously calculated diameter D for the lower loading bars and by defining $e'_b = 107\,\mathrm{mm}$ (Equ. 6.20):

$$l_{b'} = e_b - 2\cos(45)\,\frac{D_{inf}}{2} = 107\,\mathrm{mm} - 2\cos(45)\;11 = 91.5\,\mathrm{mm} \tag{6.20}$$

Similar approaches have been done for the upper loading bars. Since the length of those was smaller (68 mm), the diameter D_{sup} could be reduced to 18 mm, in order to reduced material costs and test setup volume, while keeping $\sigma_{lbar} = 635\,\mathrm{MPa}$, defining $e'_t = 70\,\mathrm{mm}$, and calculating $l'_t = 82.7\,\mathrm{mm}$. The loading bars were fixed to an upper and a lower spreader as depicted in Fig. 6.3. The spreaders were designed to guarantee a high visibility of the area to be recorded by the DIC and to ensure the correct positioning of the LVDT in

Tab. 6.2. *Overview of the most important geometrical dimensions for the 4PB test setup used in the scope of this research study.*

D_{sup} [mm]	D_{inf} [mm]	l'_t [mm]	l'_b [mm]	e'_t [mm]	e'_b [mm]
18	22	82.7	91.5	70	107

the center of the lower spreader. Further, the design was optimized with regard to the installation of the strain gauges and the cables, as well as the sensors for the AE. The instrumentation applied during the 4PB tests will be presented in more detail in Sec. 6.2.2. Finally, in order to fix the lower spreader to the tension machine, a compression plate with four M5 threaded holes with spacings of 80 mm × 38 mm, on which the lower spreader was fixed with four CHC screws, was required. The upper support was fixed with a M3 screw to an extension component specific to the tension machine.

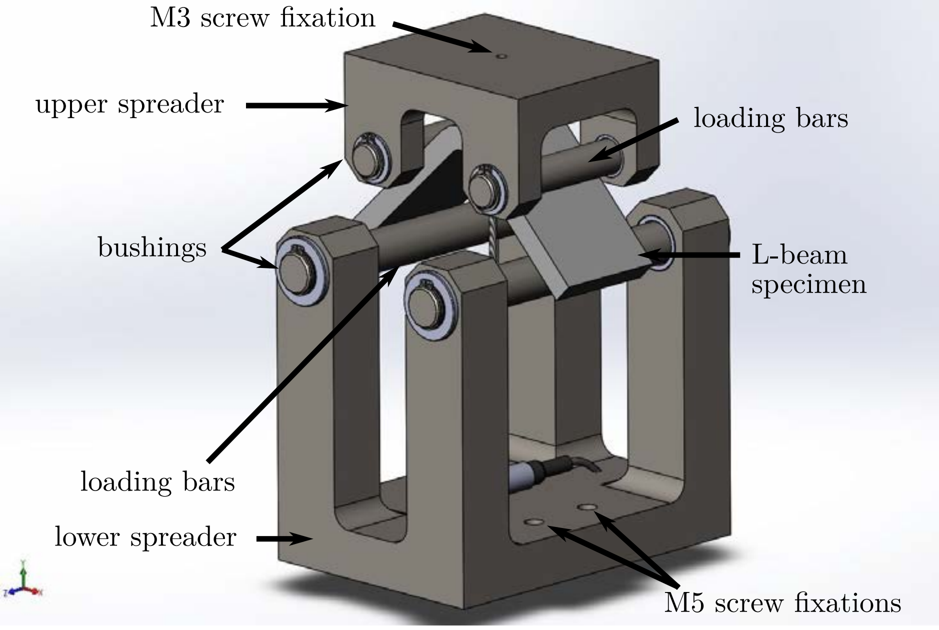

Fig. 6.3. *CAO scheme of 4PB test setup.*

6.2.1.2 Technological design of 4PB test setup

The test setup had to meet several technological functions such as rotation and axial stopping of the loading bars (pivot connection), a regular use of the test setup, and the parallelism of the loading bars.

The design of the pivot connection of the cylindrical loading bars to the upper and lower spreaders was different to that recommended in standard ASTM D6415 / D6415M-06a [2013]. In standard ASTM D6415 / D6415M-06a [2013], roller bearings were used. Since the diameters of the loading bars chosen in this research study were larger than recommended, to allow an ILTS up to 100 MPa, and the material volume of the upper and lower spreaders was kept as low as possible, to ensure the application of the instrumentation, roller bearings could not be used due to their size, and thus, alternatives had to be found to guarantee the pivot connection between the loading bars and the spreaders.

Smaller bearing types such as needle bearings could not be used as these bearings are known to support only axial loads, which therefore did not fulfil the overall function of the test setup.

The technological alternative was thus the use of bushings. A bushing is a fitted ring with or without a flange. They are usually fixed tightly on their outside diameters and the guided shaft is slidably mounted on it. Bearings have the advantage that they can withstand high multi-axial rotating and static loads compared to some standard bearings. They are less suitable for high frequency rotating systems. In the present study, bushings that met the static and dynamic loads, occurring during the 4PB tests, were finally employed.

In order to ensure the coaxiality, the machining of the each spreader was done in a single block. In order to finalize the pivot connection and to ensure that there was no axial load, a stop was made by means of a groove and an elastic ring. Finally, this part of the design did not meet the standard from a technological point of view. However, the rotation function of the bearings was respected by means of the bushings.

To ensure the regular use of the test setup, the upper and lower spreaders were made of steel in order to benefit from the high rigidity compared to the aluminium alloy, from the elastic strength, and from the resistance to impacts. Further, the machining process was well known. Finally, in order to avoid oxidation, the spreaders were treated by blackening.

6.2.2 Experimental test setup and instrumentation

The test setup presented in Sec. 6.2.1 was mounted on different universal testing machines to realize the 4PB tests with a vertical displacement speed of 0.5 $\frac{\text{mm}}{\text{min}}$. The characteristics of those machines are given in Tab. 6.3. The following measuring instruments were installed: (i) a LVDT was placed underneath the curved part of the L-beam specimen in order to measure the effective maximum beam bending displacement, (ii) a 2 mm-mono strain gauge was fixed in radial direction of the curved part of the L-beam, (iii) for the DIC analysis, the zone of interest was sprinkled with white and black spray paint, (iv) AE sensors were fixed at a distance of 170 mm along the L-shape. Fig. 6.4 and Fig. 6.5 depict the experimental test setup with instrumentation. Tab. 6.4 shows the designations and sensibilities of the applied instrumentation.

6.3 Presentation of the numerical tool NUM

A FE model was developed in order to calculate the stress fields in the curved segment of the L-beams. For its realisation, the numeric model from Charrier [2013] was taken as guideline. Two python scripts were therefore coded. The relation between both scripts named python.py and abaqus.py are given in Fig. 6.6. The content of each script is explained in the following.

The python.py file was encoded with pure python language with the aim to generate the

Tab. 6.3. *Information about the testing device.*

Information	AFP-02 to 06	AFP-09 and 10	all MAN specimens
Testing machine	Instron 5567	Instron 8803	Instron 8803
Load cell	30 kN	50 kN	500 kN
Software	BlueHill	Wavematrix	Wavematrix
Loading type	Compression		
Loading rate	0.5 $\frac{\text{mm}}{\text{min}}$		
Testing type	4PB		

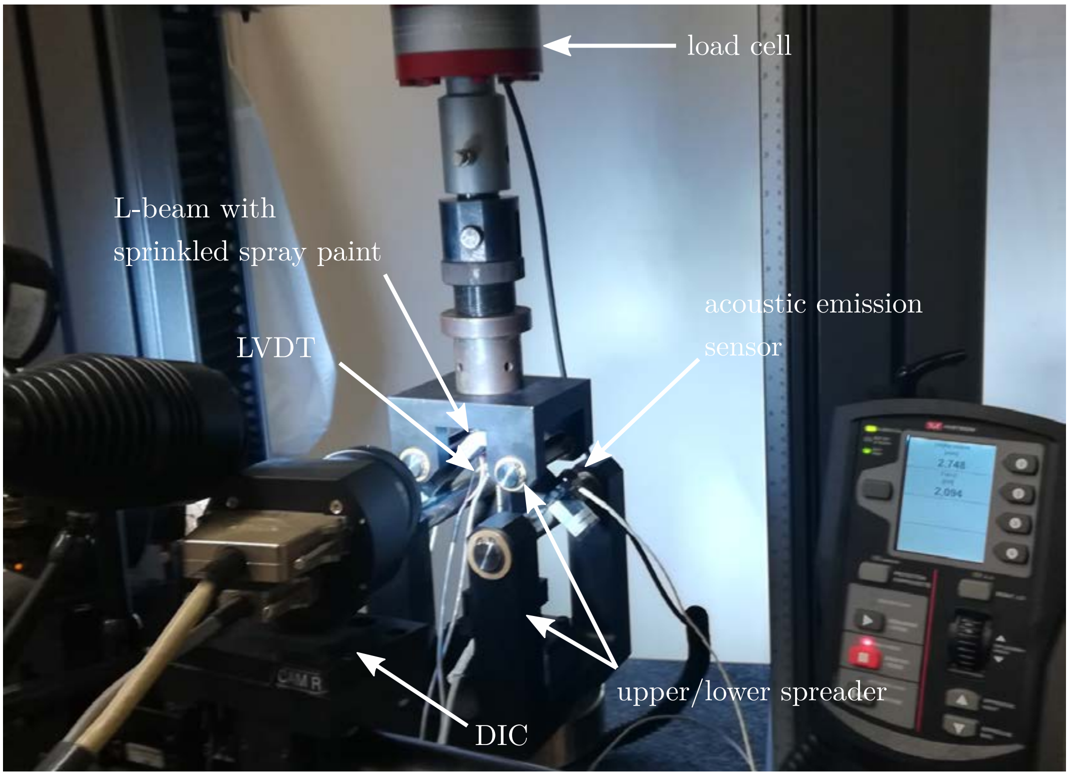

Fig. 6.4. *Experimental test setup for testing L-beam specimens in 4PB.*

Abaqus mesh of the L-beam in three dimension by writing the corresponding .inp file. The basic modules *numpy*, *sys* and *math*, as well as self-coded modules were used. The module *coords.py* created the .nod file which stored the coordinates of each node in a table. The module *connect.py* listed the connectivities (label and corresponding eight nodes for linear fully integrated elements, type C3D8) of each element in a table and stored it in a .elts file. The *nesets.py* module contained sets of nodes and elements which will serve in the abaqus.py file to define the contact between the loading bars and the L-beam specimen, the ply orientation, a reference surface for direction 3 (out-of-plane direction), as well as the boundary conditions. In contrast to Charrier [2013], whose loading bars were made of steel with isotropic material properties and 6-node linear triangular prism elements (C3D6), the loading bars in this study were assigned to be analytical rigid. The step was carried out with a geometrical non-linear solution (nlgeom ON). Finally, the assembly between the loading bars and the L-beam was created and its definition written in the .inp file. Once the python.py script was encoded, only the parameters that describe the geometry of each L-beam specimen ϕ_i, r_i, w, t, L, the dimensions of the test setup l_t, l_b, D_{inf} and D_{sup}, as well as the number of nodes along the curved segment $nxArc$, along the legs length $nxArm$ and along the width ny, to create the mesh, had to be entered in order to generate the corresponding .inp file for each L-beam specimen.

The abaqus.py file was encoded with abaqus python language. The basic modules *sys*, *abaqus*, *abaqusConstants* and *regionToolset* were used. The abaqus.py file imported the .inp file, previously generated by the python.py file, and created the missing modules such as the step, the material, the boundary conditions and the contact between the loading bars and the L-beam specimen:

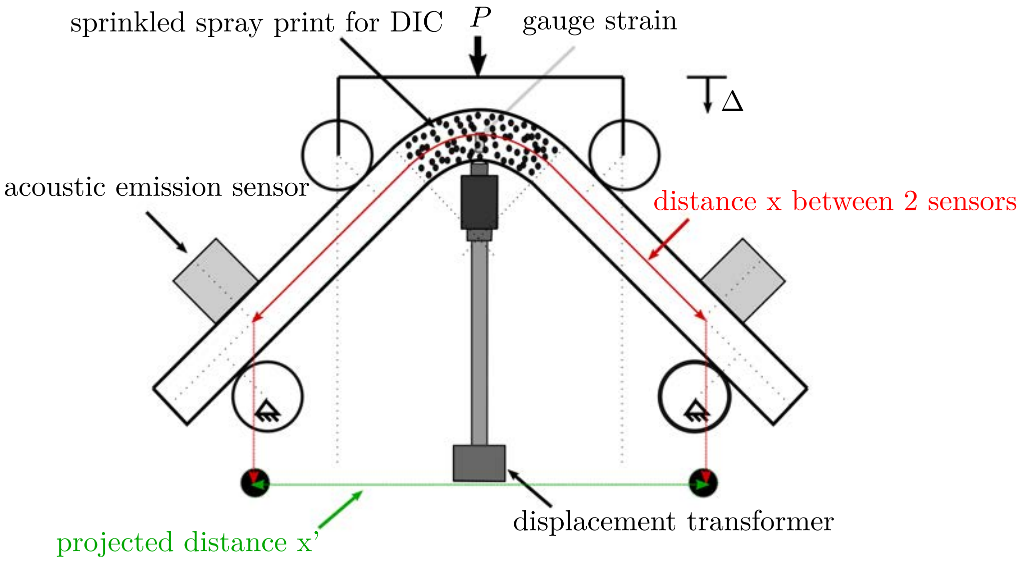

Fig. 6.5. *Schema of applied instrumentation on L-beams tested in 4PB.*

Tab. 6.4. *Characteristics of applied instrumentation*

Strain gauge	KYOWA Model: KFGS-2-120-C1-11 Gage factor: 2.13 ±1% Gage length: 2 mm Gage resistance: 119.8 Ω ± 0.2 %
DIC	Gom Aramis 4M 3D calibration Max. frequency: 7 Hz or 60 Hz Camera lenses: 35 mm/macro
Displacement transformer	Type LVDT HBM WS 20 mm Sensitivity 8.74 mV/V
AE	MISTRAS Sensor type : R15 Signal processing time parameters for composites, non-metallic: PDT: 30, HDT: 150, HLT: 300

The unidirectional plies, 42 in total, were assumed to be transverse isotropic with linear elastic behaviour. The elastic properties are given in Tab. 6.5. As depicted in Fig. 6.7, the load was applied on a reference point RF coupling the movement of both upper loading bars using rigid body constraints to enable via U_z a displacement controlled loading. The movement of the lower loading bars was blocked. The node sets CLX.nset, containing one node in the middle of the curved segment, and CLY.nset, containing two nodes at the and of the L-beam legs, were used to avoid the L-beam to move in x- and y-direction. The friction between L-beam and loading bars was assumed to be zero since the experimental test setup contained bearing bushes which were presumed to minimize friction to a negligible value. Once the abaqus.py script was encoded, only the elastic parameters and the vertical displacement had to be entered manually to generate each individual L-beam specimen. The calculation could then be launched.

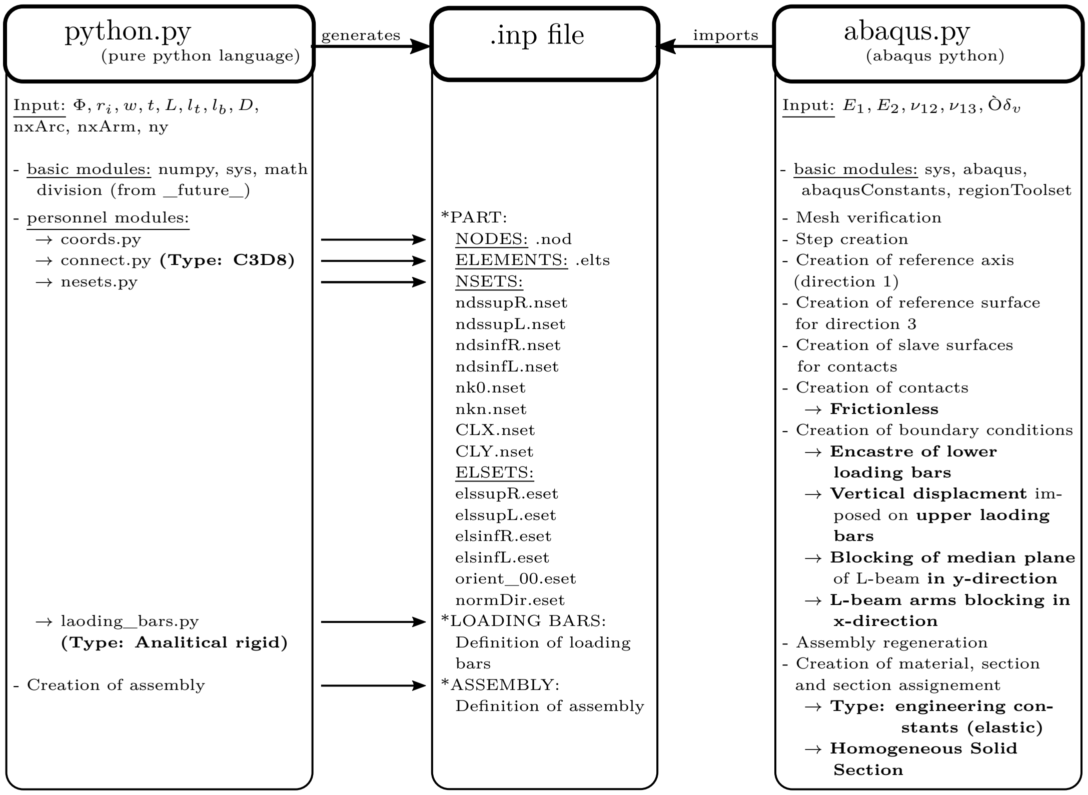

Fig. 6.6. *Scheme describing the interaction between the python.py and the abaqus.py files to create the FE models of the L-beam specimens.*

Before using the FE model, it had to be validated, first. The procedure for the validation is demonstrated in the following Sec. 6.3.1.

6.3.1 Validation of the numerical tool

In order to validate the python.py and the abaqus.py scripts with which the FE models in the present study were generated, the data from the research work of Charrier et al. [2016] were, as already done for the analytical tool in Sec. 6.1.1, taken and entered into both python scripts. In order to build up the thick (48 plies), intermediate-thick (32 plies) and thin (16 plies) specimens of Charrier et al. [2016], the data given in Tab. 6.1 were taken and completed by the data listed in Tab. 6.6, available in Charrier et al. [2016]. The calculations in Charrier et al. [2016] were carried out using a displacement controlled loading. The maximum out-of-plane stress S_{33} was then determined at the experimental load at failure and compared to those given in Charrier et al. [2016].

Tab. 6.6 shows the results of the maximum S_{33}, calculated by the numerical tool for the three specimen thicknesses, and the results given in Charrier et al. [2016]. The numerical tool, the python.py and the abaqus.py scripts, represented well the numerical calcula-

Tab. 6.5. *Elastic properties of one unidirectional ply used to create the FE models.*

$E1$ $[MPa]$	$E2$ $[MPa]$	$E3$ $[MPa]$	ν_{12}	ν_{23}	G_{12} $[MPa]$	G_{23} $[MPa]$
160000	8000	8000	0.3	0.3	4000	3077

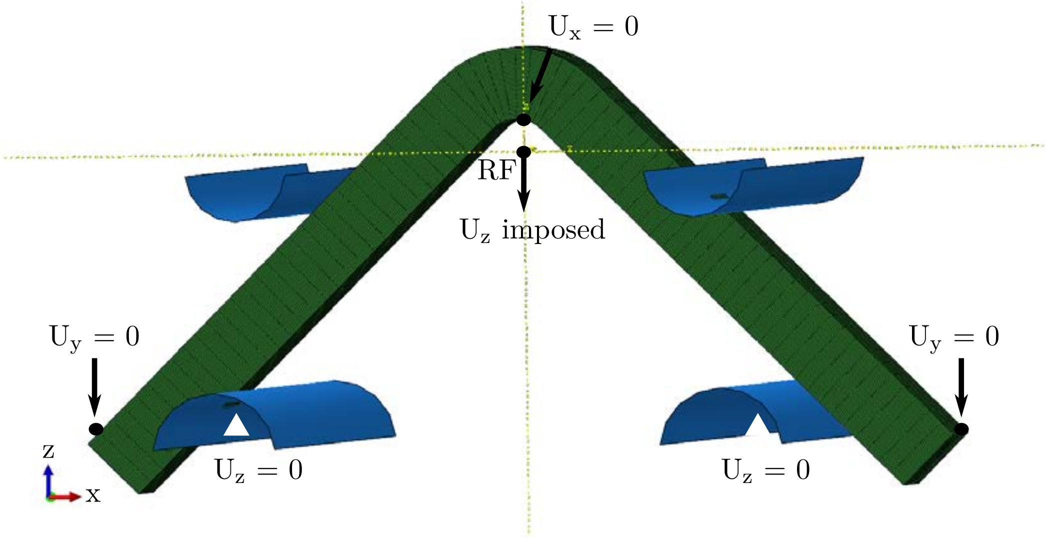

Fig. 6.7. *Boundary conditions and applied load for L-beams tested in 4PB. The load was applied on the reference point RF in U_z direction (displacement controlled loading).*

tions of Charrier et al. [2016] for thin L-beam specimens (47.5 MPa compared to 46.4 ± 2.6 MPa). For specimens with 32 plies, the S_{33} was not reported in Charrier et al. [2016]. For thick L-beam specimens the response of the numerical tool was slightly higher (0.7 MPa) as the upper born of the S_{33} given by Charrier et al. [2016] (38.7 ± 2.2 MPa = 40.9 MPa). Since this was merely slightly higher and the calculated S_{33} value for thin specimens corresponded to the value calculated by Charrier et al. [2016], the FE model was considered validated and could thus be used in the scope of the present research study.

6.3.2 Sensibility studies on the influence of the mesh and the material choice of the loading bars on the numerical results

Before applying the numerical tool, it was evaluated with regard to the sensitivity of the created mesh and the choice of material of the loading bars (rigid body, loading bars made of steel as applied in Charrier et al. [2016]). The following Sec. 6.3.2.1 and Sec. 6.3.2.2 outline the conducted FE simulations on these issues.

Tab. 6.6. *Data of L-beam specimens with unidirectional stacking sequence from Charrier et al. [2016] used for the verification of the numerical tool.*

	Data	[unit]	L-beams		
			thick (48 plies)	intermediate (32 plies)	thin (16 plies)
Geometric dimensions	L	[mm]	80	72	67
Material properties	G12	[GPa]	4.5		
	ν_{12}	[-]	0.32		
	ν_{23}	[-]	0.4		
Charrier et al. [2016]	S_{33}	[MPa]	38.7 ± 2.2	Not reported	46.4 ± 2.6
Numerical tool	S_{33}	[MPa]	41.6	42.9	47.5

6.3.2.1 Sensibility study on the influence of the mesh on the numerical results

As described in Sec. 6.3, the mesh was defined by the number of nodes along the curved segment $nxArc$, along the legs length $nxArm$ and along the specimen's width ny. In order to investigate the influence of the mesh on the results of the FE simulations, two different mesh configurations, simple and double mesh, have been tested. Tab. 6.7 depicts the number of nodes for each segment (arc, legs length, width), and the total number of elements for each mesh configuration. A L-beam test specimen with a width w of 24.58 mm, a thickness t of 13.11 mm, an inner radius r_i of 6.08 mm, and an angle between the horizontal and the specimen leg ϕ_i of 45 ° was hence modelled with simple and double mesh using the numerical tool. Fig. 6.8 plots the load-displacement curves of both FE simulations. The curves superposed almost totally. For a reaction force of 5000 N or 7000 N, the vertical displacement of the FE model with double mesh differed by 1.5 % or 1.6 % from that with simple mesh, respectively. There was thus only a slight difference in the load-displacement plots between the simple and the double mesh. Since the calculation time for the double mesh amounted to 1 h 20 min and for the simple mesh only to 12 min, FE simulations had been performed with simple mesh in the following of this research study.

Tab. 6.7. *Different mesh configurations for L-beam specimens to investigate the influence on the FE results.*

	$nxArc$	$nxArm$	ny	total C3D8 elements
Simple mesh	12	30	12	29400
Double mesh	24	60	24	131208

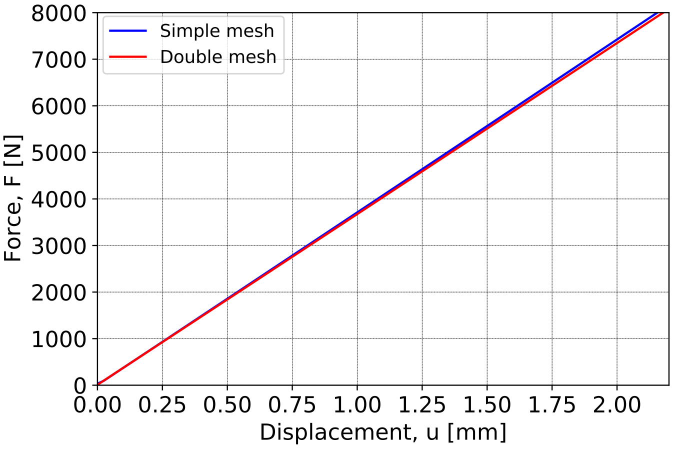

Fig. 6.8. *Comparison of the load-displacement plots of a L-beam specimen modelled with two different mesh configurations.*

6.3.2.2 Sensibility study on the influence of the material chose for the loading bars on the numerical results

In order to investigate the influence of the material of the loading bars on the results of the FE simulations, loading bars as rigid bodies were compared to loading bars with steel material properties. In order to realize this, the loading bars of the L-beam test specimen with simple mesh, modelled in Sec. 6.3.2.1, were manually replaced by loading bars with steel material properties ($E_{steel} = 210\,000\,\text{MPa}$, $\nu_{steel} = 0.3$) and with an isotropic, linear elastic material behaviour with reduced integration (type C3D8R). Contacts between loading bars and L-beam specimen as well as boundary conditions remained unchanged. The resulting load-displacement diagram is given in Fig. 6.9. No difference in the results could be observed. The load-displacement curves superposed totally. Hereinafter, the FE models of L-beam specimens made by hand lay-up and by AFP technology were be modelled with the numerical tool, presented in Sec. 6.3, containing rigid body loading bars.

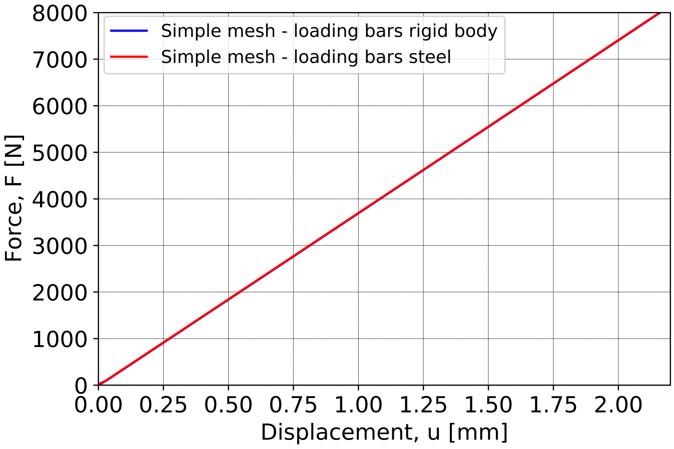

Fig. 6.9. *Comparison of the load-displacement diagrams of a L-beam specimen tested in 4PB with rigid body loading bars and loading bars with steel material properties.*

6.4 Summary of the present Ch. 6

In this chapter, the experimental, analytical and numerical tool for the determination of the ILTS of unidirectional carbon reinforced L-beam specimens were presented in Sec. 6.1, Sec. 6.2 and Sec. 6.3. The analytical and numerical tool were further validated in Sec. 6.1.1 and Sec. 6.3.1 by calculating analytically the ILTS of the L-beam specimens from Charrier et al. [2016], by modelling the same L-beam specimens numerically and by comparing the results with those given in Charrier et al. [2016].

In the following Ch. 7, the three tools will now be applied on L-beam specimens manufactured by AFP technology. The material will be first presented, followed by the presentation of the fabrication process. The experimental procedure will then be described. Finally, the experimental, numerical and analytical results will be presented in detail.

7

4PB study on L-beam specimens manufactured by AFP technology

Contents

In the present Ch. 7, 4PB tests on unidirectional carbon fibre reinforced L-beam specimens fabricated by automated fibre placement (AFP) will be carried out using the experimental tool presented in Sec. 6.2. The material used and the fabrication process applied will be therefore presented in Sec. 7.1. This will be followed by a detailed protocol of the 4PB test realisation and a presentation of the applied instrumentation in Sec. 7.2. Finally, in Sec. 7.3, the results of the 4PB tests will be presented. The analysis will be focused on the reproducibility of the 4PB tests, the exact localization of the first failure cracks, the influence of the specimen thickness on the stiffness, the answer to the question why load-displacement curves are not linear at the test beginning and why the analytically estimated ILTS using Kedward et al.'s solution fits better the calculated out-of-plane strength S_{33}, and last, whether Lekhnitskii's solution for estimating analytically the localization of the ILTS can be used to accurately detect the experimentally observed first failure cracks of the AFP L-beam specimens.

7.1 Material properties and fabrication process of AFP L-beam specimens

The material used for the AFP L-beam specimens came from a 400 mm wide prepreg roll. In order to be laid-up by a C1-Coriolis Composites AFP robot, the prepreg was cut into 6.35±0.125 mm wide strips. Several strips laid-up side by side formed thus one ply. The prepreg batch, hence equivalent to one laid-up ply, was composed of an epoxy matrix Se84LV from Gurit, and of carbon fibres with intermediate modulus IM2C from Hexcel. The elastic modulus of the matrix, 3.8 GPa, was obtained from tensile tests on the pure resin, as described in Mechin et al. [2019]. The elastic modulus of the carbon fibres was 296 GPa. The prepreg batch had a 34.42 % resin weight content (product weight of 459.75 $\frac{\mathrm{g}}{\mathrm{m}^2}$) and a fibre weight of 301.5 $\frac{\mathrm{g}}{\mathrm{m}^2}$. The estimated volume fraction of the fibres was 56.6 %, the mean ply thickness before autoclave curing 307 µm, and the longitudinal tensile modulus (rule of mixtures) 169.2 GPa, respectively.

In the following, the fabrication process of the AFP L-beam specimens will be considered in more detail.

7.1.1 Stacking generation and autoclave curing

The manufacturing process of the L-beam specimens was carried out by engineers and technicians from AvelRobotics. As mentioned above, the prepreg material underwent first an additional operation permitting the processing with the C1-Coriolis Composites AFP robot. The CAD programme of the AFP lay-up process was performed on CATIA and the meshes were made using Rhino. The stacking scheme of the AFP L-beam specimens consisted of 42·[0°] plies. Fig. 7.1 illustrates the CAO model indicating the 0°-fibre-direction. The 42 plies were distributed over four surfaces (10/10/10/12). The surfaces were correctly projected on top of each other using the CATIA VS CADFIber export tool from Coriolis. The mesh in the curved part of the panel was finer than in the panel legs. The contours of the plies were automatically created in the CAD programme to avoid staircases at the edges of the panel.

The plies were laid-up on an aluminium mould in a one-shot sequence. Fig. 7.2 shows the lay-up process of the AFP panel. Before the plies were laid-up with a compaction force of the robot head of 5 bar, also referred to as the lay-up contact pressure, they were heated

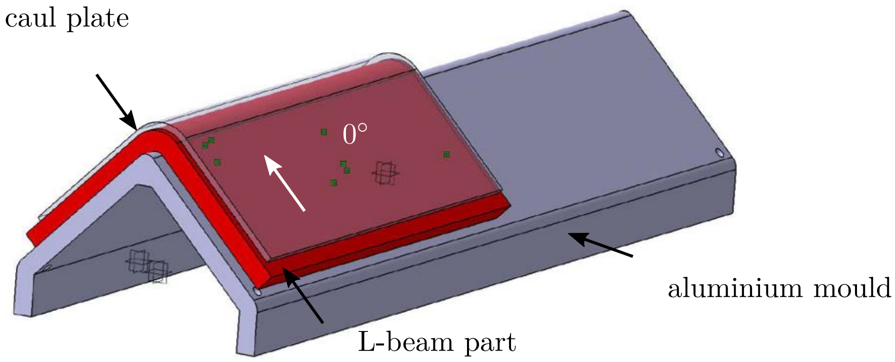

Fig. 7.1. *CAO of L-beam panel fabricated by AFP technology.*

to 35-45 °C. This was assumed to guarantee sufficient adhesion between the plies, so that intermediate debulking was not applied. A polycarbonate (PC) caul plate was then applied on the AFP panel. Two thermocouples were fixed close to the mould and close to the caul plate side. During autoclave curing, the prepreg panel was monitored. No exothermic reaction was detected. The maximum pressure and temperature were respectively 7 bars and 120 °C. The weight of the panel before and after autoclave curing was 1244 g and 1242 g, respectively. The thicknesses of the panel before autoclave curing, measured by a calliper, were between 12.0 mm and 13.3 mm. These measurements were taken on the panel's arms as the calliper was to small to access the curved segment. The thicknesses after autoclave curing, measured using *ImageJ*, are given in Tab. 7.1. In the following, the thickness measurement procedure with *ImageJ* and the test realisation will be presented in more detail.

Fig. 7.2. *Manufacturing of AFP L-beam panel. Lay-up time 1h05min.*

7.2 Test realisation of AFP L-beam specimens

In this study, seven specimens produced by AFP technology were tested in 4PB. After receiving the samples from mitre saw cutting, the cross sections (front and back side) of each specimen were drawn on a sheet. The latter was then scanned, in order to measured the specimen thicknesses at 18 different measuring points with the mean of *ImageJ*. Thus, the maximum and minimum thicknesses and the mean thickness of each L-beam could be determined. A schema of the measuring sections is given in Fig. 7.3. In *ImageJ*, the scale was set to 118 px/cm, corresponding to an accuracy of 1 px per 0.085 mm. Using the same setting, the inner radii were then measured selecting the tool *fit circle* in *ImageJ*. The mean width was determined from at least seven measuring points along the L-beam specimens. This was done using a calliper. Tab. 7.1 lists the geometric dimensions of the AFP L-beam specimens prior to testing.

The strain gauges were then fixed at one third from the inner radius in thickness direction in the curved segment of the specimens. For this, the surfaces were first roughened with fine-grained abrasive paper to ensure a higher adhesion of the gauges, and carefully

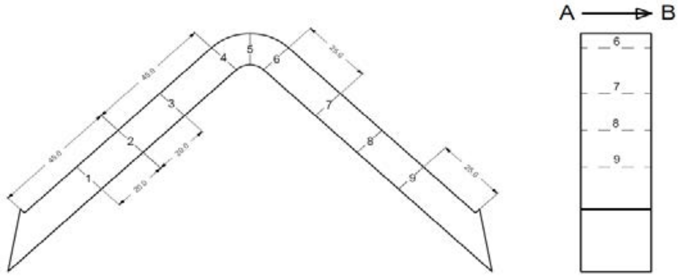

Fig. 7.3. *Schematic depicting $2 \cdot 9 = 18$ measuring points on the front (A) and back (B) side for the determination of the maximum, minimum an mean thicknesses.*

cleaned with acetone. Finally, the strain gauges were degreased and fixed using the products 770 and 406 from *Loctite*. The correct data recording of the LVDT was verified by a Mitutoyo micrometer, previously. The LVDT was then positioned in the center of the lower spreader and mounted using a 3D printed plastic support. White and black spray paint where applied on the front side of the specimens that were instrumented by DIC. Tab. 7.2 gives an overview of the instrumentation applied on each specimen.

Tab. 7.1. *Metrology of AFP L-beam specimens.*

	N°	w [mm]	t_{max} [mm]	t_{mean} [mm]	t_{min} [mm]	t_{max}-t_{min} [mm]	r_i [mm]	ϕ_i [°]
AFP-	02	24.68	13.07	12.66	12.28	0.79	5.19	45
	03	24.60	13.25	12.74	12.46	0.79	6.05	45
	04	24.70	13.22	12.85	12.53	0.69	6.28	45
	05	24.58	13.66	13.11	12.66	1.0	6.08	45
	06	24.68	13.35	13.04	12.59	0.76	6.28	45
	09	24.74	13.63	13.10	12.72	0.91	6.12	45
	10	24.81	13.34	12.74	12.22	1.12	5.95	45
	Mean value	24.68	13.36	12.89	12.49	0.87	5.99	45
	SD	0.07	0.20	0.18	0.17	0.14	0.35	0
	CV [%]	0.3	1.5	1.4	1.4	16.2	5.8	0

Tab. 7.2. *Overview of applied instrumentation of AFP L-beam specimens.*

	N°	LVDT	Strain gauge	AE	DIC
AFP-	02-06	yes	yes	no	no
	09-10	yes	yes	yes	yes

Due to the availability of the testing machines and the measuring instruments, the experimental procedure was divided into two parts. First, the specimens AFP-02 to 06, then the specimens AFP-09 and AFP-10 were tested using the testing machines presented in Tab. 6.3. The experimental procedure of each specimen was the same:

1. Installing the sample on the lower loading bars, so that the tip of the LVDT coincide as best as possible with the center of the curved segment width.
2. Approach of the upper loading bars to the sample. Noting the pre-load (if applied) and taring the force of the machine's software programme (BlueHill/WaveMatrix).

3. Connecting and verification of the cable of the strain gauge. Verification of the gage factor in the acquisition programme. Modification, if necessary.

4. Connecting and verification of the cable of the LVDT.

5. If AE applied: Installation of the sensors.

6. If DIC applied: Performing a simple start/stop measuring mode to ensure the correct detection of the black and white pattern.

7. Taking photo of the L-beam specimen prior to testing.

8. Test realisation: Launching the recording of AE and DIC, if applied. Starting 4PB method programmed in the machine's software programme (BlueHill/WaveMatrix).

9. Test completion after first failure drop. Stopping recording of applied instrumentation.

10. Taking photo after test completion. Making notes, if necessary. Remove tested specimen.

This test procedure was hence applied to each AFP L-beam specimen. In the following section, the results of the 4PB tests will be discussed.

7.3 Results of AFP L-beam specimens tested in 4PB

In this section, the results of the AFP L-beam specimens tested in 4PB will be presented. In Sec. 7.3.1, the results of the experimental part will be shown, first. Plots of load-displacement diagrams, results of the AE data and crack locations will be considered within this section. Then, the results of the FE calculations will be discussed in Sec. 7.3.2. Finally, the ILTS estimated using the analytical tool will be presented in Sec. 7.3.3 and compared to those calculated by the FE model.

7.3.1 Experimental results of AFP L-beam specimens tested in 4PB

7.3.1.1 Reproducibility and stiffness

Seven specimens manufactured by AFP technology were tested in 4PB. The experimental procedure of each specimen was according to the protocol presented in Sec. 7.2.
The mean load at failure amounted to 6661 ± 427 N with a Coefficient of variation (CV) of 15.6 %. The reader is referred to Tab. B.1 to access the individual failure loads of each AFP specimen.
In Fig. 7.4, the load-displacement curves of the AFP L-beam specimens are plotted. It can be observed that with exception of specimen AFP-10 the curves superpose almost perfectly. The unusual test behaviour of L-beam specimen AFP-10 is assumed to be due to an incorrect positioning of the LVDT.

The non-linearity that is observed between a vertical displacement of 0 and approximately

0.5 mm was investigated by applying linear regressions between different loading ranges as given in Tab. 7.3. First, the mean stiffness, the SD and the $CV_{N°}$ of each linear regression, denominated N°1, N°2 and N°3, were calculated. Then, the deviations in % of linear regression N°2 and N°3 were calculated with regard to linear regression N°1 which was supposed to be the reference one.

It was found that within the linear regressions N°1 and N°2, the $CV_{N°}$ was small (2.8 % and 1.5 % for N°1 and N°2, respectively) and slightly higher for linear regression N°3 (6.5 %). Further, the mean stiffness of linear regression N°2 (3.5 %) differed only less from the reference value. The stiffness from 3000 N up to failure of all AFP L-beam specimens was thus assumed to be uniform. The 4PB tests were hence highly reproducible. The non-linearity at test beginning, represented by a high deviation of linear regression N°3 (17.5 %) from the reference range, will be discussed in more detail in Sec. 7.3.2.

Tab. 7.3. *Mean stiffness, SD and $CV_{N°}$ of different loading ranges for AFP L-beam specimens. The percentage deviation of linear regression N°2 is, with regard to N°1, small.*

Linear regression N°	Loading range [N]-[N]	Mean stiffness $[\frac{N}{mm^2}]$	$CV_{N°}$ [%]	Deviation [%]
1 (reference)	5000-6000	3742 ± 104	2.8	0
2	3000-4000	3613 ± 54	1.5	3.5
3	0-1000	3087 ± 201	6.5	17.5

The reproducibility oft the 4PB thus validate the experimental test setup presented in Sec. 6.2. Due to the well superposition of the load-displacement plots, the results of specimen AFP-09 are presented, representatively for all AFP specimens, in more detail below. For results of the remaining AFP L-beam specimens, the reader is referred to the annex Sec. B.3.

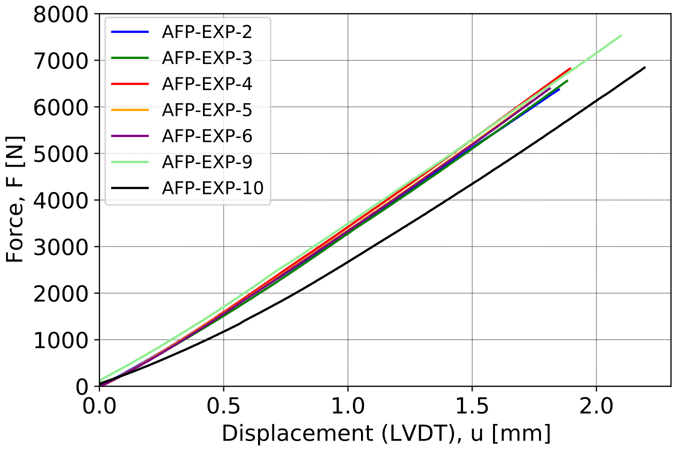

Fig. 7.4. *Load-displacement curves of AFP L-beam specimens tested in 4PB show a high reproducibility with a uniform stiffness from 3000 N up to failure. The experimental test setup is thus validated.*

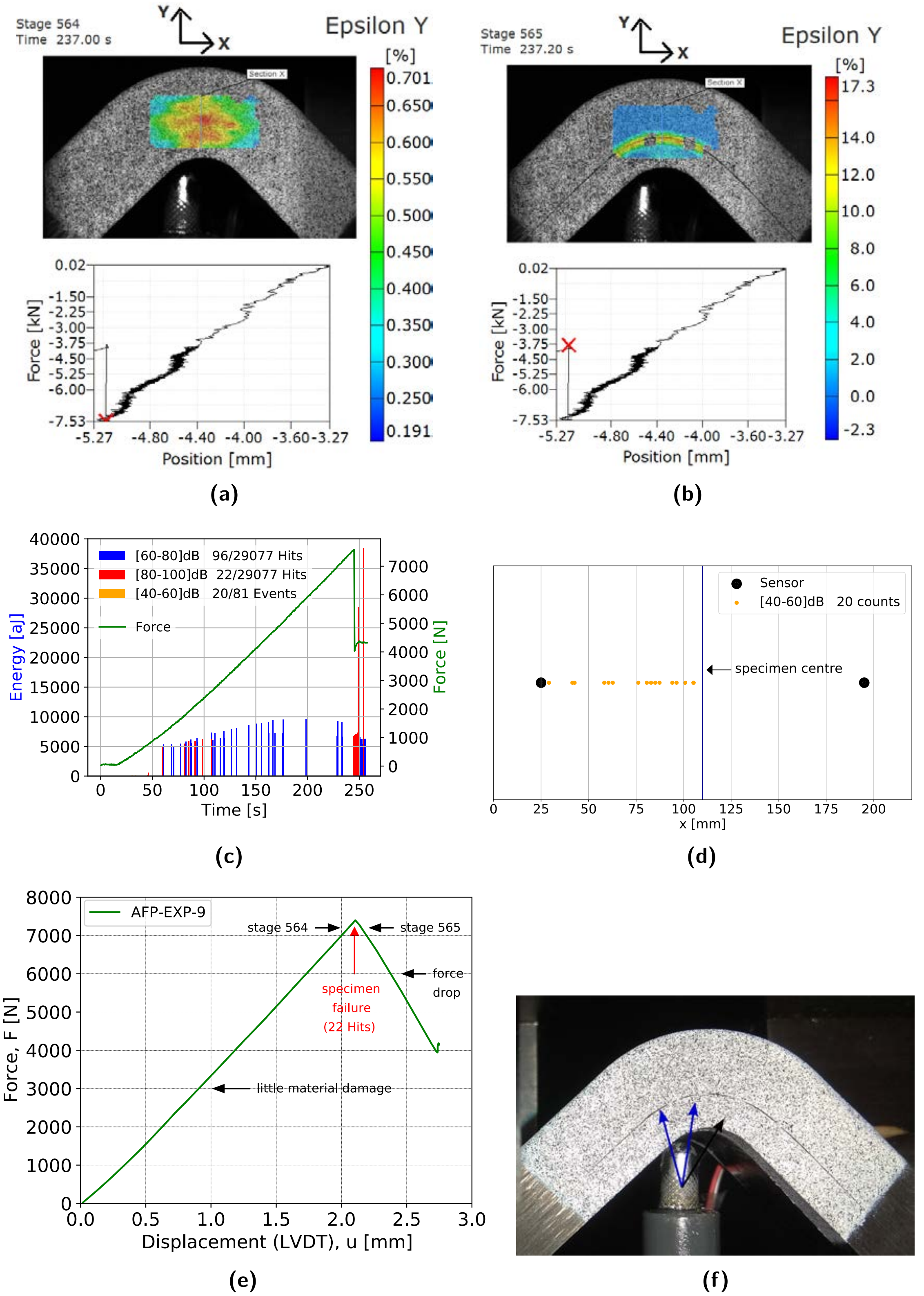

Fig. 7.5. *DIC images of L-beam specimen AFP-09 (a) prior to failure and (b) just after first failure crack. (c) Energy of hits and events, and the load as a function of the time. (d) Location of the events between the sensors. (e) Load-displacement diagram (LVDT) with force drop, and (f) the first failure crack formation indicated by blue arrows.*

7.3.1.2 First failure cracks

Photos of the cracks were taken from the front side (sprinkled face) and the back side (untouched side) of the AFP L-beam specimens after test completion. Tab. 7.4 lists which of the faces of each specimen were photographed and how many cracks in total are shown. First failure cracks of specimen AFP-09 were first determined using the DIC image given in Fig. 7.5b. They are identified in Fig. 7.5f by blue arrows. It was assumed that the longest crack formation corresponded to the first failure crack. This assumption was further based on correlations between the load-displacement diagrams, the strain gauge signals, and the acoustic emission locations. The DIC image of AFP-09 thus shows that the specimen failed approximately at one third from the inner radius. Similar observations were done by Charrier [2013] and Ranz et al. [2017] whose crack localisations of L-beams of 12.48 mm and 9.9 mm thicknesses, respectively, were detected at one third from the inner radius.

Using images taken with an optical microscope from the face where the strain gauge was fixed (see for instance Fig. 7.6), and the photos taken after test completion (Fig. 7.5f), fractured interfaces and plies were identified preciously. They are listed in Tab. 7.4. Values in bold correspond to the longest crack formations.

For specimen AFP-09, the interface between ply 14 and 15 was thus identified as longest crack formation. This corresponded to a crack location $r_{failure}$ at 0.33 (normalized value over the thickness), measured from the inner radius.

The procedure of identifying preciously the first failure crack locations was applied to all AFP specimens. Photos taken after test completion of the remaining AFP L-beam specimens are given in the annex Sec. B.3.1, the results are summarized in Tab. 7.4.

First failure crack formations for five out of seven AFP specimens were thus primarily located between 0.26 and 0.36 (normalized value over the thickness), measured from the inner radius.

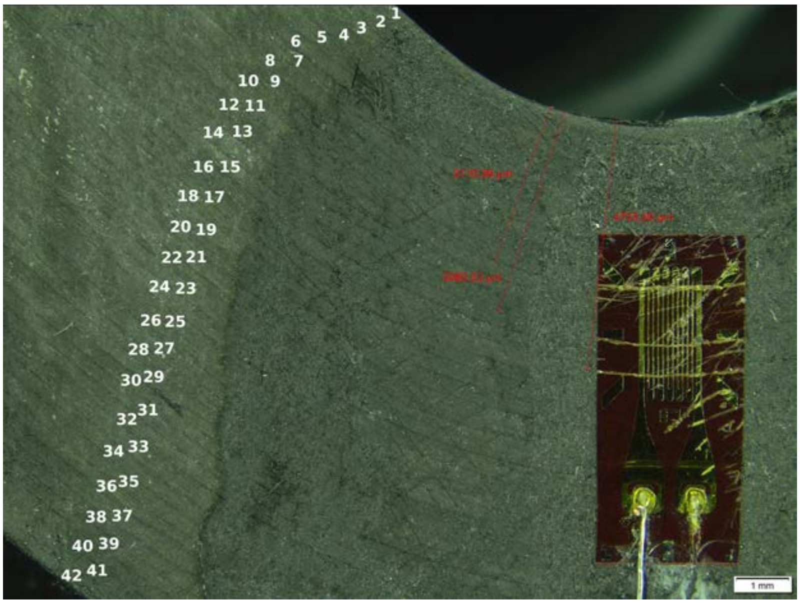

Fig. 7.6. *Typical photo taken with the optical microscope for counting fractured plies and interfaces (photo of specimen AFP-09).*

Tab. 7.4. *Overview of photos taken after test completion and crack localisation of AFP L-beam specimens.*

AFP-N°	PHOTOS		CRACK LOCALISATION		
	sprinkled face	untouched face	How many cracks?	$r_{failure}$[a]	Fractured interfaces/plies[b]
02	no	yes	3	at 0.4, **0.57**	17/18;24;**24/25**
03	no	yes	2	at **0.33, 0.43**	**14/15;18/19**
04	no	yes	6	0.19, **0.36**-0.45	8/9;**15/16/17**;19/20
05	no	yes	1	at **0.17**	**7/8**
06	no	yes	2	at 0.31, **0.33**	13;**13/14/15**
09	yes	no	3	at 0.19, 0.26, **0.33**	8;11/12;**14/15**
10	yes	no	2	at **0.21, 0.26**	**9/10; 11/12**

[a] Normalized distribution over the thickness, calculated from the fractured interfaces/plies. The reference surface is the first ply laid-up on the mould. Values marked in blue correspond to the crack localisation observed on the first image made by the DIC after occurrence of the first force drop.

[b] Counted from the inner radius using an optical microscope. Values written in **bold** correspond to the longest crack formation over the specimen front face.

7.3.1.3 Acoustic emissions (AE)

Further, AE were applied to specimen AFP-09. Fig. 7.5c shows a typical diagram of the energy of the hits and the events, and the load as a function of the time. Fig. 7.5d shows the localisation of the events between the two captors having a distance x along the specimen surface (x' = projected distance, see Fig. 6.5). Events are a particular form of hits. While the location of hits between the sensors cannot be localized, the localisation of events can. The AE system knows the velocity v of the wave with that it pass through the material, as well as the distance x between the two sensors. From that, the time t $= \frac{x}{v}$ a wave takes to travel the distance between the two AE sensors can be calculated. If the first sensor now records a hit and the second sensor records the same hit within a time less than $\frac{x}{v}$, the hit is localized and is identified as an event. Conversely, if the time is greater than $\frac{x}{v}$ the hit cannot be localized, hence it is not an event.

Care was taken when evaluating hits as machine and ambient noises up to 60 dB transmitted sounds to the specimen, which were then erroneously recorded. This was the case when testing the AFP L-beam specimens. Therefore, hits between 40 and 60 dB are not plotted in Fig. 7.5c, but events that appeared during test execution.

Fig. 7.5c thus show the hits and the events of specimen AFP-09 recorded during test execution. The released energy of the events, whose exact localizations are given in Fig. 7.5d, appeared in the time range from 25 to 35 s and amounted maximally to 80 aJ. They are thus not visible in Fig. 7.5c due to the scale. For AFP-09, little material damage with an released energy of maximally 10 000 aJ happened during the experimental procedure and high material damage at specimen failure, represented by hits between 80 and 100 dB.

7.3.1.4 DIC images and strain gauge

Last, Fig. 7.5e shows the load-displacement plot of AFP-09 indicating the DIC stages prior to (stage 564, Fig. 7.5a) and after (stage 565, Fig. 7.5b) specimen failure. The stage number refers to the photos that have been recorded since test begin. The DIC image indicated a maximum radial deformation of 0.7 % prior to failure, corresponding to the value of the strain gauge that amounted to 0.72 %. Despite little material damage that occurred during loading, failure occurred suddenly since a strong force drop was observed. In the following, the results of the numerical tool will be presented.

7.3.2 FE results of AFP L-beam specimens tested in 4PB

Using Abaqus CAE, FE simulations were performed for each L-beam specimen. They were modelled and simulated using the numerical tool presented in section Sec. 6.3. The tool permitted to easily set the different geometrical dimensions (thickness t, width w, inner radius r_i and the angle between the horizontal and the specimen leg ϕ_i, see Tab. 7.1) of each specimen. The mesh (see Sec. 6.3.2.1) with one linear volume element per ply thickness (8 nodes and linear interpolation, 42 plies in total), the material properties (see Tab. 6.5), assumed to be transverse isotropic with linear elastic behaviour, the 0°-orientation of the plies, the diameter of the loading bars and the distances between the vertical centre lines of the lower and upper loading bars (see Tab. 6.2) remained the same for each specimen. The contact between loading bars and L-beams was assumed to be frictionless for all AFP L-beams.

Before considering the results of the FE calculations, the question mentioned in Sec. 7.3.1 concerning the non-linearity of the load-displacement curves at test beginning will be discussed.

7.3.2.1 Non-linearity of load-displacement diagrams

In order to find an explanation to the question, FE simulations on the stiffness of the test setup were performed, first. The results have shown that the assembly was sufficiently rigid and its compliance did not explain the non-linearity at test beginning.

Then, the design of the test setup with its tolerances, the positioning of the L-beam at test beginning and the contact point between L-beam and LVDT tip were considered, next. It was found that the non-linearity at test beginning results from the change in the contact point between L-beam and LVDT tip due to a slight difference in the vertical alignment of the lower loading bars. Until the L-beam finds its loading position (according to ASTM D6415 / D6415M-06a [2013], the test setup permits the L-beam specimen to center itself between the loading bars), the contact point changes.

The misalignment of one lower loading bar was modelled numerically using a random vertical misalignment value of 1 mm, as depicted in Fig. 7.7. The job was conducted using the metrology of specimen AFP-05. The vertical displacement was measured at three different nodes, node 9999 and its neighbour nodes 4001 and 8001, as shown in Fig. 7.8. The transversal displacement (0°-direction) of node 9999 was also calculated. The reference point marked in Fig. 6.7 was chosen as measuring point for the reaction force.

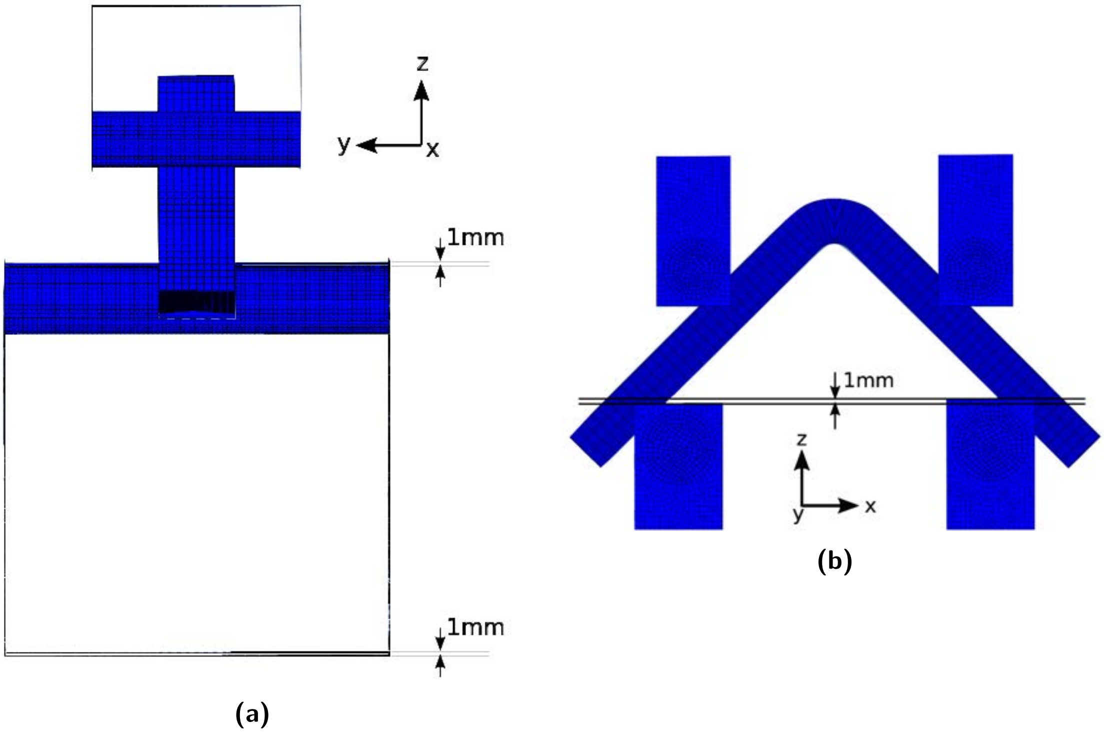

(a)

(b)

Fig. 7.7. *(a) Side and (b) front view of 4PB test setup with the lower left loading bar positioned at* 1 mm *from the horizontal in vertical direction.*

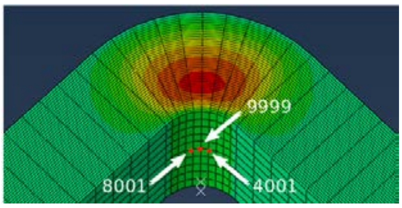

Fig. 7.8. *Three different nodes to plot the load-displacement curves in order to examine their behaviour.*

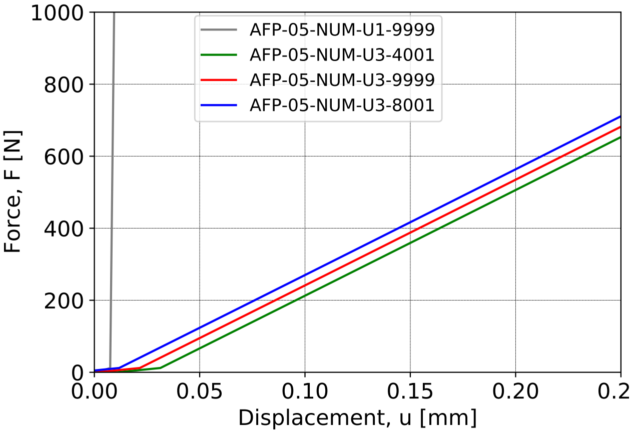

Fig. 7.9. *Load-displacement plots of the nodes 4002, 9999 and 8001 (U1 = circumferential direction, U3 = radial direction).*

The non-linearity at test beginning can thus be explained by the fact that merely a slight vertical misalignment of one lower loading bar may lead to a change in the measuring point at test beginning and hence to the observed non-linearity in the load-displacement diagram until the contact point remains unchanged.
When the contact point hence changes, which means that the measuring system moves from one node to the other, the start of the curves can be reproduced qualitatively and almost quantitatively as given in Fig. 7.9. Further, the transverse displacement of the L-beam (grey curve in Fig. 7.9) shows a slight movement during the simulation.

With this knowledge, the FE calculations on the AFP L-beam specimens had been performed. For this, the ideal case, which means that the contact point between LVDT tip and L-beam specimen stays unchanged, was assumed. Therefore, node 9999 was chosen as measuring point of the vertical displacement. The reference point marked in Fig. 6.7 was taken as measuring point for the reaction force.

In the following the results of the FE calculations with focus on the different specimen thicknesses (t_{max}, t_{mean}, t_{min}) will be given.

7.3.2.2 FE calculations on AFP L-beam specimens

Fig. 7.10 shows a sequential procedure comparing the numerical material response of specimen AFP-05 for the three different specimen thicknesses (t_{max}, t_{mean}, t_{min}) with the experimental stiffness. Fig. 7.10a first shows the experimental load-displacement plot of specimen AFP-05. A linear regression in the range of the load at failure and the load 2000 N prior to failure was added to this plot in Fig. 7.10b. Then, this linear regression was shifted to the origin (0/0), as depicted in Fig. 7.10c. As expected, when considering the numerical curves, an increase in the specimen thickness results in an increase of the material stiffness. This has an impact on the reaction force. The difference between t_{max}

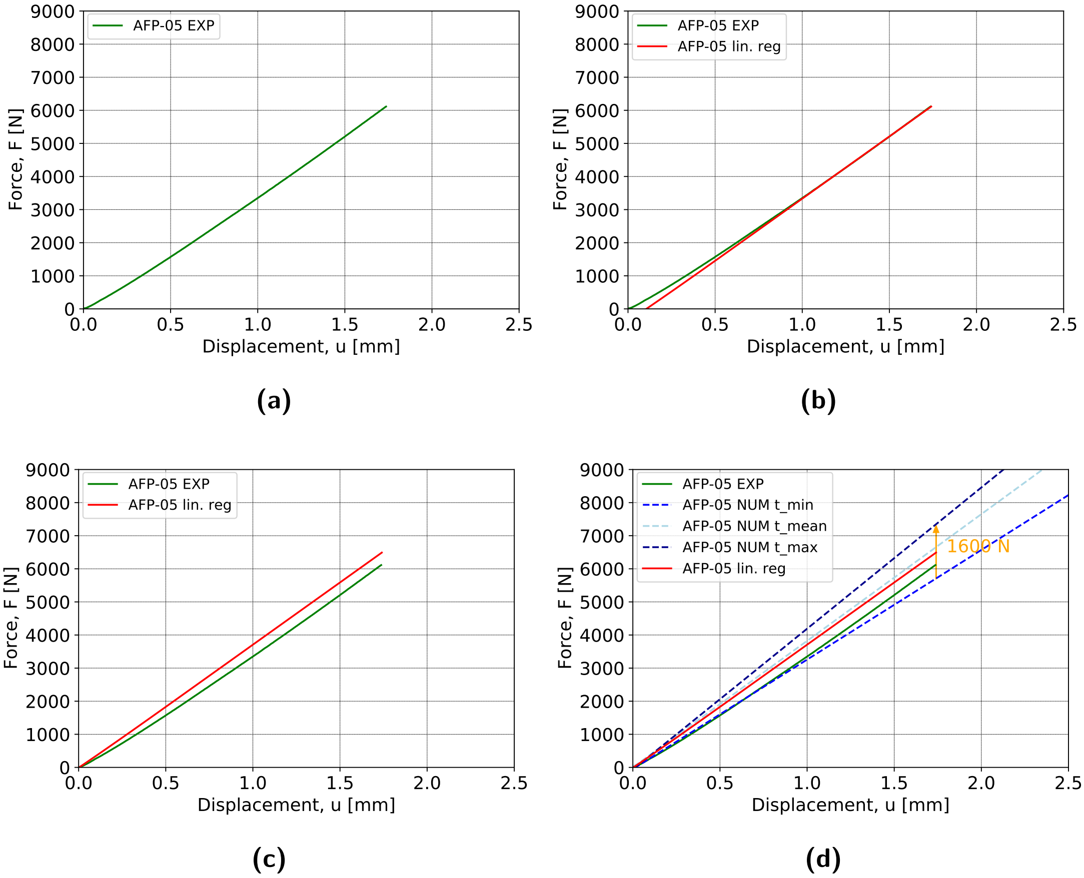

Fig. 7.10. *(a) Experimental load-displacement plots of L-beam specimen AFP-05 with (b) a linear regression in the range of the failure load and the load 2000 N prior to failure. (c) Linear regression shifted to the origin of the plot. (d) Addition of FE simulations calculated from three different specimen thicknesses (t_{max}, t_{mean}, t_{min}). For specimen L-beam AFP-05, the numerical curve with t_{mean} fits well the experimental material stiffness.*

and t_{min} of 1 mm for specimen AFP-05, results in a reaction force up to 1600 N higher at the given experimental displacement at failure. Similar observations were made for all AFP L-beam specimens. Last, it can be noted that for specimen AFP-05, the numerical curve with t_{mean} fits well the experimental material stiffness.

The upper procedure was applied to all AFP L-beam specimens. The load-displacements plots with shifted linear regressions of the remaining AFP L-beam specimens are given in the Sec. B.3.2. It was observed that three linear regressions out of seven were well represented by the numerical curves with t_{max}, three out of seven were between t_{max} and t_{mean} and one out of seven was between t_{mean} and t_{min}.

The normalized stresses S_{ij} along the thickness, in the center of the specimen, as well as along the width at the maximum calculated radial stress $S_{33,max}$ were further investigated.

The maximum strengths of each S_{ij} came from data sources that are commonly used in nautical design offices. They are listed in Tab. 7.5. The measuring paths are given in Fig. 7.11a and Fig. 7.12a. Along the thickness, the path went from the inner to the outer radius. Along the width, the start point was set on one edge for a specimen width $w = 0$, and the finish point to the opposite edge where w equalled the specimen width. The measuring point which both paths had thus in common was hence at r_{max}, at half the specimen width, as marked in Fig. 7.11a and Fig. 7.12a by a white node.

Tab. 7.5. *Maximum tensile and compressive strengths commonly used in nautical design offices.*

		S11	S12	S13	S22	S23	S33
Tensile strength	[MPa]	1500	50	55	35	40	$S_{33,max}$
Compressive strength	[MPa]	-2700			-100		N/A

The 3-, 2- and 1-directions denoted the radial (out-of-plane), the transverse (along the width), as well as the circumferential (0°-) direction, respectively.

The resulting plots for specimen AFP-09 are given in Fig. 7.11b and Fig. 7.12b. To access the plots of all other AFP L-beam specimens, the reader is referred to the annex Sec. B.3.3.

As expected, it was found that the calculated shear stresses S_{12} and S_{13} were practically zero, along the thickness, as well as along the width of the specimen, as this is the principle of 4PB tests: no shearing between the upper loading bars.

Weak shear stresses S_{23} along the width might result from edge effects.

The transverse stress S_{22} is negative when it is towards the inner radius, as $S_{11}>0$ and $S_{33}>0$. At $S_{22}=0$, the Poisson effect generated by the compression through S_{11} compensates the Poisson effect of the traction generated by S_{33} so that $\nu_{12} \cdot \varepsilon_{11} = \nu_{32} \cdot \varepsilon_{33}$. The confidence in this curve is therefore based on confidence in the Poisson coefficients that were entered in the numerical tool (Sec. 6.3).

S_{11} along the thickness is, as expected, positive close to the inner radius and negative at the outer radius. However, the exact evolution of S_{11} along the thickness was difficult to predict. The result is surprising, as it is not linear in the positive range, almost linear in the negative range and the inflection point is close to the specimen center. At this point, this evolution cannot be further explained.

Last, as expected, the radial stress S_{33} is the clearly dominating stress which has its maximum approximately at one third from the inner radius (Fig. 7.11b) and is, except for the edge effects, constant along the width (Fig. 7.12b).

At the common measuring point, at r_{max} and at half the specimen width, the S_{ij} values, along the thickness and the width, are therefore equal. This is depicted by arrows in Fig. 7.11b and Fig. 7.12b.

In the following Sec. 7.3.3 the analytical results of the AFP L-beam specimens will be presented.

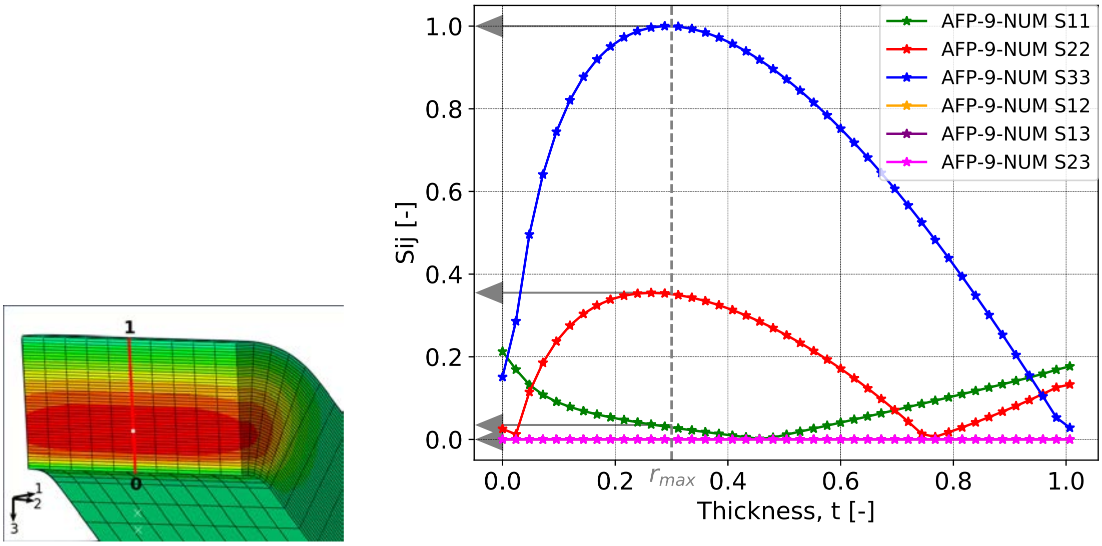

(a) **(b)**

Fig. 7.11. *(a) Node path along the specimen thickness over which the stresses S_{ij} were measured. The white measuring point corresponds to the same measuring point along the width (at r_{max} and at half the specimen width). (b) Normalized stresses S_{ij} as a function of the normalized mean thickness of L-beam specimen AFP-09. Arrows indicate the equal S_{ij} stresses at the common measuring point along the width (Fig. 7.12b).*

7.3.3 Analytical results of AFP L-beam specimens tested in 4PB

In this section, the analytical tool, presented in Sec. 6.1, was applied in order to determine the ILTS which corresponds to the maximum out-of-plane stress occurring in the curved segment of the L-beam specimen. The ILTS may cause the composite to fail by delamination.

The analytical tool consisted in a script encoded with python, validated in Sec. 6.1.1, containing the solutions of Lekhnitskii and Kedward et al. to estimate analytically the ILTS. Further, the solution of Lekhnitskii permitted to calculate the radial position r_{max} of the ILTS.

Below, the ILTS determined through equation Equ. 6.5 and Equ. 6.11 will be compared to the S_{33}, numerically calculated. Further, using Equ. 6.9, the ILTS will be compared to the first failure crack locations, presented in Tab. 7.4.

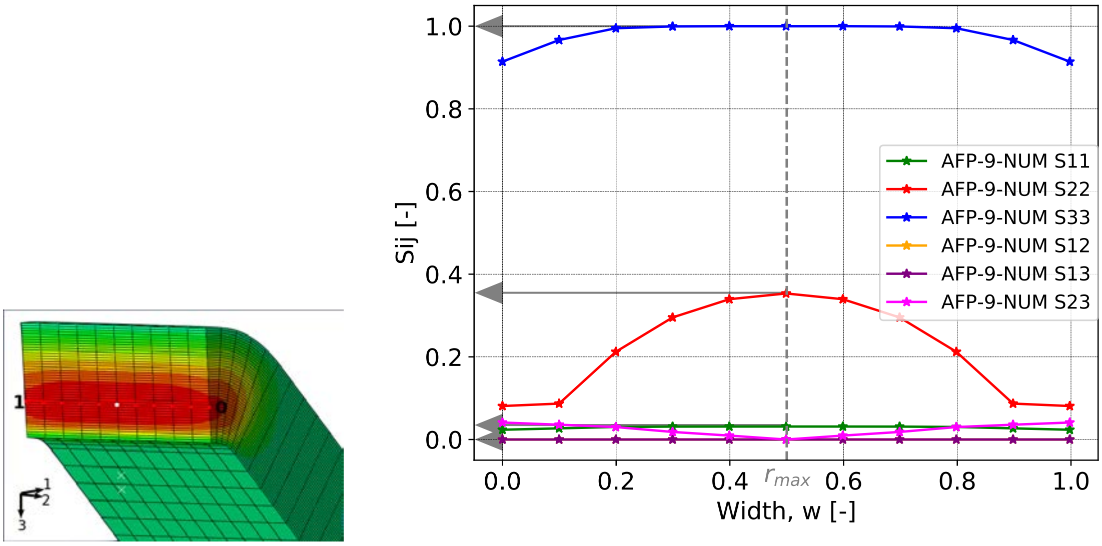

(a) **(b)**

Fig. 7.12. *(a) Node path along the specimen width over which the stresses S_{ij} were measured. The white measuring point corresponds to the same measuring point along the thickness (at r_{max} and at half the specimen width). (b) Normalized stresses S_{ij} as a function of the normalized width of L-beam specimen AFP-09. Arrows indicate the equal S_{ij} stresses at the common measuring point along the thickness (Fig. 7.11b).*

7.3.3.1 Confrontation of $\mathrm{ILTS}_{\text{Kedward et al.}}$ and $\mathrm{ILTS}_{\text{Lekhnitskii}}$ to S_{33}

In order to calculate the ILTS with both solutions, the geometric dimensions given in Tab. 7.1, the elastic moduli in tangential and radial direction, listed in Tab. 6.5 ($E_\theta = E_1$, $E_r = E_2$), as well as the force and the vertical displacement at failure for each specimen were entered into the python script. Taking into account the three different specimen thicknesses (t_{max}, t_{mean}, t_{min}), three calculations with Lekhnitskii's and three calculations with Kedward et al.'s solution were performed for each AFP L-beam specimen.

Below, the results will be described progressively. Complementarily, the reader is informed that Tab. B.1 contains a summary of the recorded experimental data, as well as the analytical and numerical calculations.

Tab. 7.6 shows the ILTS mean values, calculated with Kedward et al.'s and Lekhnitskii's solutions, for the mean values of the three different specimen thicknesses ($t_{min,mean}$, $t_{mean,mean}$, $t_{max,mean}$).

Considering the ILTS mean values calculated using Kedward et al.'s solution, it was found that the results for all specimen mean thicknesses were close to those calculated by the FE (less than 5 %). In comparison, the solution of Lekhnitskii differed between 12 and 15 % from the numerical results.

The better estimation of Kedward et al.'s solution can be explained by replicating Fig. 5.2 with the elastic material properties used in this research study:

Fig. 7.13 depicts the normalized out-of-plane (radial) stresses of the curved L-beam specimens as a function of the degree of anisotropy and of the specimen geometry. Horizontal dashed lines represent Equ. 6.11, solid lines with dots Equ. 6.5 and the triangles the FE

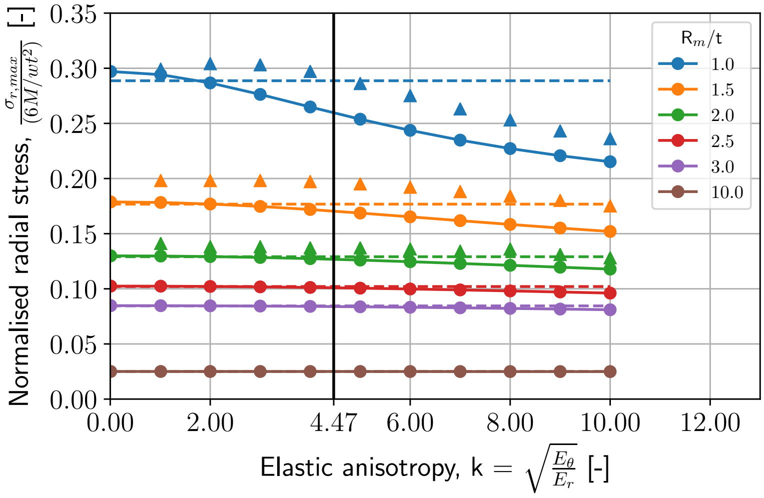

Fig. 7.13. *Normalized stress as a function of the degree of anisotropy and the specimen geometry. Dotted lines represent Kedward et al.'s solution, solid lines with dots Lekhnitskii's solution and the triangles represent the FE calculations. Kedward et al.'s solution is close to the numeric calculation due to the specific elastic properties of the material.*

calculations. Using

$$k = \sqrt{\frac{E_\theta}{E_r}}, \tag{7.1}$$

and the material properties given in Tab. 6.5 (E_θ=E_1, E_r=E_2), the coefficient of anisotropy results in $\kappa = 4.47$. For the geometric dimensions of the AFP L-beam specimens, resulting in $\frac{R_m}{t} = \frac{r_i+r_o}{2t} = 0.99$, Fig. 7.13 thus shows that the ILTS obtained by Kedward et al.'s solution is almost equal to the S_{33}, numerically calculated, and that the solution of Lekhnitskii results in clearly smaller ILTS estimations. Whether the solution of Kedward et al. or Lekhnitskii is closer to the numeric calculation depends hence on the elastic properties of the material.

7.3.3.2 Normalized stresses S_{ij}, $\sigma_{33,Kedw.}$ and $\sigma_{33,Lekhn.}$ along the specimen thickness and width

Fig. 7.14 replicates the evolution of the calculated stresses and shear stresses S_{ij} from Fig. 7.12 and exhibits further the normalized analytical solutions along the specimen thickness and width from Lekhnitskii ($\sigma_{33,Lekhn.}$, $\sigma_{11,Lekhn.}$) and from Kedward et al. ($\sigma_{33,Kedw.}$) for specimen AFP-09. Lekhnitskii's solutions in radial and circumferential directions along the width are plotted at the analytically determined radial position of the ILTS, r_{max}.

Once again, it can be stated, that Kedward et al.'s solution is closer to the numerical calculation. This is due to the specific elastic properties of the material.

Further, the circumferential stress S_{11} and the analytical solution $\sigma_{11,Lekhn.}$ superpose sufficiently good.

Arrows indicate further the S_{ij} stresses, and the $\sigma_{33,Lekhn.}$ and $\sigma_{\theta\theta,Lekhn.}$ at the common measuring point, at r_{max} along the thickness, and at half the specimen width along the width.

For the plots of all other AFP L-beam specimens, the reader is referred to the annex Sec. B.3.3.

The significance of the determined ILTS results of the AFP L-beam specimens will be discussed further in Ch. 9, when comparing the experimental, analytical, and numerical results of L-beam specimens manufactured by traditional hand lay-up with those produced by AFP technology.

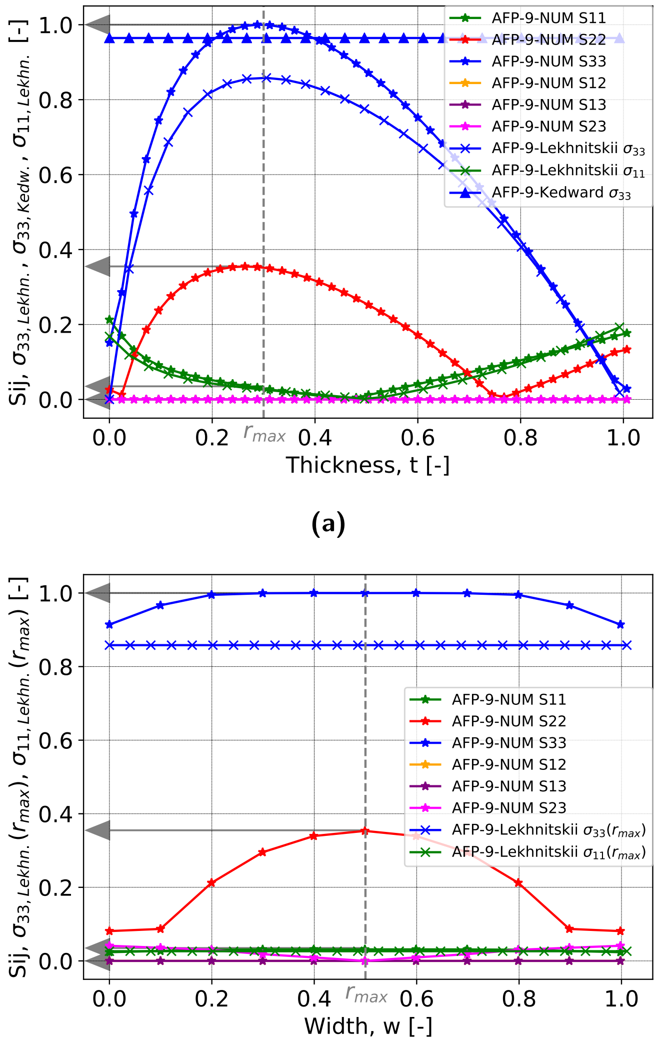

(a)

(b)

Fig. 7.14. *Normalized stresses S_{ij} and analytically estimated radial and circumferential stresses $\sigma_{33,Lekhn.}$, $\sigma_{11,Lekhn.}$ (Lekhnitskii) and $\sigma_{33,Kedw.}$ (Kedward et al.) as a function of the normalized (a) thickness and (b) width of L-beam specimen AFP-09. Arrows indicate the equal stress values at half the specimen width along the width, and at r_{max} along the thickness.*

7.3.3.3 Analytically calculated radial position r_{max}

Tab. 7.7 lists the estimated radial position r_{max} of the ILTS for the thicknesses t_{max}, t_{mean} and t_{min} of each AFP L-beam specimen, as well as the ply that is subjected to the maximum radial stress, theoretically. According to this, the radial position r_{max} of the ILTS for all AFP specimens was approximately at 0.30 (normalized value over the thickness) from the inner radius.

Assuming that the longest crack formation, written in bold in Tab. 7.4, and replicated in Tab. 7.7, corresponds to the first failure crack, it can be concluded that specimen AFP-06 broke mechanically, since the analytical solution (ply 13) is very close to the experimentally failed plies (13/14/15).

The same conclusions are made for the specimens AFP-10, and AFP-03 and AFP-09 which broke experimentally at ply 11/12 and 14/15, respectively, hence both close to the analytically calculated ply 13, as well as for specimen AFP-04 which is close to the analytical solution, too.

However, for the specimens AFP-02 and AFP-05, it can be concluded that they did not break mechanically but due to defects and heterogeneities in the material, as r_{max} does not match the observed first failure crack localisation.

Tab. 7.6. *ILTS*$_{\mathrm{mean}}$*, calculated through Kedward et al.'s and Lekhnitskii's solutions from* $t_{max,mean}$*,* $t_{mean,mean}$ *and* $t_{min,mean}$*, of AFP L-beam specimens, compared to the FE results. Error values correspond to the percentage error relative to the simulated* S_{33} *values.*

Specimen mean thicknesses [mm]	Kedward et al.				Lekhnitskii				Finite element method (FEM)		
	ILTS$_{\mathrm{mean}}$ [MPa]	Error [%]	SD [MPa]	CV [%]	ILTS$_{\mathrm{mean}}$ [MPa]	Error [MPa]	SD [%]	CV [MPa]	$S_{33\mathrm{mean}}$ [%]	SD [MPa]	CV [%]
$t_{max,mean}$	71.2	-0.9	4.36	6.12	62.9	-12.5	3.59	5.71	71.9	4.67	6.49
$t_{mean,mean}$	73.7	-3.8	4.61	6.25	65.5	-14.5	3.84	5.85	76.7	5.51	7.19
$t_{min,mean}$	76.1	-4.9	4.67	6.15	67.9	-15.0	3.90	5.74	80.0	5.60	7.01

Tab. 7.7. *Normalized radial position of the ILTS, calculated using Lekhnitskii's Equ. 6.9, and the corresponding ply counted from the inner radius. These values are compared to the normalized first failure crack distribution observed experimentally.*

AFP-	02		03		04		05		06		09		10	
	[-]	ply	[-]	ply	[-]	ply	[-]	ply	[-]	ply	[-]	ply	[-]	ply
$\mathrm{r}_{\mathrm{max,t_{max}}}$	0.28	12	0.30	13	0.30	13	0.29	12	0.30	13	0.29	12	0.29	12
$\mathrm{r}_{\mathrm{max,t_{mean}}}$	0.29	12	0.30	13	0.30	13	0.30	13	0.30	13	0.30	13	0.30	13
$\mathrm{r}_{\mathrm{max,t_{min}}}$	0.29	12	0.30	13	0.30	13	0.30	13	0.30	13	0.30	13	0.30	13
Normalized first failure crack over the thickness (from Tab. 7.4)	**0.57**	**24/25**	**0.33** **0.43**	**14/15** **18/19**	**0.36**	**15/16/17**	**0.17**	**7/8**	**0.33**	**13/14/15**	**0.33**	**14/15**	**0.21** **0.26**	**9/10** **11/12**

7.4 Summary of AFP specimens tested in 4PB

In this chapter, the experimental, numerical and analytical tool, which were presented in Ch. 6, were applied on unidirectional carbon fibre reinforced composite L-beam specimens, fabricated by AFP technology.

First, the material used and the fabrication process of the AFP L-beam specimens were presented in Sec. 7.1. The experimental procedure was presented in Sec. 7.2. Last, the results of the study were discussed in Sec. 7.3.

The experimental tool, which consisted in the design of the test setup, and the application of the different instrumentation during test execution, was validated since a high reproducibility of the 4PB tests was given. The load-displacement curves in Fig. 7.4 superposed, with exception of specimen AFP-10, almost perfectly. The AFP L-beam specimens had, from 3000 N up to failure, the same material stiffness.

AE sensors, applied on specimen AFP-09, have shown little material damage occurring during test execution, and high material damage prior to specimen failure (80-100 dB). Further, the failure occurred instantaneously since an important force drop was observed. This was found to be consistent with the statements of Charrier et al. [2016].

Fig. 7.5b and Fig. 7.5f have shown the (first failure) crack locations of specimen AFP-09. Fractured plies and interfaces were identified using the photos taken after test completion, and by using an optical microscope. It was noted that five out of seven AFP specimens delaminated between 0.26 and 0.36 (normalized values of the thickness) measured from the inner radius.

In Sec. 7.3.2, the non-linearity of the load-displacement curves at test beginning was explained, numerically. A slight vertical misalignment of one lower loading bar was assumed to result in a change of the measuring point of the LVDT tip until the L-beam specimen has found its final position. Further it was noted, that an increase in the specimen thickness resulted in an increase in the material stiffness which had an high impact on the reaction force (Fig. 7.10).

In Sec. 7.3.3, the ILTS was calculated using Lekhnitskii's and Kedward et al.'s solutions and compared to the numerical calculations. It was found that Kedward et al.'s solution fits better the S_{33} ($< 5\,\%$) asLekhnitskii's one ($12\,\%$ $15\,\%$). This was demonstrated by replicating Kedward et al.'s Fig. 5.2, and by adding the FE calculations as done in Fig. 7.13. The better estimation was hence due to the elastic properties of the material.

Further, using Lekhnitskii's Equ. 6.9, the radial location of the ILTS, r_{max}, was calculated and compared to the experimentally observed first failure crack locations, listed in Tab. 7.4. As given in Tab. 7.7, r_{max} was, for five out of seven specimens, almost equal to the experimentally observed first failure cracks. From this it was concluded that those specimens broke mechanically, i.e. at the radial position of the maximum out-of-plane stress, and two out of six specimens due to defects and heterogeneity in the material.

In the following Ch. 8, the 4PB study on L-beam specimens made by traditional hand lay-up, with the same material that was used for the AFP L-beam specimens, will now be presented.

8

4PB study on L-beam specimens manufactured by traditional hand lay-up (MAN)

Contents

In the present Ch. 8, the 4PB study on unidirectional carbon fibre reinforced L-beam specimens fabricated by traditional hand lay-up (MAN) will be presented. The material used will be given in Sec. 8.1, and the fabrication process of the MAN L-beam specimens in Sec. 8.2. The realisation of the 4PB followed the protocol presented in Sec. 7.2. Then, in Sec. 8.4, the results of the 4PB tests will be presented. As for AFP L-beam specimens, the focus of the analysis will be on the reproducibility of the 4PB tests, the exact localization of the first failure cracks, compared to the analytically determined radial location of the ILTS, r_{max}, the influence of the specimen thickness on the stiffness, and the determination of the ILTS.

8.1 Material properties of MAN L-beam specimens

In Sec. 7.1 the material used to manufacture the AFP L-beam specimens was presented. The material roll from which the prepreg batches for the manual hand lay-up process were cut from did not correspond to same batch which was used for the AFP L-beam production, but to a another one that had practically identical material properties.
The prepreg batches for the MAN L-beam specimens were, as for AFP L-beam specimens, composed of the epoxy matrix Se84LV from Gurit, and of carbon fibres with intermediate modulus IM2C from Hexcel. The elastic moduli of the matrix and of the carbon fibres were the same as given in Sec. 7.1. The prepreg batches had a 34.4 % resin weight content (product weight of 459.75 $\frac{\mathrm{g}}{\mathrm{m}^2}$) and a fibre weight of 301.25 $\frac{\mathrm{g}}{\mathrm{m}^2}$. The estimated volume fraction of the fibres and the longitudinal tensile modulus were the same as for AFP L-beam specimens (see Sec. 7.1). The mean ply thickness of the MAN prepreg batches before autoclave curing was 302 µm.
Below, the fabrication process of the MAN L-beam specimens will be presented in detail.

8.2 Fabrication process of MAN L-beam specimens

The MAN L-beam specimens were produced in the manufacturing hall of Avel Robotics in Lorient, a specialist in hydrofoil constructions. The material used, presented in Sec. 8.1, had to be thawed before manipulation. The thawing time was 24 h. Thereafter, the production process of the MAN L-beam specimens could be started. The manufacturing protocol was as follows:

1. Cutting of all 42 prepreg plies from material roll (400 mm x 23 mm) (Fig. 8.1) and double-sided numbering of all plies (Fig. 8.2).
2. Spyking of all 42 plies (Fig. 8.3).
3. Preparing the aluminium mould with a teflon layer. Hand lay-up of 42 plies on the mould in 0°-direction and intermediate debulking every 3 plies during 20 min with the following compaction drain sequence (Fig. 8.5):

> 3.1 No removing of the protection sheet of the last stacked ply.
> 3.2 Red release film to prevent the plies from sticking to the grids.
> 3.3 Green grid for air draining.
> 3.4 Yellow elastic vacuum sealant.

4. Measurement and weighing before autoclave curing.
5. Bagging sequence (Fig. 8.5):

  5.1 Preparing an aluminium plate with an teflon layer and a red release film.
  5.2 Positioning of thelaid-up panel on the aluminium plate.
  5.3 Installation of a thermocouple (TC) close to the mould.
  5.4 Application of the red release film.
  5.5 Positioning of a 10 mm thick polycarbonate caul plate (Fig. 8.6).
  5.6 Application of the red release film.
  5.7 Application of a white polyester breather.
  5.8 Application of the green grid.
  5.9 Application of a white polyester breather.
  5.10 Application of a green vacuum sealant.

6. Set under vacuum.
7. Autoclave curing:
   The curing cycle consisted in a one-shot curing. As observed for the curing of the AFP L-beam panel, no exothermic reaction was monitored. The maximum pressure and temperature were 7 bars and 120 ° during the whole cycle.
8. Measurement and weighing after autoclave curing.
9. L-beam cutting by mitre saw.

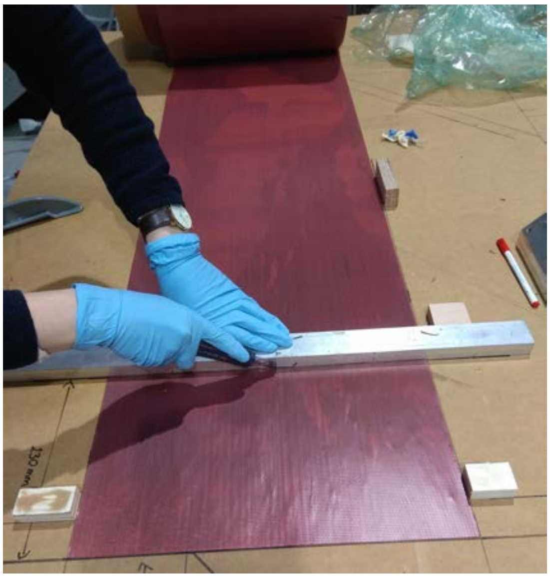

Fig. 8.1. *Cutting of prepreg plies.*

Fig. 8.2. *Front and back side numbering of cut prepreg plies.*

Before and after autoclave curing, the L-beam panel was measured and weighed. The thicknesses of the L-beam panel before autoclave curing, measured by a calliper, were between 12.42 and 12.85 mm. Those values were only taken at the L-beam panel's legs and not in the curved zone as the measuring instrument did not allow to reach the curved segment. The thicknesses after autoclave curing, measured using *ImageJ*, are given in Tab. 8.1. The table shows higher thickness mean values after autoclave curing. This is firstly explained by the fact, that the thickness measurements before autoclave curing were only taken at the legs of the L-beam panel. It is assumed that the thicknesses in the curved segment were higher than those in the L-beam panel's legs (12.42-12.85 mm). It must secondly be taken into account that two different measurement instruments (calliper and *ImageJ*) were used to measure the thicknesses before and after autoclave curing. The measurement accuracy of the calliper was estimated to 0.2 mm. The thickness values after autoclave curing were hence taken in the further study and investigated in more detail. Much higher thickness values close to the panel's legs were observed, and smaller ones in the curved part of the L-beam panel.

The weight of the L-beam panel before and after autoclave curing was 1790 g and 1760 g, respectively. Resin residues were found along the thermocouple wire. It was further assumed that resin had accumulated during curing at the edges of the legs of the L-beam panel, which was then torn off after removing of the bagging ensemble.

To conclude this part, Fig. 8.8 shows the hand laid-up L-beam part after autoclave curing and mitre saw cutting.

In the following Sec. 8.3, the test implementation will be presented.

Fig. 8.3. *Spyking of each ply before hand lay-up.*

Fig. 8.4. *Use of a spatula on the sides and the the thumbs at the corner of the panel to ensure good adhesion between the plies.*

Fig. 8.5. *Intermediate debulking every 3 plies during* 20 min. *Total lay-up time* 9 h20 min.

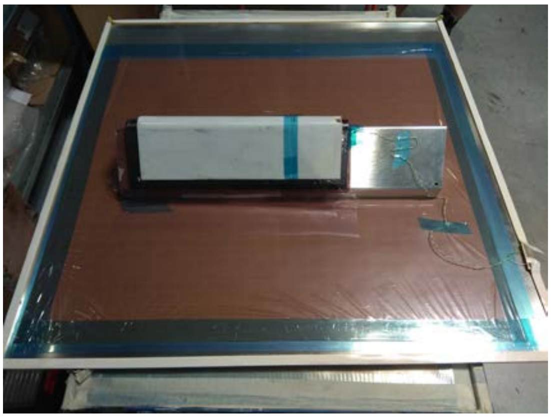

Fig. 8.6. *Positioning of PC caul-plate and application of thermocouple.*

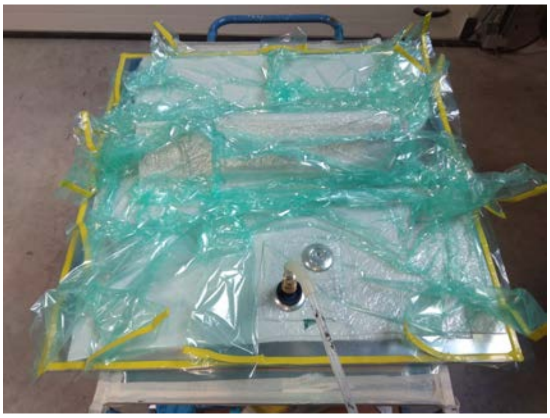

Fig. 8.7. *Bagging before autoclave curing. Successive placing of clamps around the vacuum area ensure better air extraction.*

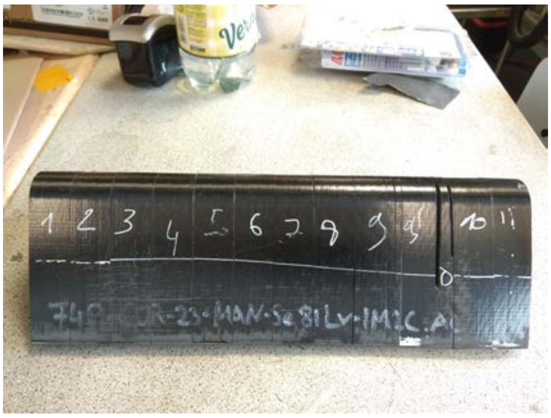

Fig. 8.8. *L-beam panel after autoclave curing and mitre saw cutting.*

8.3 Test realisation of MAN L-beam specimens

Seven MAN L-beam specimens produced by manual hand lay-up were tested in 4PB. Equal to the AFP L-beam specimens, thickness measurements at 18 different points were taken from the cross sections of each MAN L-beam specimen, using *ImageJ*. A schema of the measuring sections was given in Fig. 7.3. The scale was set to 118 px/cm, corresponding to an accuracy of 1 px per 0.085 mm. The inner radii were measured using the same setting and the tool *fit circle*. The specimen widths were measured using a calliper. Tab. 8.1 lists the metrology of the MAN L-beam specimens prior to testing.

In the same manner as described for the AFP L-beam specimens, 2 mm-mono strain gauges were fixed at one third from the inner radius in thickness direction (surfaces roughening using fine-grained abrasive paper, degreasing of the surface, and fixing of the gauges using the products 770 and 406 from *Loctite*).

The test realisation of all MAN L-beam specimens followed the same instructions as given in Sec. 7.2, using the testing device presented in Tab. 6.3. Tab. 8.2 lists the applied instrumentation for each MAN L-beam specimen.

In the following Sec. 8.4, the results of the MAN L-beam specimens tested in 4PB will be discussed.

8.4 Results of MAN L-beam specimens tested in 4PB

In this section, the results of the 4PB study on MAN L-beam specimens will be presented. First, the results of the experimental part will be shown in Sec. 8.4.1. Load-displacement diagrams, results of the AE data, and first failure crack locations will be considered within this section. Then, the results of the FE calculations will be discussed in Sec. 8.4.2. Finally, the ILTS, determined using the analytical tool, will be presented in Sec. 8.4.3 and compared to the results given by the FE models.

Tab. 8.1. *Metrology of MAN L-beam specimens.*

	N°	w [mm]	t_{max} [mm]	t_{mean} [mm]	t_{min} [mm]	t_{max}-t_{min} [mm]	r_i [mm]	ϕ_i [°]
MAN-	01	25.08	13.73	13.00	11.87	1.86	6.11	45
	04	25.02	13.90	13.27	12.20	1.70	5.98	45
	05	25.21	13.75	13.16	12.42	1.33	5.94	45
	06	25.41	13.78	13.13	12.25	1.53	6.27	45
	07	24.46	13.81	13.17	12.25	1.56	5.94	45
	08	25.46	13.90	13.17	12.29	1.61	5.98	45
	09	25.06	13.93	13.22	12.33	1.60	5.83	45
	Mean value	25.10	13.83	13.16	12.23	1.65	6.02	45
	SD	0.28	0.09	0.07	0.15	0.16	0.13	0
	CV [%]	1.1	0.64	0.56	1.27	9.9	2.2	0

Tab. 8.2. *Overview of applied instrumentation of MAN L-beam specimens.*

	N°	LVDT	Strain gauge	AE	DIC
MAN-	01, 04-09	yes	yes	yes	yes

8.4.1 Experimental results of MAN L-beam specimens tested in 4PB

8.4.1.1 Reproducibility and stiffness

Seven specimens manufactured by traditional hand lay-up were tested in 4PB. The experimental test procedure of each specimen was the same as for the AFP L-beam specimens (protocol presented in Sec. 7.2).

The mean load at failure of the MAN L-beam specimens amounted to 3983 ± 740 N with a CV of 18.6 %. The reader is referred to Tab. B.2 to access the individual failure loads of each MAN L-beam specimen.

Fig. 8.9 shows the load-displacement plots. Four out of seven curves superpose perfectly. Three out of seven show a non-uniform behaviour at test beginning. The overall non-

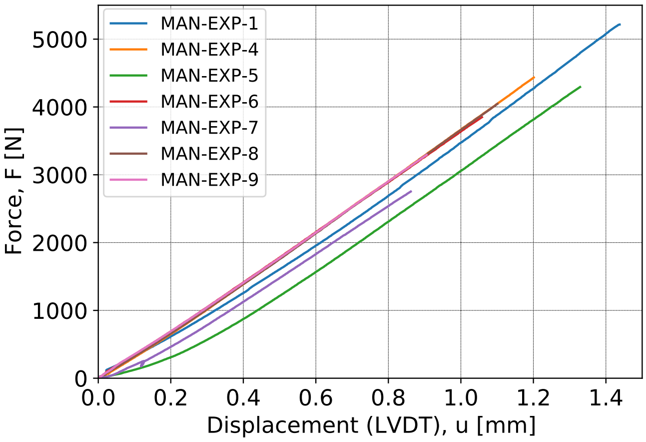

Fig. 8.9. *Load-displacement curves of MAN L-beam specimens tested in 4PB show a good reproducibility with a uniform stiffness from* 1000 N *up to failure.*

linearity at test beginning, which is more or less pronounced for the MAN L-beam specimens, was investigated by applying linear regressions between different loading ranges as already performed for the AFP L-beam specimens.

The calculated stiffnesses are listed in Tab. 8.3. From this it can be concluded that within linear regressions N°1 and N°2, the CV_{N° was small (2.8 % for linear regressions N°1 and N°2) and higher for linear regression N°3 (13.6 %). Further, the mean stiffness of linear regression N°2 (3.6 %) differed only less from the reference value (linear regressions N°1), while the mean stiffness of linear regression N°3 (16.9 %) differed highly. The stiffness from 1000 N until failure of all MAN L-beam specimens was hence considered to be uniform, and the 4PB tests were assumed to be reproducible.

Tab. 8.3. *Mean stiffness, SD and CV_{N° of different loading ranges for MAN L-beam specimens. The percentage deviation of linear regression N°2 is, with regard to N°1, small.*

Linear regression N°	Loading range [N]-[N]	Mean stiffness $[\frac{N}{mm^2}]$	CV_{N° [%]	Deviation [%]
1 (reference)	2000-2750	3735 ± 104	2.8	0
2	1000-2000	3602 ± 101	2.8	3.6
3	0-1000	3103 ± 421	13.6	16.9

8.4.1.2 First failure cracks

Photos of the cracks were taken from the sprinkled face after test completion. Tab. 8.4 lists how many cracks in total were shown. As performed for the AFP L-beam specimens, the location of the first failure crack, assumed to correspond to the longest crack observed, was first roughly determined using the DIC images, then more preciously using the photos of the cracks taken after test completion, as well as the photos taken with an optical microscope, showing the fractured plies and interfaces.

Fig. 8.10b exhibits exemplarily the DIC image of MAN-08 after the first force drop, and Fig. 8.10d the corresponding photo taken after test completion. Fig. 8.11 shows further the photo of specimen MAN-08 that was taken with the optical microscope.

Tab. 8.4 resumes the observations that have been done for all MAN L-beam specimens. It lists the fractured interfaces and plies, and the corresponding normalized locations over the specimen thickness. First failure cracks are printed in bold. For five MAN L-beam specimens out of seven, the first failure crack localisation varied thus between 0.38 and 0.5 (normalized value over the thickness), measured from the inner radius.

8.4.1.3 Acoustic emissions (AE)

AE were applied to all MAN L-beam specimen. However, it was found that the machine noises coming from the 500 kN cell had been extremely high (between 60 and 80 dB), so that the recorded hits and events could not be assigned to material damage. The analysis of the AE data could therefore not be performed.

Tab. 8.4. *Overview of photos taken after test completion and crack localisation of MAN L-beam specimens.*

MAN-N°	PHOTOS	CRACK LOCALISATION		
	sprinkled face	How many cracks?	$r_{failure}$[a]	Fractured interfaces/plies[b]
01	yes	2	at 0.33,**0.38**	14/15;**16/17**
04	yes	1	at **0.38**	**16/17**
05	yes	1	at **0.5**	**21/22**
06	yes	1	at **0.55**	**23/24**
07	yes	1	at **0.43**	**18/19**
08	yes	1	at **0.43**	**18/19**
09	yes	1	at **0.19**	**8**

[a] Normalized distribution over the thickness, calculated from the fractured interfaces/plies. The reference surface is the first ply laid-up on the mould. Values marked in blue correspond to the crack localisation observed on the first image made by the DIC after occurrence of the first force drop.

[b] Counted from the inner radius using an optical microscope. Values written in **bold** correspond to the longest crack formation over the specimen front face.

8.4.1.4 DIC images and strain gauge

To complete, Fig. 8.10c show the load-displacement plot of specimen MAN-08 indicating the DIC stages prior to (stage 150, Fig. 8.10a) and after (stage 151, Fig. 8.10b) specimen failure. The stage number refers to the photos that have been recorded since test begin. The maximum deformation value given by the DIC image prior to specimen failure in radial direction (0.64 %) did not match the strain gauge value (0.15 %), as the DIC measured local maximum deformations that occur on the specimen front face outside the measuring zone of the strain gauge. Similar observations were made for all MAN L-beam specimens.

8.4.2 FE results of MAN L-beam specimens tested in 4PB

In Fig. 7.10, a step by step procedure for comparing the FE calculations for different specimen thicknesses (t_{max}, t_{mean}, t_{min}) with the experimental stiffness was presented. The same procedure was applied to all MAN L-beam specimens. Fig. 8.12 shows, representatively for all MAN L-beam specimens, the load-displacement correlation of specimen MAN-08.

As assumed, an increase in the specimen thickness resulted in an increase in the stiffness. The difference between t_{max} and t_{min} of 1.61 mm for specimen MAN-08, resulted in a reaction force up to 1300 N higher at the given displacement at failure. Similar observations were made for the remaining MAN L-beam specimens.

Last, it can be noted that for specimen MAN-08, the numerical curve with t_{mean} fitted well the experimental stiffness.

All load-displacements plots with shifted linear regressions are given in the annex Sec. B.4.2. It was found that for one specimen out of seven, the specimen stiffness was located between t_{mean} and t_{max}, for three specimens out of seven between t_{min} and t_{mean} and for three specimens out of seven, the stiffness coincided with t_{mean}.

In Sec. 8.4.3 the analytical results of the MAN specimens tested in 4PB will be presented and compared to those calculated by FE simulation.

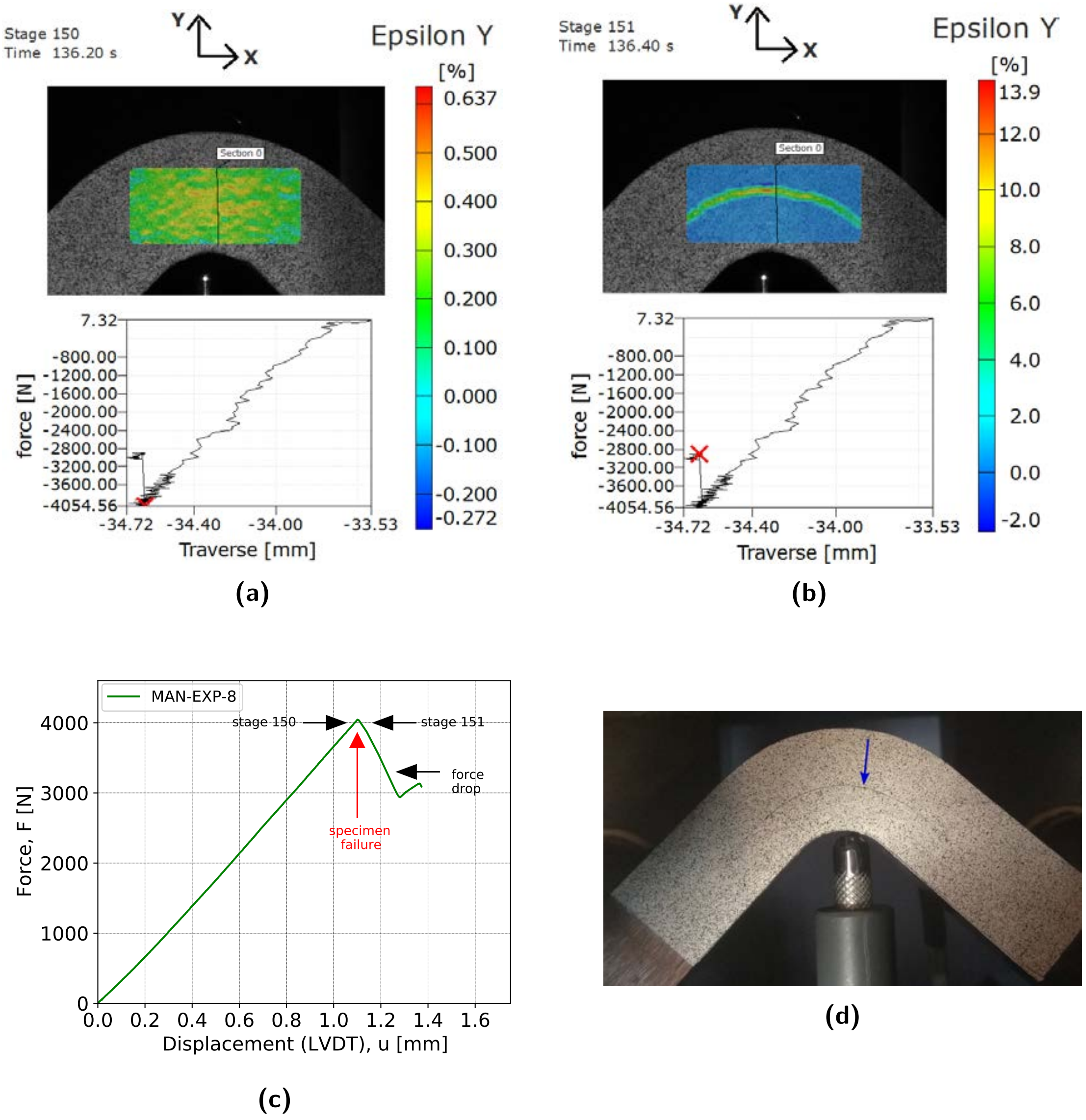

Fig. 8.10. *DIC images of L-beam specimen MAN-08 (a) prior to and (b) just after the first failure crack. (c) Load-displacement diagram (LVDT) with force drop, and (c) the first failure crack formation indicated by blue arrows.*

8.4.3 Analytical results of MAN L-beam specimens tested in 4PB

In this section, the analytical tool was applied on MAN L-beam specimens in order to determine the ILTS, corresponding to the maximum out-of-plane stress occurring in the curved segment of the L-beam specimen. The analytical tool consisted in the solutions from Lekhnitskii and from Kedward et al.. The analytical tool was presented in Sec. 6.1.

8.4.3.1 Confrontation of ILTS$_{\text{Kedward et al.}}$ and ILTS$_{\text{Lekhnitskii}}$ to S_{33}

The ILTS was estimated in the same way as for the AFP L-beam specimens. The geometric dimensions given in Tab. 8.1, the elastic moduli in tangential and radial directions listed in Tab. 6.5 ($E_\theta = E_1$, $E_r = E_2$), as well as the force and the vertical displacement at failure for each specimen were entered into the python script. Taking into account the three different specimen thicknesses (t_{max}, t_{mean}, t_{min}), three calculations with Lekhnit-

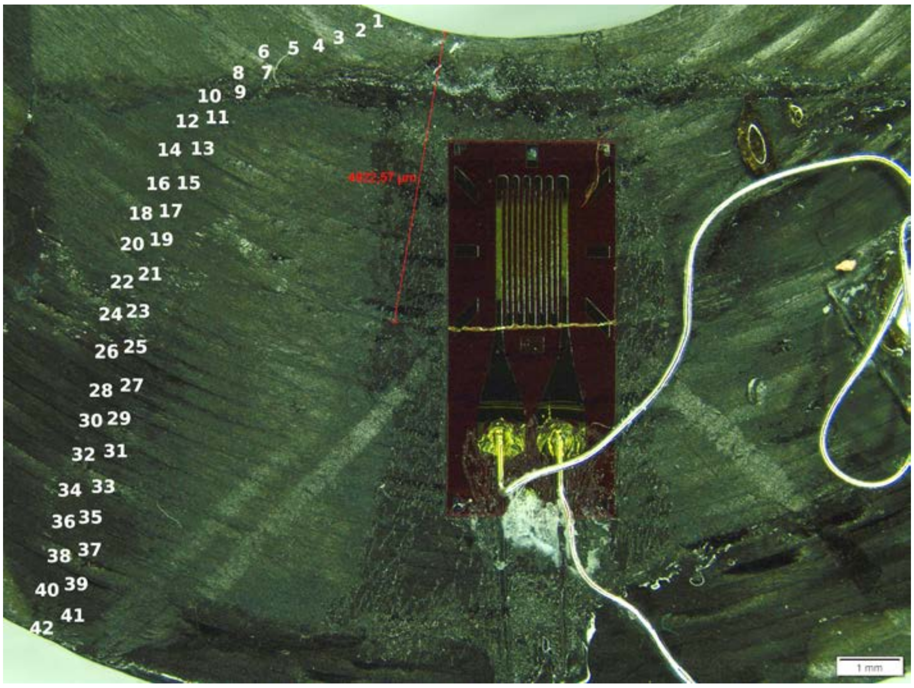

Fig. 8.11. *Photo taken with the microscope for counting the fractured interfaces of specimen MAN-08.*

skii's and three calculations with Kedward et al.'s solution were performed on each MAN specimen.

In order to determine the S_{33}, the experimental measured load at failure of each MAN L-beam specimen was imposed via the negative vertical displacement U_z (displacement controlled). Three FE calculations, differing by t_{max}, t_{mean}, t_{min}, were performed on each MAN L-beam specimen.

Tab. 8.5 shows the ILTS and the S_{33} mean values for the three different mean thicknesses. To access the individual estimations and calculations of each MAN L-beam specimen, the reader is referred to Tab. B.2.

As observed for the AFP L-beam specimens, the percentage ILTS error of Kedward et al.'s solution was less than 5%. In comparison, the solution of Lekhnitskii differed between 8 and 13 % from the FE results. The better estimation of the ILTS calculated by Kedward et al.'s solution was explained in Fig. 7.13 and can be applied to the MAN L-beam specimens since the same material was used.

8.4.3.2 Normalized stresses S_{ij}, $\sigma_{33,Kedw.}$ and $\sigma_{33,Lekhn.}$ along the specimen thickness and width

Fig. 8.13 plots further the normalized evolutions of the strains and stresses S_{ij}, and the analytical solutions from Lekhnitskii ($\sigma_{33,Lekhn.}$, $\sigma_{11,Lekhn.}$) and from Kedward et al. ($\sigma_{33,Kedw.}$) of specimen MAN-08 along the specimen thickness and width. For the plots of all other MAN L-beam specimens, the reader is referred to the annex Sec. B.4.3.

Along the specimen width, Lekhnitskii's solutions were plotted at the analytically determined radial localisation of the ILTS, r_{max}.

It was found that the evolution of the stresses and strains S_{ij} are similar to those of the AFP L-beam specimens, discussed in Sec. 7.3.2, only less pronounced as lower stresses

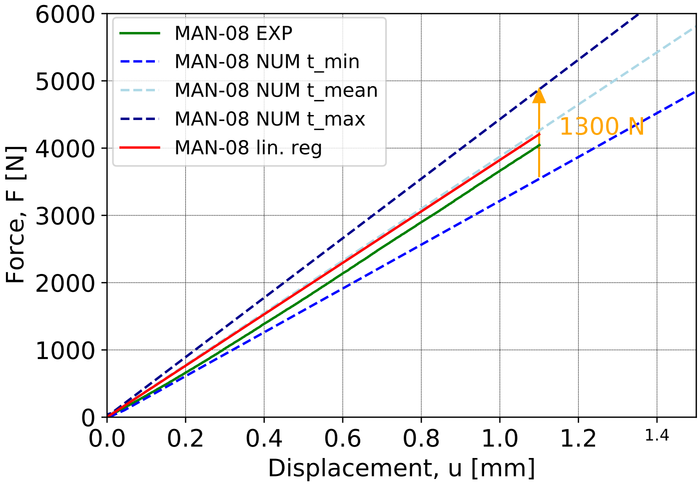

Fig. 8.12. *Numerical FE simulations with three different specimen thicknesses (t_{max}, t_{mean}, t_{min}). For specimen MAN-08, the numerical curve with t_{mean} fits well the experimental stiffness.*

were achieved during specimen testing.

Numerically and analytically (Lekhnitskii's solution), the ILTS occurred at approximately one third from the inner radius. Once again it can be seen that Kedward et al.'s solution is closer to the FE calculation.

Further, Fig. 8.13a shows that the S_{11} stress and the analytical solution $\sigma_{11,Lekhn.}$ superpose almost perfectly.

In Fig. 8.13a and Fig. 8.13b, arrows indicate the S_{ij} stresses and strains, and the analytically estimated $\sigma_{33,Lekhn.}$ and $\sigma_{\theta\theta,Lekhn.}$ at the common measuring point, marked by white nodes in Fig. 7.11a and Fig. 7.12a.

The significance of the determined ILTS values will be discussed further in Ch. 9 when comparing the experimental, analytical and numerical results of L-beam specimens manufactured by traditional hand lay-up with those produced by AFP technology.

8.4.3.3 Analytically calculated radial position r_{max}

Last, Tab. 8.6 lists the analytically calculated radial position r_{max} of the ILTS for the thicknesses t_{max}, t_{mean}, t_{min} of each MAN L-beam specimen, as well as the first failure crack locations, replicated from Tab. 8.4.

It was found that the experimentally measured first failure crack location was at 0.19, 0.55, and between 0.38 and 0.5 (normalized values over the thickness), measured from the inner radius. The analytically determined location of the ILTS, r_{max}, was between 0.29 and 0.30. For MAN L-beam specimens it can hence be concluded, that the MAN L-beam specimens do not break mechanically, i.e. at the radial position of the ILTS, but most likely due to defects and heterogeneities in the material.

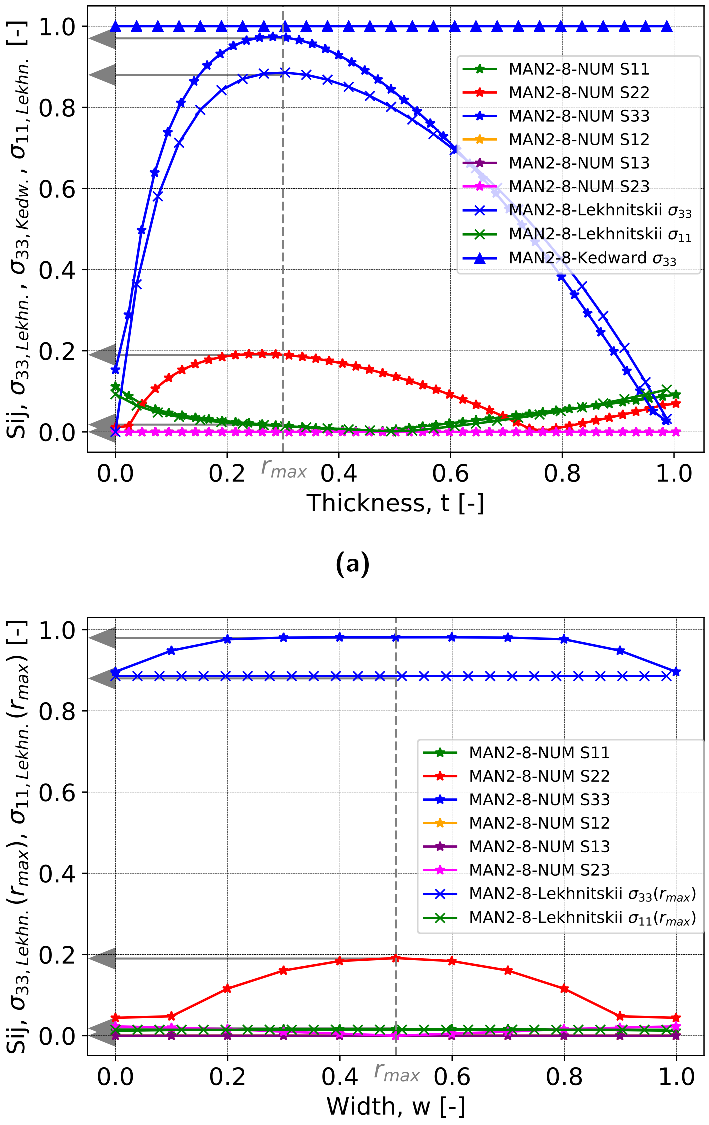

(a)

(b)

Fig. 8.13. *Normalized calculated stresses and strains S_{ij}, and analytically estimated radial and circumferential stresses $\sigma_{33,Lekhn.}$, $\sigma_{11,Lekhn.}$ (Lekhnitskii) and $\sigma_{33,Kedw.}$ (Kedward et al.) as a function of the normalized (a) thickness and (b) width of specimen MAN-08. Arrows indicate the equal stress and strain values at half the specimen width along the width and at r_{max} along the thickness.*

Tab. 8.5. *$ILTS_{mean}$, calculated through Kedward et al.'s and Lekhnitskii's solutions from $t_{max,mean}$, $t_{mean,mean}$ and $t_{min,mean}$, of MAN L-beam specimens, compared to the FE results. Error values correspond to the percentage error relative to the simulated S_{33} values.*

Specimen mean thicknesses	Kedward et al.				Lekhnitskii				FEM		
	$ILTS_{mean}$	Error	SD	CV	$ILTS_{mean}$	Error	SD	CV	S_{33mean}	SD	CV
[mm]	[MPa]	[%]	[MPa]	[%]	[MPa]	[MPa]	[%]	[MPa]	[%]	[MPa]	[%]
$t_{max,mean}$	41.5	4.2	7.18	17.1	36.9	-8.37	6.40	17.35	40.3	7.12	17.68
$t_{mean,mean}$	44.1	4.9	7.60	17.2	39.1	-10.53	6.76	17.30	43.7	7.97	18.24
$t_{min,mean}$	47.5	-2.4	8.45	17.8	42.6	-12.42	7.70	18.10	48.6	9.73	20.02

Tab. 8.6. *Normalized radial position of the ILTS, calculated using Lekhnitskii's Equ. 6.9, and the corresponding ply counted from the inner radius. These values are compared to the normalized first failure crack distribution observed experimentally.*

MAN-	01		04		05		06		07		08		09	
	[-]	ply	[-]	ply	[-]	ply	[-]	ply	[-]	ply	[-]	ply	[-]	ply
$r_{max,t_{max}}$	0.29	12	0.29	12	0.29	12	0.30	12	0.29	12	0.29	12	0.29	12
$r_{max,t_{mean}}$	0.30	13	0.29	12	0.29	12	0.30	13	0.29	12	0.30	12	0.29	12
$r_{max,t_{min}}$	0.31	13	0.30	13	0.30	13	0.31	13	0.30	13	0.31	13	0.30	13
Normalized first failure crack over the thickness (from Tab. 8.4)	**0.38**	**16/17**	**0.38**	**16/17**	**0.50**	**21/22**	**0.55**	**23/24**	**0.43**	**18/19**	**0.43**	**18/19**	**0.19**	**8**

8.5 Summary of MAN L-beam specimens tested in 4PB

In Ch. 8, the 4PB study on L-beam specimens manufactured by traditional hand laid-up was presented. The material used, and the fabrication process of the MAN L-beam specimens were presented in Sec. 8.1, and Sec. 8.2. The applied experimental test procedure was the same as for AFP L-beam specimens (see Sec. 7.2). The results of the study were discussed in Sec. 8.4.

The load-displacement diagrams of the MAN L-beam specimens, given in Fig. 8.9, superposed well (four specimens out of seven). The MAN L-beam specimens had, from 1000 N up to failure, the same stiffness.

Since high machine noises up to 80 dB perturbed the recording of the AE signals, the data could not be analysed.

Fig. 8.10b and Fig. 8.10d have shown the first failure crack localisation of specimen MAN-08. Fractured plies and interfaces were identified using the photos taken after test completion, and by optical microscope. It was noted that five MAN L-beam specimens out of seven delaminated between 0.38 and 0.5 (normalized values of the thickness) measured from the inner radius.

In Sec. 8.4.2, linear regressions applied to the experimental load-displacement curves have shown, that for one specimen out of seven, the specimen stiffness was located between t_{mean} and t_{max}, for three specimens out of seven between t_{min} and t_{mean}, and for three specimens out of seven, the stiffness coincided with t_{mean}. The difference of 1.61 mm between t_{max} and t_{min} for specimen MAN-08 resulted in a reaction force up to 1300 N higher for the same vertical displacement. Similar results were found for all MAN L-beam specimens. As expected, the specimen thickness had a high influence on the material behaviour.

In Sec. 8.4.3, the ILTS was calculated using Equ. 6.5 and Equ. 6.11, and compared to the numerically calculated data. It was found that Kedward et al.'s solution was close to the numerical calculation (error $< 5\,\%$). In Fig. 8.13a and Fig. 8.13b it was shown, that the radial stress in out-of-plane direction is the dominating one.

Further, the radial location of the ILTS, r_{max}, was calculated analytically using Equ. 6.9, and compared to the experimentally observed first failure crack locations which were listed in Tab. 8.4. As given in Tab. 8.6, r_{max} was for five specimens out of seven between 0.29 and 0.3 (normalized values over the thickness). Taking into account the experimentally observed delamination locations, it was concluded that MAN L-beam specimens did not break mechanically, i.e. at the radial position of the maximum ILTS, but probably due to defects and heterogeneity in the material.

In the following Ch. 9, the 4PB studies on L-beam specimens fabricated by traditional hand lay-up and by AFP technology will be confronted.

9

Confrontation of results of AFP and MAN L-beam specimens tested in 4PB

Contents

Ch. 7 and Ch. 8 have shown two studies that dealt with the 4PB testing of L-beam specimens that were produced by classical hand lay-up and by AFP technology. The objective of these to studies is to compare the influence of the manufacturing processes on the results of the 4PB tests and on the design. Therefore, in the present Ch. 9, the results of both studies will be compared in terms of reproducibility, metrology, CBS and stiffness, first failure crack location, loads at failure and ILTS, macroscopic defects, and porosity. Last, the influence of the manufacturing process, especially of the compaction mode, on the ILTS will be discussed.

9.1 Test reproducibility

Seven specimens fabricated by AFP technology, as well as sevens specimens produced by traditional hand lay-up were tested in 4PB. A high reproducibility in test realisation was found for both L-beam types. These observations are replicated in Tab. 9.2. Failure occurred instantaneously for all L-beam specimens as a strong force drop was observed. The non-linearity of the curves at test beginning was due to the positioning of the LVDT which was not exactly in the symmetry plane. The non-linear phase corresponded to a realignment of the measuring system with the specimen.

9.2 Metrology, CBS and stiffness

9.2.1 Influence of specimen metrology on the Interlaminar tensile strength

AFP and MAN specimens were compared in terms of their geometrical dimensions. The influence of the specimen width w, the inner radius r_i, and specimen thicknesses $t_{max,mean}$, $t_{mean,mean}$ and $t_{min,mean}$ on the ILTS will be briefly discussed, below. The metrology of both specimen types were listed in Tab. 7.1 and Tab. 8.1. Their mean values are replicated in Tab. 9.1.

Tab. 9.1. *Metrology mean values (mean width w_{mean}, mean maximum thickness $t_{max,mean}$, mean mean thickness $t_{mean,mean}$, mean minimum $t_{min,mean}$, mean inner radius $r_{i,mean}$) of AFP and MAN L-beam specimens.*

	w_{mean} [mm]	$t_{max,mean}$ [mm]	$t_{mean,mean}$ [mm]	$t_{min,mean}$ [mm]	$t_{max,mean}$ - $t_{min,mean}$ [mm]	$r_{i,mean}$ [mm]
AFP	24.68±0.07	13.36±0.20	12.89±0.18	12.49 ±0.17	0.87	5.99±0.35
MAN	25.10±0.28	13.83±0.09	13.16±0.07	12.23±0.15	1.60	6.02±0.13
Difference [%]	1.7	3.5	2.1	2.1		0.5

Specimen mean width

The specimen mean width w_{mean} amounted to 24.68 mm for AFP and to 25.10 mm for MAN specimens. Taking into account the accuracy of the calliper used (between 0.2-0.3 mm) for measuring the specimen widths, it is concluded that this geometrical parameter had no influence on the results as the specimen mean widths differed hardly from each other. To complete, Jackson & Martin [1993] mentioned that the specimen width w has only a slight effect on the ILTS, an other reason why no further attention was paid to this parameter.

Specimen mean inner radius

The same applied to the mean inner radii $r_{i,mean}$. This parameter was almost equal for both specimen types (5.99 mm for AFP, and 6.02 mm for MAN specimens) and thus felt within the range of accuracy of the measuring tool (*ImageJ*, 1 px per 0.085 mm).
To complete, Jackson & Martin [1993] stated in an analytical study that the inner radius

r_i influences the location of the ILTS. *As the inner radius increased, the maximum radial stress decreased, and the location of maximum radial stress moved towards the center of the thickness* [Jackson & Martin, 1993]. In the case of the present study, it can hence be assumed, that the inner radius had no influence on the ILTS and on the location of the first failure crack.

Specimen mean thicknesses

As given in Fig. 7.3, the specimen thicknesses were measured at 18 different measuring points along the specimen to define the maximum, mean, and minimum thicknesses t_{max}, t_{mean}, t_{min}. The measured thickness values at each point is given in Fig. 9.1a for AFP and in Fig. 9.1b for MAN L-beam specimens. The color gradient indicates whether the specimen was thicker (blue) or thinner (red) at the given position. Without looking at the exact measured values, it was found that the thickness of AFP L-beam specimens is more constant along the whole specimen, than the thickness of MAN L-beam specimens. In the curved segment, MAN L-beam are thinner than on the specimen arms.
This difference was also replicated in Tab. 9.1 ($t_{max,mean}$-$t_{min,mean}$). The thickness variation of MAN L-beam specimens is almost twice as large as that of the AFP L-beam specimens (0.87 mm for AFP, and 1.60 mm for MAN L-beam specimens). This will be discussed in more detail in Sec. 9.7.

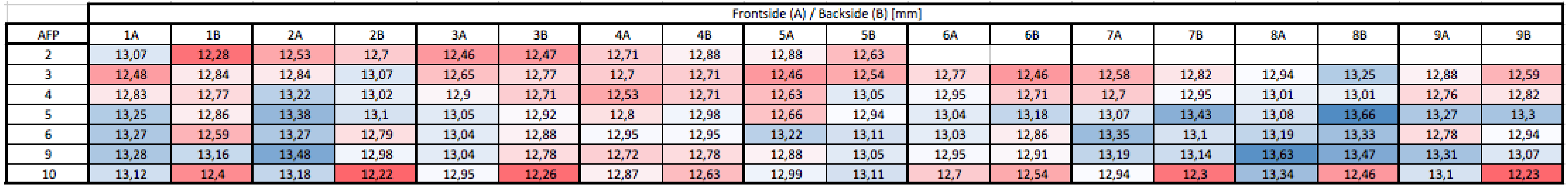

	Frontside (A) / Backside (B) [mm]																	
AFP	1A	1B	2A	2B	3A	3B	4A	4B	5A	5B	6A	6B	7A	7B	8A	8B	9A	9B
2	13,07	12,28	12,53	12,7	12,46	12,47	12,71	12,88	12,88	12,63								
3	12,48	12,84	12,84	13,07	12,65	12,77	12,7	12,71	12,46	12,54	12,77	12,46	12,58	12,82	12,94	13,25	12,88	12,59
4	12,83	12,77	13,22	13,02	12,9	12,71	12,53	12,71	12,63	13,05	12,95	12,71	12,7	12,95	13,01	13,01	12,76	12,82
5	13,25	12,86	13,38	13,1	13,05	12,92	12,8	12,98	12,66	12,94	13,04	13,18	13,07	13,43	13,08	13,66	13,27	13,3
6	13,27	12,59	13,27	12,79	13,04	12,88	12,95	12,95	13,22	13,11	13,03	12,86	13,35	13,1	13,19	13,33	12,78	12,94
9	13,28	13,16	13,48	12,98	13,04	12,78	12,72	12,78	12,88	13,05	12,95	12,91	13,19	13,14	13,63	13,47	13,31	13,07
10	13,12	12,4	13,18	12,22	12,95	12,26	12,87	12,63	12,99	13,11	12,7	12,54	12,94	12,3	13,34	12,46	13,1	12,23

(a)

	Frontside (A) / Backside (B) [mm]																	
MAN	1A	1B	2A	2B	3A	3B	4A	4B	5A	5B	6A	6B	7A	7B	8A	8B	9A	9B
1	13,37	13,34	13,73	13,30	13,28	13,07	12,58	12,32	12,08	11,87	12,59	12,47	13,25	13,22	13,66	13,43	13,33	13,16
4	13,63	13,52	13,82	13,84	13,46	13,60	12,71	12,70	12,20	12,42	12,67	12,59	13,69	13,36	13,90	13,78	13,45	13,51
5	13,51	13,28	13,66	13,61	13,36	13,43	12,65	12,76	12,42	12,42	12,83	12,67	13,54	13,24	13,75	13,43	13,36	13,04
6	13,31	13,19	13,69	13,78	13,33	13,39	12,53	12,50	12,33	12,25	12,62	12,62	13,51	13,18	13,73	13,48	13,45	13,39
7	13,46	13,30	13,69	13,63	13,27	13,40	12,71	12,44	12,33	12,25	12,62	12,58	13,45	13,33	13,81	13,73	13,72	13,30
8	13,24	13,25	13,57	13,66	13,30	13,39	12,56	12,59	12,29	12,42	12,85	12,86	13,57	13,39	13,90	13,54	13,36	13,39
9	13,42	13,43	13,69	13,78	13,27	13,39	12,50	12,67	12,33	12,33	12,80	12,46	13,63	13,45	13,87	13,93	13,60	13,48

(b)

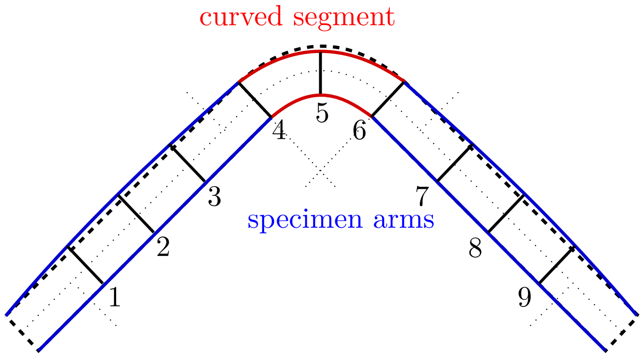

(c)

Fig. 9.1. *Thickness measurements of (a) AFP and (b) MAN L-beam specimens from 18 different measuring points (see Fig. 7.3) on the front (A) and back (B) sides. The color gradient indicates whether the specimen is, at the given position, thicker (blue) or thinner (red). A schematic is given in (c). The thickness of AFP L-beam specimens is hence more constant, than that of MAN L-beam specimens. MAN L-beam specimens are thinner in the curved segment (red zone), and thicker on the specimen arms (blue zone). Thickness values of AFP-02 are only partly given, as the specimen was sectioned along the symmetry plane and one part was taken away for further material investigations.*

9.2.2 Confrontation of stiffnesses of AFP and MAN L-beam specimens

In order to evaluate the stiffness difference, the load-displacement diagrams of each AFP and MAN L-beam specimens were superposed. As the mean thickness values $t_{mean,mean}$ (see Tab. 9.1) differed only slightly from each other (12.89 mm for AFP, and 13.16 mm for MAN L-beam specimens), similar stiffnesses were expected. The superposition of the load-displacement diagrams is given in Fig. 9.2. Keeping in mind the non-linearity of the load-displacement curves at test beginning, which was more or less pronounced for both specimen types, the load-displacement diagrams of the MAN L-beam specimens are located in the same range as those of the AFP L-beam specimens. This can be confirmed by the linear regressions made for the different loading ranges in Tab. 7.3 and Tab. 8.3 (mean stiffness of AFP L-beam specimens amounted to 3742 $\pm 104\,\frac{\mathrm{N}}{\mathrm{mm}^2}$, that of MAN L-beam specimens to 3735 $\pm 104\,\frac{\mathrm{N}}{\mathrm{mm}^2}$, resulting in a difference of 0.3 %). It can hence be concluded that no differences between MAN and AFP manufacturing was found in terms of elasticity. These observations are finally replicated in Tab. 9.2.

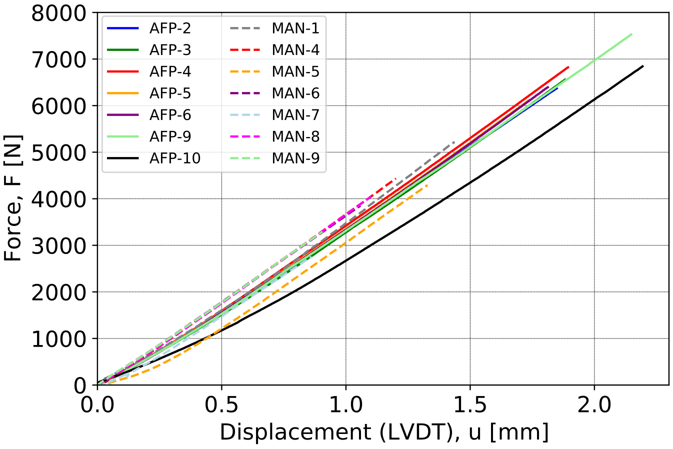

Fig. 9.2. *Correlation of experimental load-displacement plots of AFP and MAN L-beam specimens.*

9.2.3 Impact of corrected ϕ_i calculation on the ILTS

As given in Equ. 6.2, the Curved Beam Strength (CBS) is a function of P, Δ, d_x, ϕ_i, D, t and w and takes thus into account, i.a., the geometrical properties of each specimen.

The analytical estimations of the ILTS and the numerical calculations of the S_{33} were realized with a constant initial angle between the horizontal line and the specimens' arms ϕ_i of 45 °, as the corner of the aluminium mould, on which both L-beam panels were laid-up, corresponded to this angle.

Before testing the MAN L-beam specimens in 4PB, the exact ϕ_i of all MAN specimens was measured. This was done at the same time as the inner radii and the specimen thicknesses were measured. The sheet with the specimens' cross sections was scanned and the *Angle tool* from *ImageJ* (accuracy of 1 px per 0.085 mm) was used to measure the exact ϕ_i from the left and the right arm of each specimen. The mean value of both arms defined hence the exact ϕ_i. For all MAN L-beam specimens, the corrected ϕ_i was in the range of 45.0 °

and 45.2 °.
After test realisation, the CBS was then plotted with and without ϕ_i correction as function of the vertical displacement (LVDT) for each MAN L-beam specimen. The plots are given in Fig. 9.3. Dotted lines represent the CBS calculated with the corrected ϕ_i, solid lines that calculated with $\phi_i = 45\,°$.

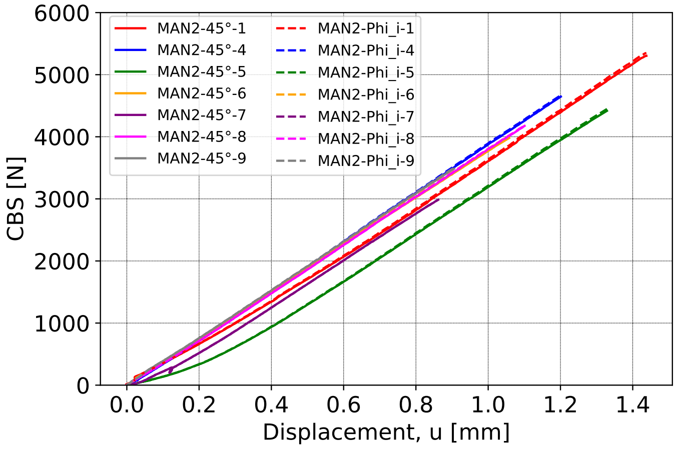

Fig. 9.3. *Correlation of CBS-displacement (LVDT) plots of MAN L-beam specimens with and without* ϕ_i *correction.*

It was found that a correction of ϕ_i up to 0.2 ° had a negligible influence on the CBS. Dotted and solid lines were almost identical.
Since AFP and MAN L-beam specimens were laid-up on the same aluminium mould, it was assumed that the exact angles ϕ_i for the AFP L-beam specimens were in the same range as those of the MAN L-beam specimens (no measures of the ϕ_i of AFP L-beam specimens were taken prior to sample testing). Fig. 9.4 shows finally the superposition of the CBS as a function of the vertical displacement (LVDT) of all AFP and MAN L-beam specimens for $\phi_i = 45\,°$. The distribution of the resulting plots is similar to the load-displacement

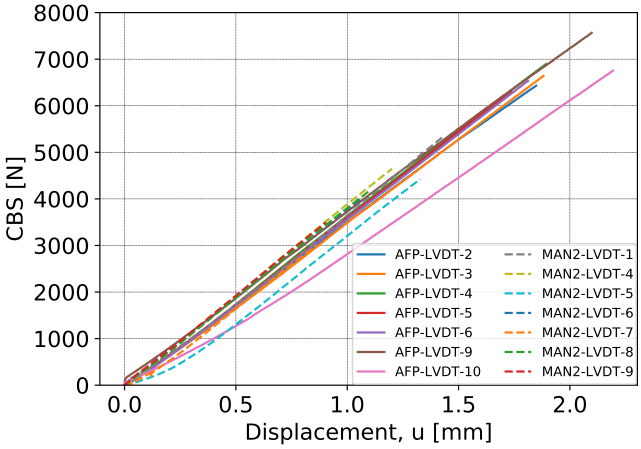

Fig. 9.4. *CBS as a function of the vertical displacement (LVDT) of AFP and MAN L-beam specimens for* $\phi_i = 45\,°$.

curves, that were given in Fig. 9.2. This is due to the following reasons. First, d_x, a function of l_t and l_b, D and ϕ_i are constant values and equal in the calculation of the CBS. Second, P and Δ are specimen specific parameters recorded during the experimental test realisation. Last, the mean width and thicknesses of the tested AFP and MAN L-beam specimens differ only slightly from each other as stated above.

9.3 First failure crack locations

9.3.1 Analytically estimated first first failure crack locations

The first failure crack locations r_{max} were determined analytically using Equ. 6.9 and were listed in Tab. 7.7 and Tab. 8.6 for AFP and MAN L-beam specimens, respectively. $\frac{r_{max}-r_i}{r_i}$ was hence estimated to be between 0.28 and 0.31 for both specimen types. The small geometrical differences, discussed in Sec. 9.2.1, had no influence on r_{max}. The variability on the analytical prediction of the location of the first failure crack was $\pm 0.02\,\mathrm{mm}$, calculated from the ply ($\sim 0.3\,\mathrm{mm}$) and the specimen thicknesses.

9.3.2 Numerically calculated first failure crack locations

The numerical calculations of the first failure crack locations r_{FE} were determined for AFP and MAN L-beam specimens at the node of the highest out-of-plane stress. For both L-beam types, this node was on the symmetry plane, at half of the specimen width, between the plies 12 and 13, corresponding to a first failure crack location r_{FE} of approximately 0.3. This value corresponded hence to that found analytically.

9.3.3 Experimentally observed first failure crack locations

The experimentally observed first failure crack locations $r_{failure}$ were given in Tab. 7.4 and Tab. 8.4, and were replicated in Tab. 7.7 and Tab. 8.6 for AFP and MAN L-beam specimens, respectively.

It was assumed that the longest crack formation localised on the first DIC image taken after failure corresponded to the first failure crack. This was based on preciously investigations of the DIC images after failure (e.g. Fig. 7.5b), the images from the fractioned surfaces taken by the optical microscope (e.g. Fig. 7.6), and the photos taken directly after test completion (e.g. Fig. 7.5f). Further, the strong force drop after specimen failure (e.g. Fig. 7.5e), and the AE signals (e.g. Fig. 7.5c) supported the assumption that the longest failure crack observed corresponded to the first failure crack.

In contrast to the analytical and numerical first failure crack locations r_{max} and r_{FE}, the experimental first failure crack location $r_{failure}$ of the MAN L-beam specimens differed from those fabricated by AFP technology.

For six out of seven MAN L-beam specimens, $r_{failure}$ was between 0.38 and 0.55. That of L-beam specimen MAN-09 was at 0.19. None of those L-beam specimens broke thus close to the analytically estimated (and numerically calculated) location. It can hence be concluded, that the MAN L-beam specimens did not break mechanically, i.e. at the radial position of the ILTS, but most likely due to defects and heterogeneities in the composite material that caused premature material failure.

In contrast, five out of seven AFP L-beam specimens broke at a location very close to the analytically estimated and numerically calculated radial positions r_{max} and r_{FE}. For those five AFP L-beam specimens it can hence be assumed that defects within the material were sufficiently small to exclude premature specimen failure during loading. The mechanical limit of the those specimens has therefore been reached.

The observations on the experimental first failure crack locations are summarized in Tab. 9.2.

9.4 Load at failure and ILTS

As depicted in Fig. 9.2, AFP L-beam specimens failed at higher loads then MAN L-beam specimens. The mean load at failure of AFP L-beam specimens amounted to 6661 ± 427 N, that of MAN specimens to 3983 ± 740 N corresponding to a difference of 40.2 %. These results are replicated in Tab. 9.2.

Further, Tab. 9.2 contrasts the ILTS mean values of both specimens types for the specimen thicknesses $t_{max,mean}$, $t_{mean,mean}$ and $t_{min,mean}$, estimated by Kedward et al.'s solution and by FE calculation at r_{FE}.

The mean ILTS of the MAN L-beam specimens estimated by Kedward et al.'s solution is, regardless of the specimen thickness, 40.2 % smaller than that of the AFP L-beam specimens. The difference of the mean S_{33} at r_{FE} amounts to 43.0 %.

The S_{33} value was further defined at the experimentally observed first failure crack location $r_{failure}$ for all AFP and MAN L-beam specimens. For $t_{mean,mean}$, the resulting mean values (67.0±6.6 MPa for AFP and 35.6±5.4 MPa for MAN L-beam specimens) show that the difference in the out-of-plane strength between AFP and MAN L-beam specimens increases to 46.8 % (see Tab. 9.2).

The L-beam specimens fabricated by AFP technology resulted hence in more consistent material responses and higher ILTS values than the MAN L-beam specimens.

9.5 Macroscopic defects

AFP and MAN L-beam specimens were investigated in terms of macroscopic defects that might have triggered premature specimen failure. Therefore, the specimens were polished during 2 min with #500 abrasive papers from Struers, and, during 1 min 30 sec, with #2000 and #4000 abrasive papers, each. The polished sections were finally investigated with the stereo microscope MZ16 from LEICA, using the software LCmicro, version 2.2, from Olympus. Fig. 9.5a and Fig. 9.5b show the microstructure of the specimen arms and of the curved segment of L-beam specimen AFP-09, and Fig. 9.5c and Fig. 9.5d the microstructure of specimen MAN-02. No macroscopic defects (ply wrinkling) could be detected for MAN L-beam specimens. A lay-up defect was found for specimen AFP-09. This can be seen in Fig. 9.5b. This defect is most likely the end of a 6.35 mm wide tape which was not noticed during manufacturing of the AFP L-beam panel. This defect, corresponding to ply 29, can be considered as an isolated event, as it was only one tape, and

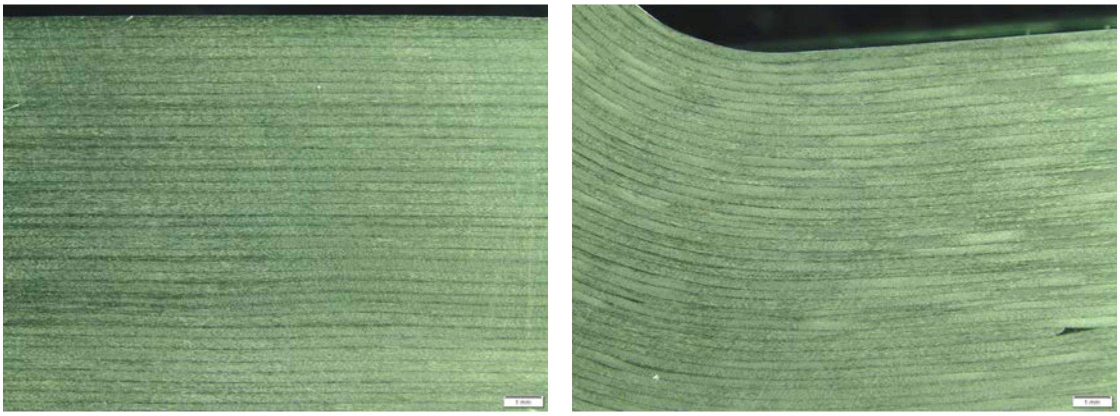

(a) *AFP-09, mircostructure of the L-beam's arm.* **(b)** *AFP-09, mircostructure of curved segment.*

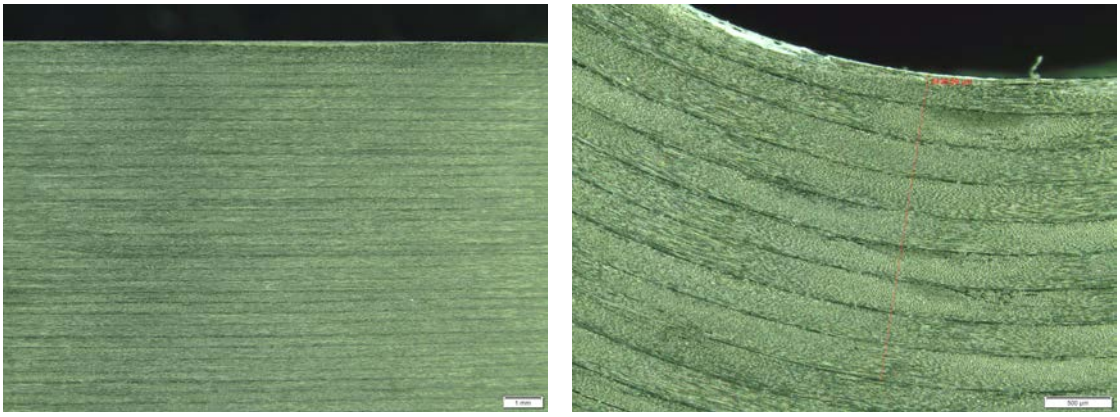

(c) *AFP-02, mircostructure of the L-beam's arm.* **(d)** *AFP-02, mircostructure of curved segment.*

Fig. 9.5. *Images of microstructure of L-beam specimen (a), (b) AFP-09 and (c), (d) MAN-02. The scale of (a), (b) and (c) is set to* 1 mm, *that of (d) to* 500 µm.

had finally no influence on the first failure crack formation (the first failure crack location of AFP-09 was between ply 14/15, see Tab. 7.4). It can be stated, that the microstructure of AFP and MAN L-beam specimens was similar and did not give an explanation on the higher ILTS results of AFP L-beam specimens.

Tab. 9.2. *Confrontation of results of AFP and MAN L-beam specimens tested in 4PB*

	AFP			Difference	MAN		
	$t_{max,mean}$	$t_{mean,mean}$	$t_{min,mean}$		$t_{max,mean}$	$t_{mean,mean}$	$t_{min,mean}$
Reproducibility	very good (7/7 L-beam specimens)			0 %	very good (7/7 L-beam specimens)		
Load at failure [N]	6661 ± 427			40.2 %	3983 ± 740		
Mean stiffness $[\frac{N}{mm^2}]$ (reference value)	3743 ± 104			0.3 %	3735 ± 104		
Location of the first failure crack	For 5/7 L-beams at the analytically estimated r_{max} → 5/7 L-beams broke mechanically			71.4 %	For 0/7 L-beams at the analytically estimated r_{max} → 0/7 L-beams broke mechanically		
ILTS$_{\text{Kedward et al.}}$ [MPa]	76.1 ± 4.7	**73.7 ± 4.6**	71.2 ± 4.4	40.2 %	47.5 ± 8.5	**44.1 ± 7.6**	41.5 ± 7.2
S_{33} (r_{FE}) [MPa]	80.0 ± 5.6	**76.7 ± 5.5**	71.9 ± 4.7	43.0 %	48.6 ± 9.7	**43.7 ± 8.0**	40.3 ± 7.1
S_{33} $(r_{failure})$ [MPa]		**67.0 ± 6.5**		46.8 %		**35.6 ± 5.4**	

9.6 Investigation of the cross sections of AFP and MAN L-beam specimens

The L-beam specimens were sectioned after test completion and the zone in the curved segment containing the cracks was investigated using an optical microscope.

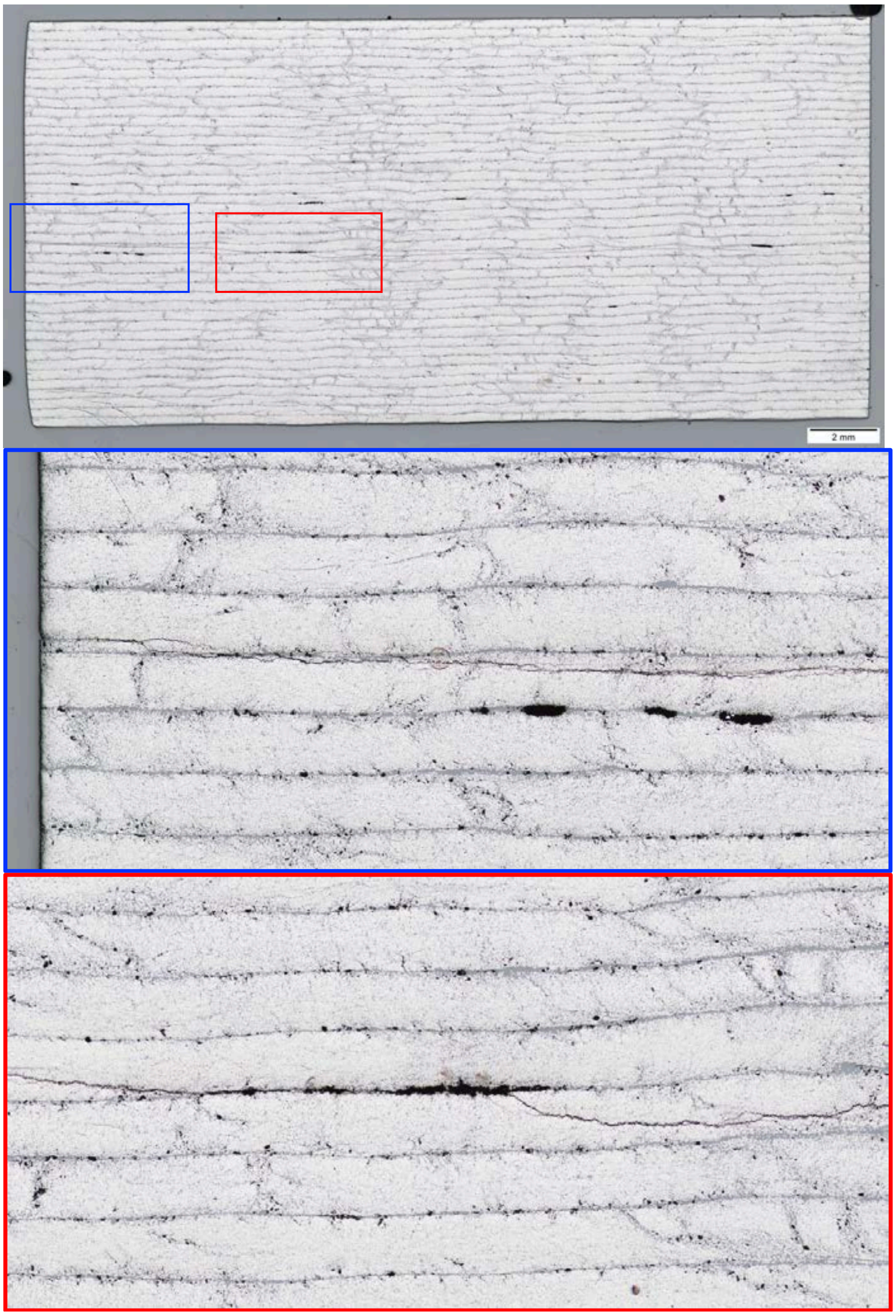

à

Fig. 9.6. *Cross section of L-beam specimen MAN-06. The crack path is mostly intralaminar and interlaminar when pockets of porosity are given.*

It was found that for MAN L-beam specimens, localised porosity was observed between some plies. This is exemplarily shown in Fig. 9.6 for L-beam specimen MAN-06. These observations were primarily made for MAN L-beam specimens where the first failure crack location differed from the analytically estimated one (see Tab. 8.6) and for which the ILTS values were the lowest. For all MAN L-beam specimens, the crack was further straight through the width. Its location on the face was identical to that inside. Indeed, the crack always ran on two plies. Most of its path was intralaminar. It was interlaminar when porosity pockets were observed.

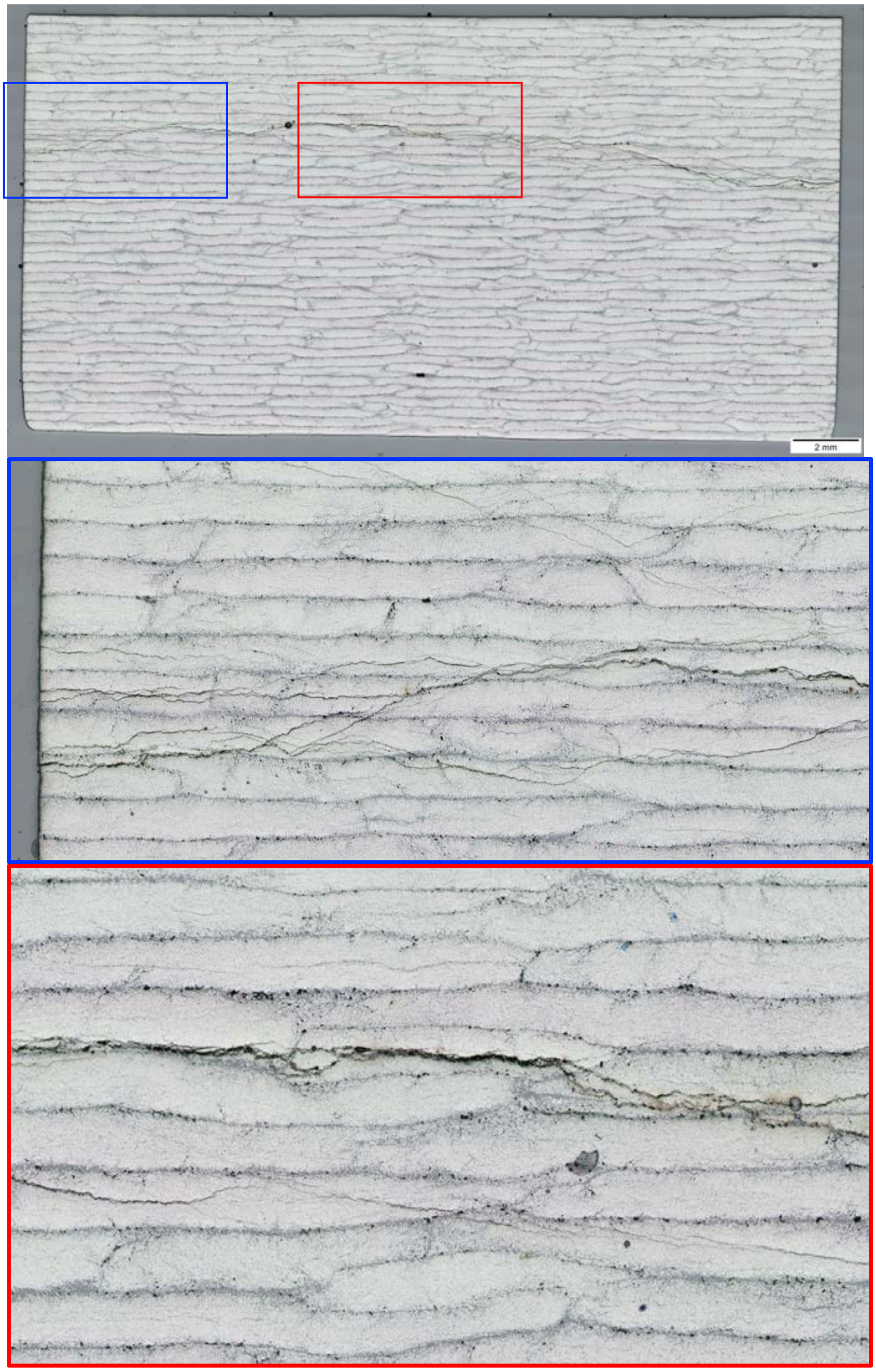

à

Fig. 9.7. *Cross section of L-beam specimen AFP-09. The porosity is more diffuse and located between the tapes, so that "between" and "inside" each ply. The crack is translaminar, running through several plies (up to 6).*

In contrast, for AFP L-beam specimens, areas of local porosity, if existing, were much smaller than for MAN L-beam specimens. Fig. 9.7 shows this exemplarily for L-beam specimen AFP-09. The porosity was more diffuse and located between the tapes, hence *between* each ply and *inside* each ply. It was further observed that the crack was translaminar, which means that it ran through several plies. It is assumed that the crack originated from the inside of the specimen and propagated through the thickness where it branched many times, so that many cracks reached the free surfaces. The difference between the location of the initiation crack and the positions of the observed cracks may differ by up to three plies in the different L-beam specimens.

9.7 Influence of the manufacturing processes on the ILTS

With regard to the manufacturing processes of AFP and MAN L-beam specimens, the following similarities and differences can be noted. MAN and AFP L-beam specimens were made from the same material. They were laid-up on the same aluminium mould and experienced the same curing cycle. Both L-beam panels were machined by mitre saw to defined L-beam widths. Both specimen types had the same stiffnesses.
Differences were given in the spyking process, as well as in the lay-up process. This needed hence to be discussed in more detail, especially the compaction mode.

Spyking

A difference between the two manufacturing processes concerned the ply preparation before manual hand lay-up. Spyking of the prepreg sheets (see Fig. 8.3) generally allowed to release some blocked air between the plies during curing. This created, however, small holes and local fibre misalignment.
Looking at the automated process, on can state that AFP tapes exhibited a certain variability in their width (6.35 ± 0.125 mm). Further, the robot's head accuracy was ±0.125 mm. This led to the fact that the robot left a gap of ~0.5 mm between each of the bands of the plies, each band was composed of 8 tapes. This means, that there was a creation of structures of longitudinal gaps (air inclusions). Lan et al. [2015] demonstrated, however, that those gaps, created during tape laying by the robot, are healed during curing when using a caul plate.

Compaction modes

AFP and MAN L-beam specimens experienced different compaction modes.
The robot compacted each ply with a lay-up contact pressure of ~5 bar. During tape deposition, the previous layered tape was reheated by the robot head to $\sim$35-45 °C. This lowered the viscosity (1000 Pa s) and increased the tacking between the plies.
According to Marchandise [2020], the action of the compacting of the robot head is always perfectly in line with the normal of the mould surface (Fig. 9.8), resulting in constant ply thicknesses. Such a constant pressure could not be obtained by laying-up plies manually with thumbs and a spatula as this was the case for the hand lay-up fabrication.
Unlike specimen manufacturing with AFP technology, the vacuum compaction in the hand lay-up process acts normal to the surface of the prepreg (Fig. 9.9) and not to the surface of the mould [Marchandise, 2020]. The consequences of this for MAN L-beam specimens

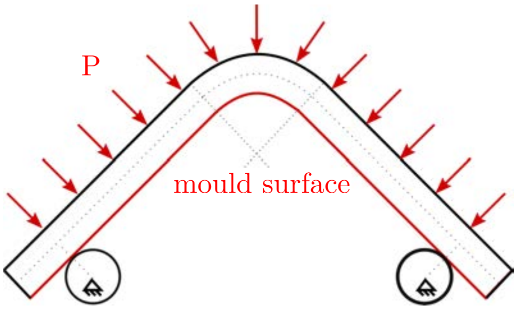

Fig. 9.8. *Compaction normal to the mould surface. The ply thicknesses are regular.*

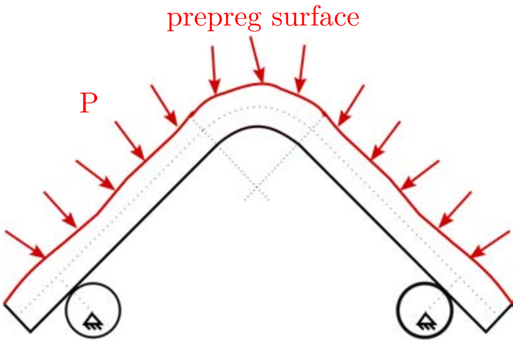

Fig. 9.9. *Compaction normal to the prepreg surface. The ply thicknesses are irregular.*

were irregular specimen thicknesses over the prepreg panel, the first aspect to keep in mind.

For intermediate debulking sequences every three plies (in the hand lay-up process), the developed length of the third ply was further always longer than that of the first (and second) ply, the second aspect to remember.

An irregular ply thickness may hence be responsible for the apparition of irregularities on the surface of the prepregs, such as plies that were not correctly oriented, resulting in a misleading of the vacuum direction compaction.

From Marchandise [2020] it is known that the second aspect results in differences in fibre tensions within a three plies sequence. This is due to the fact that the first ply is applied on a vacuum compacted surface, and the two subsequent plies on an heterogeneously manually compacted surface.

In the scope of the confrontation of the compaction modes of AFP and MAN L-beam specimens, the compaction irregularities during the hand lay-up process had the following consequences:

1. The impact of small geometrical irregularities on the prepreg surfaces were exacerbated during autoclave curing. This was due to the differences in the compaction force and in the resulting velocity of the prepreg. Intermediate debulking happened at ~1 bar with a prepreg viscosity of 10 000 Pa s, autoclave curing was at ~7 bar with a viscosity of 10 Pa s. It can be assumed that the panel surface of AFP L-beam specimens was sufficiently regular to ensure a compaction normal to the mould during autoclave curing. The caul plate stiffness was sufficient to correct small irregularities of the AFP panel surface. This was, however, not the case for MAN L-beam specimens.

2. The second consequence is the results of the geometrical irregularities that are exacerbated during autoclave curing. It promoted an uncontrolled resin flow from the curved segment to the L-beam arms, as this was observed in Fig. 9.1b. The fibre volume fraction has hence increased in the curved segment, whereas it has decreased in the L-beams arms.

3. The third consequence comes from the initial reason why intermediate debulking is applied during the prepreg lay-up: avoiding blocked air that can lead to porosity

after autoclave curing. The porosity levels of AFP and MAN L-beam specimens were similar, however bigger areas of localised porosities between the plies were found for MAN L-beam specimens, compared to AFP L-beam specimens (see Fig. 9.6 and Fig. 9.7).

These reflections and observations are replicated in Tab. 9.3.

9.8 Conclusion on the present study

It can be concluded, that the AFP manufacturing process has a high influence on the specimen geometry, and on the mechanical behaviour of the L-beam specimens, especially on the ILTS. The key features of the AFP technology (staggering, compaction at every ply, and enhanced tacking between layers) play a decisive role.

It is assumed that the totality of the factors and consequences given in Tab. 9.3 (variation in ply thickness due to manual ply application, developed lengths of the first, second and third plies, compaction normal to the prepreg surface, generation of small defects on the prepreg surface, difference in fibre volume fraction curved segment/specimen's arms, and especially the presence of areas of localised porosities) are responsible for the lower ILTS values of the MAN L-beam specimens.

The failure locations of the AFP L-beams were those expected by the analytical or numerical estimations (see Sec. 9.3).

AFP L-beam specimens have further shown no large areas of localised porosity. It was diffuse and located between the tapes (see Fig. 9.7). The crack path was translaminar, and ran through several plies, exhibiting many branches.

In contrast, the manual hand lay-up was intolerant to smallest lay-up defects resulting in an instability of the composite structure causing premature specimen failure. The ILTS values were 40.2 % lower (Kedward et al.'s solution) than that of the AFP L-beam specimens and more scattered. The scattering was related to specimens for which the ILTS value was low, the failure location differed from the estimated one and for which relatively large areas of localised porosity were observed, and from which the crack mostly originated. When the ILTS was high, no such areas were observed, so that no *defect*, corresponding to weak zones, was at stake. For all MAN L-beam specimens, the crack path was straight through the width and mostly intralaminar. It was interlaminar when pockets of porosity were observed. Nevertheless, the maximum ILTS value for MAN L-beam specimens was lower than the minimum value of the AFP ones. The enhanced bonding between the plies during the AFP processing was probably responsible for this.

For further studies, it is proposed, to investigate more precisely the material defects (porosities, fibre misalignment, ply thickness variations) within the microstructure, as well as the differences in fibre volume fraction in order to categorize more exactly the impact of each factor on the ILTS.

Taking a look at the literature, similar observations concerning the compaction method and the resulting ILTS have been done by Charrier [2013] for L-beam specimens with different ply orientations. The author studied two different specimen types whose major difference was based on the intermediate debulking. As mentioned in Sec. 5.1, Charrier applied intermediate debulking every forth to sixth ply on STAF and every second ply on STRENGTH L-beam specimens. Charrier [2013] stated that the ILTS of STRENGTH L-beam specimens was 10 % higher than that of STAF L-beam specimens.

Considering the given context, L-beam specimens were chosen as they represented a simplified geometry of the hydrofoil elbow. The following train of thoughts taking into account the size difference between L-beam specimen and hydrofoil remains.
Manufacturing processes lead necessarily to defects in the material. Created defects in L-beam specimens are smaller compared to defects that are created in semi-structures (Fig. 1.5) or in hydrofoils. The L-beam specimen represented the smallest specimen size studied in the laboratory in the scope of the present study. The developed analytical and numerical tools for the ILTS determination were already very complex at this scale. As given above, these tools did not take into account any material defects or variations in the specimen geometry. Perfect specimens were assumed. Numerical and analytical methods to determine the ILTS of semi-structures or hydrofoils would hence be much more complex, since material defects on the micro (porosity, voids), meso (ply waviness and wrinkling, fibre waviness), and macro scale (variations in the geometry) over a more important geometry (greater thicknesses t, widths w, lengths L, inner r_i and outer r_o radii) would have to be taken into account. This is of greatest challenge. Effort and benefit must be weighed carefully.

Tab. 9.3. *Compaction modes applied in AFP and MAN L-beam manufacturing and impact on ILTS results.*

MAN	**AFP**
Given: - Variation in the ply thickness due to manual ply application. - Developed length of third ply is always longer than that of first and second ply.	
↓	
Compaction modes	
↓	↓
MAN: Intermediate debulking normal to the prepreg surface.	AFP: Robot head compaction normal to the mould surface.
↓ ∼1 bar At room temperature. Prepreg viscosity: 10 000 Pa s t = 20 min	↓ ∼5 bar T = 35-45 °C Prepreg viscosity: 1000 Pa s t = 10 sec
Leads to: - Hetrogeneous lay-up compaction. - Generation of small defects on the prepreg surface. - Variations in the ply thickness.	Leads to: - Homogeneous lay-up compaction. - Constant specimen thickness.
↓	↓
Autoclave curing (at 7 bar and 120 °, prepreg viscosity: 10 Pa s, curing time > 600 min)	
↓	↓
Consequences: Differences in: - Ply thickness curved segment/specimen arm. - Fibre volume fraction curved segment/specimen arm. Areas of localised porosities (Fig. 9.6) Not conform to the FE model / analytical solutions: - Macroscopic variations in the geometry (Fig. 9.1c).	Consequences: - Constant ply thickness. - Homogeneous fibre volume fraction. - Conform to the FE model /analytical solutions.
⇓	⇓
Low ILTS results	High ILTS results

PART IV

SUMMARY AND PERSPECTIVES

"One cannot not communicate."

—PAUL WATZLAWICK

Summary and Perspectives

The research work of the present thesis addressed two issues, both related to the revaluation of hydrofoils, made from carbon fibre reinforced composite materials.
The first issue dealt the confrontation of two experimental methods by which the compressive strengths of seven different CFRP specimens, referred to as series 1 to 7, were determined. The first method contained tensile tests on ±45° specimens, the determination of the fibre misalignment angle, and the application of the analytical solutions of Budiansky & Fleck and Grandidier et al.. The second method based on 4PB tests. The focus of this study was on the determination of the in- and out-of-plane fibre misalignment angles using Yurgartis's method. The objective was to relate the determined misalignment angle to the (mis-)matching of the compressive strengths, determined by both methods. Therefore, cartographies of the spatial fibre distribution were established in order to evaluate the results.
The second issue dealt with the question of the influence of the fabrication process of unidirectional CFRP L-beam specimens on the material behaviour, especially on the ILTS. This question arose, as hydrofoils are nowadays manufactured by traditional hand lay-up, and more recently by automated fibre placement technology. L-beams specimens were hence fabricated by both technologies, tested in 4PB, and their results were confronted.
These two issues were chosen as hydrofoils are dimensioned in terms of compressive strength, and ILTS.

Part II: The compressive strength X_c

The first part started with a brief introduction to fibre micro buckling models. The kink-band model of Budiansky & Fleck [1993], as well as the model from Grandidier et al. [2012], taking into account the structural effect, were presented. It was stated that the matrix plasticity seemed to have a governing impact on the development of fibre instability mechanisms in local regions, and that the fibre misalignment angle was one of the most concerned parameters [Grandidier et al., 2012]. Then, the terms *fibre misalignment* and *fibre waviness* were concretised, by referring to definitions found in the literature. Afterwards, a review on the origin of fibre misalignment, and other material defects related to the manufacturing process were discussed. The review of Potter [2009] should be mentioned, as his taxonomic diagram visualised well the origins of different defect types, i.a. those of fibre misalignments. The consequences of fibre misalignment on the mechanical properties of composite structures were then given. Last, existing methods on fibre misalignment and fibre waviness determination were presented. The advantages, and limitations, as well as references found in the literature were listed.

The theory of Yurgartis's method was then introduced by describing the different sample sectioning directions, along the specimen thickness and width, as well as the trigonometric functions to calculate the in- and out-of-plane fibre misalignment angles. Two parameters, the fibre diameter, and the length of the major axes of the ellipses, were to be determined. In practice, several steps were carried out to get from the raw sample to the determination of the fibre misalignment angles: sample sectioning along the specimen thickness and width, resin coating and polishing, image recording with an optical microscope, image post-processing with *ImageJ*, calculation of fibre misalignment angles. One SD of the normal distribution was therefore taken.

Before determining the in- and out-of-plane fibre misalignment angles, a sensibility study on the fibre diameter was realised. Fibre misalignment angles determined from four different diameter sources were compared. The mean diameter was first determined by sectioning the samples perpendicularly to their fibre direction. This was the common procedure in Yurgartis's method. The fibre diameter was second taken from the carbon fibre data sheet, directly. Last, the minor axis of the ellipses were considered to correspond to the fibre diameter. The simple minor axes, and the mean value of the minor axes were the third and fourth diameter source. It was found, that the diameter from perpendicularly sectioning, and the mean value of the minor axes were the consistent diameter sources in the determination of the in- and out-of-plane fibre misalignment angles. The mean value of the minor axes was finally chosen as it required one less machining step.
It was further found, that the fibre section of the first and second series were not circular, but had deformed shapes, resembling to *kidney beans*. Similar observations were made by Paluch [1994]. The fibre mean diameter could hence not be correctly determined. Series 1 and 2 were therefore excluded from the further study.

The first experimental method required the realisation of tensile tests on ±45° laminates to determine the parameters of the Ramberg-Osgood (RO) constitutive law. These tests were realised according to the standard NF EN ISO 14129 (NF EN ISO, 1998). All necessary parameters (those of the RO constitutive law, and the fibre misalignment angle) were hence determined to apply the analytical solutions of Budiansky & Fleck and Grandidier et al..
The second experimental method to determine the compressive strength required the realisation of 4PB tests. This was done according to the standard ASTM D6272 (ASTM, 2008).
For detailed information on the test implementations, the reader was referred to Mechin et al. [2019].

The confrontation of the compressive strengths determined by both methods was done by plotting the compressive strengths as a function of the in- and out-of-plane fibre misalignment angles.
The results were evaluated with regard to the spatial fibre distributions along the x- and y-axis from which the fibre misalignment angles were determined. Therefore, cartographies of the fibre alignment distributions were created, and the arrangement of the fibres was classified into different categories: clusters of fibres ≤-1σ or ≥1σ, single fibres strongly

misaligned, or inhomogeneous fibre distributions.

It was found, that the (mis-)matching of both compressive strengths was related to the fibre angle distribution, when the analytically estimated compressive strength was calculated using the out-of-plane fibre misalignment angle. This means that a good match of both compressive strengths was given, when less clusters or strongly misaligned fibres were given, or a poor match was given, when clusters and strongly misaligned were highly present. This was the case in 70-80 % of the obervations.
These observations could not be done for compressive strengths determined analytically using the in-plane fibre misalignment angle. Only of the 10-50 % (mis-)matchings of the compressive strengths were in accordance with the observed fibre alignment distributions.

For future studies it was finally proposed to programme an algorithm detecting the dimensions and positions of all ellipses from the images taken along the specimen widths and thicknesses, in order define the fibre misalignment angle more preciously, and to introduce another parameter into the discussion: the fibre volume fraction.

Part III: The interlaminar tensile strength (ILTS)

The second part started with a bibliographic review on the ILTS determination with regard to the specimen production, as well as on literature discussing the confrontation of results of specimens of different shapes fabricated by hand lay-up and by automated fibre placement technology.
Research works on tensile test specimens [Kitching et al., 1984; Lagace & Weems, 1989; Hodgkinson et al., 1992], and on curved specimens, such as semi-circular Hiel et al. [1991]; Ko & Jackson [1989], semi-elliptical Hiel et al. [1991]; Ko & Jackson [1990], L-shape Charrier et al. [2016]; Jackson & Ifju [1996]; Ranz et al. [2017]; Shivakumar et al. [1994], horseshoe Ko & Jackson [1990], and humpback Wisnom & Jones [1996], loaded in different bending configurations, were discussed.
The test configuration developed by Jackson & Ifju [1996], as well as the analytical solutions of Lekhnitskii [1968] and of Kedward et al. [1989] were implemented in the standard ASTM D6415 / D6415M-06a [2013], and form, nowadays, the basis for the ILTS determination of unidirectional CFRP composites.

The three tools which were developed in the scope of this study to confront the results of AFP and MAN L-beam specimens tested in 4PB were then presented.
The analytical tool included the setting up of the analytical solutions of Lekhnitskii [1968] and Kedward et al. [1989] within a script encoded with python language. The analytical tool was validated with results from the literature [Charrier et al., 2016].
The experimental tool contained the creation of the 4PB test setup. Geometrical, mechanical and technological aspects were discussed. Further, the applied instrumentation (DIC, AE, LVDT, strain gauges) during test execution, as well as the settings during test implementation were presented.

The numerical tool, the creation of the FE model, was finally introduced. Therefore, the commercial code Abaqus 6 was used. In order to automate the model creation, scripts encoded with python and Abaqus python languages were developed. Sensibility studies of the influence of the mesh size, and of the material chose for the loading bars on the numerical results were conducted. The mesh was refined until differences of less than 1 % on the load-displacement diagrams were obtained. The loading bars were taken as rigid, as the deformability of steel loading bars was found to be of very little influence. Last, the numerical tool was validated with results from the literature [Charrier et al., 2016].

Afterwards, the material properties, as well as the manufacturing processes of the L-beam specimens, the traditional hand lay-up and the automated fibre placement technology, were presented. Differences between the manual application of the prepreg sheets on the aluminium mould, and the tape laying process with the robot head were in the focus. A protocol of the realisation of the 4PB tests on AFP and MAN L-beam specimens was finally given.

First, an explication to the non-linearity of the load-displacement diagrams at test beginning, was given. FE calculations were performed to explore that the non-linearity resulted from the change in the contact point between L-beam and the LVDT tip due to a slight difference in the vertical alignment of the lower loading bars.

It was further found that the analytical solution of Kedward et al. [1989] provided ILTS results closer to the numerical calculation, than the solution of Lekhnitskii [1968]. The percentage error of Kedward et al.'s solution was less than 5 %. That of Lekhnitskii [1968] differed between 10 and 15 %. By replicating Fig. 5.2 from Kedward et al. [1989] with the elastic material properties used in this research study, and by adding the FE calculations, it was found, that the better estimation was due the elastic properties of the material.

The results of the AFP and the MAN L-beam specimens tested in 4PB were then confronted.

High test reproducibility of both specimen types were found for both specimen types (seven out of seven tested specimens, each).

Differences in the specimen widths and inner radii were found to be within the accuracy of the measuring instruments and were hence considered to be zero. The initial angles between the horizontal line and the specimens' arms were equal, as well. The specimen thicknesses measured in the curved segment and at the specimens' arms distinguished, however, from each other. The curved segment of MAN L-beam specimens were thinner compared to that of AFP L-beam specimens. The specimen arms MAN L-beam specimens were thicker than that of AFP L-beam specimens. It was found that the thickness variations of MAN L-beam specimens were twice as large as that that of AFP L-beam specimens. This was related to the compaction mode during the manufacturing process.

AFP and MAN L-beam specimens were then compared in terms of their stiffnesses. No differences between manual hand lay-up and AFP manufacturing was found in terms of elasticity.

First failure crack locations were compared analytically, numerically and experimentally. Analytically and numerically, the first failure crack locations were located at approximately 0.3 (normalized value over the thickness) from the inner radius. This corresponded to a theoretically failure location between ply 12 and 13. Experimentally, five out of seven AFP L-beam specimens broke at a location very close to the theoretical location. None of the MAN L-beam specimens failed close to the analytical/numerical value. It was hence concluded that MAN L-beam specimens did not failure at the radial position of the ILTS but due to material defects and heterogeneities that caused premature failure. Contrarily, AFP L-beam specimens reached their mechanical limit, as material defects were assumed to be sufficiently small to exclude premature material failure.

AFP and MAN L-beam specimens were investigated in terms of macroscopic material defects. The specimens were polished and examined with a stereo microscope. No macroscopic defects (ply wrinkling) that might caused premature specimen failure could be observed.

The mean loads at failure of AFP and MAN L-beam specimens differed by 40.2 %. The same applied to the analytically estimated ILTS values of both specimen types. The ILTS of AFP L-beam specimens was 40.2 % higher than that of MAN L-beam specimens. The difference in the numerically calculated out-of-plane tensile strength value S_{33} amounted 43.0 %. Calculating the S_{33} at the experimentally observed first failure crack location, the difference in S_{33} increased to 46.8 %. AFP L-beam specimens reached hence much higher ILTS results that MAN L-beam specimens.

An explanation of this difference was found in the compaction modes during the manufacturing processes. Intermediate debulking was normal to the prepreg surface and not normal to the mould, as this was the case for plies laid-up by AFP technology [Marchandise, 2020].

During manual hand lay-up, thickness variations in the plies were created. As intermediate debulking was applied every three plies, the developed length of the third ply was always longer than that of the first ply which was laid-up on a compacted ply. This resulted in different fibre tensions within a three ply sequence. Irregularities on the compacted surfaces were hence given. These small geometrical irregularities were multiplied during autoclave curing (at 7 bar), as the viscosity of the prepreg (10 Pa s) was 1000 times lower than that during intermediate debulking (10 000 Pa s, à 1 bar). The above mentioned thickness differences between the curved segment and the specimen arms of MAN L-beam specimens was one macroscopic consequence.

For AFP L-beam specimens, the panel surface was sufficiently regular and the caul plate stiffness sufficed to correct small irregularities of the AFP panel.

AFP L-beam specimens have shown no large areas of localised porosity. It was diffuse and located between the tapes. The crack path was translaminar, and ran through several plies, exhibiting many branches.
For MAN L-beam specimens, large areas of localised porosity were observed, from which the crack mostly originated. The crack path was straight through the width and intralaminar. It was interlaminar when porosity pockets were observed.

For future studies it was proposed to investigate the factors related to the compaction mode and their consequences (compaction normal to the prepreg surface, variation in ply thickness, generation of small defects on the prepreg surface, resulting differences in the fibre volume fraction curved segment/specimen arms, macroscopic variations in the geometry, and porosity) that led to the poor mechanical response of the MAN L-beam specimens, in order to know the influence of each one.
Furthermore, attention was drawn to the fact that the L-beam specimen was a simplified shape of the hydrofoil elbow. Material defects resulting from the manufacturing process of semi-structures or hydrofoils have a more important impact on the material behaviour due to the size effect. To date, this is not a mastered issue.
The analytical solutions and the numerical model assumed further perfect L-beam specimens. Their application on AFP L-beam specimens were hence more coherent than for MAN L-beam specimens. Due to the size effect, the development of such tools for semi-structures and hydrofoils is a complex task.

COMMUNICATIONS AND PUBLICATIONS

Communications and publications

National communications (France)

MECAMAT, Rupture des Matériaux et des Structures

Aussois, 21-25 January 2019
M. Grabow, V. Keryvin, C. Baley, J.-C. Grandidier, O. Fagherazzi, A. Marchandise
"Corrélation expérimental/numérique sur la détermination du comportement mécanique hors plan de composites à fibres de carbone continues pour le nautisme de compétition" (Poster session)

21ème Journées Nantionales sur les Composites

Bordeaux, 1-3 July 2019
M. Grabow, V. Keryvin, C. Baley, J.-C. Grandidier, O. Fagherazzi, A. Marchandise
"Experimental/numerical correlation on the determination of the out-of-plane behaviour of continuous carbon fibre composites for competitive sailing" (Poster session)

International communications

6th Symposium from Groupe Indentation Multi-Echelle (GIME)

Liège (Belgium), 11-14 September 2018
M. Grabow, V. Keryvin
"Preliminary study on the feasibility of estimating the elastic constants of highly anisotropic fibres by instrumented nanoindentation" (Poster session)

22. Symposium Verbundwerkstoffe und Werkstoffverbunde

Kaiserslautern (Allemagne), 16-18 June 2019
M. Grabow, V. Keryvin, C. Baley, J.-C. Grandidier, O. Fagherazzi, A. Marchandise
"Experimental/numerical correlation on the determination of the out-of-plane behaviour of continuous carbon fibre composites for competitive sailing" (Poster session)

Publications

M. Grabow, V. Keryvin, J.-C. Grandidier, C. Baley, A. Marchandise, C. Le Guennec and O. Fagherazzi, *"Influence of the manufacturing process on the inter laminar tensile strength of continuous fibres / epoxy matrix composites: hand lay-up versus automated fibre placement"*, submission expected in April 2021 in Composites Part A: Applied Science and Manufacturing

ANNEXES

A.1 Misalignment angle results sources of series 4, 6 and 7 determined from different diameter

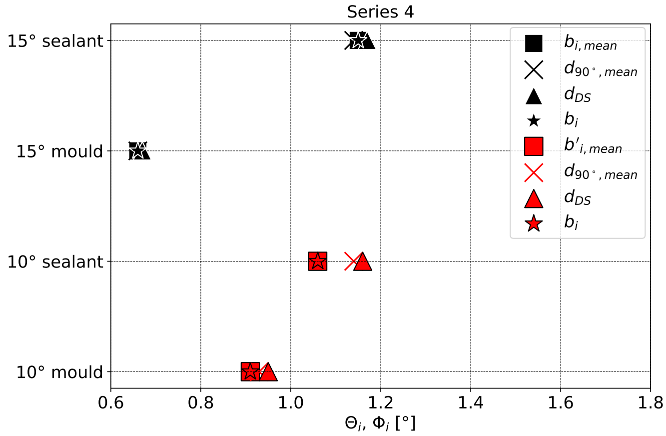

Fig. A.1. *Confrontation of fibre misalignment angles as a function of different fibre diameters for series 4.*

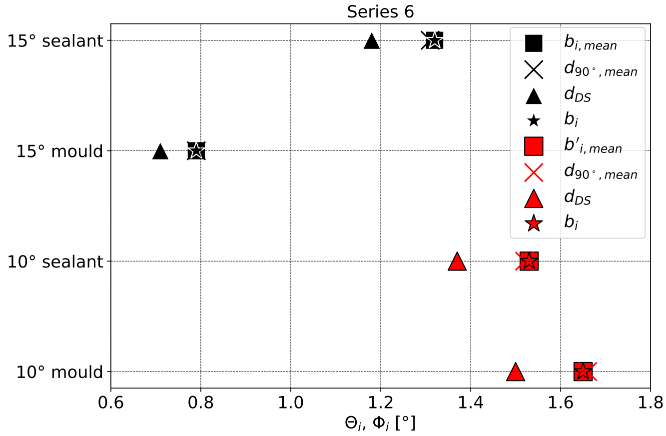

Fig. A.2. *Confrontation of fibre misalignment angles as a function of different fibre diameters for series 6.*

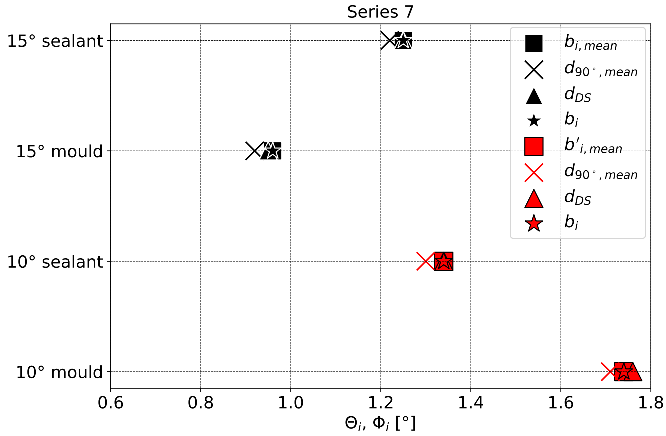

Fig. A.3. *Confrontation of fibre misalignment angles as a function of different fibre diameters for series 7.*

B.2 Design drawing of 4PB testing setup

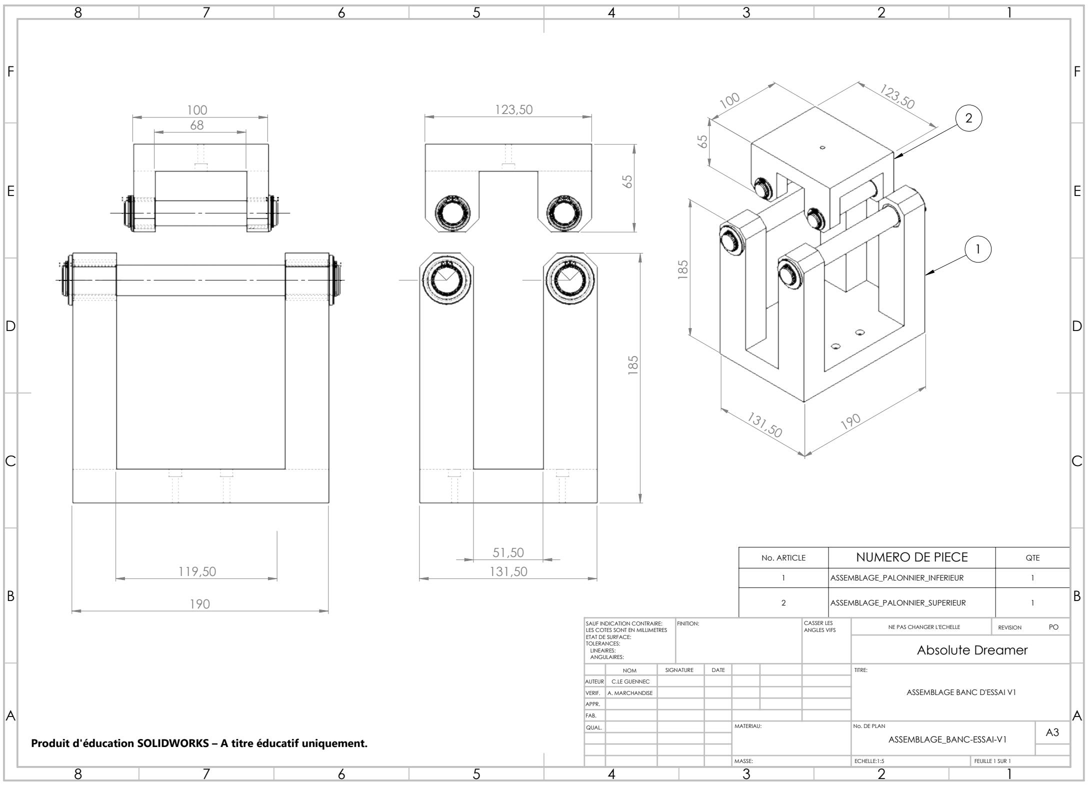

Fig. B.1. *Design drawing of 4PB test setup.*

B.3 Results AFP L-beam specimens

B.3.1 Crack localisations of AFP L-beam specimens tested in 4PB

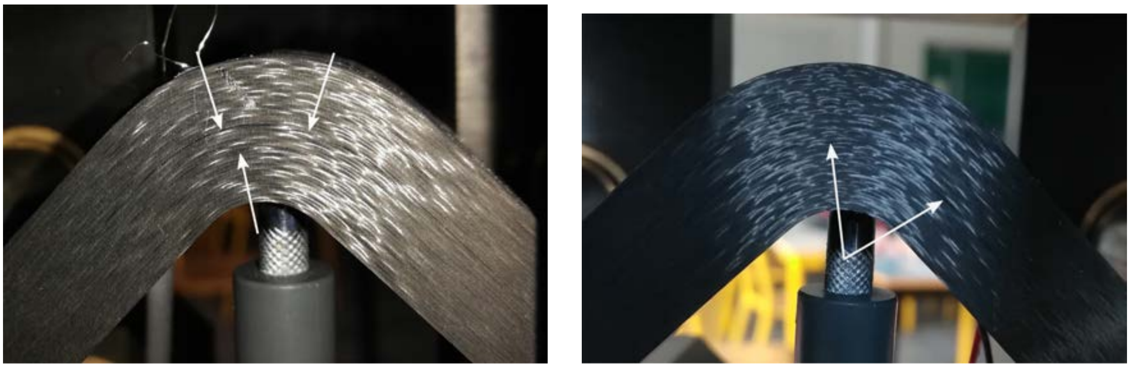

(a) *AFP-02* **(b)** *AFP-03*

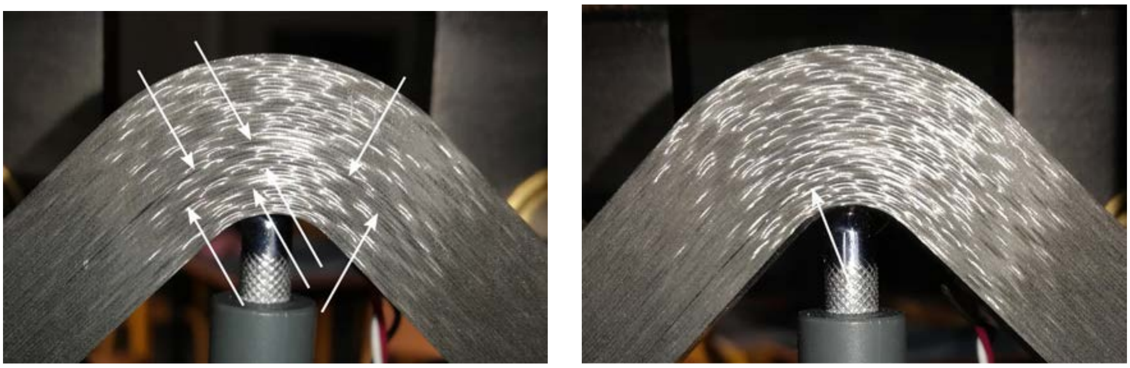

(c) *AFP-04* **(d)** *AFP-05*

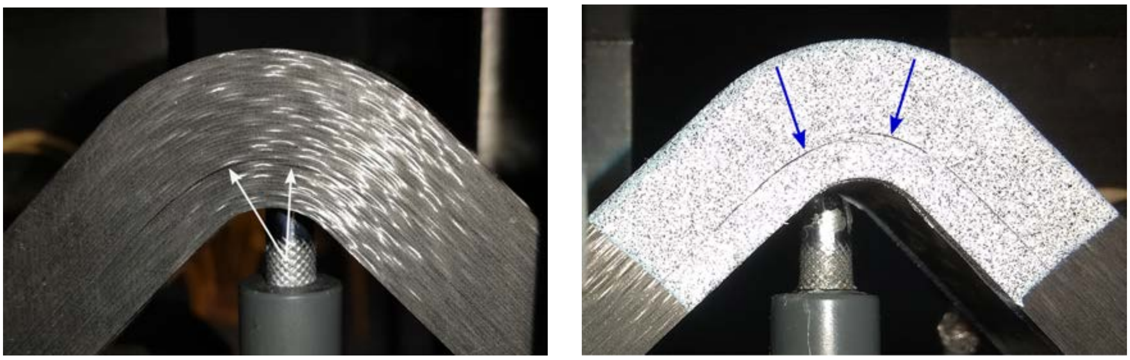

(e) *AFP-06* **(f)** *AFP-10*

Fig. B.2. *Photos of AFP L-beam specimens after test completion. White arrows show crack locations. First failure crack locations, identified by DIC, are marked by blue arrows.*

B.3.2 Experimental/numerical correlation of load-displacement diagrams of AFP L-beam specimens

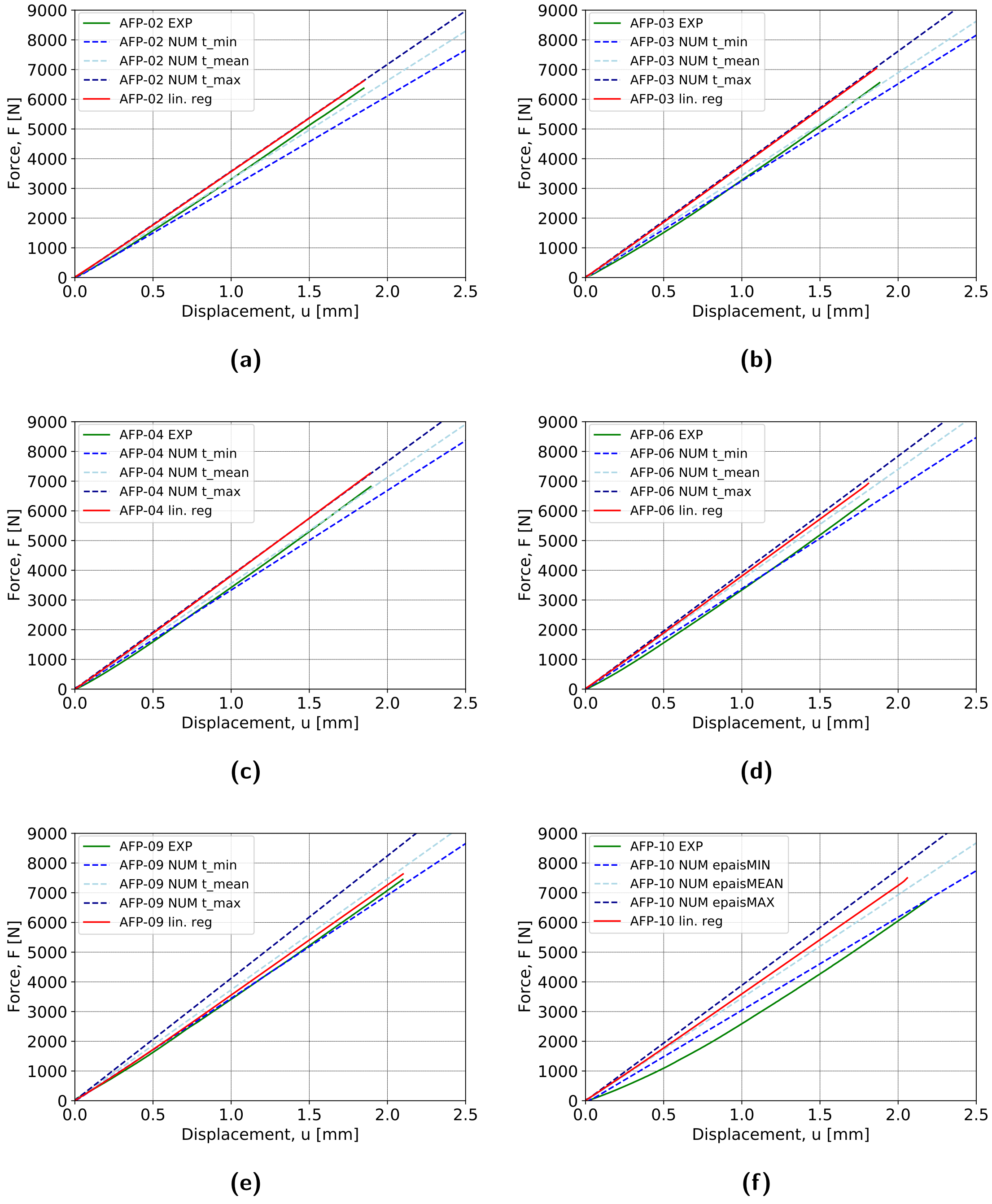

(a) **(b)**

(c) **(d)**

(e) **(f)**

Fig. B.3. *Force-displacement diagrams of AFP L-beam specimens. The specimen stiffness is located between* t_{mean} *and* t_{max} *for (d) AFP-06 and (f) AFP-10, between* t_{min} *and* t_{mean} *for specimen (c) AFP-09 and coincide with* t_{max} *for specimen (a) AFP-02, (c) AFP-03 and (d) AFP-04.*

B.3.3 Normalized S_{ij} as a function of the normalized thickness/width of AFP L-beam specimens

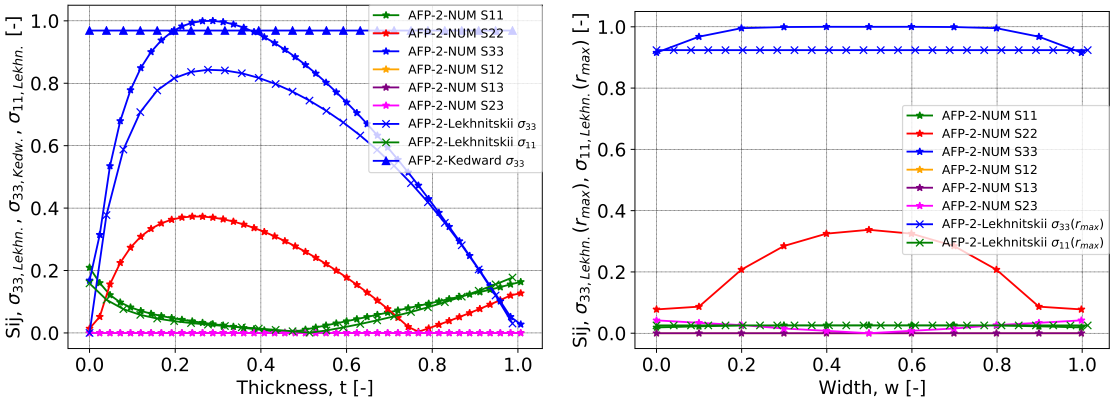

(a) **(b)**

Fig. B.4. *Normalized calculated stresses and strains S_{ij}, and analytically estimated radial and circumferential stresses $\sigma_{33,Lekhn.}$, $\sigma_{11,Lekhn.}$ (Lekhnitskii) and $\sigma_{33,Kedw.}$ (Kedward et al.) as a function of the normalized (a) thickness and (b) width of specimen AFP-02.*

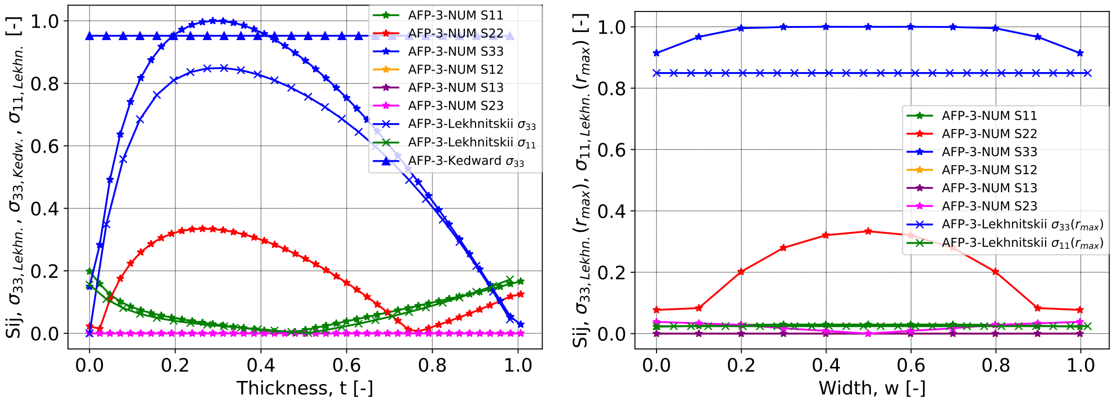

(a) **(b)**

Fig. B.5. *Normalized calculated stresses and strains S_{ij}, and analytically estimated radial and circumferential stresses $\sigma_{33,Lekhn.}$, $\sigma_{11,Lekhn.}$ (Lekhnitskii) and $\sigma_{33,Kedw.}$ (Kedward et al.) as a function of the normalized (a) thickness and (b) width of specimen AFP-03.*

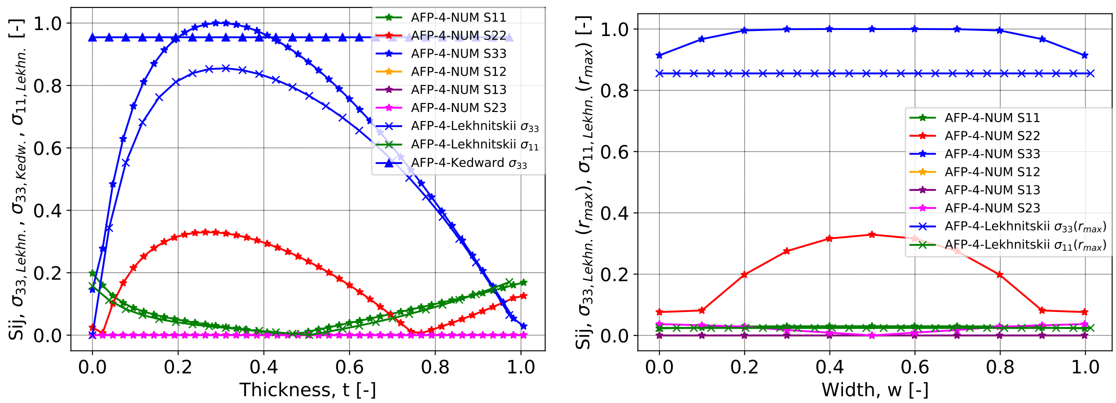

(a) **(b)**

Fig. B.6. *Normalized calculated stresses and strains* S_{ij}*, and analytically estimated radial and circumferential stresses* $\sigma_{33,Lekhn.}$*,* $\sigma_{11,Lekhn.}$ *(Lekhnitskii) and* $\sigma_{33,Kedw.}$ *(Kedward et al.) as a function of the normalized (a) thickness and (b) width of specimen AFP-04.*

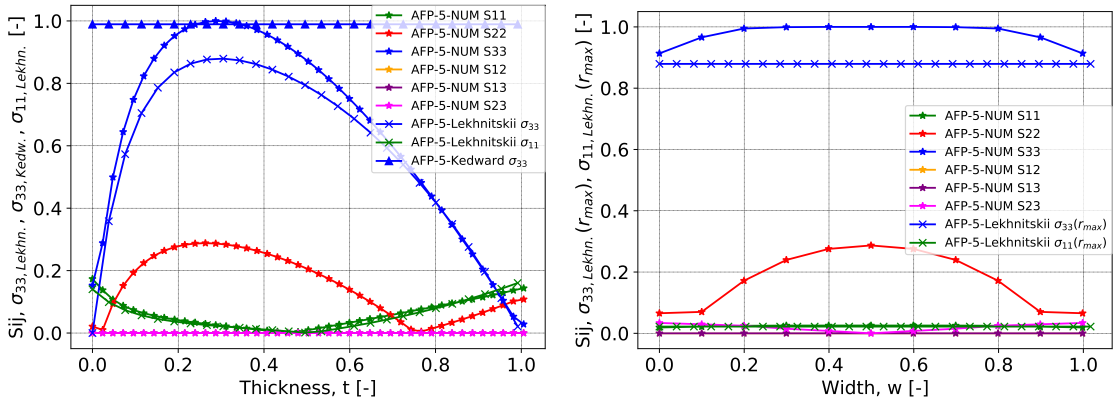

(a) **(b)**

Fig. B.7. *Normalized calculated stresses and strains* S_{ij}*, and analytically estimated radial and circumferential stresses* $\sigma_{33,Lekhn.}$*,* $\sigma_{11,Lekhn.}$ *(Lekhnitskii) and* $\sigma_{33,Kedw.}$ *(Kedward et al.) as a function of the normalized (a) thickness and (b) width of specimen AFP-05.*

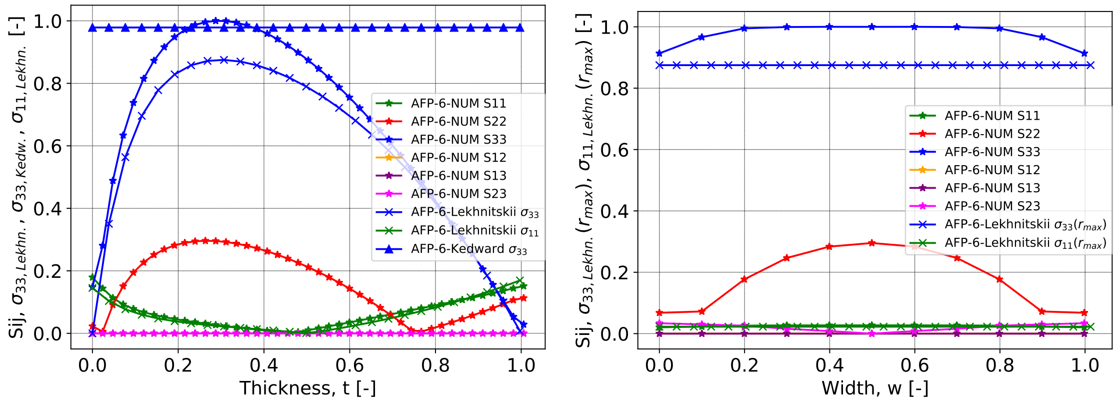

(a) **(b)**

Fig. B.8. *Normalized calculated stresses and strains* S_{ij}*, and analytically estimated radial and circumferential stresses* $\sigma_{33,Lekhn.}$*,* $\sigma_{11,Lekhn.}$ *(Lekhnitskii) and* $\sigma_{33,Kedw.}$ *(Kedward et al.) as a function of the normalized (a) thickness and (b) width of specimen AFP-06.*

B.3.4 Summary of the analytical, experimental and numerical results of AFP L-beam specimens tested in 4PB

Tab. B.1. *Comparison of the analytically estimated ILTS and the numerically calculated S_{33} of AFP L-beam specimen. S_{33} was determined by at the experimental measured force at failure. Error values in percent refer to the numerically calculated value.*

AFP	Specimen thickness			EXP											FEM		
		t [mm]	t_{max}-t_{min} [mm]	F_0 [N]	F_f [N]	Error [%]	d_f [mm]	Error [%]	ILTSKedward et al. [MPa]	Error [%]	ILTS Lekhnitskii [MPa]	Error [%]	$r_{max,Lekhnitskii}$ [%]	[mm]	RF [N]	U3 [mm]	S_{33} [MPa]
2	**max**	13.07				-0.8		-2.0	76.7	0.0	66.4	13.4	28.3	3.70	6322	1.81	76.7
	mean	12.66	0.79	-	6372	0.3	1.85	6.5	79.1	3.2	68.9	15.7	28.6	3.62	6394	1.98	81.7
	min	12.28				-0.3		13.1	81.6	4.3	71.4	16.3	28.9	3.54	6356	2.13	85.3
3	**max**	13.25				0		-5.0	70.7	1.5	62.6	12.8	29.6	3.92	6556	1.77	71.8
	mean	12.74	0.79	-	6558	1.0	1.86	5.7	73.4	4.8	65.5	15.1	29.9	3.81	6624	1.97	77.1
	min	12.46				0.3		10.5	75.0	5.4	67.2	15.3	30.1	3.76	6578	2.08	79.3
4	**max**	13.22				-1.1		-4.4	71.4	1.1	63.7	11.8	29.9	3.96	6748	1.81	72.2
	mean	12.85	0.69	-	6820	0.9	1.89	4.6	73.4	4.6	65.8	14.5	30.2	3.88	6880	1.98	77.0
	min	12.53				-0.3		9.7	75.3	4.9	67.7	14.5	30.4	3.81	6802	2.09	79.1
5	max	13.66				-0.3		-12.7	64.2	-1.2	56.7	10.6	29.3	4.01	6094	1.54	63.5
	mean	13.11	1.00	-	6113	-0.6	1.74	-3.1	66.8	1.1	59.4	12.1	29.7	3.90	6076	1.69	67.6
	min	12.66				-0.7		5.5	69.2	2.9	61.8	13.3	30.0	3.80	6068	1.84	71.3
6	max	13.35				-0.1		-7.7	66.7	1.1	59.4	11.9	29.9	3.89	6388	1.68	67.4
	mean	13.04	0.76	-	6393	-0.4	1.81	-2.2	68.2	2.2	61.0	12.5	30.1	3.92	6366	1.77	69.7
	min	12.59				-1.1		6.2	70.6	3.5	63.5	13.2	30.4	3.83	6326	1.93	73.2
9	max	13.63				-0.2		-11.5	76.9	0.8	68.0	12.3	29.4	4.01	7510	1.88	77.5
	mean	13.10	0.91	49	7528	0.1	2.10	-1.5	79.9	3.5	71.1	14.2	29.8	3.90	7534	2.07	82.8
	min	12.72				0.1		5.7	82.2	5.2	73.5	15.2	30.0	3.82	7532	2.23	86.7
10	max	13.34				0.3		-20.7	72.1	3.0	63.7	14.3	29.4	3.92	6860	1.81	74.3
	mean	12.74	1.12	-	6842	-0.7	2.19	-6.7	75.4	6.8	67.1	17.0	29.8	3.79	6794	2.05	80.9
	min	12.22				-0.4		2.9	78.5	7.4	70.3	17.1	30.2	3.69	6818	2.26	84.8
Mean value					6661		1.88										
SD					454		0.11										
CV [%]					6.9		5.9										

B.4 Results MAN L-beam specimens

B.4.1 Crack localisations of MAN L-beam specimens tested in 4PB

(a) *MAN-01* **(b)** *MAN-04*

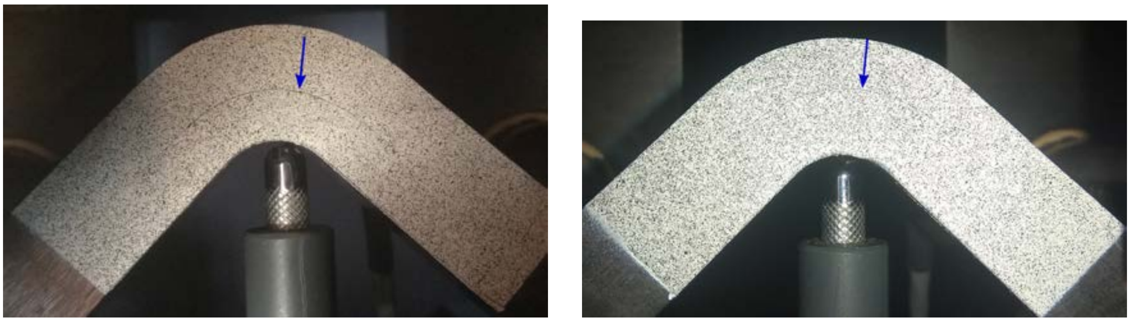

(c) *MAN-05* **(d)** *MAN-06*

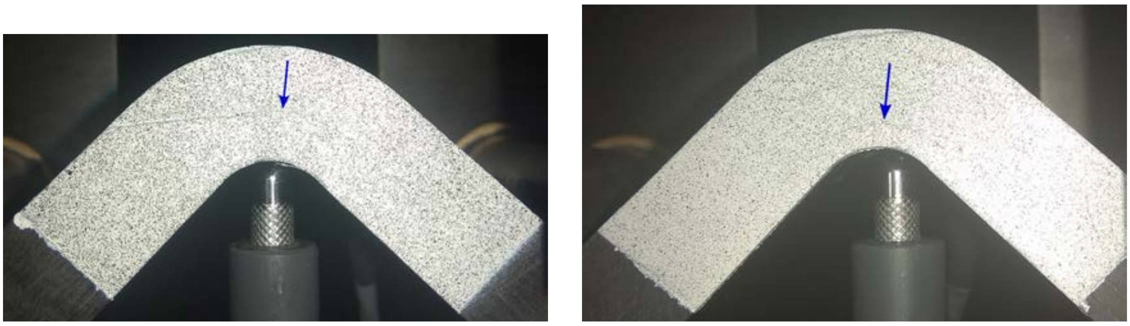

(e) *MAN-07* **(f)** *MAN-09*

Fig. B.9. *Photos of MAN L-beam specimens taken after test completion. First failure crack locations, identified by DIC, are marked by blue arrows. Black arrows show further cracks.*

B.4.2 Experimental/numerical correlation of load-displacement diagrams of MAN L-beam specimens

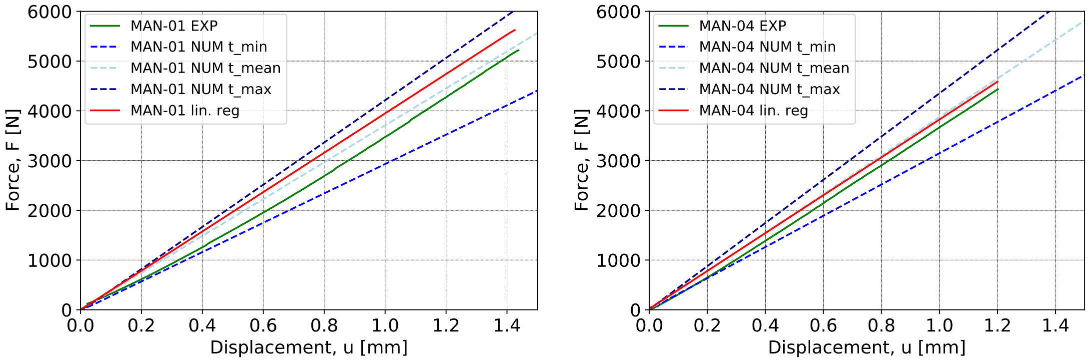

(a) *MAN-01* **(b)** *MAN-04*

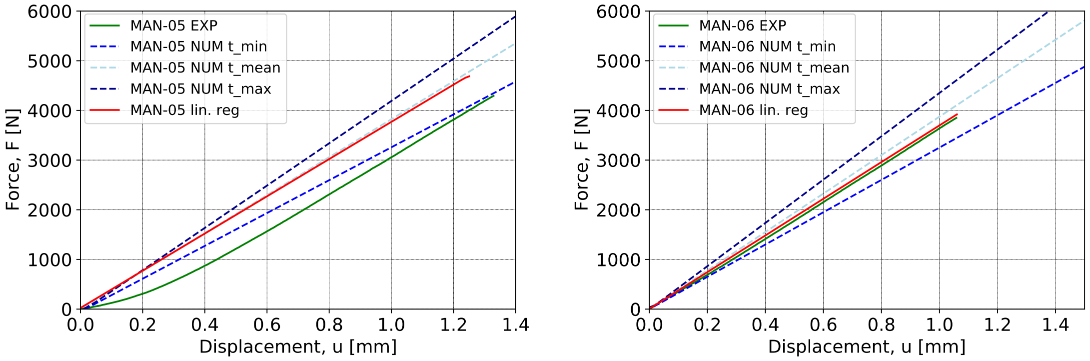

(c) *MAN-05* **(d)** *MAN-06*

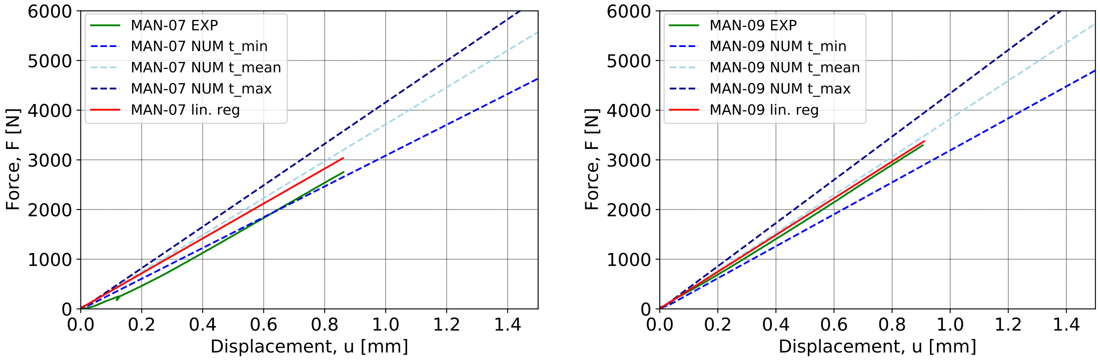

(e) *MAN-07* **(f)** *MAN-09*

Fig. B.10. *Force-displacement diagrams of MAN L-beam specimens. The specimen stiffness is located between t_{mean} and t_{max} for (a) MAN-01, between t_{min} and t_{mean} for specimen (d) MAN-06, (e)MAN-07 and (f) MAN-09 and coincide with t_{mean} for specimen (b) MAN-04 and (c) MAN-05.*

B.4.3 Normalized S_{ij} as a function of the normalized thickness/width of MAN L-beam specimens

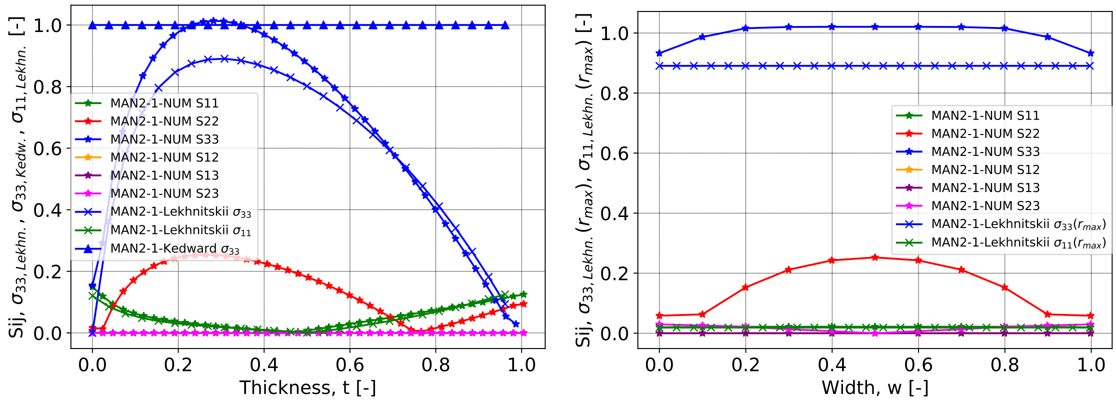

(a) **(b)**

Fig. B.11. *Normalized calculated stresses and strains S_{ij}, and analytically estimated radial and circumferential stresses $\sigma_{33,Lekhn.}$, $\sigma_{11,Lekhn.}$ (Lekhnitskii) and $\sigma_{33,Kedw.}$ (Kedward et al.) as a function of the normalized (a) thickness and (b) width of specimen MAN-01.*

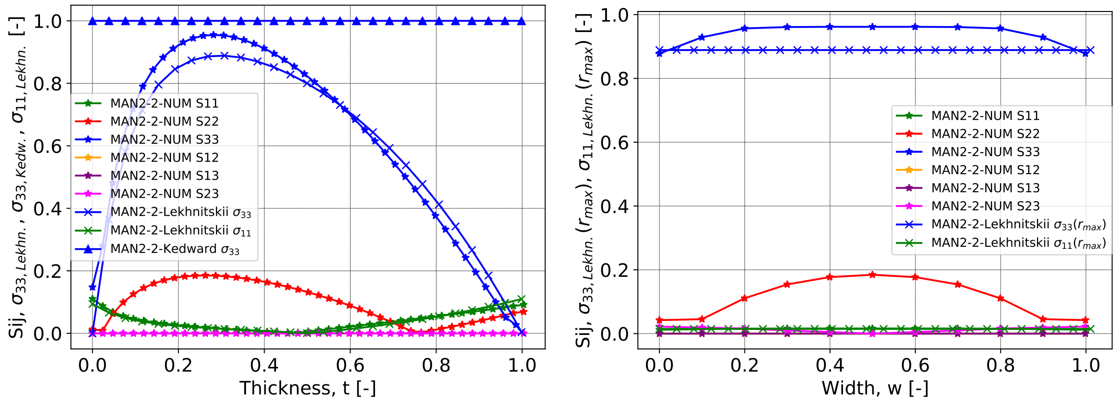

(a) **(b)**

Fig. B.12. *Normalized calculated stresses and strains S_{ij}, and analytically estimated radial and circumferential stresses $\sigma_{33,Lekhn.}$, $\sigma_{11,Lekhn.}$ (Lekhnitskii) and $\sigma_{33,Kedw.}$ (Kedward et al.) as a function of the normalized (a) thickness and (b) width of specimen MAN-02.*

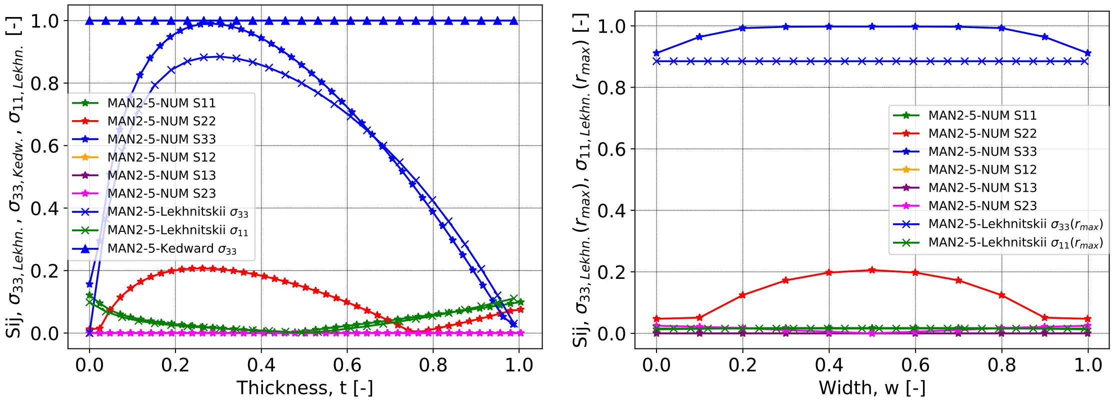

(a) **(b)**

Fig. B.13. *Normalized calculated stresses and strains S_{ij}, and analytically estimated radial and circumferential stresses $\sigma_{33,Lekhn.}$, $\sigma_{11,Lekhn.}$ (Lekhnitskii) and $\sigma_{33,Kedw.}$ (Kedward et al.) as a function of the normalized (a) thickness and (b) width of specimen MAN-05.*

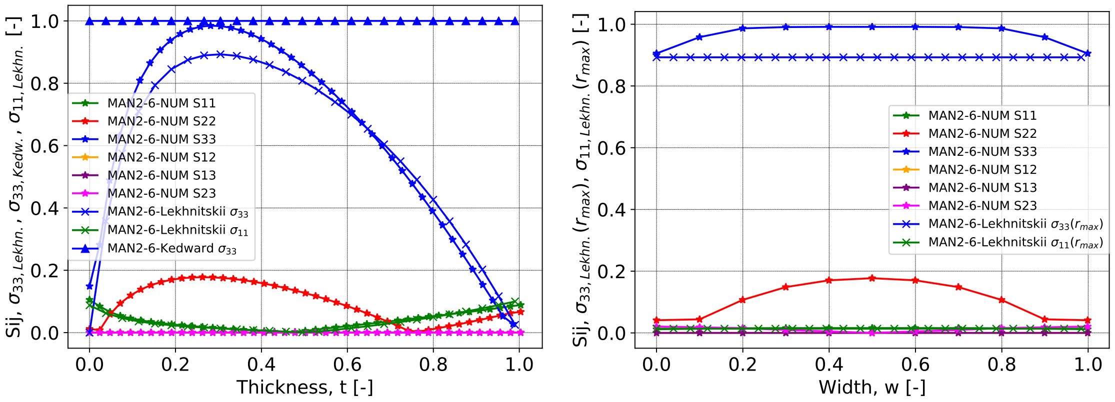

(a) **(b)**

Fig. B.14. *Normalized calculated stresses and strains S_{ij}, and analytically estimated radial and circumferential stresses $\sigma_{33,Lekhn.}$, $\sigma_{11,Lekhn.}$ (Lekhnitskii) and $\sigma_{33,Kedw.}$ (Kedward et al.) as a function of the normalized (a) thickness and (b) width of specimen MAN-06.*

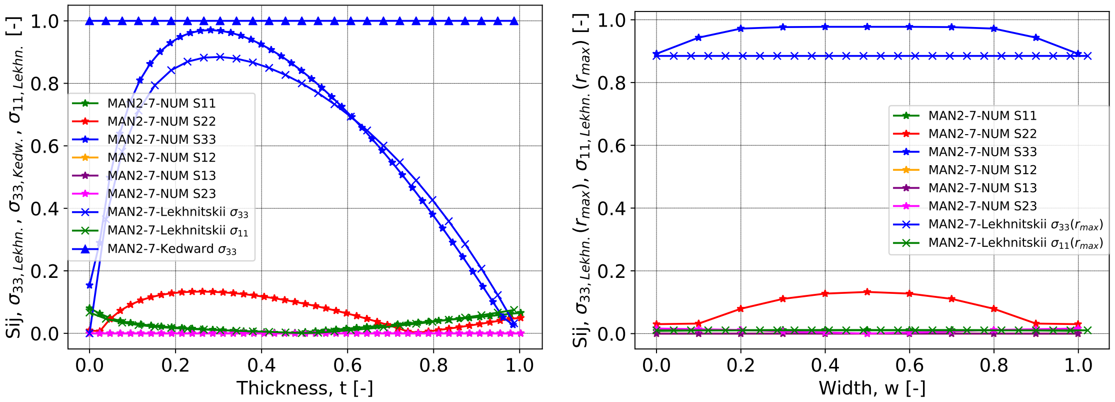

(a) **(b)**

Fig. B.15. *Normalized calculated stresses and strains S_{ij}, and analytically estimated radial and circumferential stresses $\sigma_{33,Lekhn.}$, $\sigma_{11,Lekhn.}$ (Lekhnitskii) and $\sigma_{33,Kedw.}$ (Kedward et al.) as a function of the normalized (a) thickness and (b) width of specimen MAN-07.*

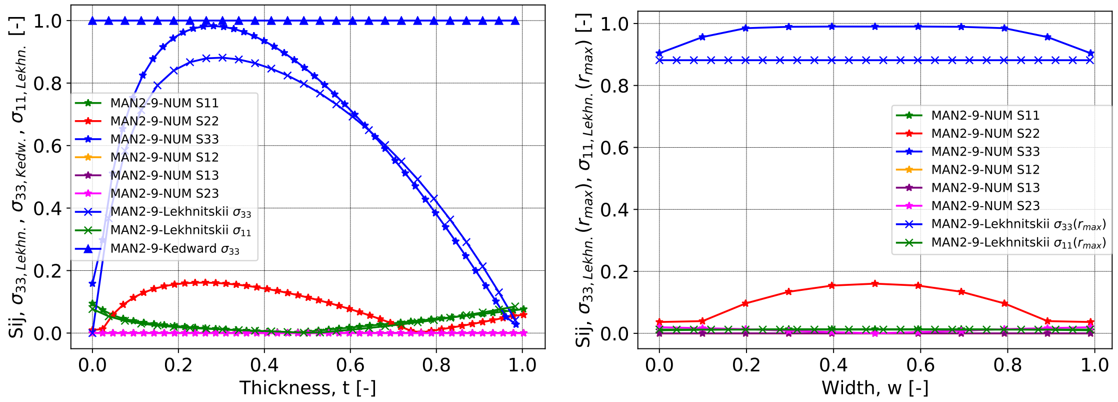

(a) **(b)**

Fig. B.16. *Normalized calculated stresses and strains S_{ij}, and analytically estimated radial and circumferential stresses $\sigma_{33,Lekhn.}$, $\sigma_{11,Lekhn.}$ (Lekhnitskii) and $\sigma_{33,Kedw.}$ (Kedward et al.) as a function of the normalized (a) thickness and (b) width of specimen MAN-09.*

B.4.4 Summary of the analytical, experimental and numerical results of MAN L-beam specimens tested in 4PB

Tab. B.2. *Comparison of the analytically estimated ILTS and the numerically calculated S_{33} of MAN L-beam specimens. S_{33} was determined at the experimental measured force at failure. Error values in percent refer to the numerically calculated value.*

MAN	Specimen thickness			EXP											FEM		
		t [mm]	t_{max}-t_{min} [mm]	F_0 [N]	F_f [N]	Error [%]	d_f [mm]	Error [%]	ILTS_{Kedward et al.} [MPa]	Error [%]	ILTS_{Lekhnitskii} [MPa]	Error [%]	r_{max,Lekhnitskii} [%]	[mm]	RF [N]	U3 [mm]	S_{33} [MPa]
1	max	13.73	1.86	-	5215	-0.6	1.44	-12.1	54.1	-3.2	47.8	8.8	29.3	4.03	5186	1.28	52.4
	mean	13.00				1.3		2.4	57.1	2.0	50.8	12.8	29.8	3.88	5286	1.48	58.3
	min	11.87				0.6		23.5	62.5	6.2	56.4	15.3	30.7	3.64	5244	1.88	66.6
4	max	13.90	1.70	-	4434	1.3	1.20	-8.3	46.8	-3.5	41.1	9.1	29.0	4.03	4494	1.11	45.2
	mean	13.27				-1.4		-1.8	49.0	-3.3	43.3	8.7	29.5	3.91	4374	1.18	47.4
	min	12.20				0.4		19.7	53.2	3.5	47.7	13.4	30.2	3.69	4452	1.50	55.1
5	max	13.75	1.33	8	4294	0.4	1.33	-23.4	45.3	-3.0	39.8	9.5	29.1	4.00	4310	1.08	44.0
	mean	13.16				0.5		-12.9	47.3	-0.1	41.9	11.3	29.5	3.88	4314	1.18	47.2
	min	12.42				-1.2		1.3	50.1	1.6	44.8	12.0	30.0	3.73	4242	1.35	50.9
6	max	13.78	1.53	8	3850	-1.7	1.06	-13.9	39.4	-6.3	34.9	5.8	29.5	4.07	3786	0.93	37.1
	mean	13.13				0.7		-0.9	41.3	-0.8	36.9	9.9	30.0	3.94	3876	1.05	41.0
	min	12.25				0.4		16.4	44.3	2.7	39.9	12.3	30.6	3.75	3864	1.27	45.5
7	max	13.81	1.56	12	2753	0.9	0.86	-17.1	30.6	-5.3	26.8	7.8	29.0	4.01	2778	0.73	29.1
	mean	13.17				0.7		-8.0	32.0	-2.1	28.4	9.4	29.5	3.88	2772	0.80	31.3
	min	12.25				-1.9		9.1	34.5	-0.8	30.8	10.0	30.1	3.69	2702	0.95	34.2
8	max	13.90	1.61	22	4045	-0.9	1.1	-12.2	42.2	-6.4	37.0	6.7	29.0	4.0	4010	0.98	39.7
	mean	13.17				0		-0.5	44.5	-2.0	39.4	9.7	29.5	3.89	4044	1.09	43.6
	min	12.29				1.7		15.0	47.6	0.6	42.7	10.8	30.2	3.71	4116	1.29	47.9
9	max	13.93	1.60	28	3293	-2.6	0.91	-6.1	35.4	-2.6	30.9	10.4	28.8	4.01	3208	0.867	34.5
	mean	13.22				1.3		1.4	37.3	-1.0	32.9	10.9	29.3	3.87	3338	0.92	36.9
	min	12.33				-1.8		15.2	40.0	0	35.7	10.7	29.9	3.69	3234	1.07	40.0
Mean value					3983		1.13										
SD					740		0.20										
CV [%]					18.6		17.34										

Bibliography

Adams, D. O. & Bell, S. J. (1995). Compression strength reductions in composite laminates due to multiple-layer waviness. *Composites science and Technology*, *53*(2), 207–212. 54

Agarwal, B. D., Broutman, L. J., & Chandrashekhara, K. (1990). Analysis and performance of fiber composites, John Wiley & Sons. *Inc, New York, NY*, (-). 54

Argon, A. (1972). Fracture of Composites. In *Treatise on Materials Science and Technology*, volume 1 (pp. 79–114). New York: Elsevier. 44

ASTM D6415 / D6415M-06a (2013). Standard Test Method for Measuring the Curved Beam Strength of a Fiber-Reinforced Polymer-Matrix Composite. 5, 37, 119, 124, 125, 126, 137, 138, 139, 140, 141, 142, 143, 161, 209, 244

Berbinau, P., Soutis, C., & Guz, I. A. (1999). Compressive failure of 0 unidirectional carbon-fibre-reinforced plastic (CFRP) laminates by fibre microbuckling. *Composites Science and technology*, *59*(9), 1451–1455. 56

Blanc, R., Germain, C., Baylou, P., & Cataldi, M. (2006). Fiber orientation measurements in composite materials. *Composites Part A: applied science and manufacturing*, *37*(2), 197–206. 64

Bloom, L. D., Wang, J., & Potter, K. D. (2013). Damage progression and defect sensitivity: an experimental study of representative wrinkles in tension. *Composites Part B: Engineering*, *45*(1), 449–458. 52

Bolotin, V. V. (1966). Theory of a reinforced layered medium with random initial irregularities. *Polymer Mechanics*, *2*(1), 7–11. 53

Bracewell, R. N. (1986). *The Fourier transform and its applications*, volume 31999. McGraw-Hill New York. 63

Budiansky, B. (1983). Micromechanics. *Computers & Structures*, *16*(1-4), 3–12. 44, 46

Budiansky, B. & Fleck, N. (1993). Compressive failure of fibre composites. *Journal of the Mechanics and Physics of Solids*, *41*(1), 183–211. 3, 4, 21, 35, 44, 45, 53, 55, 56, 68, 69, 87, 88, 89, 91, 93, 95, 96, 97, 108, 110, 111, 112, 113, 114, 115, 207, 208

Chakrapani, S. K., Dayal, V., Barnard, D. J., Eldal, A., & Krafka, R. (2012). Ultrasonic Rayleigh wave inspection of waviness in wind turbine blades: Experimental and finite element method. In *AIP Conference Proceedings*, volume 1430, (pp. 1911–1917). American Institute of Physics. 59, 60

Chaplin, C. R. (1977). Compressive fracture in undirectional glass-reinforced plastics. *Journal of Materials science*, *12*(2), 347–352. 44

Charrier, J.-S. (2013). *Développement de méthodologies dédiées à l'analyse robuste de la tenue de structures composites sous chargements complexes tridimensionnels.* PhD thesis, ENSAM, France. 34, 37, 126, 127, 140, 144, 145, 159, 201, 202

Charrier, J.-S., Laurin, F., Carrere, N., & Mahdi, S. (2016). Determination of the out-of-plane tensile strength using four-point bending tests on laminated L-angle specimens with different stacking sequences and total thicknesses. *Composites Part A: Applied Science and Manufacturing*, *81*, 243–253. 5, 6, 121, 127, 128, 129, 139, 147, 148, 150, 171, 209, 210, 243, 249, 250

Clarke, A. R., Archenhold, G., Davidson, N. C., Slaughter, W. S., & Fleck, N. A. (1995). Determining the power spectral density of the waviness of unidirectional glass fibres in polymer composites. *Applied Composite Materials*, *2*(4), 233–243. 64

Creighton, C., Sutcliffe, M., & Clyne, T. (2001). A multiple field image analysis procedure for characterisation of fibre alignment in composites. *Composites Part A: Applied Science and Manufacturing*, *32*(2), 221–229. 64, 65, 66, 241

Davies, E. R. (1990). Machine Vision. London. Academic Press. 63

Davis, J. G. (1975). Compressive strength of fiber-reinforced composite materials. In *Composite reliability*. ASTM International. 44

Drapier, S., Grandidier, J.-C., & Potier-Ferry, M. (1997). Theoretical study of structural effects on the compressive failure of laminate composites. *Comptes Rendus de l'Académie des Sciences-Series IIB-Mechanics-Physics-Chemistry-Astronomy*, *324*(4), 219–227. 15, 45, 94

Drapier, S., Grandidier, J.-C., & Potier-Ferry, M. (1999). Towards a numerical model of the compressive strength for long fibre composites. *European Journal of Mechanics-A/Solids*, *18*(1), 69–92. 55

Drapier, S., Grandidier, J.-C., & Potier-Ferry, M. (2001). A structural approach of plastic microbuckling in long fibre composites: comparison with theoretical and experimental results. *International Journal of Solids and Structures*, *38*(22-23), 3877–3904. 55, 56, 241

Garcea, S. C., Wang, Y., & Withers, P. J. (2018). X-ray computed tomography of polymer composites. *Composites Science and Technology*, *156*(-), 305–319. 60, 61

Ghassemieh, E., Acar, M., & Versteeg, H. (2002). Microstructural analysis of non-woven fabrics using scanning electron microscopy and image processing. Part 1: Development and verification of the methods. *Proceedings of the Institution of Mechanical Engineers, Part L: Journal of Materials: Design and Applications*, *216*(3), 199–207. 62, 63, 64

Goris, S. & Osswald, T. A. (2015). Fiber orientation measurements using a novel image processing algorithm for micro-computed tomography scans. In *Proceedings of Society of Plastics Engineers, 15th Annual Automotive Composites Conference and Exhibition*. 67

Grandidier, J.-C., Casari, P., & Jochum, C. (2012). A fibre direction compressive failure criterion for long fibre laminates at ply scale, including stacking sequence and laminate thickness effects. *Composite Structures*, *94*(12), 3799–3806. 3, 4, 15, 16, 19, 21, 22, 35, 45, 46, 53, 58, 68, 69, 85, 87, 88, 89, 91, 93, 94, 95, 96, 97, 108, 110, 111, 112, 113, 114, 115, 207, 208

Graupner, N., Beckmann, F., Wilde, F., & Müssig, J. (2014). Using synchroton radiation-based micro-computer tomography (SR μ-CT) for the measurement of fibre orientations in cellulose fibre-reinforced polylactide (PLA) composites. *Journal of Materials Science*, *49*(1), 450–460. 61

Hahn, H. T. & Williams, J. G. (1986). Compression failure mechanisms in unidirectional composites. In *Composite materials: testing and design (seventh conference)*. ASTM International. 44

Hernandez, J. P., Tschohl, K. A., Wagner, H., & Osswald, T. A. (2003). A NOVEL Fiber Orientation Evaluation Using a Directional Imagine Processing Technique. In *ANTEC-CONFERENCE PROCEEDINGS-*, volume 2, (pp. 2178–2182). UNKNOWN. 67

Hiel, C. C., Sumich, M., & Chappell, D. P. (1991). A Curved Beam Test Specimen for Determining the Interlaminar Tensile Strength of a Laminated Composite. *Journal of Composite Materials*, *25*(7), 854–868. 5, 121, 129, 209

Hodgkinson, J., Ayache, S., & Matthews, F. L. (1992). In-plane and out-of-plane property measurements on thick woven glass/polyester laminates. 5, 129, 209

Hoerrmann, S., Viechtbauer, C., Adumitroaie, A., & Schagerl, M. (2015). The effect of fiber waviness as manufacturing defect on the fatigue life of CFRP materials. In *20th International Conference on Composite Materials*. 59, 60

Hough, P. V. C. (1962). Method and means for recognizing complex patterns. 63

Hsiao, H. M. & Daniel, I. M. (1996). Effect of fiber waviness on stiffness and strength reduction of unidirectional composites under compressive loading. *Composites Science and Technology*, *56*(5), 581–593. 54, 55, 241

Imoca (2021). https://www.sailingscuttlebutt.com/2016/11/08/history-of-the/ (04/04/2021). 30, 241

Jackson, W. C. & Ifju, P. G. (1996). Through-the-Thickness Tensile Strength of Textile Composites. In R. B. Deo & C. R. Saff (Eds.), *Composite Materials: Testing and Design: Twelfth Volume* (pp. 218–238). West Conshohocken, PA: ASTM International. 5, 121, 123, 124, 137, 209

Jackson, W. C. & Martin, R. H. (1993). An Interlaminar Tensile Strength Specimen. In E. T. Camponeschi (Ed.), *Eleventh Volume: Composite Materials—Testing and Design* (pp. 333–354). West Conshohocken, PA: ASTM International. 122, 123, 125, 128, 129, 188, 189, 243

Jochum, C. & Grandidier, J. C. (2000). Modeling approach of carbon epoxy cure-application to microbuckling instabilities. *Zeitschrift für angewandte Mathematik und Mechanik*, *80*. 49

Jochum, C., Grandidier, J.-C., & Smaali, M. (2008). Proposal for a long-fibre microbuckling scenario during the cure of a thermosetting matrix. *Composites Part A: Applied Science and Manufacturing*, *39*(1), 19–28. 49

Joyce, P. & Moon, T. J. (1997). Compression strength reduction in composites with in-plane fiber waviness. In *ASTM Special Technical Publication*, volume 1330, (pp. 76–96). 47, 51, 53

Joyce, P. J., Kugler, D., & Moon, T. J. (1997). A technique for characterizing process-induced fiber waviness in unidirectional composite laminates-using optical microscopy. *Journal of composite materials*, *31*(17), 1694–1727. 47

Jumahat, A. (2011). *Effect of Nanofillers on Thermo-Mechanical Properties of Polymers and Composite Laminates*. PhD thesis, Faculty of Enginering University of Sheffield, UK. 56, 57

Jumahat, A., Soutis, C., Jones, F., & Hodzic, A. (2010). Fracture mechanisms and failure analysis of carbon fibre/toughened epoxy composites subjected to compressive loading. *Composite Structures*, *92*(2), 295–305. 57, 64

Kedward, K., Wilson, R., & McLean, S. (1989). Flexure of simply curved composite shapes. *Composites*, *20*(6), 527–536. 5, 6, 11, 12, 21, 37, 38, 121, 122, 123, 135, 139, 151, 152, 165, 166, 167, 168, 170, 171, 173, 181, 182, 183, 184, 185, 186, 194, 196, 201, 209, 210, 223, 224, 225, 228, 229, 230, 231, 243, 245, 246, 247, 250

Keryvin, V., Marchandise, A., Mechin, P.-Y., & Grandidier, J.-C. (2020). Determination of the longitudinal non linear elastic behaviour and compressive strength of a CFRP ply by bending tests on laminates. *Composites Part B: Engineering*, *187*, 107863. 92

Kitching, R., Tan, A., & Abu-Mansour, T. (1984). The influence of through thickness properties on glass reinforced plastic laminated structures. *Composite Structures*, *2*(2), 105–151. 5, 129, 209

Ko, W. L. & Jackson, R. H. (1989). *Multilayer Theory for Delamination Analysis of a Composite Curved Bar Subjected to End Forces and End Moments*, (pp. 173–198). Dordrecht: Springer Netherlands. 5, 121, 209

Ko, W. L. & Jackson, R. H. (1990). Open-mode delamination stress concentrations in horseshoe and elliptic composite curved bars subjected to end forces. 5, 121, 209

Kozaczuk, K. (2016). Automated fiber placement systems overview. *Prace Instytutu Lotnictwa, Nr 4 (245)*, 52—-59. 130

Kratmann, K. K., Sutcliffe, M. P. F., Lilleheden, L. T., Pyrz, R., & Thomsen, O. T. (2009). A novel image analysis procedure for measuring fibre misalignment in unidirectional fibre composites. *Composites Science and Technology*, *69*(2), 228–238. 63, 64, 66, 86

Krause, M., Hausherr, J. M., Burgeth, B., Herrmann, C., & Krenkel, W. (2010). Determination of the fibre orientation in composites using the structure tensor and local X-ray transform. *Journal of Materials Science*, *45*(4), 888–896. 61, 62

Kulkarni, P., Mali, K. D., & Singh, S. (2020). An Overview of The Formation of Fibre Waviness and Its Effect on The Mechanical Performance of Fibre Reinforced Polymer Composites. *Composites Part A: Applied Science and Manufacturing*, (-), 106013. 48, 51, 53, 59, 60, 61

Lagace, P. A. & Weems, D. B. (1989). A Through-the-Thickness Strength Specimen for Composites. In C. C. Chamis (Ed.), *Test Methods and Design Allowables for Fibrous Composites: 2nd Volume* (pp. 197–207). West Conshohocken, PA: ASTM International. 5, 120, 121, 129, 209

Lager, J. R. & June, R. R. (1969). Compressive strength of boron-epoxy composites. *Journal of Composite Materials*, *3*(1), 48–56. 44

Lam, P. W. K. & Piggott, M. R. (1989). The durability of controlled matrix shrinkage composites. *Journal of Materials Science*, *24*(12), 4427–4431. 57

Lan, M., Cartié, D., Davies, P., & Baley, C. (2015). Microstructure and tensile properties of carbon–epoxy laminates produced by automated fibre placement: Influence of a caul plate on the effects of gap and overlap embedded defects. *Composites Part A: Applied Science and Manufacturing*, *78*, 124–134. 130, 131, 199, 243

Lekhnitskii, S. G. (1968). *Anisotropic plates.* Gordon & Breach; Reprint edition (January 1, 1968). 5, 6, 7, 11, 12, 21, 22, 37, 121, 122, 123, 127, 135, 138, 139, 151, 152, 165, 166, 167, 168, 170, 171, 173, 181, 182, 183, 184, 185, 209, 210, 223, 224, 225, 228, 229, 230, 231, 243, 245, 246, 247, 250

Luo, G. M., Sadegh, A. M., & Cowin, S. C. (1991). The mean intercept length polygons for systems of planar nets. *Journal of Materials Science*, *26*(9), 2389–2396. 68

Marchandise, A. (2020). *Impact des procédés de fabrication sur les performances mécaniques critiques d'un hydrofoil. Mise en place de solutions automatisées.* PhD thesis, Université Bretagne Sud. 8, 199, 200, 211

Martin, R. & Sage, G. (1986). Prediction of the fatigue strength of bonded joints between multidirectional laminates of CFRP. *Composite Structures*, *6*(1-3), 141–163. 120, 243

McManus, H. & Mak, Y.-P. (1993). *STRAIN RATE AND MANUFACTURING TECHNIQUE EFFECTS ON THE DAMAGE TOLERANCE OF COMPOSITE LAMINATES.* 130

Mechin, P.-Y. (2017). *Contribution à l'étude de la résistance à la compression de stratifiés composites à fibres de carbone haut module: cas de chargements statiques et cycliques.* PhD thesis, University of South Brittany, Lorient. 89, 92, 94

Mechin, P.-Y., Keryvin, V., Grandidier, J.-C., & Glehen, D. (2019). An experimental protocol to measure the parameters affecting the compressive strength of CFRP with a fibre micro-buckling failure criterion. *Composite Structures*, *211*, 154–162. 4, 58, 64, 65, 88, 92, 93, 153, 208

Mespoulet, S. (1998). *Through-thickness test methods for laminated composite materials.* PhD thesis, London Univ. (United Kingdom). 129

Mrse, A. & Piggott, M. (1993). Compressive properties of unidirectional carbon fibre laminates: II. The effects of unintentional and intentional fibre misalignments. *Composites Science and Technology*, *46*(3), 219–227. 53, 54, 64, 241

Mukhopadhyay, S., Jones, M. I., & Hallett, S. R. (2015). Tensile failure of laminates containing an embedded wrinkle; numerical and experimental study. *Composites Part A: Applied Science and Manufacturing*, *77*, 219–228. 52, 241

Nguyen, M. H., Vijayachandran, A. A., Davidson, P., Call, D., Lee, D., & Waas, A. M. (2019). *Effect of Automated Fiber Placement (AFP) Manufacturing Signature on Mechanical Performance.* 131, 132, 133, 243

Olsson, R. (2011). A survey of test methods for multiaxial and out-of-plane strength of composite laminates. *Composites Science and Technology*, *71*(6), 773–783. 129, 137

Ouestfrance (2020). https://www.ouest-france.fr/vendee-globe/vendee-globe-mais-au-fait-a-quoi-servent-les-foils-7044144 (18/12/2020). 30

Paluch, B. (1994). Analyse des imperfections géométriques affectant les fibres dans un matériau composite à renfort unidirectionnel. *La recherche aéronautique*, *6*(-), 431–448. 4, 47, 49, 64, 80, 208

Parry, T. V. & Wronski, A. S. (1981). Kinking and tensile, compressive and interlaminar shear failure in carbon-fibre-reinforced plastic beams tested in flexure. *Journal of Materials Science*, *16*(2), 439–450. 44

Piggott, M. (1995). The effect of fibre waviness on the mechanical properties of unidirectional fibre composites: A review. *Composites Science and Technology*, *53*(2), 201–205. 51

Piggott, M. R. & Lam, P. W. K. (1991). Fatigue Failure Processes in Aligned Carbon-Epoxy Laminates. In T. K. O'Brien (Ed.), *Composite Materials: Fatigue and Fracture (Third Volume)* (pp. 686–695). West Conshohocken, PA: ASTM International. 57

Potter, K. D. (2009). Understanding the origins of defects and variability in composites manufacture. In *International conference on composite materials (ICCM)-17, Edinburgh, UK*, (pp. 18–25). 3, 49, 50, 51, 207, 241

Pourdeyhimi, B., Dent, R., & Davis, H. (1997). Measuring Fiber Orientation in Nonwovens Part III: Fourier Transform. *Textile Research Journal*, *67*(2), 143–151. 62, 63

Pourdeyhimi, B. & Kim, H. S. (2002). Measuring Fiber Orientation in Nonwovens: The Hough Transform. *Textile Research Journal*, *72*(9), 803–809. 63, 64

Pourdeyhimi, B., Ramanathan, R., & Dent, R. (1996). Measuring Fiber Orientation in Nonwovens: Part II: Direct Tracking. *Textile Research Journal*, *66*(12), 747–753. 62, 63

Pyrz, R. (1999). Application of X-ray microtomography to the study of polymer composites. *SAE transactions*, (-), 1312–1316. 60, 61

Ramberg, W. & Osgood, W. R. (1943). Description of stress-strain curves by three parameters. *National Advisory Committee For Aeronautics*, -, Technical Note No. 902. 44

Ranz, D., Cuartero, J., Miravete, A., & Miralbes, R. (2017). Experimental research into interlaminar tensile strength of carbon/epoxy laminated curved beams. *Composite Structures*, *164*, 189–197. 5, 121, 125, 126, 159, 209, 243

Rosen, B. W. (1965). Mechanics of composite strengthening. (-). 43, 44, 46, 53, 241

Rueden, C. T., Schindelin, J., Hiner, M. C., DeZonia, B. E., Walter, A. E., Arena, E. T., & Eliceiri, K. W. (2017). ImageJ2: ImageJ for the next generation of scientific image data. *BMC bioinformatics*, *18*(1), 1–26. 4

Sadowsky, M. A., Pu, S. L., & Hussain, M. A. (1967). Buckling of microfibers. (-). 43

Sander, E. A. & Barocas, V. H. (2009). Comparison of 2D fiber network orientation measurement methods. *Journal of Biomedical Materials Research Part A*, *88A*(2), 322–331. 63, 67, 68

Schultheisz, C. R. & Waas, A. M. (1996). Compressive failure of composites, part I: testing and micromechanical theories. *Progress in Aerospace Sciences*, *32*(1), 1–42. 43, 44, 51, 53

Shivakumar, K. N., Allen, H. G., & Avva, V. S. (1994). Interlaminar tension strength of graphite/epoxy composite laminates. *AIAA Journal*, *32*(7), 1478–1484. 5, 121, 122, 123, 124, 125, 209, 243

Sklansky, J. (1978). On the Hough technique for curve detection. *IEEE Transactions on computers*, (10), 923–926. 63

Smith, R., Nelson, L., Xie, N., Fraij, C., & Hallett, S. (2015). Progress in 3D characterisation and modelling of monolithic carbon-fibre composites. *Insight - Non-Destructive Testing and Condition Monitoring*, *57*(3). 59

Steif, P. S. (1988). A simple model for the compressive failure of weakly bonded, fiber-reinforced composites. *Journal of composite materials*, *22*(9), 818–828. 44

Straumit, I., Lomov, S. V., & Wevers, M. (2015). Quantification of the internal structure and automatic generation of voxel models of textile composites from X-ray computed tomography data. *Composites Part A: Applied Science and Manufacturing*, *69*, 150–158. 61, 62

Sutcliffe, M. P. F., Lemanski, S. L., & Scott, A. E. (2012). Measurement of fibre waviness in industrial composite components. *Composites Science and Technology*, *72*(16), 2016–2023. 66

Swift, D. G. (1975). Elastic moduli of fibrous composites containing misaligned fibres. *Journal of Physics D: Applied Physics*, *8*(3), 223–240. 49

Syerko, E., Oter, L., Pawar, A., Binetruy, C., Advani, S., & Eck, B. (2019). Comparative Study of Methods for the Quantification of Fiber Orientations of Composite Reinforcements. In *JNC21*, (pp. 1–9)., Bordeaux. 61, 67

Talreja, R. (2015). 5 - Manufacturing defects in composites and their effects on performance. In P. E. Irving & C. Soutis (Eds.), *Polymer Composites in the Aerospace Industry* (pp. 99–113). Woodhead Publishing. 48, 49

Van de Werken, N., Reese, M. S., Taha, M. R., & Tehrani, M. (2019). Investigating the effects of fiber surface treatment and alignment on mechanical properties of recycled carbon fiber composites. *Composites Part A: Applied Science and Manufacturing*, *119*, 38–47. 82

Vassilopoulos, A. P. (2013). Fatigue life prediction of wind turbine blade composite materials. In *Advances in wind turbine blade design and materials* (pp. 251–297). Elsevier. 58

Waas, A. M. (1992). Effect of interphase on compressive strength of unidirectional composites. *ATJAM*, *59*(2), S183–S188. 44

Waas, A. M., Babcock Jr, C. D., & Knauss, W. G. (1990). A mechanical model for elastic fiber microbuckling. (-). 44

Wang, B., Uda, N., Ono, K., & Nagai, H. (2018). Effect of micro in-plane fiber waviness on compressive properties of unidirectional fabric composites. *Journal of Composite Materials*, *52*(15), 2065–2074. 57

Wang, J., Potter, K. D., Hazra, K., & Wisnom, M. R. (2012). Experimental fabrication and characterization of out-of-plane fiber waviness in continuous fiber-reinforced composites. *Journal of Composite Materials*, *46*(17), 2041–2053. 47, 241

Wang, Y., Soutis, C., & Withers, P. (2014). X-ray microtomographic imaging of kink bands in carbon fibre-epoxy composites. In *Proceedings of the 16th European Conference on Composite Materials, Seville*, (pp. 22–26). 60, 61

Weaver, C. W. & Williams, J. (1975). Deformation of a carbon-epoxy composite under hydrostatic pressure. *Journal of Materials Science*, *10*(8), 1323–1333. 44

Wilhelmsson, D. & Asp, L. E. (2018). A high resolution method for characterisation of fibre misalignment angles in composites. *Composites Science and Technology*, *165*, 214–221. 66, 67

Wisnom, M. R. (1990). The effect of fibre misalignment on the compressive strength of unidirectional carbon fibre/epoxy. *Composites*, *21*(5), 403–407. 44, 45, 46, 53

Wisnom, M. R. (1993). Nonlinear analysis of misaligned unidirectional carbon fibre-epoxy compression specimens. *Composites Engineering*, *3*(6), 547–556. 46

Wisnom, M. R. & Jones, M. I. (1994). A Comparison between Interlaminar and In-plane Shear Strength of Unidirectional Glass Fibre-epoxy. *Advanced Composites Letters*, *3*(2), 096369359400300205. 129

Wisnom, M. R. & Jones, M. I. (1996). Size effects in interlaminar tensile and shear strength of unidirectional glass fibre/epoxy. *Journal of reinforced plastics and composites*, *15*(1), 2–15. 5, 121, 209

Wu, C., Gu, Y., Luo, L., Xu, P., Wang, S., Li, M., & Zhang, Z. (2018). Influences of in-plane and out-of-plane fiber waviness on mechanical properties of carbon fiber composite laminate. *Journal of reinforced plastics and composites*, *37*(13), 877–891. 47

Wu, Q., Li, M., Gu, Y., Wang, S., Wang, X., & Zhang, Z. (2015). Reaction of carbon fiber sizing and its influence on the interphase region of composites. *Journal of Applied Polymer Science*, *132*(18). 82

Xu, B. & Yu, L. (1997). Determining fiber orientation distribution in nonwovens with hough transform techniques. *Textile research journal*, *67*(8), 563–571. 63, 64

Yoshimura, A., Hosoya, R., Koyanagi, J., & Ogasawara, T. (2016). X-ray computed tomography used to measure fiber orientation in CFRP laminates. *Advanced Composite Materials*, *25*(1), 19–30. 60, 61

Yurgartis, S. (1987). Measurement of small angle fiber misalignments in continuous fiber composites. *Composites Science and Technology*, *30*(4), 279–293. 3, 4, 9, 10, 23, 29, 35, 36, 41, 44, 46, 48, 53, 56, 58, 64, 65, 66, 68, 69, 70, 71, 72, 73, 74, 75, 76, 77, 78, 79, 80, 81, 82, 84, 85, 86, 88, 95, 96, 97, 108, 111, 112, 114, 207, 208, 241, 249

Yurgartis, S. (1995). Techniques for the quantification of composite mesostructure. *Composites Science and Technology*, *53*(2), 145–154. 15

Zardan, J. P., Gueudré, C., & Corneloup, G. (2013). Study of induced ultrasonic deviation for the detection and identification of ply waviness in carbon fibre reinforced polymer. *NDT & E International*, *56*, 1–9. 59, 60, 241

Zhao, C., Xiao, J., Li, Y., Chu, Q., Xu, T., & Wang, B. (2017). An experimental study of the influence of in-plane fiber waviness on unidirectional laminates tensile properties. *Applied Composite Materials*, *24*(6), 1321–1337. 52, 53

Zumaquero, P. L., Justo, J., & Graciani, E. (2018). On the Thickness Dependence of ILTS in Curved Composite Laminates. In *Advances in Fracture and Damage Mechanics XVII*, volume 774 of *Key Engineering Materials*, (pp. 523–528). Trans Tech Publications Ltd. 125, 126, 127, 243

List of Figures

List of Tables

SE 84LV

LOW TEMPERATURE CURE EPOXY PREPREG

- Versatile, high-strength prepreg system
- Curable at temperatures as low as 80°C (176°F)
- Can be processed with vacuum-only processing
- Excellent tack
- Low Viscosity – Ideal for use with heavy fibre weights
- Lloyd’s Register and DNV-GL Certified Formats Available

INTRODUCTION

SE 84LV is an exceptionally versatile hot-melt, epoxy prepreg. It can be cured at temperature as low as 80°C (176°F), or can be used for faster moulding of components at 120°C (248°F). This is achieved with an extremely good outlife of up to 8 weeks at 18-22°C (64-72°F). It is a toughened system, and offers excellent mechanical properties on a wide variety of reinforcing fabrics and fibres.

SE 84LV is commonly used in vacuum bagging, press-moulding, autoclave and other pressure moulding processes.

SE 84LV is a very low viscosity system used with heavy fibre weights where low-flow processing conditions (vacuum bag pressure and minimum cure temperature), are likely to be used. With its high compressive strength it is widely used in large heavily loaded components, such as yacht hulls, and spars. It has been selected for use by various America’s Cup syndicates and boats racing in the Volvo Ocean Race.

SE 84LV is widely used in sandwich structures with honeycomb, foam and balsa cores, primarily with the toughened SA 80 Adhesive Film.

PROCESSING NOTES - GENERAL

PREPARATION

When preparing the lay-up the prepreg should be removed from the freezer and allowed to thaw in a sealed bag. This may take 6 to 24 hours depending on roll size. This prevents atmospheric moisture from condensing on the prepreg which may cause voiding on cure. The mould surface should be release coated and must have been tested for vacuum integrity prior to lay-up.

LAYING-UP

The following procedure is recommended for preparing vacuum cured laminates.

1. Place the lay-up on a tool or caul sheet which has been treated with a release agent or film. Insert a thermocouple into the lay-up near the centre ply of the thickest edge section, outside the net trim line. A separate prepreg nylon peel ply is available for covering a mould tool prior to lay-up in order to leave a clean, textured surface for subsequent bonding.

2. Apply a peel ply to the surface of the lay-up. Note that for good secondary bonding of a peel-plied surface of an SE 84LV prepreg laminate, a nylon peel ply, such as Gurit's Stitch Ply A, is strongly recommended. This is particularly important where the cure temperatures are in excess of 90°C (194°F). Cover the peel ply entirely with a perforated release film. Normally, no edge resin bleeder system is used. For thin sections, Gurit WL3600P90 grade release film are recommended, while for sections of 4mm and above, Gurit WL3600P release film is also suitable. With WL3600P the amount of resin bled away is controlled by the number of dry plies of resin bleeder cloth placed over the perforated release film.

3. Install a vacuum bag by standard techniques. Insert at least two vacuum stems through the bag connecting one to the vacuum source and the other, at a point on the part furthest from the source, to a calibrated vacuum gauge. Position part in the oven or autoclave and draw vacuum to check for bag or system leaks.

4. Commence the heat-up cycle, typically between 0.3°C(0.5°F)/min and 2°C(3.6°F)/min to the final cure temperature. At 85°C (185°F), the temperature should be held up for 10 hours. Faster cures may be obtained at elevated temperatures, e.g. 6 hours at 90°C (194°F), 3 hours at 100°C (212°F) or 1 hour at 120°C (248°F). All temperatures measured by the previously installed thermocouple. When curing at 80°C (176°F) a minimum of 12 hours is recommended. Vacuum should be maintained as high as possible, with a minimum of 85% throughout the cure cycle.

5. Upon completion of cure, turn off heat and cool until part temperature has fallen below 60°C (140°F). When fully cooled, the part may be debagged, trimmed and machined as necessary. A post-cure is not required.

PROCESSING NOTES - CURING

CURE CYCLES

For a good balance of composite properties, it is recommended that the laminate is cured at 80°C (176°F) for a minimum of 12 hours. A laminate may be cured in two stages - if, for example, making a cored component. However in a two stage cure, a minimum of 4 hours at 85°C (185°F) or 5 hours at 80°C (176°F) is recommended before debagging a skin, and it must be ensured that this skin is cured for the equivalent of at least 10 hours at 85°C (185°F) or 12 hours at 80°C (176°F) before going into service.

SE 84LV may be cured at higher temperatures for a shorter time. At a cure temperature of 100°C (212°F) cure can be achieved in 3 hours or at 120°C (250°F) cure can be achieved in 1 hour.

It is not recommended to cure SE 84LV under vacuum pressures of less than 85%. If a ramp rate of less than 0.3°C/min (0.5°F/min) is used, users should satisfy themselves that this allows adequate flow.

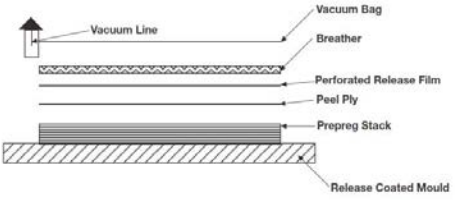

CURING AT 80°C (176°F)

When curing at 80°C (176°F) it is important to ensure the temperature is monitored off the trailing thermocouple. 80°C (176°F) should be treated as the minimum cure temperature for SE 84LV; 70-75°C (158-167°F) will not generate adequate mechanical properties.

THIN LAMINATES

When using very thin laminates (e.g. with a total laminate fibre weight of less than 300gm^2), care needs to be taken to avoid extracting excessive amounts of resin during the cure process. To avoid this, a microporous release film can be used, and for particularly critical components, a prepreg peel ply should be used.

CORE BONDING

This product can be used in conjunction with typical core materials. Representative test panels should be made to ensure that the laminate construction, curing method and other variables allow full filling of any cuts or slits in the foam. The cure cycles given in this datasheet are for typical monolithic flat panels and may not be appropriate for sandwich panels.

When using Nomex™ or aluminium honeycombs, the separate SA 80 adhesive film is recommended and full details of use are provided on the separate SA 80 data sheet. This adhesive film is supplied on a lightweight glass carrier, or in some cases it can be supplied directly coated onto one face of the SE 84LV prepreg.

The system is fully compatible with Ampreg wet layup epoxy systems and therefore all types of cores may be bonded to a first skin by using a separate 'wet-bonding' operation. In this case, the addition of filler powders to the appropriate resin system is required to provide the correct paste-like consistency.

PRODUCT INFORMATION

AVAILABILITY

SE 84LV prepregs are available in a wide variety of fabric forms and collimated unidirectional tapes. Unidirectional materials are normally supplied on a single release paper and fabrics on a single polythene film. Please contact Customer Support to discuss specific requirements and availability. The product formats listed below also benefit from 3rd Party Certification.

PRODUCT DESCRIPTION	STATUS	CERTIFICATION
SE 84LV HEC, HMC & IMC UD Prepreg 145-600g/m^2 29 – 40% Resin Content	Valid	DNV-GL TAK000015K
SE 84LV HEC UD Prepreg 200-600g/m^2	Valid	Lloyds Register MATS/4718-1
SE 84LV IMC UD Prepreg 300-600g/m^2	Valid	Lloyds Register MATS/4888-1
SE 84LV HMC UD Prepreg 300-600g/m^2	Valid	Lloyds Register MATS/4887-1
SE 84LV XC Series Prepreg 290 – 640 g/m^2 35 – 45% Resin Content	Valid	DNV-GL TAK00015Z
SE 84LV XC Series Prepreg XC305, XC411, XC611	Valid	Lloyds Register MATS/4721-1
SE 84LV RC200T & RC400T Prepreg	Valid	Lloyds Register MATS/4719-1
SE 84LV RC416T Prepreg	Valid	Lloyds Register MATS/4720-1

PREPREG PROPERTIES

RHEOLOGY DATA

SE 84LV resin viscosity profile conducted at 1°C (1.8°F) per minute.

PROPERTY	VALUE	
Minimum Viscosity	2.9 Pa.s	28.8 P
Temperature at Minimum Viscosity	99°C	210°F

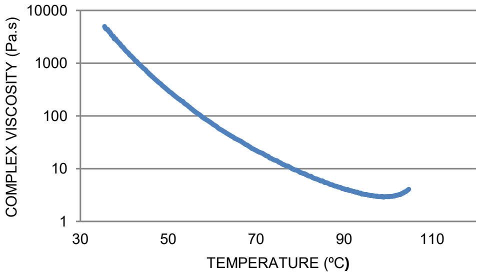

TRANSPORT & STORAGE

When stored sealed & out of direct sunlight.

STORAGE TEMP		UNIT	VALUE
-18°C	0°F	months	24
+18-22°C	+64-72°F	weeks	8

All prepreg materials should be stored in a freezer when not in use to maximise their useable life, since the low temperature reduces the reaction of resin and catalyst to virtually zero. However, even at -18℃ (0°F), the temperature of most freezers, some reaction will still occur. In most cases after some years, the material will become unworkable.
When not in use SE 84LV products should be maintained at -18℃ (0°F). To avoid contamination on their surfaces, allow rolls to reach room temperature before unwrapping.

HEALTH AND SAFETY

Please refer to product SDS for up to date information specific to this product.

MINIMUM CURE TIME & TEMPERATURE

Recommended minimum cure is 12 hours at 80°C (176°F) using vacuum bag processing.

PROPERTY	OVEN / VAC BAG		TEST STANDARD
Typical Laminate	8 plies of SE 84 LV 300g/m^2 unidirectional prepreg with 35% resin content		-
Typical Ramp Rate	1 – 2°C (2 – 4°F) per minute		-
Cure Temperature	80°C (176°F)	120°C (248°F)	-
Cure Dwell Time	12 (hours)	1 (hour)	-
Cure Pressure	-1bar (14.5Psi)		-
De-mould Temperature	< 60°C (140°F)		-
Dry Tg_1 (DMA)	98°C / 208°F	115°C / 239°F	ISO 6721 (DMA)

*suitable for use in conjunction with hot-in / hot-out rapid component manufacture is possible using appropriate press tooling

CURING LARGE STRUCTURES

Gurit provides detailed processing notes for large structures to be built using SE84LV / SA 80; these notes are available from the Technical Department on request.

MECHANICAL PROPERTIES

Cured using standard vacuum bag processing techniques and a minimum cure time of 12hrs at 80°C (176°F). Values are representative of the typical properties to be expected but do not constitute a guaranteed specification.

CURED RESIN PROPERTIES

PROPERTY	SYMBOL	SE 84LV RESIN CAST	TEST STANDARD
Tensile Strength	σ_T	82 MPa	ISO 527-2
Tensile Modulus	E_T	3.9 GPa	ISO 527-2
Flexural Strength	σ_F	123 MPa	ISO 178
Flexural Modulus	E_F	3.5 GPa	ISO 178
Compressive Strength	σ_C	163 MPa	ISO 604
Glass Transition Temperature	Tg_1	115°C	ISO 6721

UNIDIRECTIONAL LAMINATE PROPERTIES

Properties presented are averages of multiple batch data from a variety of fibre suppliers. Customers with specific requirements should contact Gurit technical support who can recommend appropriate fibres and formats.

PROPERTY	SYMBOL	UNIT	HEC FIBRE*	IMC FIBRE*	HMC FIBRE*	UHMC FIBRE*	TEST STANDARD
Typical Fibre Density	ρ_{fibre}	g/cm^3	1.8	1.79	1.82	1.84	-
Fibre Modulus	E_{fibre}	GPa	227 - 257	275 - 310	365 - 405	420 - 455	-
Resin Content	%	%	32 - 37	32 - 37	33 - 37	35	ASTM D 3171 Method II
Fibre Volume Fraction	ν_t	%	55.0	55.5	54.4	54.3	ASTM D 3171 Method II
0° Tensile Strength**	X_T	MPa	2458	2894	2658	1980	ISO 527-5
0° Tensile Modulus**	E_t	GPa	134	170	222	250	ISO 527-5
0° Compressive Strength**	X_C	MPa	1354	1417	1166	1070	SACMA SRM1-94
0° Compressive Modulus**	E_{C11}	GPa	121	153	192	227	SACMA SRM1-94
90° Tensile Strength	Y_T	MPa	39.2	33.2	30.1	26.0	ISO 527-5
90° Tensile Modulus	E_{T22}	GPa	8.3	8.4	7.1	6.6	ISO 527-5
0° Flexural Strength	X_F	MPa	1448	1406	-	-	ISO 14125
0° Flexural Modulus	E_{F11}	GPa	106	129	-	-	ISO 14125
0° ILSS	X_{ILSS}	MPa	86.6	88.6	82.3	77.8	ISO 14130

*HEC = High Elongation Carbon, IMC = Intermediate Modulus Carbon, HMC = High Modulus Carbon, UHMC = Ultra-High Modulus Carbon

**Normalised to 60% fibre volume fraction

WOVEN LAMINATE PROPERTIES

Properties presented are averages of multiple batch data, where possible witnessed by a third party surveyor on a standard fibre type. Customers with specific requirements should contact Gurit technical support who can recommend suitable fibres and formats.

PROPERTY	SYMBOL	UNIT	RC200T	RC416T	TEST STANDARD
Resin Content	-	%	42	40	ASTM D 3171 Method II
Cured Ply Thickness	-	mm	0.23	0.43	ASTM D792
Fibre Volume Fraction	-	%	47 - 53	50 - 59	ASTM D 3171 Method II
0° Tensile Strength*	X_T	MPa	719	1006	ISO 527-4
0° Tensile Modulus*	E_t	GPa	60.6	59.1	ISO 527-4
90° Tensile Strength*	Y_T	MPa	662	858	ISO 527-4
90° Tensile Modulus*	E_{T22}	GPa	61.6	58.9	ISO 527-4
0° Compressive Strength*	X_C	MPa	759	649	SACMA SRM1-94
0° Compressive Modulus*	E_c	GPa	58.3	55.6	SACMA SRM1-94
90° Compressive Strength*	Y_C	MPa	731	659	SACMA SRM1-94
90° Compressive Modulus*	E_{C22}	GPa	59.0	55.2	SACMA SRM1-94
0° Flexural Strength	X_F	MPa	847	895	ISO 14125
0° Flexural Modulus	E_{F11}	GPa	51.2	49.4	ISO 14125
90° Flexural Strength	Y_F	MPa	857	892	ISO 14125
90° Flexural Modulus	E_{F22}	GPa	51.5	50.6	ISO 14125
ILSS	τ_M	MPa	74.8	55.8	ISO 14130

*Normalised to 55% fibre volume fraction

MULTIAXIAL LAMINATE PROPERTIES

Properties presented are multiple batch data, where possible witnessed by a third party surveyor on a standard fibre type. Customers with specific requirements should contact Gurit technical support who can recommend suitable fibres and formats.

PROPERTY	SYMBOL	UNIT	XC411	TEST STANDARD
Resin Content	-	%	40	ASTM D 3171 Method II
Cured Ply Thickness	-	mm	0.43	ASTM D792
Fibre Volume Fraction	-	%	47 - 59	ASTM D 3171 Method II
+45° Tensile Strength*	X_T	MPa	1124	ISO 527-4
+45° Tensile Modulus*	E_t	GPa	63.8	ISO 527-4
-45° Tensile Strength*	Y_T	MPa	1237	ISO 527-4
-45° Tensile Modulus*	E_{T22}	GPa	64.5	ISO 527-4
+45° Compressive Strength*	X_C	MPa	595	SACMA SRM1-94
+45° Compressive Modulus*	E_c	GPa	62.0	SACMA SRM1-94
-45° Compressive Strength*	Y_C	MPa	645	SACMA SRM1-94
-45° Compressive Modulus*	E_{C22}	GPa	60.2	SACMA SRM1-94
+45° Flexural Strength	X_F	MPa	815	ISO 14125
+45° Flexural Modulus	E_{F11}	GPa	41.5	ISO 14125
-45° Flexural Strength	Y_F	MPa	1004	ISO 14125
-45° Flexural Modulus	E_{F22}	GPa	57.0	ISO 14125
ILSS	τ_M	MPa	49.7	ISO 14130

*Normalised to 55% fibre volume fraction

NOTICE

All advice, instruction or recommendation is given in good faith but the selling Gurit entity (the Company) only warrants that advice in writing is given with reasonable skill and care. No further duty or responsibility is accepted by the Company. All advice is given subject to the terms and conditions of sale (the Conditions) which are available on request from the Company or may be viewed at Gurit's Website: www.gurit.com/terms-and-conditions.aspx

The Company strongly recommends that Customers make test panels in the final process conditions and conduct appropriate testing of any goods or materials supplied by the Company prior to final use to ensure that they are suitable for the Customer's planned application. Such testing should include testing under conditions as close as possible to those to which the final component may be subjected. The Company specifically excludes any warranty of fitness for purpose of the goods other than as set out in writing by the Company. Due to the varied nature of end-use applications, the Company does, in particular, not warrant that the test panels in the final process conditions and/or the final component pass any fire standards.

The Company reserves the right to change specifications and prices without notice and Customers should satisfy themselves that information relied on by the Customer is that which is currently published by the Company on its website. Any queries may be addressed to the Technical Services Department.

Gurit is continuously reviewing and updating literature. Please ensure that you have the current version by contacting your sales contact and quoting the revision number in the bottom left-hand corner of this page.

TECHNICAL CONTACT INFORMATION

For all other enquiries such as technical queries:

Telephone	+ 44 1983 828000 (08:30 – 17:00 GMT)
Email	technical.support@gurit.com

24-HOUR CHEMICAL EMERGENCY NUMBER

For advice on chemical emergencies, spillages, fires or exposures:

Europe	+44 1273 289451
Americas	+1 646 844 7309
APAC	+65 3158 1412

E customer.support@gurit.com

W www.gurit.com

DOCTORAT
BRETAGNE SCIENCES
LOIRE POUR L'INGENIEUR

Université
Bretagne Sud

Titre : Contribution à l'étude des résistances en compression et au délaminage de composites stratifiés à fibre continues dans le contexte du nautisme de compétition

Mot clés : CFRP, résistance en compression, résistance hors plan, désalignement de fibre, placement de fibres automatisé, drapage manuel, secteur nautique, critères de résistance

Résumé :

Les hydrofoils, des ailes sous-marines en matériau composite stratifié (fibre de carbone, matrice époxy), sont dimensionnés en résistance en compression et en résistance hors-plan. Les contraintes de compression agissent principalement dans la zone de cale basse de l'hydrofoil. Dans le cas de l'inversion de portance, les contraintes hors plan peuvent engendrer une rupture du coude par délaminage. La détermination des deux résistances est encore aujourd'hui un défi. Ces dernières décennies, des modèles micro-mécaniques ont été développés pour décrire le comportement fibre-matrice des stratifiés composites sollicités en compression. L'un des paramètres dominants est l'angle de désalignement de fibres, car il est responsable des instabilités locales de la matrice. Jusqu'à présent, la résistance hors plan a été principalement étudiée dans les secteurs aérospatial et aéronautique, ce sujet n'étant toujours pas entièrement maîtrisé. Les travaux de cette thèse sont divisés en deux parties. La première est consacrée à la confrontation de deux méthodes expérimentales pour déterminer les résistances en compression de sept matériaux (fibre de carbone/matrice époxy) différents. Ces derniers sont fréquemment utilisés dans le secteur nautique. L'accent était mis sur la détermination de l'angle de désalignement de fibres en utilisant la méthode de Yurgartis. Les résistances en compression ont été confrontées en prenant en compte la distribution spatiale de fibres. La deuxième partie traite la confrontation des résistances hors plan des cornières unidirectionnelles en fibre de carbone/matrice époxy, fabriquées à la main et par la technologie de placement automatisé de fibres (AFP). Des essais de flexion quatre points ont été mis en mesure et la résistance hors plan a été déterminée en utilisant les solutions de Lekhnitskii et de Kedward. Des simulations par éléments finis ont confirmées les résultats estimés. Des valeurs plus élevées de la résistance hors plan des cornières fabriquées par AFP ont été discutées en faisant la liaison au processus de fabrication, en particulier au mode de compactage.

Title: Contribution to the investigation of the compressive strength and delamination of continuous fibre laminated composites in the context of competitive sailing

Keywords: CFRP, compressive strength, interlaminar tensile strength, fibre misalignment, automated fibre placement, hand lay-up, nautical sector, strength criteria

Abstract:

Hydrofoils, appendices made from CFRP composite materials, are dimensioned in terms of compressive and out-of-plane tensile strengths. The latter is also called inter-laminar tensile strength (ILTS). Compressive stresses are predominantly acting in the lower bearing zone of the hydrofoil. Out-of-plane tensile stresses may cause the hydrofoil elbow to fail by delamination. The determination of both strengths is a current challenge, to date. In the last decades, micromechanical failure theories have been developed to describe the fibre-matrix behaviour of laminated structures under compression. One dominating parameter is the fibre misalignment angle as it triggers local matrix instabilities. The ILTS was mainly researched in the aerospace and aeronautic sector, to date. However, it is still not a fully mastered issue. The present work is divided into two parts. The first part is devoted to the confrontation of two experimental methods to determine the compressive strengths of seven different CFRP materials, frequently used in the nautical sector. The focus will be on the determination of the fibre misalignment angle using Yurgartis method. The compressive strengths will be confronted with regard to the spatial fibre alignment distributions. The second part deals with the confrontation of the ILTS of unidirectional CFRP L-beam specimens, fabricated by hand lay-up and by automated fibre placement (AFP) technology. Four-point-bending tests were carried out. The ILTS was then determined using Lekhnitskii's and Kedward's solutions. Finite element simulations confirmed the estimated results. Higher ILTS values of AFP L-beam specimens were discussed and related to the fabrication process, especially to the compaction mode.